RL-965

Millimeter-Wave Polarimetric Radar System as an Advanced Vehicle Control and Warning Sensor (Doctoral Dissertation)

Eric Shih-Syou Li

October 1998

RL-965 = RL-965

MILLIMETER-WAVE POLARIMETRIC RADAR SYSTEM AS AN ADVANCED VEHICLE CONTROL AND WARNING SENSOR

by

Eric Shih-Syou Li

A dissertation submitted in partial fulfillment
of the requirements for the degree of
Doctor of Philosophy
(Electrical Engineering)
in The University of Michigan
1998

Doctoral Committee:

Associate Professor Kamal Sarabandi, Chairperson
Professor Fawwaz T. Ulaby
Professor Linda P.B. Katehi
Associate Professor Kim A. Winick
Assistant Research Scientist Adib Y. Nashashibi
Dr. Bakhtiar B. Litkouhi, Staff Research Engineer, GM

ABSTRACT

MILLIMETER-WAVE POLARIMETRIC RADAR SYSTEM AS AN ADVANCED VEHICLE CONTROL AND WARNING SENSOR

by

Eric Shih-Syou Li

Chairperson: Professor Kamal Sarabandi

By its invention at the turn of this century, the automobile has had a revolutionary impact on human society. Since the invention of the early automobiles, much effort has been devoted to providing a safer and more efficient transportation environment. The increasing importance of driving safety issues has initiated a great deal of research activities. The focus is both on minimizing injuries in such accidents as may occur and also in preventing the driving errors which may precipitate these accidents. "Passive" safety features such as seat belts and air bags were developed by the automotive industry, resulting in a significant reduction in fatal injuries due to accidents. Technology now becomes available to further reduce these accident statistics. "Active" safety features are designed to avoid accidents by detecting impending collision or unsafe driving conditions. Many of the new technologies are spin-offs from the aerospace and defense industries. However, the challenge lies not

only in bringing these new technologies to market at affordable prices, but also in integrating them into the complex transportation environment to perform the expected functions. For example, the existing automotive radar sensors have been criticized for their intolerable false alarm rate. This disappointing performance is attributed to the lack of a systematic characterization of the traffic environment.

Radar polarimetry is one way to characterize targets for identification. Besides solving the inherent problems in wave propagation and radar scattering, namely interference, multi-path, and signal to noise ratio, the polarization spectrum can be used to achieve target discrimination when targets fall within the same range gate. However, this application requires a thorough knowledge of the radar scattering behavior of different traffic targets, their associated interactions, and clutter.

This thesis provides both theoretical and experimental approaches to the polarimetric characterization of traffic targets and clutter frequently encountered in the highway environment. Many scattering models are developed to accurately predict the backscatter behavior of road surfaces at near grazing incidence angles. The study examines the backscatter response of road surfaces of different varieties (asphalt and concrete) and surface roughness (smooth and rough), under various weather conditions (dry, wet, ice-covered, and snow-covered). Backscattering from debris and faults on road surfaces as well as from the roadside boundary is also covered in this investigation. The knowledge can be used to design safety features for automotive radar sensors; it also provides valuable information for adaptive cruise control applications. For the purpose of target categorization, a stochastic technique (the genetic algorithm) is developed to search for the optimum polarizations of transmit and receive antennas. This allows multiple target classification using a simple non-polarimetric radar. A prerequisite of this method is the *a priori* knowledge of the

polarimetric response of the intended targets, which can be supplied by the theoretical models. A practical application of the genetic algorithm is the optimum design of an affordable non-polarimetric automotive radar sensor that can assess the physical condition of road surfaces.

This thesis is dedicated to my father Sheng-Hsin and my mother Ho-May for their support and encouragement.

ACKNOWLEDGEMENTS

It has been a long journey, fortunately I am not alone. The foremost of my thanks goes to Professor Kamal Sarabandi who has served as my intelligent radar system and guided me to the destination. His knowledge and insight guarantee zero false alarm on this trip in the academic research realm. His persistence and trust always accompanied me through all the frustration and encouraged me to continue this journey.

I would like to thank Dr. Adib Nashashibi who provided me with all the assistance and training when I started this millimeter-wave research project. I am also grateful to Mr. Craig Wilsen for his enthusiasm in proofreading the entire thesis at the end of my degree pursuit.

During these years in the Radiation Laboratory, I have had the privilege to encounter and interact with many remarkable individuals. My gratitude goes to Dr. Valdis Liepa, Dr. Leland Pierce, Dr. Paul Siqueira, Dr. Roger De Roo, Dr. Tsen-Chieh Chiu, Dr. Jian Gong, Mr. Stéphane Legault, Ms. Rashaunda Henderson, Mr. Bryan Hauck, and Ms. Hua Xie. All of you have made this journey delightful. I would also like to express my appreciation to Ms. Carol Truszkowski and Ms. Sharon Ryder for their long-time support.

Finally I would like to acknowledge an inspiring teacher: Professor Chen-To Tai. His demonstration of the old saying "*Never too old to learn*" in real life has been one of the major impetuses for me to complete this journey.

TABLE OF CONTENTS

LIST OF FIGURES

Figure

LIST OF TABLES

Table

LIST OF APPENDICES

Appendix

CHAPTER I

INTRODUCTION

1.1 Motivations and Objectives

According to the National Highway Traffic Safety Administration, traffic accidents are among the leading causes of death in industrial countries. With the goals of the reduction of the number of traffic accidents and the prevention of physical injury to passengers, the concept of Automated Highway Systems (AHS) has been introduced. The aim of the program is to provide new functionality for highways and public transportation, including improvement of travel efficiency, safety, environmental quality, and energy saving. There are many different elements of AHS technology. Advanced vehicle control systems (AVCS) are an essential part of the AHS program. The collision avoidance sensor is an example of AVCS, proposed for identifying nearby vehicles and other obstacles in order to prevent collisions. A study has shown that 90% of rear-end and 60% of head-on collisions could have been prevented, had the drivers been given one extra second of warning [15]. Advanced sensors that alert drivers to potential hazards on the road (which cause many accidents), such as stationary vehicles and slippery surfaces, could improve traffic safety drastically. Three different sensors have been proposed for AVCS related applications: (1) optical systems (CCD camera), (2) infrared systems, and (3) millimeter-wave (MMW)

radar systems. Optical and infrared based systems offer high resolution and easily interpretable images. Other important information such as the range and velocity of nearby traffic, easily obtained from a MMW radar system, cannot be directly retrieved from these sensors. In addition to this unique feature, performance of MMW radars is not affected by inclement weather conditions, as the electromagnetic wave propagates through fog, rain, and snow. This radar system can also act as a black box that aids in reconstructing the events leading up to the collision. Data gathered by this function can provide invaluable information to insurance adjustors, litigators, and law enforcement officials trying to determine responsibility for the accident. The miniature size of the radar components operating at MMW frequencies make this part of the electromagnetic spectrum most suitable for the AVCS applications.

Advances in MMW technology have made radar an economically viable sensor for automotive applications. In recent years considerable effort has been devoted by the automobile industry and government agencies to the development of these MMW sensors. For example, Eaton VORAD Technologies, Inc. has recently developed a radar based vehicle collision warning system [75]. The system consists primarily of two radars operating at microwave frequencies (less than 30 GHz). The first radar which operates at 10.525 GHz is mounted on the side of the vehicle and is intended to monitor the presence of other vehicles in the "Blind Spot". The second radar which operates at 24.725 GHz is mounted in front of the vehicle and is intended for range and speed detection of other vehicles on the road. Recently, the TRW and MilliTech companies have independently developed MMW radar systems operating at 94 GHz and 77 GHz respectively. However, since roadways are very complex radar environments, the initial optimism in developing MMW automotive radars has not yet led to the development of a radar with a tolerable false alarm rate. The main

reason for the lack of success in this regard can be attributed to the fact that there has not been a systematic effort toward characterization of the backscatter behavior of different traffic targets, their associated interactions, and clutter.

1.2 Radar Polarimetry

In radar scattering problems in which target discrimination cannot be accomplished on the basis of a difference in range, the polarization spectrum (signature) may be the appropriate tool to differentiate between different targets or between targets and clutter. This idea stems from the fact that the polarization for which the radar receives the maximum or minimum scattered power from a target (the optimum polarization) may be different from the optimum polarizations of the other targets or of the surrounding clutter. The literature concerning the application of wave polarization to the enhancement of target detection dates back about five decades to the pioneering work of Kennaugh and Huynen [28,33]. The concept of optimum polarization has long been used by radar engineers to reduce the effect of clutter such as hydrometeors in reconnaissance radars [24,41]. Since the early work of Kennaugh much effort has been devoted towards utilizing the polarimetric responses of targets in inverse problems [7] and in a variety of remote sensing applications [64,70]. Procedures for evaluating the statistics of the polarimetric backscatter responses of distributed targets and their relationship to the target physical parameters have also been investigated intensively [8,13,31,52].

Success of a target discriminator based on the optimum polarization relies on the *a priori* knowledge of Stokes scattering operators [64] of the clutter and the desired target. The Stokes scattering operator of a given target describes its polarimetric radar backscatter response and is influenced by two sets of parameters: (1) radar

parameters such as frequency, polarization, and incidence angle, and (2) physical parameters such as the dielectric constant and shape of the target. There are a number of empirical approaches to discriminate between or classify different targets. These are based on measured radar cross sections (RCSs) and polarization signatures. The polarization signature of a target is generated by computing the RCS for all possible transmit and receive polarization configurations. The RCS is defined as

$$\sigma_{rt}(\psi_r, \chi_r; \psi_t, \chi_t) = 4\pi \, |\hat{p}^r . \boldsymbol{S} . \hat{p}^t|^2$$

where $\hat{p}^i = \mathbf{E}^i/|\mathbf{E}^i|$ $(i = r, t)$ is a unit complex vector specifying the polarization, $\boldsymbol{S}$ is the scattering matrix of the target [64], and σ_{rt} is the RCS at a given transmit (t) and receive (r) polarization. The rotation angle ψ_i and ellipticity angle χ_i define the polarization of a propagating electric field $\mathbf{E}^i$

$$\mathbf{E}^i = \hat{v} + a_i e^{-j\delta_i} \hat{h}$$

where $\hat{v}$ and $\hat{h}$ are orthogonal unit vectors along the vertical and horizontal directions, and

$$\begin{aligned} a_i &= \frac{1 - \cos(2\psi_i)\cos(2\chi_i)}{1 + \cos(2\psi_i)\cos(2\chi_i)} \\ \delta_i &= \tan^{-1} \frac{\tan(2\chi_i)}{\sin(2\psi_i)}. \end{aligned}$$

The benefits of polarization synthesis are demonstrated by considering the radar detection of an angular piece of iron on a road surface. The co- ($\psi_r = \psi_t$ and $\chi_r = \chi_t$) and cross- ($\psi_r = \psi_t + \pi/2$ and $\chi_r = \chi_t + \pi/2$) polarization signatures of a dihedral corner reflector and a dry asphalt surface measured at 94 GHz and incidence angle of 70° are shown in Figure 1.1 and Figure 1.2 respectively. The polarization synthesis of the asphalt surface shows that the maximum co-polarized response occurs at vv polarization while the minimum response is at either right-hand circular (RHC)

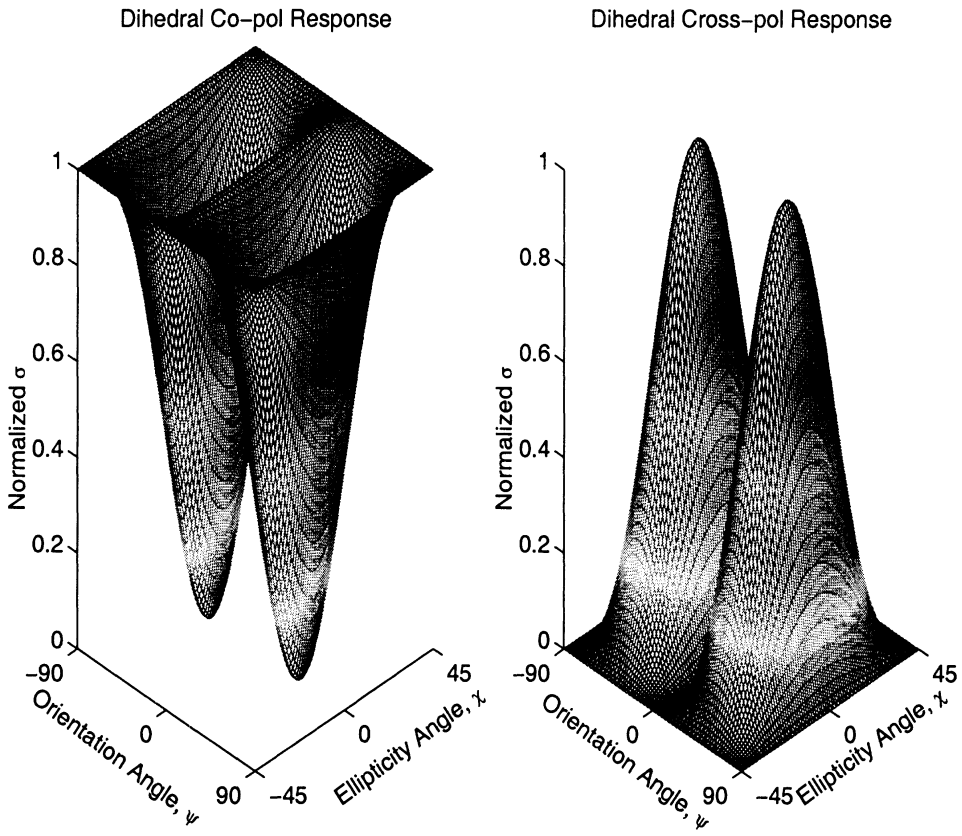

Figure 1.1: Polarization signature of dihedral corner reflector.

polarization or left-hand circular (LHC) polarization ($\chi_t = \chi_r = \pm 45°$). For the iron dihedral on the other hand, the maximum polarization response is at RHC or LHC polarization. Hence, the optimum polarization configuration of a MMW radar for detecting the iron dihedral on asphalt surfaces is circularly polarized transmit and receive antennas.

In the highway environment, a large number of targets may be present within the illuminating beam of the radar system. Depending on their physical extent, targets are categorized into two groups: (1) distributed targets such as an asphalt road, a gravel road, or a plain of short grass, and (2) point targets such as bricks, potholes, scrap metal, or road signs. Accurate knowledge of the polarimetric radar backscatter response (Stokes scattering operator) of these targets as a function of both the radar

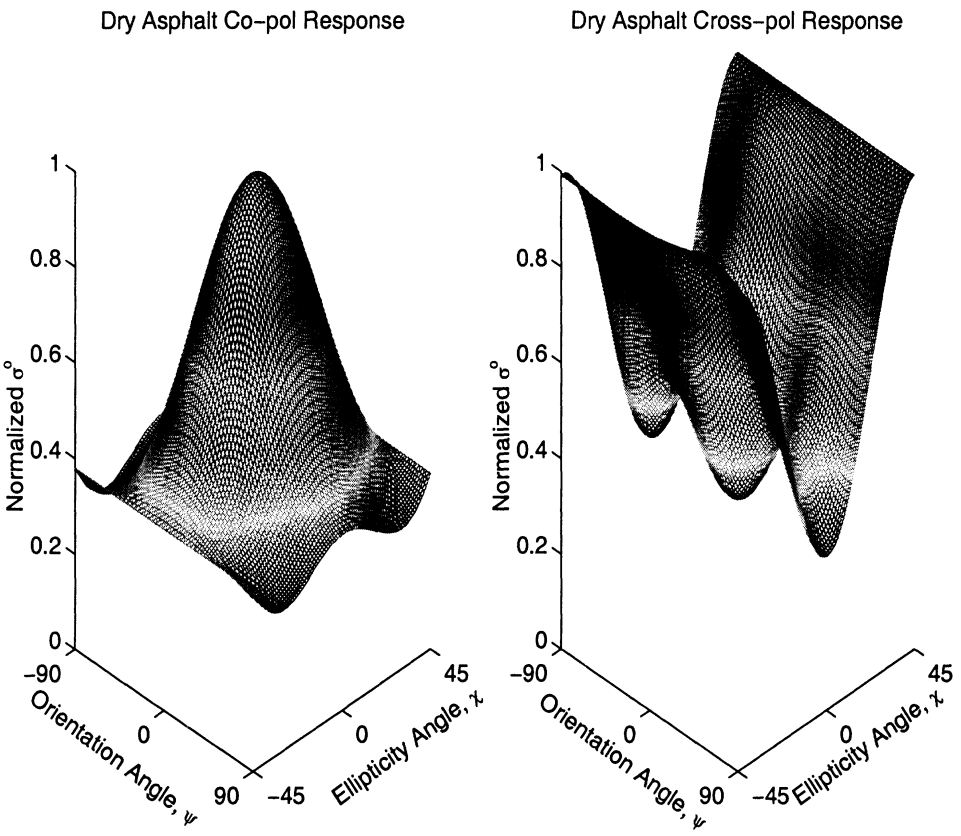

Figure 1.2: Polarization signature of dry asphalt surface measured at an incidence angle of 70° using a 94 GHz polarimetric radar.

and their physical parameters is essential for optimum radar detection. No such data base exists for incidence angles near grazing. In addition, all earlier reported radar measurements of asphalt surfaces at incidence angles less than 70° (from nadir) [21] indicate that the radar backscatter return from an asphalt surface decreases rapidly as the incidence angle increases. Hence, the feasibility of road condition assessment and obstacle detection on the road using a MMW radar sensor must be investigated.

1.3 Approaches

A reliable MMW automotive radar sensor requires complete polarimetric characterization of various traffic targets, their associated interactions, and clutter. The

investigation is pursued both experimentally and theoretically. The experimental approach is focused on the backscatter measurements of various road surfaces under different physical conditions and of faults and debris on asphalt surfaces.

The University of Michigan 94 GHz fully polarimetric radar system was selected to examine the feasibility of employing polarimetric MMW radar systems as reliable AVCS sensors. This is a network analyzer based radar system operating at a 93.5 GHz center frequency with a bandwidth of 1 GHz. The system can perform coherent measurements as well as coherent-on-receive measurements. A mechanical gimbal assembly was constructed for precise positioning of the point target measurements and independent sampling of the distributed target measurements. The azimuthal resolution of 0.1° also enables the system to perform radar imaging.

The backscatter response of road surfaces is a function of many variables, such as the surface roughness, the surface cover, the density, and effective dielectric constant of the pavement material, etc. Comprehensive measurements of the backscatter response of road surfaces under all possible physical conditions would be rather difficult. Analytical scattering models would provide complete polarimetric characterizations of road surfaces. In general, the overall scattering response of road surfaces is composed of volume and surface scattering components. A hybrid volume scattering model based on the radiative transfer method is used to formulate the backscattering coefficients of smooth road surfaces under different weather conditions. Another volume scattering model is needed to predict the backscatter response of snow-covered smooth asphalt surfaces. Experimental results also show that the surface scattering cannot be ignored when the surface roughness parameters become comparable to the radar wavelength. A surface scattering model known as the integral equation method (IEM) is incorporated into the volume scattering model to predict the

backscatter response of rough road surfaces. The validity of these models is then verified experimentally.

Another desired feature for AVCS sensors is target classification in the highway environment. Categorizing targets can be achieved by choosing appropriate polarizations for transmit and receive antennas. With the knowledge of the scattering matrices of point targets or the covariance matrices of distributed targets, the RCSs or the backscattering coefficients for a given pair of transmit and receive polarizations can be determined. A stochastic optimization method based on the genetic algorithm is proposed to search for the optimum transmit and receive polarizations which result in the RCSs or the backscattering coefficients that are most distinct. The genetic algorithm performs the global search for optimization points regardless of nonlinearity in the objective function and the large size of the parameter space. This technique determines the optimal design for polarization states of an affordable AVCS sensor that can assess traction of road surfaces.

1.4 Thesis Overview

This thesis begins with a description of the University of Michigan 94 GHz fully polarimetric radar system in Chapter 2. The principles of operation of the system are outlined first, followed by a description of the function of each major unit. The overall performance of the system is then specified. The distortion parameters associated with the imperfections of the components are characterized by the calibration technique developed earlier for the 35 GHz radar system. These systematic errors are later removed from the measured data during post-processing. The measurement accuracy of the radar system is examined by measuring the scattering matrices of a sphere and a cylinder.

The application of MMW radar imaging to vehicle collision avoidance is studied in Chapter 3. The radar polarimetry technique is proposed to solve the commonly encountered problems of interference, multi-path, and low signal to noise ratio. A high resolution 94 GHz radar system is set up to scan an arranged traffic scene. The chirp z transform transfers the collected frequency-domain data to time-domain data to provide range information. A set of co- and cross-polarized polarimetric radar images is generated for discussion.

Chapter 4 studies the backscatter behavior of smooth asphalt and concrete road surfaces. First, an experimental procedure is developed to determine the effective dielectric constant of pavement mixtures. The vector radiative transfer equation is then used to formulate the backscattering coefficient of a multi-layer medium with one layer being a dense random medium, which represents an ice-covered or water-covered road surface. The co-polarized phase difference statistics are also derived analytically. They can be used in the inversion algorithm to retrieve target parameters. The 94 GHz radar system is used to conduct backscatter measurements on smooth road surfaces at near grazing incidence angles. The phase and extinction matrices are determined from the backscatter response measured under dry condition at one incidence angle. These parameters are then substituted in the radiative transfer formulation to predict the scattering from smooth road surfaces under all conditions. The validity of the models is verified by comparing the simulation results with the corresponding measured response.

Chapter 5 continues the investigation of the backscatter response of other road surfaces. The scattering from snow-covered smooth asphalt surfaces and rough asphalt surfaces is examined here. Besides the volume scattering from pavement mixtures, the scattering from the surface cover (a random medium) or the surface rough-

ness is accounted for in the overall backscatter response. The ground-truth data of the distributed targets are characterized first. The scattering from snow particles is simulated by the Rayleigh scattering model in which the phase and extinction matrices of snow can be determined theoretically and then applied to the radiative transfer equation for the backscattering formulation. The backscatter response of rough asphalt surfaces is determined by incorporating the volume scattering from the pavement mixtures with the surface scattering from the surface roughness. The IEM is selected to characterize the surface scattering. Again, the simulation results of the models are compared with the measured results to verify their accuracy.

The investigation also includes the backscatter response of point targets on road surfaces. Chapter 6 describes the polarimetric characterization of typical faults and debris in the highway environment. The detectability of a target is evaluated by comparing the measured RCS value of the target on road surfaces with the RCS threshold value defined by the backscatter response of the road surfaces and the maximum false alarm rate. The polarization synthesis can be applied here to enhance signal to clutter ratio for target detection. Analytical models were developed to predict the backscatter response of road surface faults and targets with planar facets on road surfaces. The study also includes the backscatter response of roadside boundaries, which could enhance safety features provided by automotive radar sensors.

Chapter 7 introduces the genetic algorithm to characterize the polarization states of non-polarimetric radar transmit and receive antennas for multiple target classification. In this process it is assumed that the polarimetric response of the targets are known *a priori*. This stochastic algorithm offers several advantages over the traditional gradient-based optimization algorithm, however, in the meantime suffers

from computational inefficiency. The procedure for implementing the genetic algorithm is described in detail. The optimization algorithm is applied to two sets of data: (1) synthetic backscatter data for four point targets with similar RCSs, (2) polarimetric backscatter measurements of smooth asphalt surfaces under four different physical conditions at 94 GHz. The convergence performance is described and the final optimum polarizations are listed.

Chapter 8 summarizes the important results derived and the conclusions drawn from this investigation. Suggestions and directions are also given for future work.

CHAPTER II

SYSTEM DESCRIPTION AND CALIBRATION

2.1 Introduction

In order to characterize the polarimetric backscatter behavior of targets encountered in the highway environment at millimeter-wave frequencies, the University of Michigan 94 GHz polarimetric radar system was selected to perform the backscatter measurements of various road surfaces under different physical conditions and of objects on asphalt surfaces. This instrumentation radar system is a network analyzer based system operated at a center frequency of 93.5 GHz with a bandwidth of 1 GHz. It consists of four major units: the network analyzer, the RF unit, the polarization switch, and the control unit. The network analyzer provides the IF signal transmit and receive function; it also supplies the averaging function for system noise reduction and the range-gating function for time-domain data processing. The RF unit up-converts the IF signal received from the network analyzer to a W-band signal. The RF unit also contains a receiver implemented with two orthogonal channels (v and h channels) to down-convert the returned signal to the IF frequency to be processed by the network analyzer. Two polarization switches are cascaded to change the W-band signal to any desired transmit polarization, thereby making the system fully polarimetric. The control unit is responsible for the control of the polarization

switch and the two-dimensional scanning of the gimbal assembly. It also manages the communication between the network analyzer and the personal computer, such as commanding the network analyzer and transferring the measured data. The system can perform coherent measurements as well as coherent-on-receive measurements.

Imperfections of the components in the RF front end degrade the measurement accuracy of the radar system. A calibration procedure is required to remove the systematic errors from the measured data. The systematic errors of the 94 GHz radar system arise from the imperfection of the polarization switch, the antenna cross-talk, and the channel imbalances. Recently a calibration technique was developed for the University of Michigan 35 GHz fully polarimetric radar system by Nashashibi *et al.* [44]. This technique successfully characterizes seven distortion parameters associated with the aforementioned imperfection of the components. Basically this calibration scheme has two stages: (1) a full calibration scheme which is an indoor measurement is used to characterize the time-invariant distortion parameters from passive components, and (2) a short calibration scheme conducted during the field measurement is used to characterize the time-variant distortion parameters from active components. The same approach can be applied to the 94 GHz radar system. The validity of the backscatter measurements of the system is verified by measuring the radar cross sections (RCSs) of targets with known theoretical values. The system demonstrates excellent measurement accuracy and precision.

2.2 System Description

In this section the performance characteristics of the University of Michigan 94 GHz fully polarimetric radar system, see Figure 2.1, are described. In general, polarimetric radars can be categorized into three major groups : (1) coherent radars, (2)

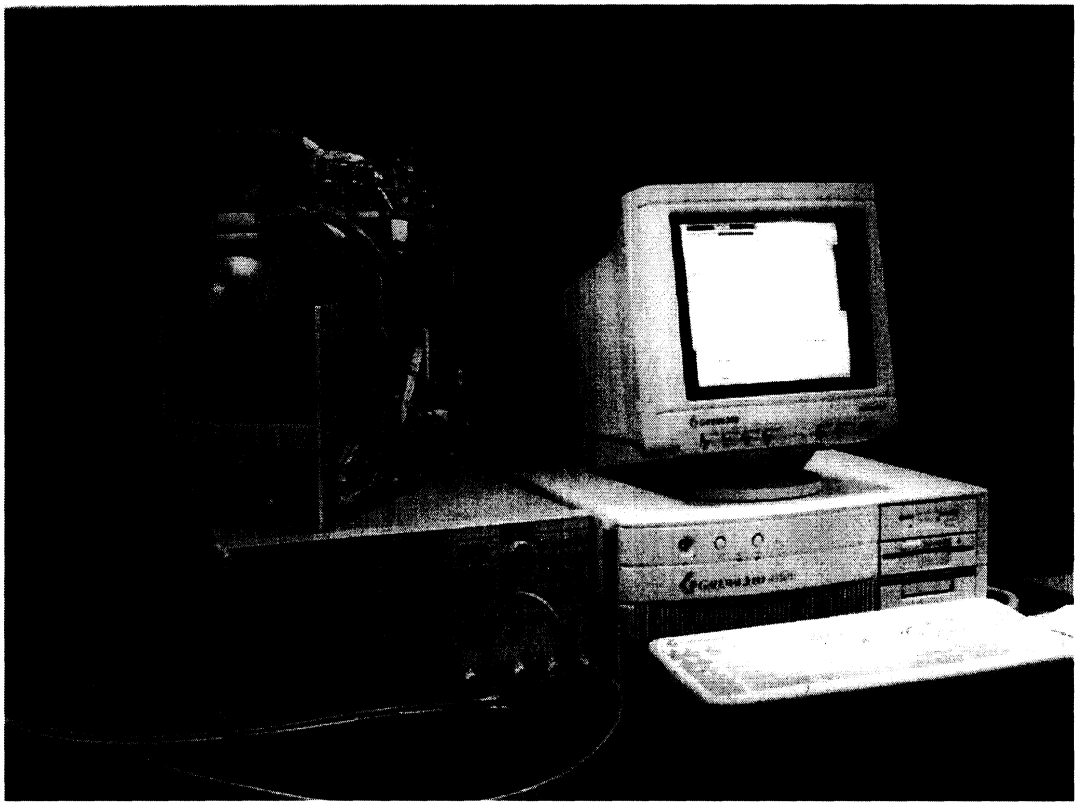

Figure 2.1: The University of Michigan 94 GHz fully polarimetric radar system.

non-coherent radars, and (3) coherent-on-receive radars. To determine the polarimetric response of a target, that is the radar response of the target to any transmit and receive antenna polarization, it is sufficient to characterize the scattering matrix of the target. For this process a coherent radar system capable of measuring both the magnitude and the phase of the backscattered fields received in two orthogonal channels for a combination of two orthogonal transmit polarizations is needed. At 94 GHz, where the wavelength is only 3.2 mm, it is very difficult to maintain the relative position of the radar platform with respect to the target to within a small fraction of a wavelength during the scattering matrix measurements. Therefore, the phase information contained in the elements of the scattering matrix can easily be corrupted due to the movement of either the target or the platform. In these situations coherent radars are incapable of measuring the target polarimetrically. For

distributed targets, the Mueller matrix, which contains the second moments of the scattered fields, is sufficient to characterize the polarimetric response of a target [64]. Non-coherent and coherent-on-receive radars can measure the Mueller matrix directly. The system developed for this investigation is a coherent-on-receive radar which can be used as a coherent radar. For the backscattering case, there are only nine unknown variables in the Mueller matrix. A linear system of equations for nine unknown variables is obtained by measuring the backscatter response to at least four independent transmit polarizations. A global minimization algorithm is employed to estimate the entries of the Mueller matrix. More details of the measurement procedure are given in Section 2.3.

This radar system uses a stepped frequency network analyzer as the IF base for vector transmitter and receiver. The network analyzer also provides functions such as IF detection, processing, and data transfer. The system operates at a center frequency of 93.5 GHz with a bandwidth of 1 GHz, which corresponds to a range resolution of 15 cm. An RF unit is designed to up-convert the network analyzer signal to 93.5 GHz and down-convert the returned radar signal back to the network analyzer frequency. The desired W-band signal is reached by using a single side-band (SSB) up-converter, which passes only the frequency $f_{RF} = f_{LO} + f_{IF}$. The down-conversion stage of the receiver passes only the difference frequency $f_{IF} = f_{RF} - f_{LO}$. Because the up-conversion and down-conversion are driven by the same local oscillator, phase coherence is maintained. Injection phase-locking is employed to keep the RF output power at 0 dBm. Two cascaded polarization switches are placed in the RF output stage. The polarization state of the transmitted wave can be changed by rotating dielectric cards inside the polarization switches. The receiver has two orthogonal ports, vertical and horizontal, which enable the system to measure the magnitude

and the phase of both orthogonal components of the scattered wave. A 486 processor based computer is the main control unit. It communicates with the network analyzer for data processing and data acquisition. It is also equipped with a motion control card to facilitate the mechanical function of the polarization switches and the two-dimensional scanning of the mechanical assembly.

2.2.1 The RF Unit

The simplified block diagram of the 94 GHz RF unit is shown in Figure 2.2. This unit comprises three major modules : (1) transmitter module, (2) bistatic transmit antenna module, and (3) transceiver module. In order to maintain the phase coherence between the up-converter and down-converter mixers in either backscatter or bistatic modes, an X-band microwave oscillator is shared by both mixer modules. This is the fundamental source, with a frequency one eighth the desired frequency of the local oscillator for the up- and down-conversion. This X-band signal is amplified to about 30 dBm and then split into two branches, one feeding the transmitter module, the other feeding the transceiver module.

The transmitter module includes a $\times 8$ multiplier, a stabilized local oscillator, and an up-converter mixer. The X-band source feeds the $\times 8$ multiplier which in turn is connected to an injection-locked Gunn oscillator. The Gunn oscillator is therefore phase-locked to the X-band source. The chirp-like output of the network analyzer (IF) is up-converted to the desired transmitted signal. The RF output power of the 94 GHz system is about 0 dBm. A self-contained hybrid circuit heater is attached to the Gunn oscillator to keep this unit thermally stable. The temperature is controlled by an external resistor. For the bistatic and coherent-on-receive modes the RF output of the transmit module is connected to the bistatic transmit antenna module and for

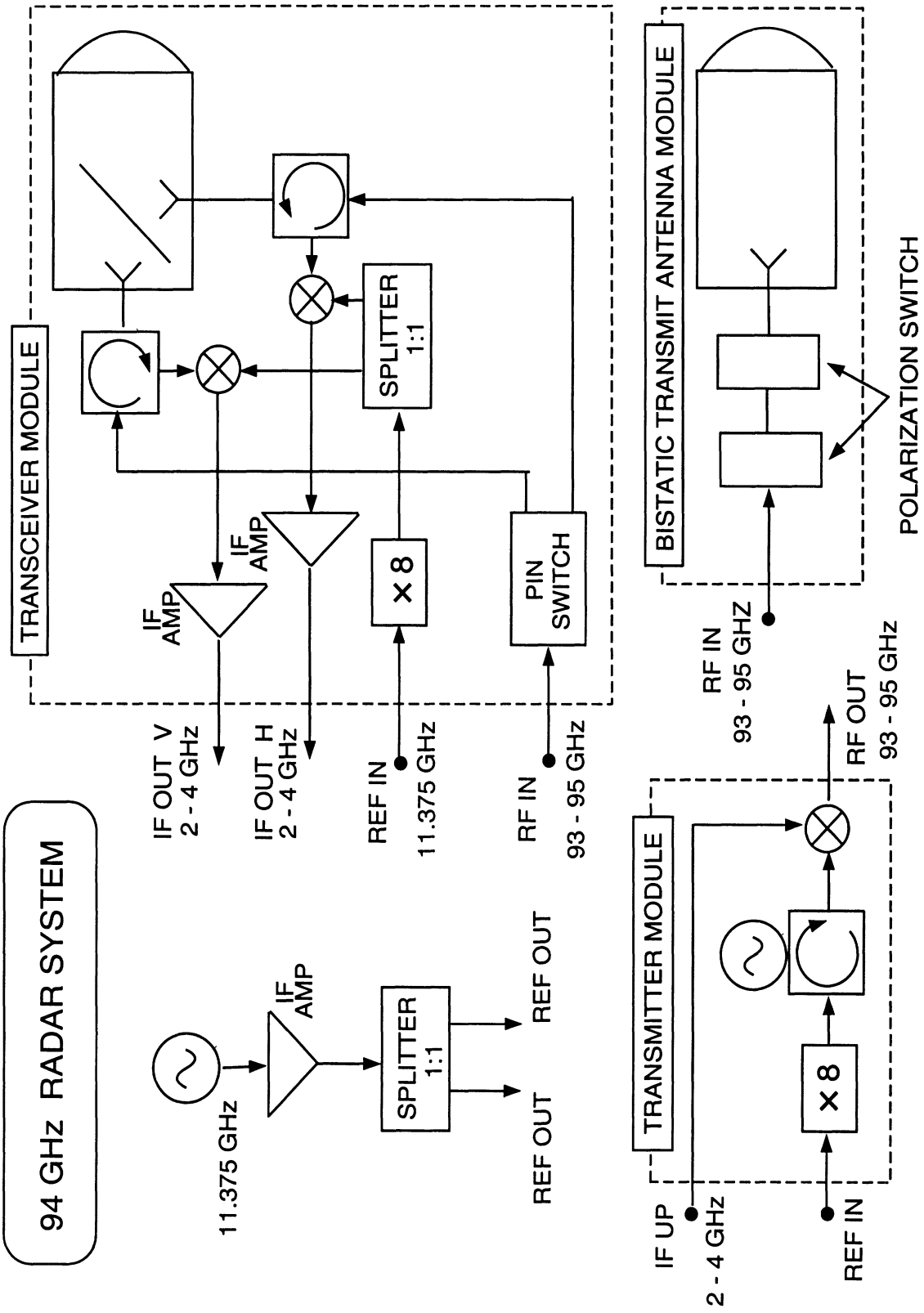

Figure 2.2: The block diagram of the RF unit of the University of Michigan 94 GHz radar system.

the monostatic mode the output is connected to the transceiver module.

The bistatic transmit antenna module consists of two polarization switches and a horn antenna. The transmit polarization of the radar system in bistatic and coherent-on-receive modes is controlled by two cascaded polarization switches. The bistatic mode transmit antenna is a lens-corrected corrugated circular horn with a Gaussian radiation pattern and a 2.8° beamwidth. In the coherent-on-receive mode the transmit module is used in either backscatter or bistatic mode to transmit a number of pre-specified polarizations.

The transceiver module is designed to operate as a transmitter and a receiver in the monostatic configuration as well as a receiver in the bistatic configuration. This module comprises a dual polarized antenna, a pair of mixers, a pair of IF amplifiers, a $\times 8$ multiplier, and a splitter. In addition, an SPDT PIN switch and a pair of circulators are included for monostatic operation. The antenna of the 94 GHz transceiver uses two separate corrugated horns and a polarization wire grid between the horns and the lens. The beamwidth of this antenna is 1.4° after lens correction. The far-field condition for the antenna is

$$R \geq \frac{2D^2}{\lambda}$$

where D is the antenna lens diameter. The lens diameter is 15 cm and therefore the far field for this 94 GHz system is $R \geq 15.6$ m. However, our experimental results show that the radiation pattern of this antenna does not change even for $R \geq \frac{D^2}{2\lambda}$. In the monostatic mode the RF output of the transmitter module is connected to the RF input of the transceiver module via a waveguide. Using the PIN switch, the desired transmit polarization (v or h) is selected. The receiver local oscillator, similar to the transmitter LO, is phase-locked by the reference X-band source. Using two

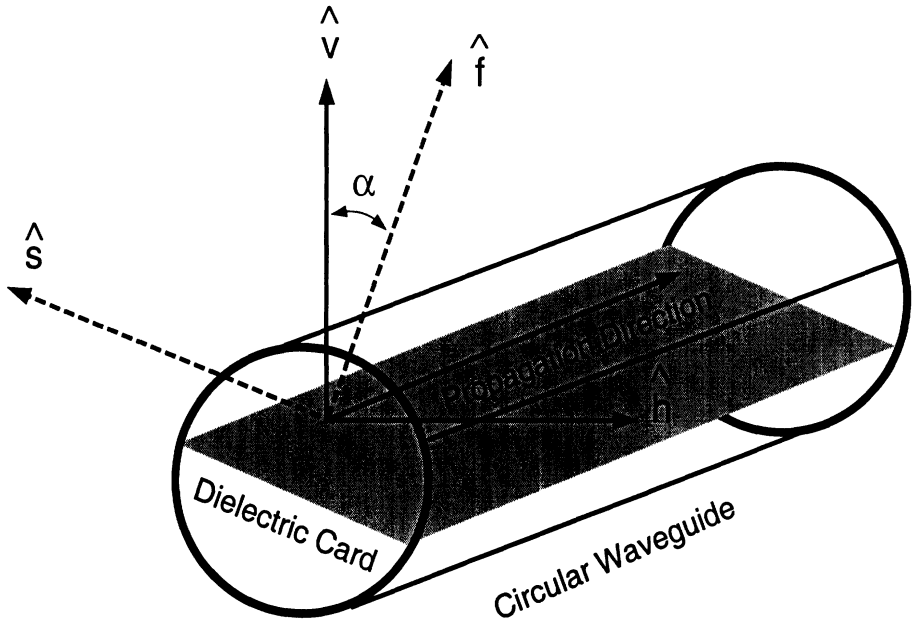

Figure 2.3: The schematic structure of the polarization switch.

balanced mixers the received signals in both v and h channels are down-converted to the IF frequency and then amplified before going to the network analyzer for further analysis and data transfer. The minimum backscattering coefficient that can be measured (noise equivalent backscattering coefficient) for this 94 GHz radar system at a range of 10 m is about -50 dB.

2.2.2 The Polarization Switch

The structure of polarization switch is shown in Figure 2.3. It consists of a circular waveguide containing a thin dielectric card that is rotatable. The thickness and dielectric constant of the dielectric card are chosen such that the reflected field is minimal over the desired bandwidth of operation. The polarization state of the transmitted wave is determined by the orientation angle of the card with respect to the polarization state of the incoming wave. When the incoming wave enters the polarization switch, the propagation constants for the electric fields perpendicular and parallel to the dielectric card are different. The perpendicular component trav-

els faster than the parallel component and therefore the polarization state of the incoming wave changes. Suppose the transmission coefficients of the card for the waves whose electric fields are parallel (slow wave) and perpendicular (fast wave) to the dielectric card are, respectively, denoted by the complex quantities Υ_s and Υ_f. Further assume that the card is oriented such that it makes an angle α with respect to the vertical direction which is defined as the direction of the electric field at the dominant mode of the rectangular waveguide connected to the rectangular-to-circular transition which feeds into the polarization switch. The unit vectors parallel and perpendicular to the card are denoted by $\hat{s}$ and $\hat{f}$ and are given by

$$\begin{aligned} \hat{s} &= \sin\alpha\,\hat{v} - \cos\alpha\,\hat{h} \\ \hat{f} &= \cos\alpha\,\hat{v} - \sin\alpha\,\hat{h}. \end{aligned}$$

If the wave incident on the card is denoted by $\mathbf{E}^i = E_v^i\hat{v} + E_h^i\hat{h}$, then by decomposing each component into components along $\hat{f}$ and $\hat{s}$ and multiplying the resultant components by the corresponding transmission coefficients Υ_f and Υ_s, the outgoing field through the polarization switch can be obtained from

$$\mathbf{E}^o = \bar{\mathbf{T}}\mathbf{E}^i$$

where $\bar{\mathbf{T}}$ is the polarization transformation matrix given by

$$\bar{\mathbf{T}} = \begin{bmatrix} \cos^2\alpha\Upsilon_f + \sin^2\alpha\Upsilon_s & \sin\alpha\cos\alpha(\Upsilon_f - \Upsilon_s) \\ \sin\alpha\cos\alpha(\Upsilon_f - \Upsilon_s) & \cos^2\alpha\Upsilon_s + \sin^2\alpha\Upsilon_f \end{bmatrix}.$$

By cascading two such polarization switches and ignoring reflections from the cards, the transmitted wave $\mathbf{E}^t$ at the output of the cascaded polarization switches is related to the incident wave $\mathbf{E}^i$ by

$$\mathbf{E}^t = \bar{\mathbf{T}}_1\bar{\mathbf{T}}_2\mathbf{E}^i$$

Rotational Angles	v	h	45°	135°	LHC	RHC
α_1	0°	45°	0°	0°	45°	−45°
α_2	0°	45°	45°	−45°	0°	0°

Table 2.1: The rotational angles of the dielectric cards for the desired polarization states of the transmitted waves.

here $\bar{\mathbf{T}}_1$ and $\bar{\mathbf{T}}_2$ are the transformation matrices of the first and the second polarization switches corresponding to the rotational angles α_1 and α_2 respectively. Assume that the electric field in the rectangular waveguide preceding the polarization switches coincides with the specified vertical direction $\hat{v}$: $\mathbf{E}^i = T_t(1,0)$, T_t is the transmitter transfer function. Introduce the parameters $\tau_i = \frac{\Upsilon_{si}}{\Upsilon_{fi}}$ $(i = 1,2)$. The transmitted wave through the polarization switches is then given in terms of τ_i and orientation angles α_i by

$$\mathbf{E}^t = T \begin{bmatrix} \cos(\alpha_1 - \alpha_2)(\cos\alpha_1 \cos\alpha_2 + \tau_1\tau_2 \sin\alpha_1 \sin\alpha_2) \\ +\sin(\alpha_1 - \alpha_2)(\sin\alpha_1 \cos\alpha_2\tau_1 - \cos\alpha_1 \sin\alpha_2\tau_2) \\ \\ \cos(\alpha_1 - \alpha_2)(\sin\alpha_1 \cos\alpha_2 - \cos\alpha_1 \sin\alpha_2\tau_1\tau_2) \\ -\sin(\alpha_1 - \alpha_2)(\cos\alpha_1 \cos\alpha_2\tau_1 + \sin\alpha_1 \sin\alpha_2\tau_2) \end{bmatrix}$$

where $T = T_t\Upsilon_{f1}\Upsilon_{f2}$. The nominal value for τ_i is $e^{-j\frac{\pi}{2}}$ and for this value Table 2.1 gives the combination of rotational angles for the desired polarization states. The precise rotation of the dielectric card inside the circular waveguide is achieved by a computer-controlled DC motor and optical encoder. An interactive user interface program written in *Microsoft Visual Basic* gives commands to the motion control card for selecting different polarization states of transmitted waves. The pulse-form output of the motion control card is amplified by the pulse width modulation (PWM)

servo amplifier which in turn drives the brush-type DC motor. The rotation mechanism of the dielectric card is accomplished by the DC motor through two gears of different sizes. The circular waveguide with the dielectric card is attached concentrically to a large gear. This gear is driven by a small gear which in turn is driven by the DC motor. The teeth ratio of these two gears is chosen to be 4.61:1 in order to obtain better resolution of the rotational angle for the larger gear. An incremental encoder is used to record the rotational angle of the DC motor shaft. Employing a feedback circuit for the motion control card, automatic error correction is accomplished. Angle measurement requires a reference position, which is chosen to be a very narrow slot on the large gear. The location of the reference point is introduced to the computer via an optocoupler transducer.

2.2.3 The HP8753 Network Analyzer

An HP8753C Network Analyzer with time-domain capability is employed as the vector transceiver of this system. The network analyzer has two receive ports which allow the reception of v and h channels simultaneously. The operation and measurement procedures can easily be programmed and controlled by a computer over an interface bus. A program written in *Microsoft Visual Basic* is used to set the desired parameters of the network analyzer and to collect and store data. The IF center frequency is set to 2.5 GHz and a bandwidth of 0.5 GHz is selected for outdoor measurements (the bandwidth could be as high as 1 GHz). In order to avoid the aliasing problem in the time domain, the number of sampling points is chosen to be 201. Based on the above setting, Δf is equal to 2.5 MHz. The quantity $\frac{1}{\Delta f}$ sets the upper limit of the time-domain span without aliasing. In our case the upper limit for the time-domain span is 400 ns. This span covers the range up to 60 m

which is sufficient for the AHS applications at near grazing angles. If higher range resolution were required, then the number of sampling points would also need to be increased to keep the same time-domain span. In that case a longer sweep time and more space for data storage would be required. The averaging function of the network analyzer can be activated to reduce the noise level of the received signal. This function is sometimes needed for near grazing angle measurements. One of the most useful processing options available on network analyzers is the time-domain operation. Because the returned signal is measured as a function of frequency, a real-time Fourier transform technique can be applied to obtain the time-domain response. In the backscatter case, this result is a measure of the radar return as a function of range. By using the time-gating technique, the signal returned from the target of interest at a particular range can be isolated from the signals scattered from other objects and the leakage signal from transmitter to receiver. The time-gated signal can then be transformed back to the frequency domain to obtain the frequency response of the target. Besides the aforementioned complicated signal processing capabilities the network analyzer also features data storage and complex math functions which are used in a calibration algorithm developed to remove systematic errors.

2.2.4 The Control Unit

A 486 processor based computer is the main control unit. *Microsoft Visual Basic* creates an interactive environment to allow efficient operation. An HP-IB card provides not only the communication between the network analyzer and the computer, but also the data transfer function. The combination of a motion control card and two linear actuators gives the system the capacity to scan in two dimensions. A computer-controlled mechanical assembly is built for the purpose of radar scanning

in horizontal and vertical directions. The motion control card receives commands from the user through a user interface program written in *Microsoft Visual Basic.* The pulse-form outputs of the motion control card, after being amplified by PWM servo amplifiers, are used to drive the DC motors which in turn drive the linear actuators. The motion of the linear actuator enables the radar to scan horizontally and vertically. Again, an incremental encoder is employed to monitor the angular rotation of the radar. Automatic error correction is done by the feedback circuit to the motion control card. The same mechanism is used by the polarization switch to change the polarization state of the transmitted wave. The voltages of power supplies used for the entire system are 18 V and 12 V; total current consumption is 4.5 A. Over-voltage protection circuits are implemented for every RF component. When the supplied voltage is above the rated voltage, the circuit automatically shuts off the system to protect the component and turns LED lights on to indicate an over-voltage situation. A solid state laser is installed parallel to the bore-sight direction of the radar system to facilitate pointing the radar toward the desired target such as a small calibration sphere.

2.3 System Calibration

Measurement accuracy and precision are critical elements of any meaningful analysis or interpretation of the measured data. Accurate knowledge of the scattering matrix of a target is important for extracting information from the target. The polarimetric radar is designed to measure the scattering matrix. In practice it is impossible to build an ideal polarimetric radar system to measure the scattering matrix or the Mueller matrix of a target. For example, it is not possible to construct antennas that are totally free of polarization contamination due to finite manufactur-

ing tolerances. The polarization state of the transmitted wave primarily depends on the orientation of the dielectric card inside the polarization switch and the transmit antenna polarization cross-talk can slightly modify the polarization state. Another factor that affects the measurement accuracy is the receive channel imbalances which include the variation in magnitude and phase of the system transfer functions for two ports of the receiver. These imperfections in the radar system components can lead to significant errors in the measured Mueller matrix. The purpose of calibration is to remove the systematic imperfections of the radar components from the measured scattered fields before constructing the measured Mueller matrix. An accurate calibration technique was recently developed at the University of Michigan for the 35 GHz radar system. The same approach can be used for the 94 GHz radar system. The procedure is briefly described below.

The sources of systematic errors are : (1) differences in the gain of each channel known as channel imbalances, (2) the cross-talk factors, and (3) the amplitude and phase variations of the polarization switches. In general, these errors can be represented by seven distortion parameters : τ_1, τ_2 (transfer functions of the polarization switches 1 and 2 respectively), c_1, c_2 (cross-talk factors of the receive antenna), c_3 (cross-talk factor of the transmit antenna), R_1, and R_2 (the receiver transfer functions describing channel imbalances). The distortion parameters τ_1, τ_2, c_1, c_2, and c_3 are time-invariant quantities because of the passive nature of the polarization switches and the antennas. Removing the systematic errors from the radar measurements of a target of interest involves two steps: (1) characterization of the system distortion parameters *via* a calibration technique, then (2) application of an inverse algorithm (i.e. correction algorithm) to the measured data.

The standard approach in finding the distortion parameters is to measure tar-

gets with known scattering matrices. A metallic sphere is an excellent candidate because its scattering matrix is orientation-independent and its RCS is known theoretically. However, measurement of only a metallic sphere, even for many transmit polarizations, is insufficient to determine the seven unknown distortion parameters of the radar system. The measurement of an additional independent de-polarizing target is needed in order to determine all distortion parameters. By applying the reciprocity theorem, the scattering matrix of the additional target need not to be known. In effect, system calibration is performed in two steps and requires measuring the backscatter response of a metallic sphere in addition to any de-polarizing target for four and two transmit polarizations respectively. Note that parameters R_1 and R_2 are affected by the instability of active components in the radar system and are time-variant parameters. Once the distortion parameters have been determined using the two calibration targets, a simpler procedure of employing only a sphere can be used to find R_1 and R_2 in subsequent calibration of the radar.

2.3.1 Application of the Calibration Technique

To demonstrate the applicability of the calibration technique to the 94 GHz radar, the distortion parameters of the system were first characterized by measuring a metallic sphere (2.54 cm diameter) and a tilted wire grid (de-polarizing target). Then, the scattering matrices of two canonical targets, acting as test targets, were measured and compared to their theoretical values.

During these measurements, in order to obtain only the sphere backscatter response, background subtraction is used, which involves subtracting the response without the sphere from the response with the sphere. The same procedure is used for the de-polarizing target. In the meantime, to increase the signal to noise ratio,

the averaging function of the network analyzer is applied. For post-processing, the time-domain gating technique is used to isolate the response of the sphere or the de-polarizing target from the response of other targets. The measured magnitude and phase of the polarization switch transfer functions (τ_1 and τ_2) are shown in Figure 2.4 as a function of frequency. It is shown that the magnitude and phase of τ_1 and τ_2 are very close to the theoretical values of 1 and $-90°$. The measured antenna cross-talk factors of the system are shown in Figure 2.5. It should be noted that the channel imbalance parameters R_1 and R_2 may vary slightly due to changes in ambient temperature. Thus a short-term calibration before and after each RCS measurement may be necessary. For the short-term calibration procedure, a metallic sphere is used as a calibration target and only two polarizations, linear 45° and linear 135°, are used to characterize R_1 and R_2. To reduce the effect of thermal noise in the calibration procedure, the target response is measured ten times for each transmit polarization and then averaged.

The validity of the calibration technique is examined by measuring the scattering matrices of a cylinder and a sphere as test targets and comparing them with their theoretical values. Figure 2.6 shows the theoretical and the measured scattering matrix elements of a sphere with a diameter of 2.54 cm. The error in magnitude of the co-polarized terms is less than 0.2 dB and the error in phase difference between the co-polarized terms is less than 1°. Excellent agreement is also achieved between the theoretical and the measured scattering matrix elements of a vertical cylinder of length 3.7 cm and diameter 0.155 cm. Figure 2.7 shows that the discrepancy is less than 1 dB in magnitude and 2° in phase difference. The experiments were repeated many times and consistent results were achieved.

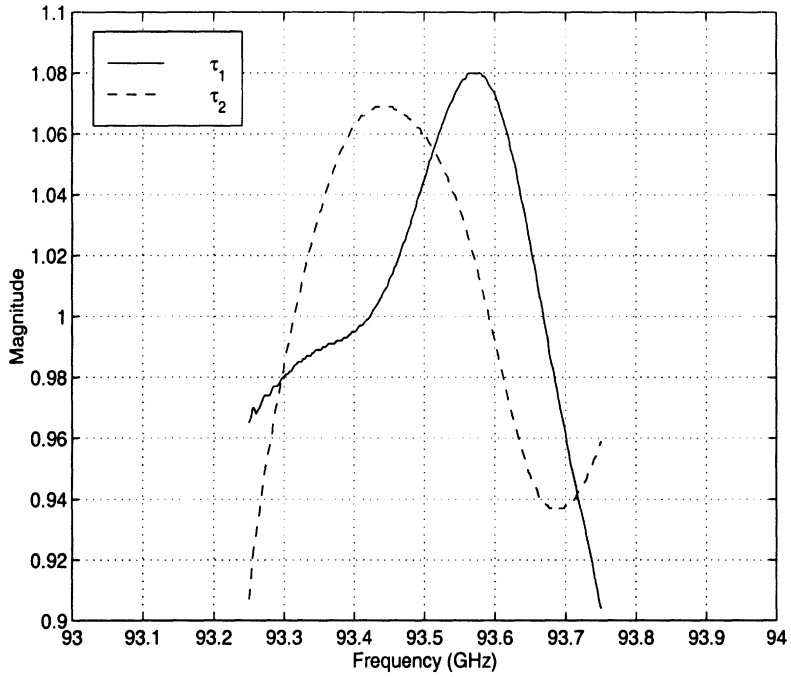

2.4(a)

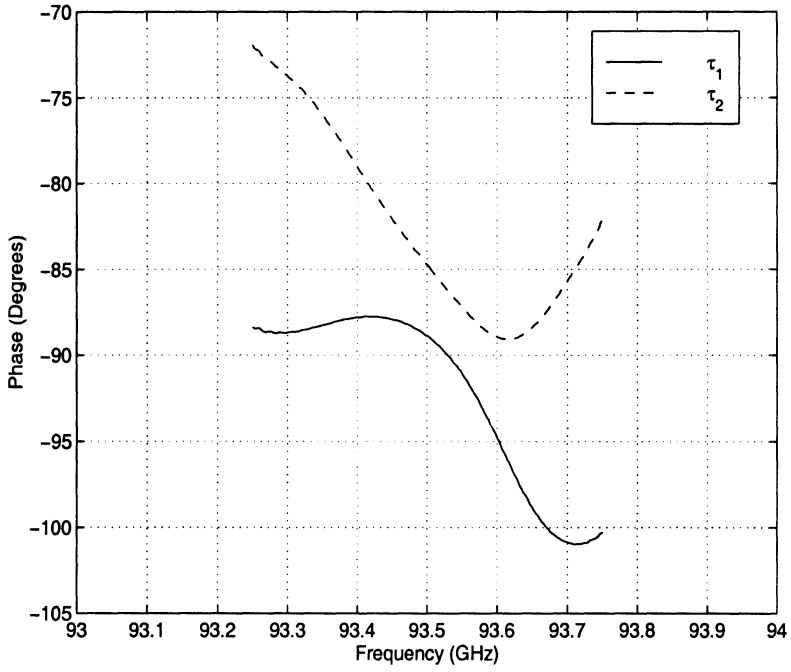

2.4(b)

Figure 2.4: The frequency variations of the (a) magnitude and (b) phase of τ_1 and τ_2.

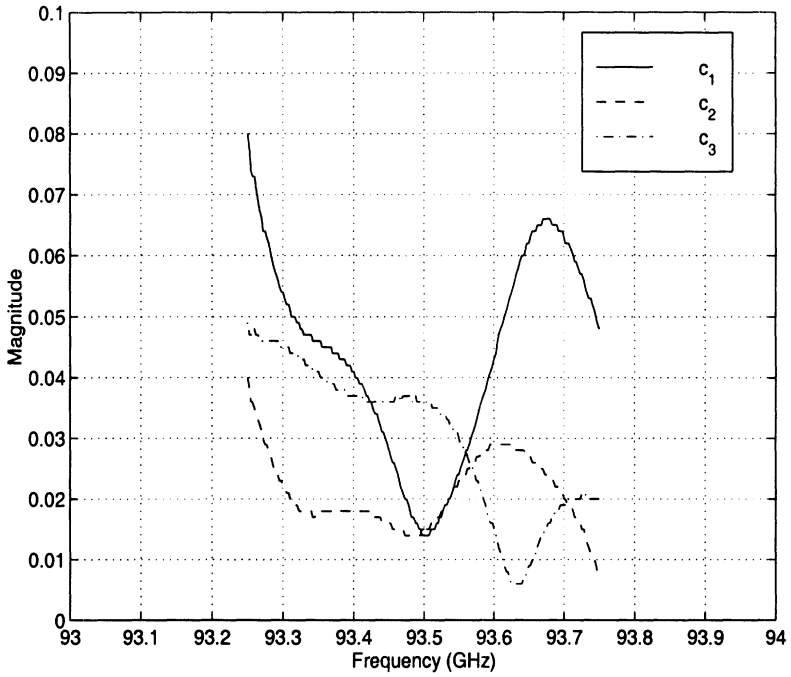

2.5(a)

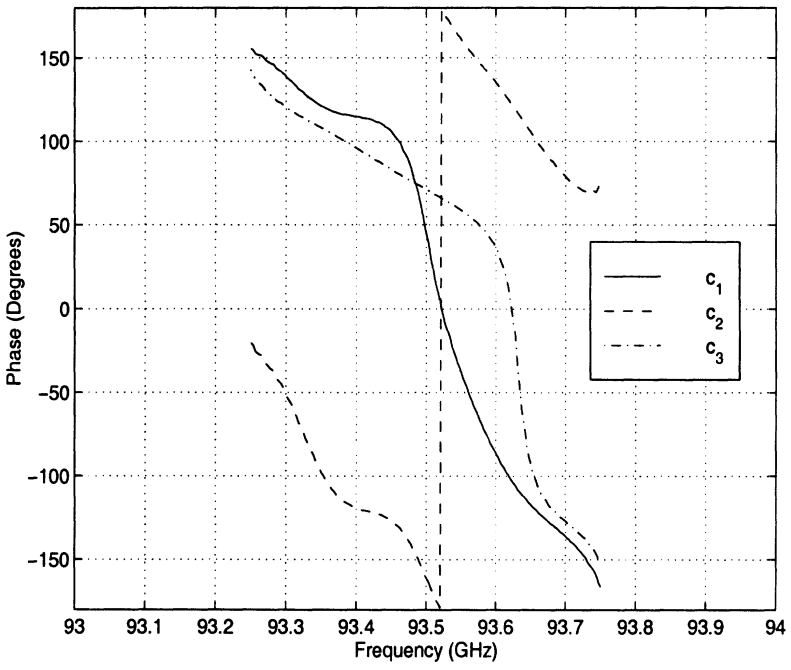

2.5(b)

Figure 2.5: The frequency variations of the (a) magnitude and (b) phase of c_1, c_2, and c_3.

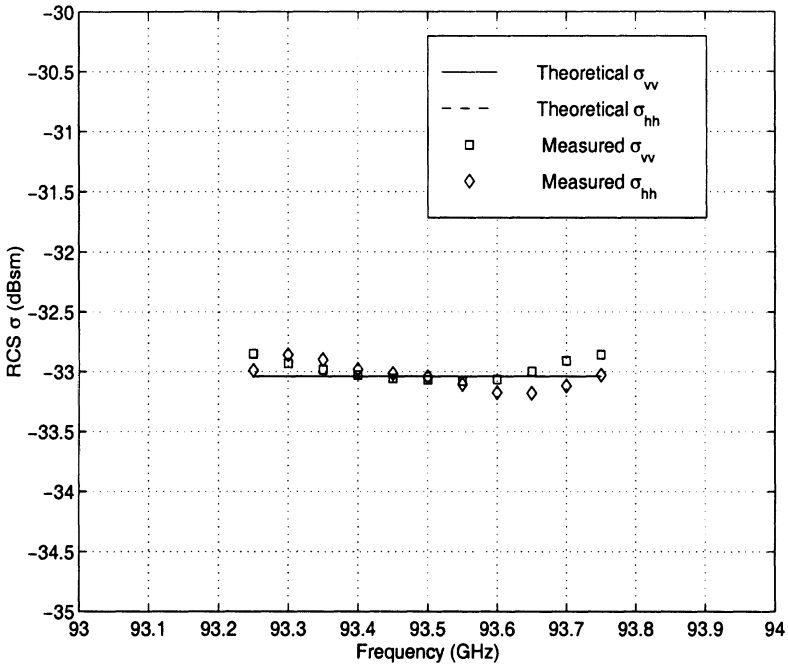

2.6(a)

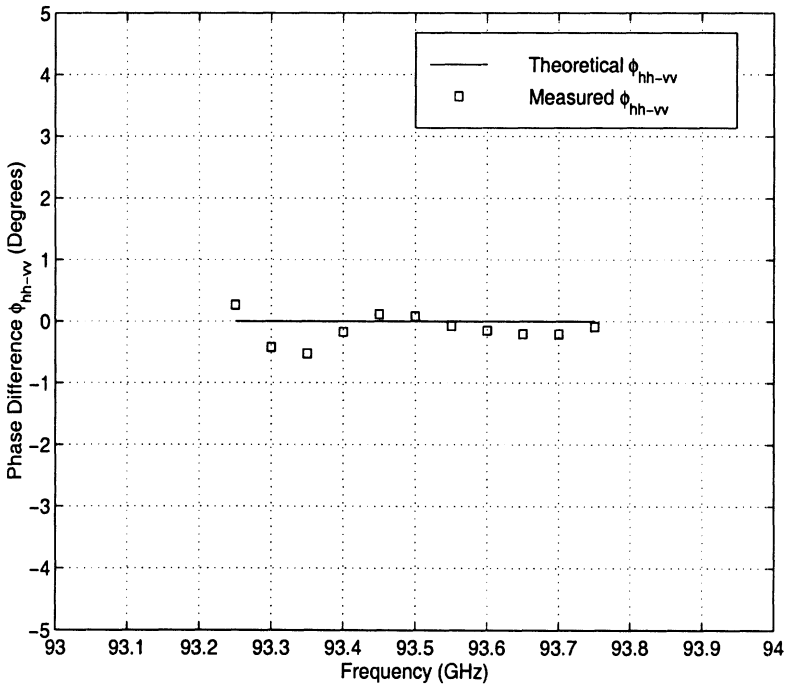

2.6(b)

Figure 2.6: The (a) magnitude and (b) phase difference of the scattering matrix elements of a sphere with a diameter of 2.54 cm.

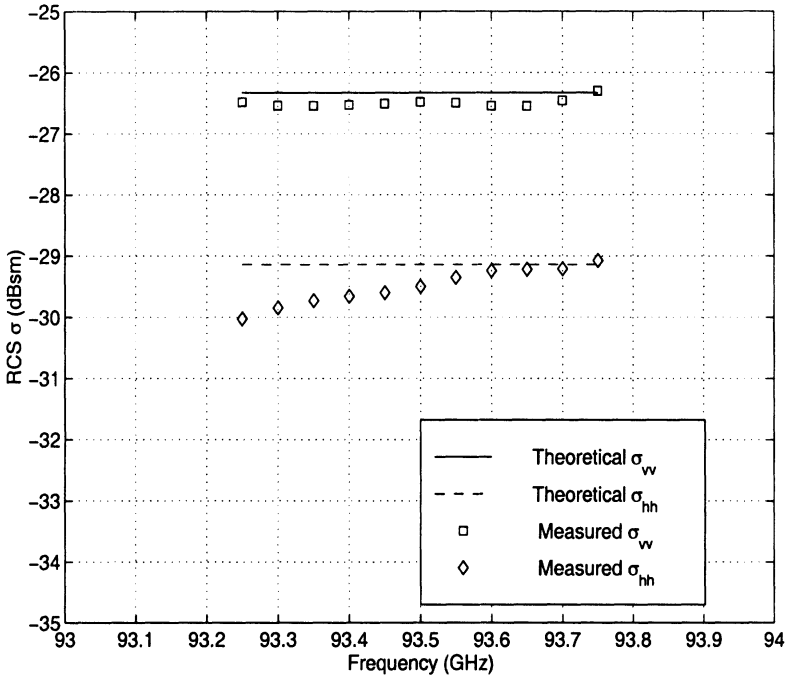

2.7(a)

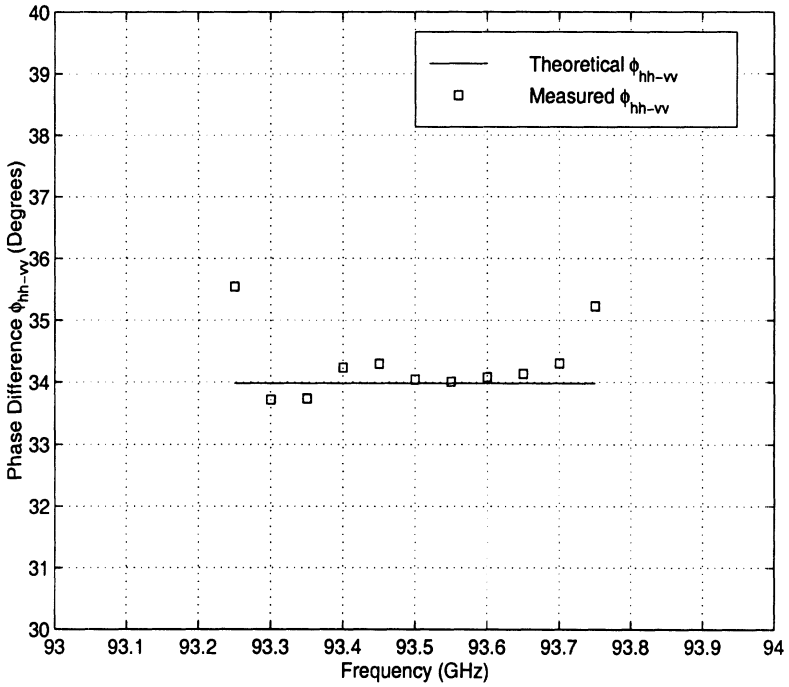

2.7(b)

Figure 2.7: The (a) magnitude and (b) phase difference of the scattering matrix elements of a vertical cylinder of length 3.7 cm and diameter 0.155 cm.

2.4 Conclusions

An instrumentation radar system is constructed to facilitate the polarimetric characterization of various road surfaces and objects in the highway environment. It is a network analyzer based system with a 93.5 GHz center frequency and a 1 GHz bandwidth. The system has four major units: the RF unit, the polarization switch, the network analyzer, and the control unit. The function of each unit is described. A calibration technique is employed to remove the systematic errors from the measured data. These errors include the imperfections of the polarization switch, the antenna cross-talk, and the channel imbalances. The overall performance of the system is evaluated by comparing the measured RCSs of the targets with their theoretical values. The results show that the system provides excellent accuracy for backscatter measurements.

CHAPTER III

MILLIMETER-WAVE POLARIMETRIC RADAR IMAGING

3.1 Introduction

A millimeter-wave (MMW) polarimetric radar system is considered for applications related to vehicle collision avoidance because it offers a number of advantages over other sensors (e.g. optical or infra-red). However, unless properly addressed in the design stage, the success of a MMW radar in a complex highway environment can be severely hampered by three unfavorable attributes of wave propagation, namely interference, multi-path, and low signal to noise ratio. It should be noted that the primary function of this radar is to transmit a signal through its directive antenna to a pre-specified portion of the 3-D space, then "listen" to the echo return from the designated space as a function of time. For proper radar operation, it is desired that all signals received during the "listening" period be the echo returns of the radar's own transmitted signal. The radar distance to a target is determined from the travel time of the radar signal. Signal interference and multi-path, when present, will therefore degrade the radar performance, unless they are properly characterized and subsequently minimized.

Interference occurs when the radar receiver detects a signal transmitted by a

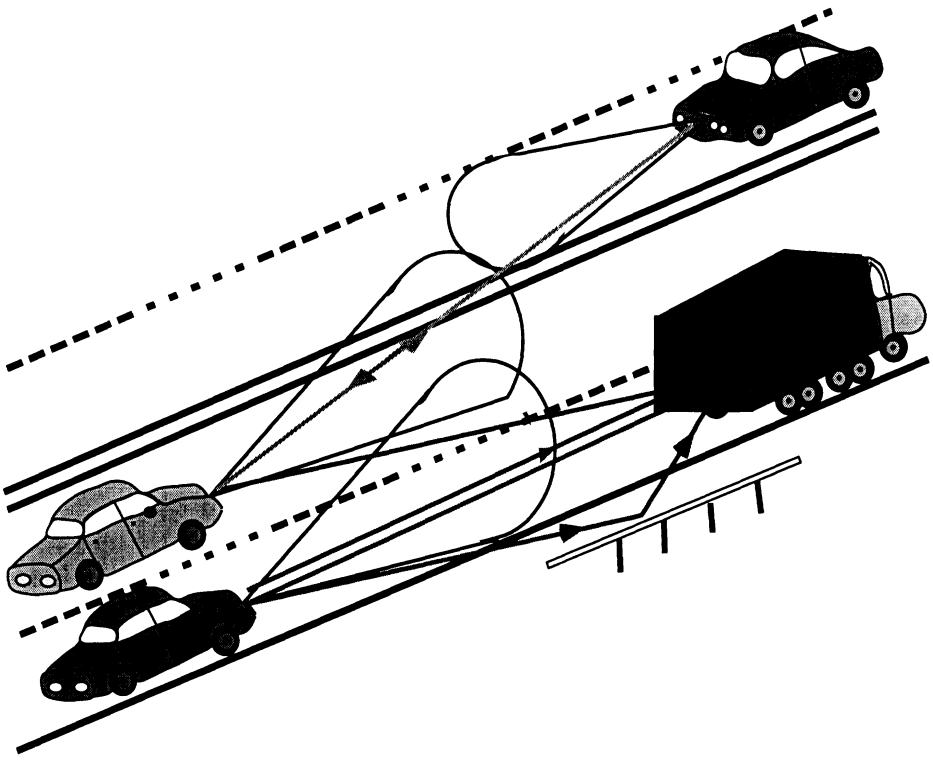

Figure 3.1: An example of how signal interference and multi-path can occur in a complex highway environment.

source other than the radar itself. As depicted in Figure 3.1, a simple form of interference can occur when the vehicle's radar receives signals transmitted by other vehicles' radars, either through a direct path for vehicles moving in opposite directions or through an indirect path for vehicles moving in the same direction. In the case of vehicles moving in opposite directions the receivers of both radars may become saturated, while in the case of adjacent vehicles, interference may result in false prediction of the target location. A possible solution to the first problem is that all vehicle radar sensors transmit and receive in orthogonal polarizations. In this configuration the direct path signal between two opposing cars will be attenuated by the polarization isolation of the two orthogonal antennas. In automotive radar applications, where the objective is to detect the traffic on the road, the received signals may include the radar returns from the desired targets and undesired targets

(clutter) such as off-road objects, road surfaces, etc. The presence of clutter in the radar returns increases the false alarm rate and in effect acts as noise corrupting the desired signal. With the proper choice of transmit and receive polarizations, it is possible to enhance the backscatter signals from the desired targets and at the same time to suppress the returns from a set of undesired targets. This is the fundamental reason behind investigating the polarimetric responses of targets at MMW frequencies in this study.

Multi-path occurs when the radar signal reflected from the intended target experiences a single reflection or multiple reflections from other objects, such as the road surface, off-road objects, or other vehicles, before reaching the radar. Since multi-path signals arrive at different time, the radar may falsely register the presence of multiple targets (ghost targets) instead of just one.

In an attempt to understand some of these problems and examine the possible advantages of radar polarimetry, high resolution polarimetric radar measurements of vehicles on the road at MMW frequencies are needed. Subsequently, the effects of radar polarization on interference, multi-path, and signal to clutter ratio maximization can be investigated. With a high resolution polarimetric MMW radar image, primary scattering points on a vehicle's body can be identified and their polarimetric response can be isolated and characterized. In addition, with the aid of a high resolution image it is possible to identify all nearby imaginary (ghost) targets.

Before discussing the technique used to generate high resolution radar images of traffic scenes, it is imperative to explain what is meant by radar resolution in range and azimuth. In a radar system, the antenna integrates over all the signals arriving through its beam at any given time. Hence, signals arriving simultaneously from different targets within the beam cannot be isolated from one another and a narrower

antenna beam may be necessary in order to isolate the radar returns of different targets separated in azimuth. The radar's ability to differentiate between signals arriving at different times (i.e. from different ranges) has to do with the pulse width for pulsed radars or the transmitted signal bandwidth for stepped frequency FM-CW radars. For the latter, the ability to resolve two targets at different ranges is inversely proportional to the signal bandwidth. For example, signals with bandwidths of 500 MHz and 2 GHz can be used to resolve two targets separated by at least 30 cm and 7.5 cm in range respectively. Hence, a radar with narrow antenna beamwidth and high range resolution can be used to create an image. However, the azimuth resolution is degraded as the range to the target is increased as depicted in Figure 3.2(a). On the other hand, a low resolution radar with both wide antenna beamwidth and narrow signal bandwidth cannot resolve closely spaced targets as illustrated in Figure 3.2(b).

The 94 GHz high resolution imaging radar, developed at the University of Michigan (see Figure 3.3), is a dual antenna system operating in monostatic mode with a 1 GHz bandwidth (15 cm range resolution). In this study, a 500 MHz bandwidth is used for the sake of data management. The beamwidths of the transmit and receive antennas are 2.8° and 1.4° respectively. An antenna with a wider beamwidth was intentionally used for transmitting the radar signal to avoid the parallax problem. With this setup, the transmit antenna illuminates a large area of the target while the receive antenna (narrower beamwidth) collects only the signal reflected from a smaller portion of the illuminated target area. Hence, the effective beamwidth of the radar antenna system is that of the receiver. As mentioned before, the spatial resolution varies with the range to the target. For example, the effective antenna spot size of the UM radar, at 10 m and 20 m from the radar, is about 0.25 m and 0.5 m in diameter, respectively.

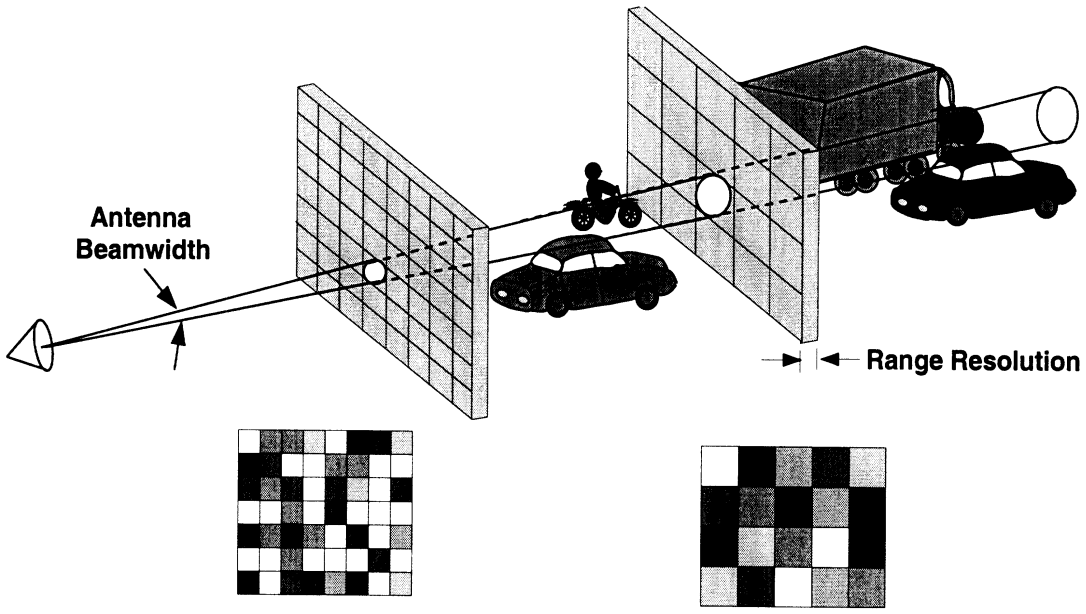

3.2(a)

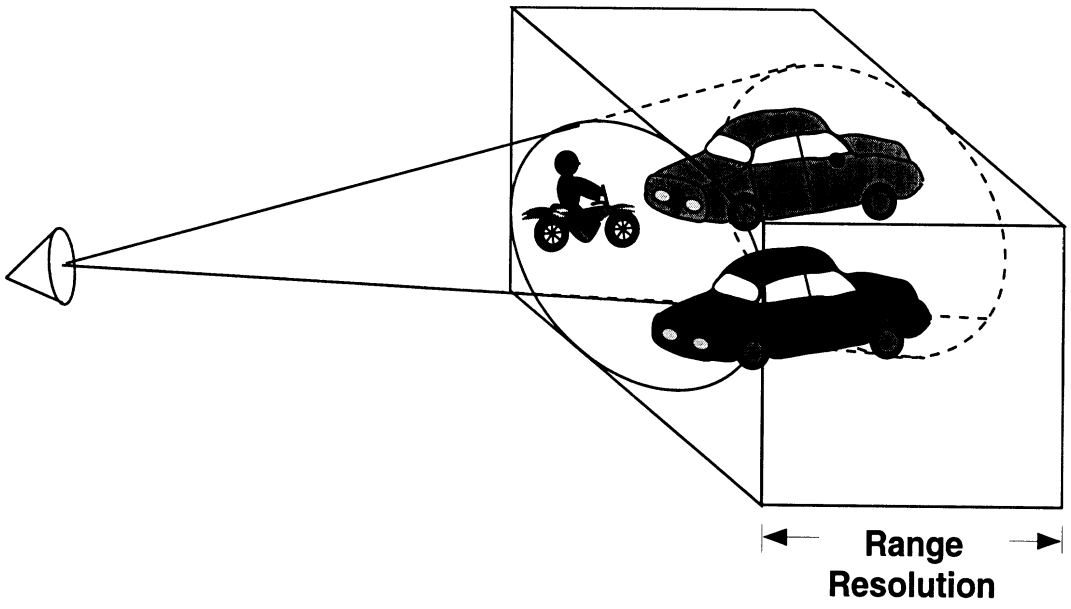

3.2(b)

Figure 3.2: Depiction of target discrimination capabilities of (a) high resolution radars, and (b) low resolution radars in a complex highway environment
.

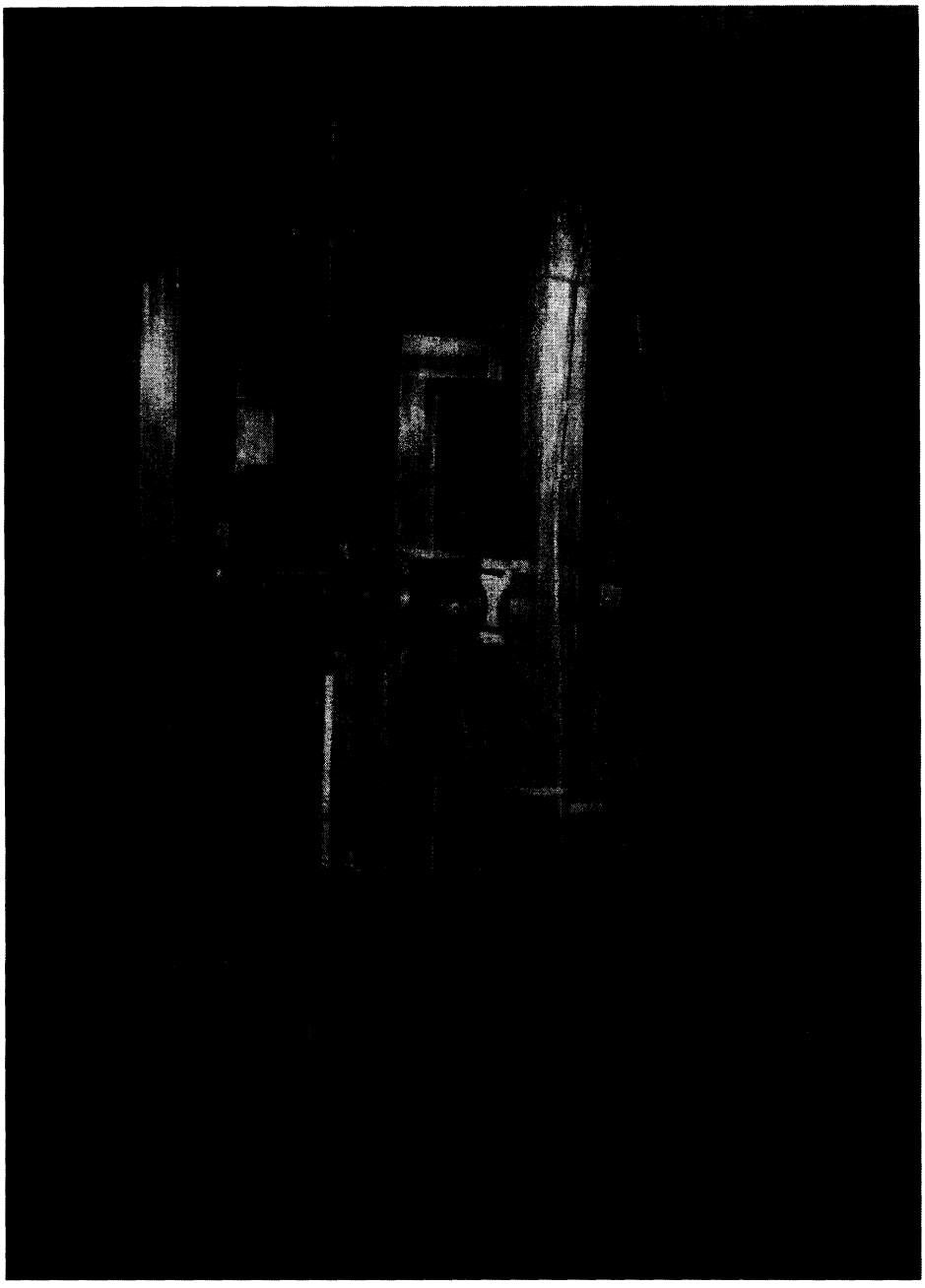

Figure 3.3: The picture of the 94 GHz high resolution imaging radar system.

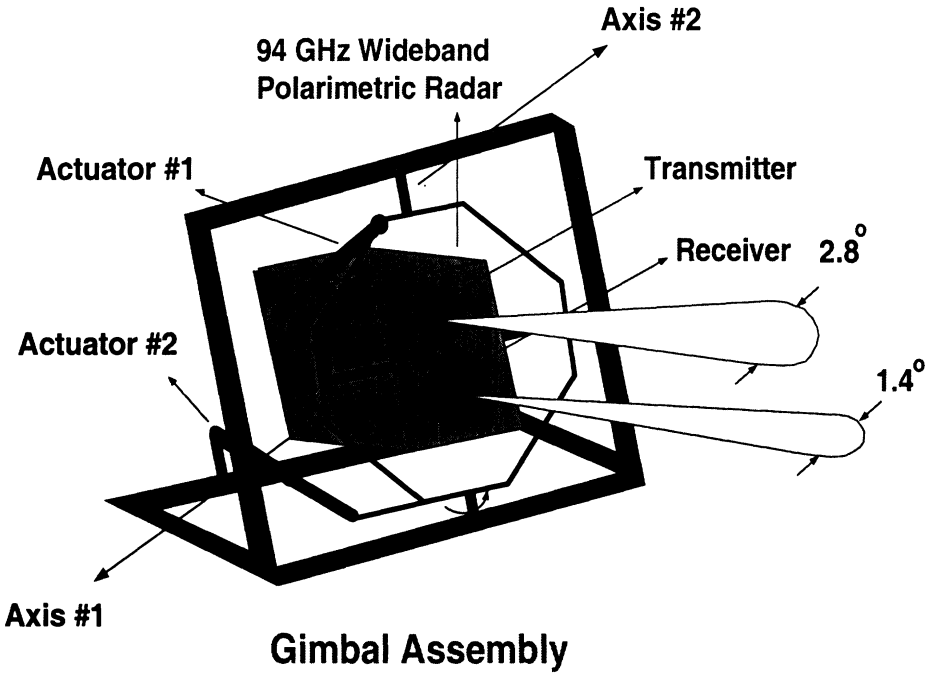

Figure 3.4: The structure diagram of the computer-controlled gimbal assembly.

The remainder of this chapter will be devoted to two issues : (1) measurement setup, procedure, and post-processing required to operate the radar in the imaging mode, and (2) details of the polarimetric image generation procedure used. In addition, samples of generated images of a specific traffic scene, for different pairs of transmit and receive polarizations, are discussed.

3.2 Measurement Setup, Procedure, and Post-Processing

The 94 GHz radar system is mounted on a computer-controlled high precision gimbal designed and built for this project. The overall gimbal structure, shown in Figure 3.4, occupies a volume of 1 m by 0.7 m by 0.6 m (height, width, and depth respectively). The dimensions were chosen so that the assembly fits into a middle size van for outdoor measurements. The gimbal is capable of scanning with angular increments of 0.1° over ±20° and ±15° angular ranges in azimuth and elevation. Further details of the gimbal construction can be found in Appendix A.

Recall that the objective is to create radar images of traffic scenes similar to what would be observed by a vehicle-mounted radar. To this end, the 94 GHz radar scans in azimuth while its antenna beam is aligned parallel to the road surface. At every azimuthal angle, the coherent polarimetric backscatter measurement, namely transmission of two different polarizations and simultaneous reception of the radar return in two orthogonal receiver channels (v and h), is conducted. Once the measurement at one azimuthal angle is complete the computer stores the data acquired by the radar and instructs the gimbal to move to the next azimuthal angle. The calibration technique described in Chapter 2 is used to determine, as a function of frequency, the seven distortion parameters of the radar system. These distortion parameters are then used to correct the errors in the measured radar return. The correction procedure described in [44] is applied to the measured frequency response at every azimuthal angle and for every measured transmit and receive polarization configuration.

The 94 GHz MMW radar is a stepped frequency system capable of measuring the amplitude and phase of the backscattered signal over the prescribed bandwidth and number of frequency points. The collected frequency-domain data does not provide the range information directly. To characterize the range information, post-processing of the data is required. Suppose the backscatter from a target at a range r_o is measured at N frequency points. The scattered field at f_n term of the scattering amplitude of the target (S) is given by

$$E_n^s = E_o \frac{e^{-j2k_n r_o}}{r_o^2} S$$

where E_o is a constant proportional to the incident field intensity and other radar parameters such as the antenna gain. It is noted that the backscatter energy is dis-

tributed in the frequency spectrum over the radiated bandwidth. Assuming that the amplitude of the scattering field is not a strong function of frequency, the backscattered energy in the frequency spectrum can be integrated coherently using the following transformation

$$V(r) = \sum_{n=1}^{N} E_n^s e^{j2k_n r}. \tag{3.1}$$

This transformation can be regarded as a focusing in the frequency domain due to the fact that when $r = r_o$, $V(r)$ assumes its maximum value and as $\Delta r = |r - r_o|$ increases $V(r)$ decreases rapidly at a rate dependent on the system bandwidth. Transformation (3.1) is simply the discrete Fourier transform (DFT) for which a very fast algorithm exists. Thus, by applying the DFT to the frequency-domain data, the time-domain (range) response of the target can be obtained. In the imaging mode, where the ranges to targets are not specified, the range correction factor (r^2) should not be applied to the frequency-domain data; but rather be applied to the time-domain data.

3.3 The Chirp z Transform

Normally the network analyzer is set to collect the target response in the frequency domain. However, only the time-domain response can provide the range information for imaging radar applications. In order to obtain the time-domain response, the Fourier transform is required. Many algorithms for Fourier transform computation are available. The brute force method, although general in terms of number of points, is very inefficient. Ordinary fast Fourier transform (FFT) algorithms are computationally efficient, but inflexible with regard to the number of points. Basically the allowable number of points in FFT algorithms are 2^m for an integer m. For the present case, the chirp z transform (CZT) is chosen because of its

high computation efficiency and flexibility [47]. The CZT is an efficient algorithm for evaluating the z transform of a finite sequence along certain contours in the complex z plane. The unit circle is one of the allowable contours. A CZT algorithm based on the circular contour is developed to evaluate the DFT of a sequence efficiently.

Let $\{x(n)\}$, $0 \leq n \leq N-1$, be a given N-point sequence with z transform

$$X(z) = \sum_{n=0}^{N-1} x(n) z^{-n}. \tag{3.2}$$

The DFT of the sequence $x(n)$ is defined as

$$X(k) = X(e^{j(\frac{2\pi}{N})k}) \qquad k = 0, 1, \cdots, N-1. \tag{3.3}$$

Using the general CZT, one can evaluate the z transform along a general contour

$$z_k = AW^{-k} \qquad k = 0, 1, \cdots, M-1$$

where M is an arbitrary integer (not necessarily equal to N) and $A = A_o e^{j\theta_o}$ and $W = W_o e^{j\phi_o}$ are arbitrary complex numbers. If $A = 1$, $M = N$, and $W = e^{-j\frac{2\pi}{N}}$, then $z_k = e^{j\frac{2\pi k}{N}}$ and the points along a unit circle are the points at which the standard N-point DFT of the sequence is evaluated. Note that if $W_o < 1$ the contour spirals in whereas for $W_o > 1$ the contour spirals out from the starting points.

To evaluate the DFT of a sequence along an arbitrary contour, let X_k be the z transform at $z = z_k$, i.e.,

$$X_k = \sum_{n=0}^{N-1} x(n) z_k^{-n},$$

substituting $z_k = AW^{-k}$, we have

$$X_k = \sum_{n=0}^{N-1} x(n) A^{-n} W^{nk} \qquad k = 0, 1, \cdots, M-1. \tag{3.4}$$

Noting that

$$nk = \frac{n^2 + k^2 - (k-n)^2}{2},$$

X_k becomes

$$\begin{aligned} X_k &= \sum_{n=0}^{N-1} x(n)A^{-n}W^{\frac{[n^2+k^2-(k-n)^2]}{2}} \\ &= \sum_{n=0}^{N-1}[x(n)A^{-n}W^{\frac{n^2}{2}}](W^{\frac{k^2}{2}})W^{\frac{-(k-n)^2}{2}} \\ &= W^{\frac{k^2}{2}}\sum_{n=0}^{N-1} y(n)v(k-n) \end{aligned} \tag{3.5}$$

where

$$\begin{aligned} y(n) &= x(n)A^{-n}W^{\frac{n^2}{2}} \\ v(n) &= W^{-\frac{n^2}{2}}. \end{aligned}$$

Equation (3.5) shows that X_k may be regarded as a weighted convolution of the sequences $y(n)$ and $v(n)$ and may thus be evaluated efficiently by high-speed convolution using the FFT. The procedure is as follows.

Based on the convolution theorem, the Fourier transform of the convolution of two functions is just the product of their individual Fourier transforms. Equation (3.5) can be solved by the following procedure.

1. Choose L, the smallest integer greater than or equal to $(N + M - 1)$ and compatible with the available FFT algorithm.

2. Form the L-point sequence $y(n)$ as

$$y(n) = \begin{cases} A^{-n}W^{\frac{n^2}{2}}x(n) & n = 0, 1, \cdots, N-1 \\ 0 & n = N, N+1, \cdots, L-1 \end{cases}$$

3. Compute the L-point DFT of $y(n)$ using the available FFT routine; call this result Y_r.

4. Define the L-point sequence $v(n)$ by

$$v(n) = \begin{cases} W^{-\frac{n^2}{2}} & n = 0, 1, \cdots, N-1 \\ W^{-\frac{(L-n)^2}{2}} & n = N, N+1, \cdots, L-1 \\ \text{arbitrary} & \text{other } n, \text{ if any} \end{cases}$$

5. Compute the L-point DFT of $v(n)$; call it V_r.

6. Multiply V_r by Y_r, point by point, to give $G_r = V_r Y_r$.

7. Compute the L-point inverse discrete Fourier transform (IDFT) of G_r; call this g_k.

8. Multiply g_k by $W^{\frac{k^2}{2}}$ to give X_k defined as

$$X_k = g_k W^{\frac{k^2}{2}} \qquad k = 0, 1, \cdots, M-1$$

The values of g_k for $k \geq M$ are not meaningful and discarded.

The advantages of the CZT algorithm over other algorithms can be summarized as follows:

1. N, the number of points in the input sequence, need not be the same as M, the number of points at which the z transform is evaluated.

2. Neither N nor M need be composite numbers, in fact, both can be primes.

3. The angular spacing of z_k is arbitrary. Thus the resolution in frequency is arbitrary.

4. If $A = 1$, $M = N$, and $W = e^{-j\frac{2\pi}{N}}$, then the CZT can be use to evaluate the DFT, even when N is a prime.

5. The total complex computation required to implement the evaluation of Eq. (3.4) using the CZT algorithm is proportional to $(N+M-1)\log_2(N+M-1)$. In contract, the direct evaluation of Eq. (3.4) requires a complex computation of order $N \times M$.

3.3.1 The Fast Fourier Transform

The most commonly used algorithm to compute the DFT is the FFT algorithm. Define W as the complex number

$$W = e^{-j\frac{2\pi}{N}}.$$

The discrete Fourier transform of $x(n)$ is

$$X_k = \sum_{n=0}^{N-1} x(n)e^{-j\frac{2\pi}{N}k} \qquad k = 0, 1, \cdots, M-1.$$

It is shown that a discrete Fourier transform of length N can be rewritten as the sum of two discrete Fourier transforms, each of length $N/2$. One is formed from the even-numbered points of the original N, the other from the odd-numbered points. This can be shown by noting that

$$\begin{aligned} X_k &= \sum_{n=0}^{N-1} x(n)e^{-j\frac{2\pi nk}{N}} \\ &= \sum_{n=0}^{N/2-1} x(2n)e^{-j\frac{2\pi(2n)k}{N}} + \sum_{n=0}^{N/2-1} x(2n+1)e^{-j\frac{2\pi(2n+1)k}{N}} \\ &= \sum_{n=0}^{N/2-1} x(2n)e^{-j\frac{2\pi(2n)k}{N}} + e^{-j\frac{2\pi}{N}k} \sum_{n=0}^{N/2-1} x(2n+1)e^{-j\frac{2\pi(2n)k}{N}} \\ &= X_k^e + W^k X_k^o. \end{aligned} \tag{3.6}$$

An important feature of the FFT is that it can be performed recursively. The reduction in the number of points can now be applied to X_k^e and X_k^o, where we now have to perform four transforms with $N/4$ points. This reduction can be repeated

until the subdivision of the data set has a length of 2. A series of steps must then be performed. The FFT algorithm is developed for a data set of sampled numbers with a length equal to a power of 2. If the length of the data set is not a power of 2, the sequence can be augmented by adding zeros up to the next power of 2. The structure of this FFT algorithm has two sections. The first section sorts the data into bit-reversed order. The second section has an outer loop that is executed $\log_2 N$ times and calculates, in turn, transforms of length 2, 4, 8, $\cdots$, N.

3.4 Polarimetric Image Generation Procedure

Knowing the Mueller matrix of a target, the radar cross section (RCS) or the backscattering coefficient of the target for any given pair of transmit and receive polarizations can be determined analytically using [64]:

$$\sigma(\psi_r, \chi_r, \psi_t, \chi_t) = 4\pi \mathbf{A}_r \bar{\mathbf{Q}} \bar{\bar{\mathcal{L}}}_m \mathbf{A}_t \tag{3.7}$$

where ψ_i and χ_i are the tilt and ellipticity angles of the polarization ellipse for transmit ($i = t$) and receive ($i = r$) antennas, $\bar{\mathcal{L}}_m$ is the Mueller matrix, $\bar{\mathbf{Q}}$ is a transformation matrix given by:

$$\bar{\mathbf{Q}} = \begin{pmatrix} 1 & 0 & 0 & 0 \\ 0 & 1 & 0 & 0 \\ 0 & 0 & 1/2 & 0 \\ 0 & 0 & 0 & -1/2 \end{pmatrix}, \tag{3.8}$$

and $\mathbf{A}_i$ is the antenna modified Stokes vector given by

$$\mathbf{A}_i = \begin{bmatrix} \frac{1}{2}(1 + \cos 2\psi_i \cos 2\chi_i) \\ \frac{1}{2}(1 - \cos 2\psi_i \cos 2\chi_i) \\ \sin 2\psi_i \cos 2\chi_i \\ \sin 2\chi_i \end{bmatrix}. \tag{3.9}$$

Once the RCS is computed for every pixel in the image, a 2-D colored image in polar coordinates can be generated. In this image the radius and angular coordinates correspond to the range and the azimuthal angle respectively. In addition, pixel color indicates the strength of the polarimetric response according to a pre-specified color coding scheme. Next, a number of images generated for a given stationary traffic scene are presented.

3.4.1 Case Study

The imaging system was set up to scan in steps of 1° over the azimuthal range ±20° giving rise to 41 sectors in this angular region. The backscatter for each sector is measured over a 500 MHz bandwidth using 201 points which provides 201 pixels in the range direction. The first 14 pixels of each sector are corrupted by system leakage. These contain no target information and are therefore removed from the image. The RCS of each pixel is compared to a reference level. Any RCS lower than –50 dBsm is set to –50 dBsm. Furthermore all pixels are passed through a two-dimensional median filter. The resultant image contains the median values of the 3×3 neighborhood around each pixel in the original image. The image is padded with –50 dBsm outside the image domain; the median values for the points along the edges may thus appear distorted. The software package *MATLAB* is employed to create the images. After the processed data is loaded to this package, the X and

Y coordinates of each pixel are calculated. The grey scale is used to depict the magnitude of the RCS with black indicating the lowest level, -50 dBsm, and white indicating the highest level, 0 dBsm.

Polarimetric images of some traffic scenes have been generated. Figure 3.5 shows a typical traffic scene consisted of a pedestrian, a motor bike, two passenger cars, and a pickup truck. The motorcycle was intentionally positioned in front of the pickup truck to block the view. The goal is to examine whether the radar can detect the pickup truck or not. Figure 3.6 shows co-polarized images of the traffic scene and Figure 3.7 shows cross-polarized images of the traffic scene. Figure 3.6(a) shows the vv response of the scene where all five targets are observable including the pickup truck. It is shown that for this polarization, the RCS of the pedestrian is smaller than that of the motorcycle, and that most of the backscatter from the motor vehicles originate from their tail. This is especially the case for the vehicle on the right (radar view) with a more aerodynamic body. For this vehicle another source of strong backscatter is the side-view mirror. Figure 3.6(b) shows the response of the same scene for horizontal polarization. It is noticed that signal to clutter ratio has improved drastically compared to vv response. This is attributed to the fact that no Brewster angle exists for the h-polarized wave incident on the asphalt. The h-polarized wave has less signal penetration into the asphalt mixtures than the v-polarized wave, and therefore less backscatter signal from the random medium. Another interesting feature observable in this figure are two weak signals (apparent targets) to the left and right of the pickup truck. This is a result of multi-path when the signal reflected from either of the two sedans scatters off the pickup truck and returns to the radar. These ghost targets also exist in the vv image, however there they may be confused with the background noise. Figure 3.6(c) shows the

Radar view

Front view

Figure 3.5: A typical traffic scene consisted of a pedestrian, a motor bike, two passenger cars, and a pickup truck.

image for 45° linear polarization where a mixture of the features of the vv and hh images is obtained as expected. The co-polarized circular polarization response is shown in Figure 3.6(d). It is shown that in this polarization configuration the ghost targets disappear which can be attributed to the reversal of vertical component of the electric field after the first reflection from the sedans. As mentioned earlier, the orthogonal polarization configuration is attractive since the direct path interference can be reduced significantly. Figure 3.7(a) shows the response of the traffic scene for a vertical transmit and a horizontal receive configuration. It is noticed that the backscattering responses of all targets are significantly smaller (about 10–15 dB). This problem is circumvented by other cross-polarized configurations, such as transmit left-hand and receive right-hand polarization, as shown in Figure 3.7(b). This example shows the significance of polarization in improving signal to clutter ratio, and reduction of multi-path and interference. It should also be mentioned that a high resolution imaging radar provides some detailed information about the size of the targets which can be used directly for target classification.

3.5 Conclusions

This chapter investigates the effects of radar polarimetry on issues such as interference, multi-path, and signal to clutter ratio maximization. These problems are commonly encountered in applications related to vehicle collision avoidance. A MMW high resolution polarimetric radar system is employed to conduct the investigation. Interference can be minimized by requiring the radar to transmit and receive in orthogonal polarizations. The signal to clutter ratio can be maximized by selecting optimum polarizations for both the transmit and receive antennas. A typical traffic scene was arranged for measurement to study the problem of multi-path. The

chirp z transform is used to convert the measured frequency-domain data to a time-domain response to provide the range information. The images of this scene were generated for different combinations of transmit and receive polarizations. It is observed that the signal level of the ghost targets caused by multi-path can be reduced significantly by choosing the appropriate polarizations. The ancillary applications of such MMW imaging system include its vision-aid capability while driving at night and the black-box capability that aids in reconstructing the events leading up to the collision.

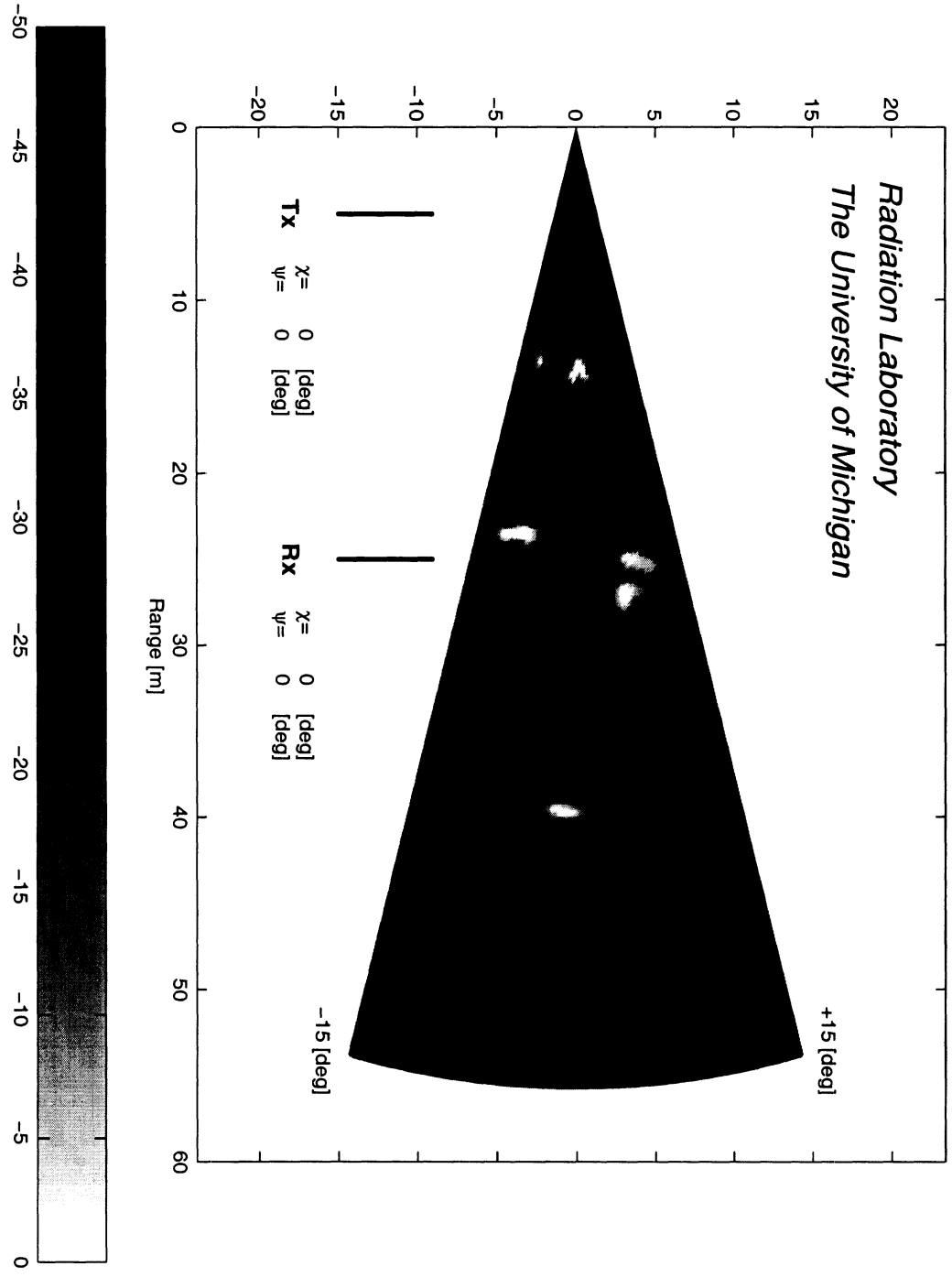

3.6(a) The vv response.

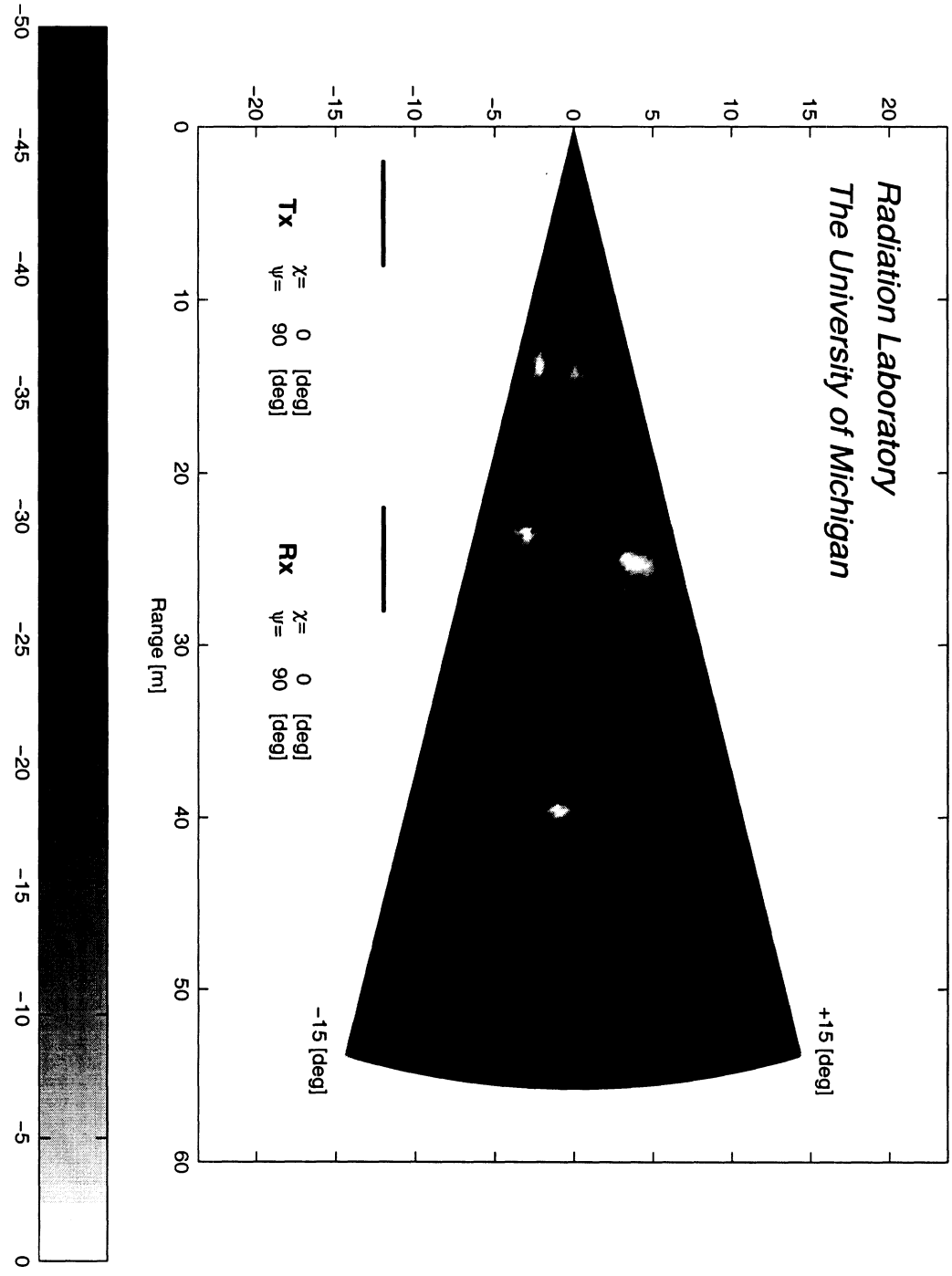

3.6(b) The hh response.

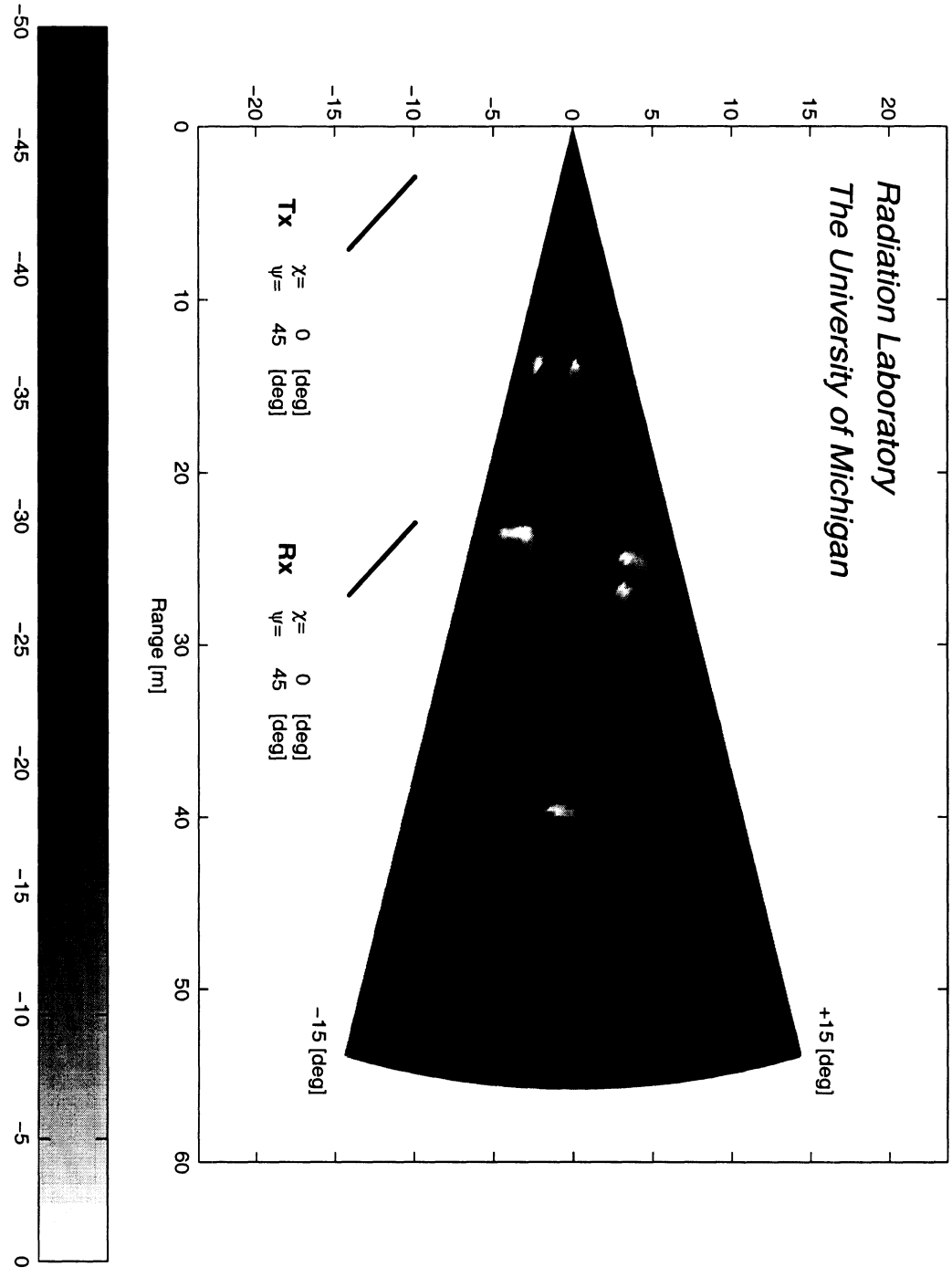

3.6(c) The linear 45°-linear 45° response.

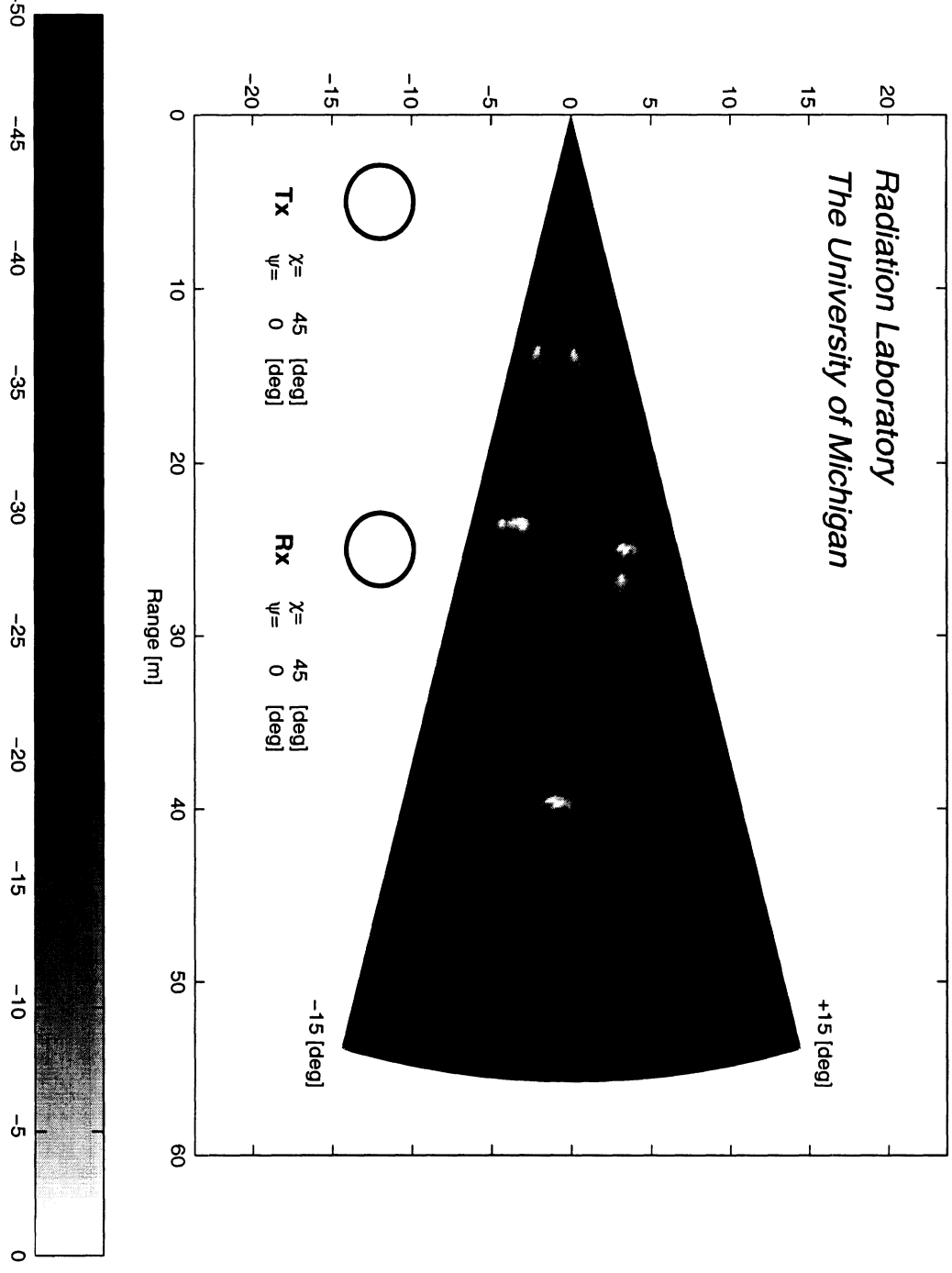

3.6(d) The LHC-LHC response.

Figure 3.6: The co-polarized responses of the traffic scene shown in Figure 3.5.

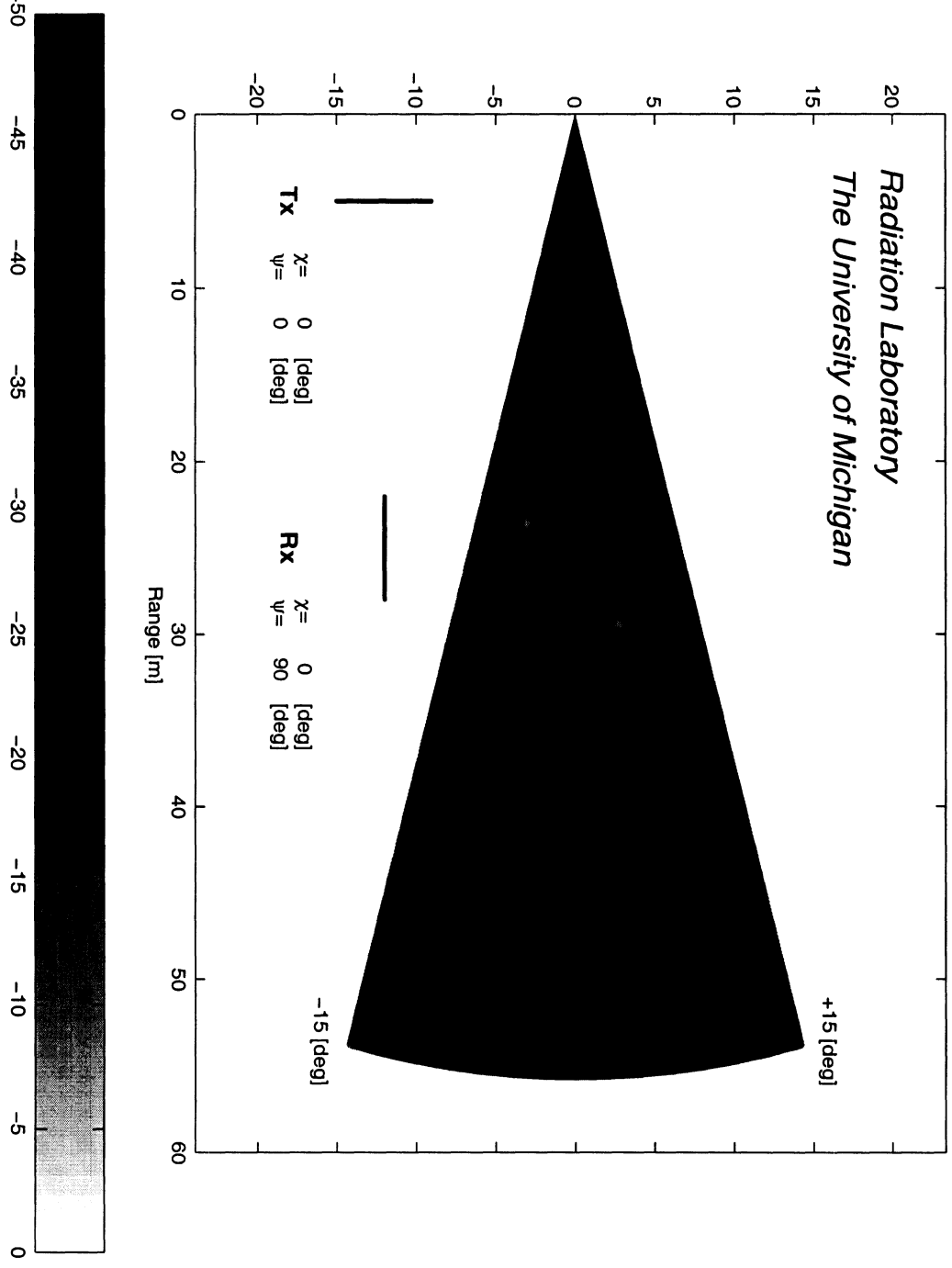

3.7(a) The vh response.

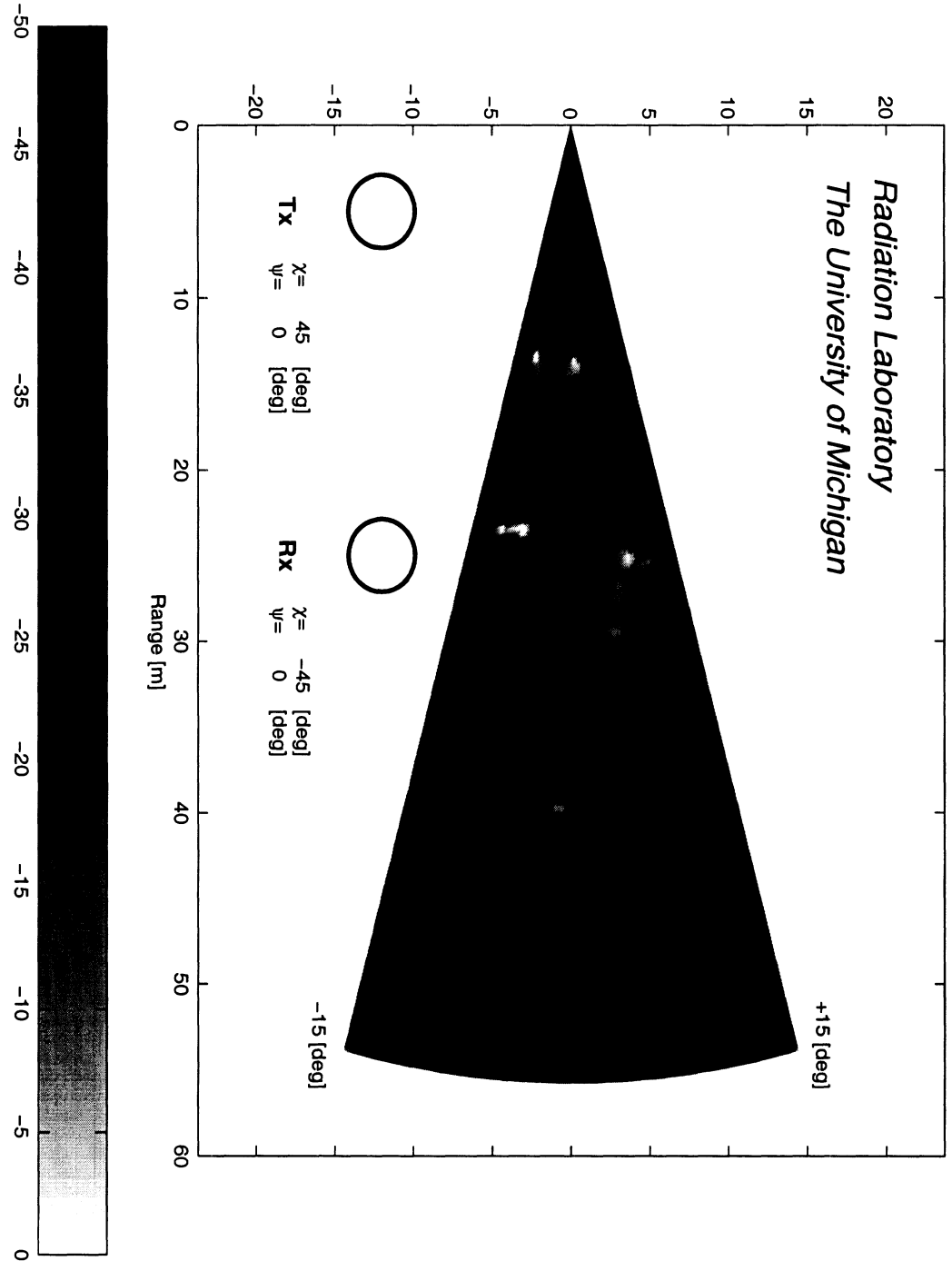

3.7(b) The RHC-LHC response.

Figure 3.7: The cross-polarized responses of the traffic scene shown in Figure 3.5.

CHAPTER IV

MODELING AND MEASUREMENT OF SCATTERING FROM ROAD SURFACES AT MILLIMETER-WAVE FREQUENCIES

4.1 Introduction

In response to the increasing demand for safety in highway transportation, different types of radar-based sensors have been proposed. These include forward looking millimeter-wave (MMW) radars for collision warning and intelligent cruise control, surface recognition sensors, lane change aid radars, etc. Design of optimum systems requires a thorough understanding of the radar phenomenology of targets in the highway environment. The study of road surfaces is thus beneficial to the development of road surface recognition sensors and the characterization of radar clutter and multipath in obstacle detection and collision warning. Characterization of the scattering response of road surfaces under different conditions is pursued both theoretically and experimentally. To fully exploit the properties of the radar backscatter for a given application, techniques offered by radar polarimetry can be used to enhance the performance. To this end extensive polarimetric backscatter measurements have been conducted at W-band for different types of road surfaces over a wide range of incidence angles. Asphalt, concrete, and gravel surfaces with varying degrees of surface

roughness and wetness were observed. The number of physical parameters influencing the radar response of road surfaces, such as surface roughness, surface wetness, density, surface cover, etc., is rather large. This makes the generation of a comprehensive data set extremely difficult if not impossible. From a theoretical point of view, the problem at hand can be regarded as obtaining the solution for backscatter from a layer of dense random medium covered by a homogeneous layer. At MMW frequencies, where the sizes of inhomogeneities in the dense random medium are comparable to the wavelength, it is not always possible to determine an accurate description of random medium parameters such as extinction and phase matrices or the pair-distribution function theoretically. The method pursued in this chapter makes use of experimental procedures to characterize the fundamental medium parameters needed in the vector radiative transfer formulation.

In what follows, first an experimental procedure for characterizing the effective dielectric constants of road pavement mixtures is developed. The effective dielectric constant is needed for determining the diffraction, propagation constant, and extinction coefficient of the mean-field in dense pavement mixtures. Next, the problem of volume scattering from a multi-layer medium is formulated using the theory of vector radiative transfer. Explicit expressions for backscattering coefficients and parameters of phase difference statistics are obtained in terms of elements of the phase and extinction matrices of the medium. In Section 4.4 experimental polarimetric backscatter data from asphalt surfaces and concrete surfaces under different physical conditions are presented and compared with their theoretical predictions.

Sieve Size in cm	% Passing
1.27	100
0.95	92
0.64	75
0.32	62
0.25	55
0.16	44
0.06	20
0.03	7
0.01	4.5

Table 4.1: Particle size distribution of asphalt specimens.

4.2 Effective Dielectric Constants of Pavement Mixtures

Pavement mixture is a composite material consisting of rocks, sand, bitumen (for asphalt mixtures), cement (for concrete mixtures), and air voids arranged randomly. Electromagnetic scattering and propagation in a random medium are mostly influenced by the contrast in the complex permittivities and sizes (relative to the wavelength) of the constituent particles. Size distribution of rocks in pavement mixtures may vary depending on the application [1]. Table 4.1 shows a typical particle size distribution in an asphalt mixture used for construction of road surfaces. Due to the high volume fraction of rocks and sand in pavement mixtures, the effective dielectric constant is mostly influenced by the complex permittivities of these particles. For example, the pebbles, crushed rocks, and sand constitute 85% - 90% of the asphalt mixtures and the rest is occupied by bitumen (5%-7%) and air voids

(5%-8%). With the exclusion of certain deleterious rocks such as clay stone or iron stone, the rocks in pavement mixtures are chosen according to availability [72].

At low frequencies where the sizes of constituent particles are much smaller than the wavelength, the effective dielectric constant (ϵ_e) of pavement mixtures can be obtained from the dielectric constants and volume fraction of constituent particles using dielectric mixing formulas such as Polder-Van Santen [46]. However, at high frequencies where the sizes of particles are comparable to or larger than the wavelength significant scattering occurs in the medium (loss of coherent power) which in effect increases the imaginary part of the effective dielectric constant. Recent experimental and numerical analyses have shown that simple low frequency mixing formulas can accurately predict the real part of the effective dielectric constants (ϵ_e') of random media at high frequencies [43,54]. The literature concerning the dielectric properties of the constituent components of pavement mixtures at W-band frequencies is rather sparse. The complex permittivities of different rocks at 450 MHz and 35 GHz are reported by Campbell and Ulrichs [9]. It is shown that the real part of the relative permittivities of rocks varies within the range 3 – 8 with a weak dependency on frequency. It is also shown that for most rocks the loss tangent is relatively low. Bitumen and cement, like rocks, are non-polar substances and their dielectric constants are expected to be gentle functions of frequency. Therefore the real part of the effective dielectric constant of pavement mixtures should be almost constant versus frequency. As mentioned earlier, this generalization does not apply to the imaginary part of the effective dielectric constant (ϵ_e'') due to the presence of strong scatterers in the medium. Evaluation of the imaginary part of the effective dielectric constant, or equivalently the extinction coefficient, of a dense random medium is not straightforward. The quasi-crystalline approximation (QCA) [38, 60], the most

advanced method that takes multiple scattering among particles into account, has been validated for single-particle type media with volume fractions less than 20%. Besides the shape and particle size distributions, QCA requires knowledge of the pair-distribution function of the particles in the medium which is very difficult to characterize.

Since the theoretical calculation of the effective dielectric constant of pavement mixtures at W-band is not easy, experimental procedures were followed. As mentioned earlier, it is expected that the real part of the effective permittivity of pavement mixtures would be almost independent of frequency and therefore a dielectric measurement at microwave frequencies should reveal the real part of the effective dielectric constant. The loss tangents of bitumen, cement, dry sand, and rocks at microwave frequencies are rather low which permits dielectric characterization using a microwave resonator. Since the measurements should be accomplished nondestructively, a partially-filled transmission line type resonator is most appropriate for this task. For this purpose the L-band microstrip ring resonator described in Appendix B was used. The resonant frequency of a ring resonator is inversely proportional to the perimeter of the ring and the square root of the effective dielectric constant of the microstrip substrate and the unknown medium. The choice of frequency determines the dimension of the ring resonator whose geometry is shown in Figure B.1. It is important that the dimension of the ring resonator be much larger than a typical dimension of the constituent particles of the mixture. This requirement ensures that the variability in the shift of the resonant frequency as a function of resonator position is relatively small.

To evaluate the effective dielectric constant of pavement mixtures at 94 GHz directly, a free-space measurement method was devised. In this approach cylindrical

samples of pavement mixtures were prepared for radar cross section (RCS) measurement. The University of Michigan 94 GHz scatterometer system was used to perform the measurements. The cylindrical samples were positioned along the radar boresight with their circular bases facing the radar. An elevation-over-azimuth positioner was used to manipulate the samples. Since the dimensions of the target (cylinder) are much larger than the wavelength (λ = 3.19 mm), the physical optics (P. O.) approximation can be used to evaluate the RCS. According to this approximation the RCS of this target can be obtained from [64]

$$\sigma_c = \frac{4\pi A^2}{\lambda^2}|\Gamma_o|^2$$

where A is the surface area of the cylinder base, λ is the wavelength, and Γ_o is the Fresnel reflection coefficient at normal incidence. The surface reflectivity of the pavement mixtures can be measured directly by comparing the backscatter of a metallic disk to that of the cylindrical sample at the same distance from the radar. Statistics of the surface reflectivity were obtained for all samples, measuring both front and back. Since the pavement mixtures are low-loss materials, the surface reflectivity is dominated by the real part of the effective dielectric constant, hence

$$\epsilon_e' = \left(\frac{1+\Gamma_o}{1-\Gamma_o}\right)^2. \tag{4.1}$$

Using the measured reflectivity in (4.1), the real part of the effective dielectric constant of the pavement mixtures at 94 GHz can be found.

Both low frequency and high frequency approaches are used to characterize the real part of the effective dielectric constants of the two most common pavement mixtures: asphalt mixtures and concrete mixtures. In the following two subsections, the measured results of the real part of the effective dielectric constant of the two

pavement mixtures are shown. Then the methods used to measure the imaginary part of the effective dielectric constants are described.

4.2.1 Asphalt Mixtures

An L-band microstrip ring resonator is used to perform the low frequency dielectric constant measurements. Placement of the sample against the ring resonator elicits changes in the resonant frequency (Δf) and the quality factor (ΔQ). Following the procedure outlined in Appendix B, the dielectric constants of 15 smooth asphalt samples were measured using the L-band microstrip ring resonator. The real part of the effective dielectric constant of the asphalt mixtures at 1.1 GHz was found to be 3.33 ± 0.12.

The high frequency approach for measuring the effective dielectric constant at W-band is accomplished by an inverse scattering algorithm. In this approach cylindrical samples of asphalt mixtures with a bitumen content of 6.2% and an air void content of 3.5% prepared by Midwest Testing Laboratories were used for RCS measurement. The particle size distribution of these specimens is listed in Table 4.1. The desired density of the asphalt mixture is achieved using the Marshall method ASTM D1559 [2]. The cylindrical samples have three different heights (1.59 cm, 2.38 cm, and 6.35 cm), all with a diameter of 10 cm. For verification of measurement consistency three specimens were made for each height. First a thick sample (6.35 cm) was placed in front of the radar and its backscatter was measured twice: the sample alone and the sample backed by a circular metallic plate with diameter equal to that of the cylinder (10 cm). No change was observed in the measured RCS upon attachment of the metallic plate. It was thus concluded that the extinction in the asphalt medium is so high that the signal reflected off the metallic plate does not contribute to the overall

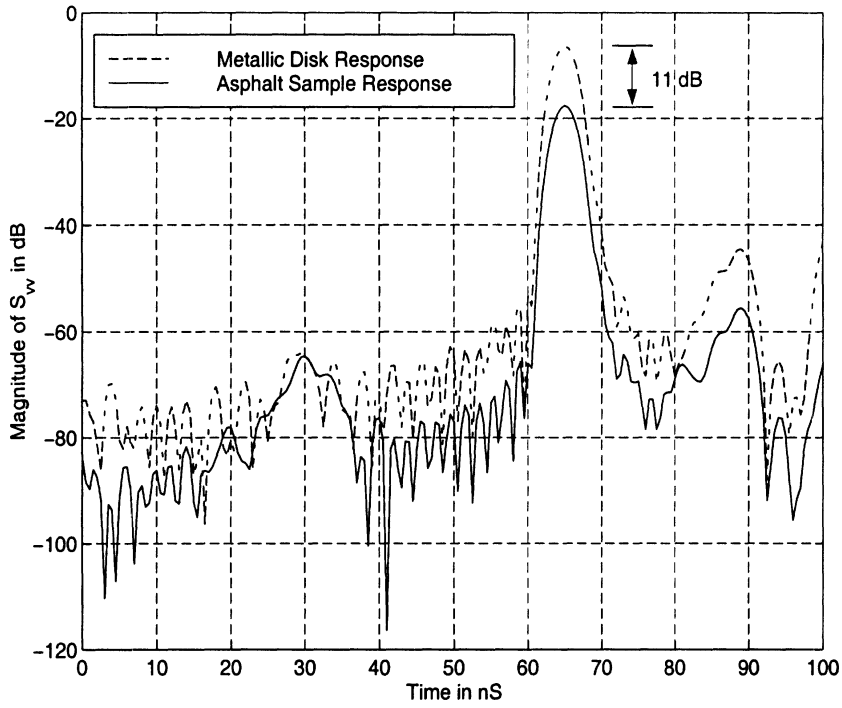

Figure 4.1: The time-domain radar backscatter response of a typical asphalt sample and the circular metallic disk.

backscatter significantly. In other words, the scattered field, in this case, originates from the lit surface of the cylinder only. Figure 4.1 shows the time-domain radar backscatter response of a typical asphalt sample and the circular metallic disk. From six independent backscatter measurements the surface reflectivity was calculated to be -11 ± 0.1 dB. Using the measured Fresnel reflection coefficient in (4.1), the real part of the effective dielectric constant of the asphalt mixtures at 94 GHz was found to be $\epsilon'_a = 3.18 \pm 0.04$. This measurement is consistent with the low frequency measurement conducted at L-band.

Next an attempt was made to evaluate the imaginary part of the effective dielectric constant using the thinner samples. RCSs of cylindrical samples of height 2.38 cm were measured and as before no change in the measured RCSs was observed when the metallic circular disk was placed behind the cylindrical samples. This indicates

that the two-way attenuation is still too high (note that the power transmissivity at the interface between air and asphalt is more than 92%). Similar experiments were conducted using the thinnest samples (1.59 cm). For these samples the change in RCSs with and without the metallic disk was of the order of only 0.1 dB. Obviously this change in RCSs is not high enough to allow for an accurate characterization of the imaginary part of the effective dielectric constant, however, an approximate estimate can be obtained. The reflection coefficient of a metal-backed layer of thickness d at normal incidence is given by:

$$\Gamma_m = \frac{\Gamma_o - e^{2jk_a d}}{1 - \Gamma_o e^{2jk_a d}} \tag{4.2}$$

where $k_a = \beta + j\alpha$ is the complex propagation constant in the asphalt mixtures. Using (4.2) the attenuation constant and the imaginary part of the effective dielectric constant of the asphalt mixtures at 94 GHz were found to be $\alpha \approx 54$ Np/m and $\epsilon_a'' \approx 0.1$. Note that although a thinner asphalt sample exhibits a higher difference between RCSs of the sample with and without the metallic disk, the calculation of ϵ_a'' would still not be accurate for two reasons: (1) the diameters of about 10% of the particles in the asphalt mixtures are larger than 1 cm which limits the thickness of the cylindrical samples, and (2) the sample must be many wavelengths long to allow for the interaction of the electromagnetic wave with the random medium.

4.2.2 Concrete Mixtures

Concrete mixture is another composite material commonly used for road pavement. The same approaches as for asphalt mixtures are used to determine the effective dielectric constant. The preliminary examination was conducted using an L-band ring resonator. Ten concrete samples prepared by Midwest Testing Laboratory were measured, 10 times each, and the average real part of the effective dielectric

constant at 1.1 GHz was found to be 4.54 ± 0.15.

The inverse scattering algorithm was used to measure the real part of the effective dielectric constant at 94 GHz. The RCSs of the concrete samples were compared to that of a circular metallic plate of the same area. The Fresnel reflection coefficient at normal incidence was calculated by finding the ratio of the RCS of the concrete sample to that of the metallic disk. The difference in the measured RCSs was seen to be 9.3 ± 0.1 dB. The average value of ϵ_c' for ten concrete samples was calculated from (4.1) as 4.17 ± 0.1 which is close to the value estimated by the L-band ring resonator.

Measurement of the imaginary part of the effective dielectric constant is often accomplished by observation of the RCS change in response to the attachment of the metallic disk to the back of the sample: ϵ_c'' can be calculated in terms of the thickness of the sample and the change in the measured RCS values. Unfortunately even the thinnest sample (2.54 cm) exhibited no changes. Therefore, this method cannot provide a solution to calculate ϵ_c''. However, the result suggests that concrete mixtures thicker than 5 cm can be considered semi-infinite . The L-band ring resonator provided an estimate of $\epsilon_c'' = 0.36 \pm 0.05$.

4.3 Theoretical Analysis

In this section the problem of scattering from a smooth road surface possibly covered with a thin layer of ice or water is considered. The geometry of the scattering problem is shown in Figure 4.2 where the ice or water layer is homogeneous with thickness d_1. The pavement mixtures are modeled as a layer of dense random medium on top of a relatively smooth gravel surface. Suppose a uniform plane wave in air (medium 0) is incident on the multi-layer medium. At the interface, the incident ray

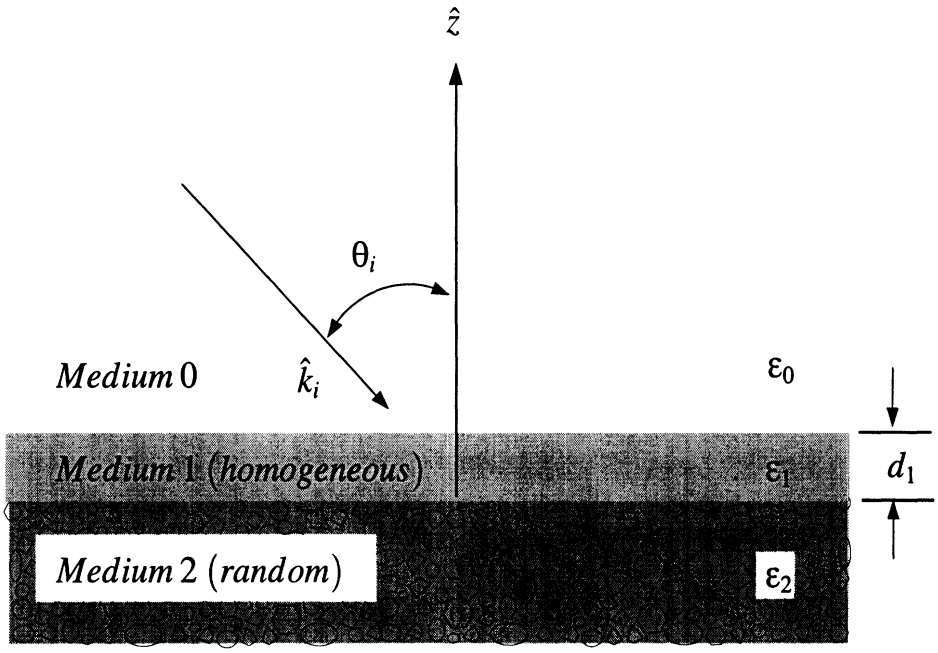

Figure 4.2: The geometry of the scattering from a smooth road surface possibly covered with a thin layer of ice or water.

refracts and enters the random medium where scattering in all directions, including the backscatter direction, takes place. Interaction of electromagnetic waves with random media can be explained using a heuristic approach known as the radiative transfer (RT) method. The formulation of RT is based on conservation of energy and has been successfully applied to many remote sensing problems [37, 65, 73]. In this theory the polarimetric flow of electromagnetic energy through a random medium follows from the solution of a vector integro-differential equation given by

$$\frac{\boldsymbol{I}(\hat{s},\boldsymbol{r})}{ds} = -\boldsymbol{\kappa}\boldsymbol{I}(\hat{s},\boldsymbol{r}) + \int\int_{4\pi} \boldsymbol{P}(\hat{s},\hat{s'})\boldsymbol{I}(\hat{s'},\boldsymbol{r})d\Omega' \tag{4.3}$$

where $\boldsymbol{I}$ is an unknown 4×1 specific intensity vector (power density per unit solid angle), $\boldsymbol{\kappa}$ is the 4×4 extinction matrix, and $\boldsymbol{P}$ is the 4×4 phase matrix. The extinction matrix characterizes the attenuation of the vector specific intensity due to absorption and scattering. The phase matrix relates the average specific intensity scattered by a unit volume of the random media into direction $\hat{s}$ to the incident

intensity upon the unit volume from the direction $\hat{s}'$.

For an elliptically polarized monochromatic plane wave the incident specific intensity $\boldsymbol{I}^i$ is defined through the modified Stokes parameters I_v, I_h, U, and V as follows:

$$\boldsymbol{I}^i = \begin{bmatrix} I_v \\ I_h \\ U \\ V \end{bmatrix} = \frac{1}{\eta_o} \begin{bmatrix} |E_v|^2 \\ |E_h|^2 \\ 2\mathrm{Re}(E_v E_h^*) \\ 2\mathrm{Im}(E_v E_h^*) \end{bmatrix} \tag{4.4}$$

where η_o is the intrinsic impedance of free space. Note that the scattered field from a distributed target is a spherical wave. The vector specific intensity is also defined in terms of Stokes parameters, but the definition includes normalization by the solid angle $A_o \cos\theta_s / r^2$, where A_o is the illumination area, r is the distance between the distributed target and the observation point, and θ_s is the angle between the outward normal to A and the vector defining the direction from the target to the observation point. Hence, the scattered intensity from a random medium is defined as:

$$\boldsymbol{I}^s = \begin{bmatrix} I_v^s \\ I_h^s \\ U^s \\ V^s \end{bmatrix} = \frac{r^2}{\eta_o A_o \cos\theta_s} \begin{bmatrix} \langle |E_v^s|^2 \rangle \\ \langle |E_h^s|^2 \rangle \\ 2\mathrm{Re}(\langle E_v^s E_h^{s*} \rangle) \\ 2\mathrm{Im}(\langle E_v^s E_h^{s*} \rangle) \end{bmatrix} \tag{4.5}$$

where $\langle \quad \rangle$ denotes ensemble average. The bistatic scattering coefficient $\sigma^\circ_{\alpha\beta}$ corresponding to a β-polarized incident plane wave giving rise to an α-polarized spherical wave can be obtained from [60]:

$$\sigma^\circ_{\alpha\beta}(\pi - \theta_0, \phi_0; \theta_s, \phi_s) = \frac{4\pi \cos\theta_s I_\alpha^s(\theta_s, \phi_s)}{I_\beta^i(\pi - \theta_0, \phi_0)} \tag{4.6}$$

where $(\pi - \theta_0, \phi_0)$ denotes the direction of the downward-going incident intensity and (θ_s, ϕ_s) denotes the direction of the upward-going scattered intensity. We note that $\theta_s = \theta_0$ and $\phi_s = \pi + \phi_0$ corresponds to the backscattering.

The phase and extinction matrices are the fundamental quantities in the RT model. That is, if these quantities could be specified, then the medium would indeed be completely characterized and scattering for any arbitrary configuration could be predicted, provided that the boundary conditions were accounted for appropriately. As mentioned earlier, pavement mixture is a complex medium for electromagnetic waves where even the most advanced theoretical methods, such as the dense medium radiative transfer model [61], are inadequate for prediction of the phase and extinction matrices. To circumvent this problem, a modeling effort based partly on radiative transfer and partly on experimental analysis is proposed. This technique, unlike standard methods, does not attempt to derive the form of the phase and extinction matrices in terms of particle size, shape, density, and permittivity. Instead, these are inverted directly from *controlled* polarimetric backscatter radar measurements. The scattering elements in the medium are considered to be clusters to underscore the point that this treatment considers "effective" particles, which may consist of correlated groups of individual physical particles and/or multiple scattering effects. To simplify the problem further, it is assumed that a first-order model can be used for the scattering. This assumption stems from the fact that the far-field scattering albedo (excluding near-field particle interactions) in a random medium is relatively small.

The standard practice in solving the RT equation iteratively is to split the intensity vector into upward-going $(\boldsymbol{I}^+(\theta, \phi, z))$ and downward-going $(\boldsymbol{I}^-(\theta, \phi, z))$ components, noting that $0 < \theta < \pi/2$. The first-order solution of the RT equation has been

reported in the literature [51,60,63] and will not be repeated here. The appropriate boundary conditions for the problem at hand are as follows. In practice, the thickness of most road pavement exceeds 5 cm. In the previous section it was shown that the attenuation constant of the mean-field in pavement mixtures exceeds 54 Np/m at 94 GHz. Hence a 5 cm layer of pavement mixtures appears to be a semi-infinite medium at W-band frequencies. This property simplifies the boundary condition at the top interface of the pavement mixture layer. The downward-going intensity just below the interface in medium 2 is related to the incident intensity above the interface between medium 0 and medium 1 and is given by

$$\boldsymbol{I}^{-}(\pi-\theta,\phi,0^{-}) = \boldsymbol{T}_{02}\boldsymbol{I}^{i}(\pi-\theta_0,\phi_0,d_1^{+})\delta(\theta-\theta_2)\delta(\phi-\phi_0) \tag{4.7}$$

where θ_2 denotes the angle of propagation of the mean-field in medium 2 calculated from the Fresnel law of refraction and $\boldsymbol{T}_{02}$ is the transmissivity matrix. The boundary condition that relates the scattered upward-going intensity in medium 2 just below the interface to the upward-going intensity in medium 0 is simply given by:

$$\boldsymbol{I}^{s}(\theta_0^s,\phi_0^s,d_1^{+}) = \boldsymbol{T}_{20}\boldsymbol{I}^{+}(\theta_2^s,\phi_0^s,0^{-}) \tag{4.8}$$

For intensity vectors constructed from Stokes parameters the transmissivity matrix can be calculated from:

$$\boldsymbol{T}_{02} = \frac{n_2^2\eta_0\cos\theta_2}{n_0^2\eta_2\cos\theta_0}\begin{bmatrix} |\,t_{02}^{v}\,|^2 & 0 & 0 & 0 \\ 0 & |\,t_{02}^{h}\,|^2 & 0 & 0 \\ 0 & 0 & \mathrm{Re}(t_{02}^{v}t_{02}^{h*}) & -\mathrm{Im}(t_{02}^{v}t_{02}^{h*}) \\ 0 & 0 & \mathrm{Im}(t_{02}^{v}t_{02}^{h*}) & \mathrm{Re}(t_{02}^{v}t_{02}^{h*}) \end{bmatrix} \tag{4.9}$$

where n_j and η_j are the index of refraction and intrinsic impedance of medium j respectively. Also t_{02}^{v} and t_{02}^{h} are the v-polarized and h-polarized field transmis-

sion coefficients from medium 0 to medium 2. Equation (4.9) can be used for the calculation of $\boldsymbol{T}_{20}$ by simply interchanging the subscripts 0 and 2.

The plane wave field transmission coefficient in layered media can be obtained following the procedure outlined in [35]. For the three-layered problem the h-polarized field transmission coefficient is given by

$$t_{02}^h = e^{jk_{1z}d_1} \frac{(1+r_{12}^h)(1+r_{01}^h)}{1+r_{01}^h r_{12}^h e^{j2k_{1z}d_1}} \tag{4.10}$$

where r_{pq}^h $(p \in 0,1,\ q \in 1,2)$ is the Fresnel reflection coefficient at the interface of medium p and medium q, given by

$$r_{pq}^h = \frac{k_{pz} - k_{qz}}{k_{pz} + k_{qz}}.$$

Here k_{pz} is the z-component of the propagation constant in medium p which can be calculated from:

$$k_{pz} = k_0 \sqrt{\epsilon_p - \sin^2\theta_0}.$$

The v-polarized field transmission coefficient can be obtained from (4.10) by multiplying the right-hand-side by η_2/η_0 and replacing r_{pq}^h with r_{pq}^v given by

$$r_{pq}^v = \frac{\epsilon_q k_{pz} - \epsilon_p k_{qz}}{\epsilon_q k_{pz} + \epsilon_p k_{qz}}.$$

The first-order iterative solution of the RT equation subject to the aforementioned boundary conditions results in the following simple expression for the backscattered intensity

$$\boldsymbol{I}^s(\theta_0, \phi_0 + \pi, d_1^+) = \boldsymbol{T}_{20}\boldsymbol{A}\boldsymbol{T}_{02}\boldsymbol{I}^i(\pi - \theta_0, \phi_0, d_1^+) \tag{4.11}$$

In (4.11) $\boldsymbol{A}$ is a 4×4 matrix whose elements are given by

$$[\boldsymbol{A}]_{ij} = \frac{1}{\lambda_i + \lambda_j} \cdot [\boldsymbol{Q}^{-1}\boldsymbol{P}\boldsymbol{Q}]_{ij}$$

where λ_i and $\boldsymbol{Q}$ are the ith eigenvalue and the matrix of eigenvectors of the extinction matrix respectively. Note that particle arrangement in pavement mixtures is statistically homogeneous and symmetrical. That is, there is no preferred orientation for the constituent particles in the medium (isotropic random medium). In this case it is expected that the extinction matrix be reduced to a scalar quantity (κ) which will further simplify (4.11) to

$$\boldsymbol{I}^s(\theta_0, \phi_0 + \pi, d_1^+) = \frac{1}{2\kappa}\boldsymbol{T}_{20}\boldsymbol{P}\boldsymbol{T}_{02}\boldsymbol{I}^i(\pi - \theta_0, \phi_0, d_1^+) \tag{4.12}$$

It is also shown that for isotropic random media the phase matrix in the backscatter direction can be expressed in terms of only four independent parameters [32]

$$\boldsymbol{P} = \begin{bmatrix} p_1 & p_2 & 0 & 0 \\ p_2 & p_1 & 0 & 0 \\ 0 & 0 & p_3 + p_2 & -p_4 \\ 0 & 0 & p_4 & p_3 - p_2 \end{bmatrix} \tag{4.13}$$

The zero entries in (4.13) are a result of lack of correlation between co- and cross-polarized components of the scattering matrix per unit volume of the random medium. Using (4.12) and (4.13) in (4.6), the following simple expressions for the backscattering coefficients are obtained:

$$\begin{aligned} \sigma^\circ_{vv} &= 4\pi \cos\theta_0 \mid t^v_{02} \mid^2 \mid t^v_{20} \mid^2 \frac{p_1}{2\kappa} \\ \sigma^\circ_{hh} &= 4\pi \cos\theta_0 \mid t^h_{02} \mid^2 \mid t^h_{20} \mid^2 \frac{p_1}{2\kappa} \\ \sigma^\circ_{vh} &= 4\pi \cos\theta_0 \mid t^h_{02} \mid^2 \mid t^v_{20} \mid^2 \frac{p_2}{2\kappa} \\ \sigma^\circ_{hv} &= 4\pi \cos\theta_0 \mid t^v_{02} \mid^2 \mid t^h_{20} \mid^2 \frac{p_2}{2\kappa} \end{aligned} \tag{4.14}$$

The phase difference between the co-polarized backscattered components contains information about the target as well. The statistics of the phase difference can be

obtained from the Mueller matrix [52]. The probability density function of the phase difference $(\phi_{hh} - \phi_{vv})$ is characterized in terms of two scalar parameters known as the degree of correlation (α) and the mean phase difference (ζ). Recognizing the product $\frac{1}{2\kappa}\boldsymbol{T}_{20}\boldsymbol{P}\boldsymbol{T}_{02}$ in (4.12) as the Mueller matrix $(\boldsymbol{M})$, the degree of correlation and the mean phase difference can be computed from:

$$\alpha = \frac{1}{2}\sqrt{\frac{(M_{33}+M_{44})^2 + (M_{34}-M_{43})^2}{M_{11}M_{22}}} \tag{4.15}$$

$$\zeta = \tan^{-1}\left(\frac{M_{43}-M_{34}}{M_{33}+M_{44}}\right). \tag{4.16}$$

After some algebraic manipulation, it follows that

$$\begin{aligned} M_{33} + M_{44} &= \{\mathrm{Re}[Z_1 Z_2]p_3 - \mathrm{Im}[Z_1 Z_2]p_4\}/\kappa \\ M_{43} - M_{34} &= \{\mathrm{Im}[Z_1 Z_2]p_3 + \mathrm{Re}[Z_1 Z_2]p_4\}/\kappa \end{aligned} \tag{4.17}$$

where $Z_1 = t_{20}^v t_{20}^{h*}$ and $Z_2 = t_{02}^v t_{02}^{h*}$. Using the above equations in (4.15) and noting that $M_{11} = \mid t_{02}^v \mid^2 \mid t_{20}^v \mid^2 \frac{p_1}{2\kappa}$ and $M_{22} = \mid t_{02}^h \mid^2 \mid t_{20}^h \mid^2 \frac{p_1}{2\kappa}$, it can easily be shown that

$$\alpha = \sqrt{\frac{p_3^2 + p_4^2}{p_1^2}}. \tag{4.18}$$

It is interesting to note that the above expression for the degree of correlation is the same as the *intrinsic* degree of correlation of the medium (α_i) obtained from the medium phase function. That is, the planar interface between a multi-layer homogeneous medium and the random medium does not affect the degree of correlation between the vertically and horizontally polarized backscattered signals. Similarly, defining the intrinsic mean phase difference of the medium by

$$\zeta_i = \tan^{-1}\frac{p_4}{p_3},$$

the mean phase difference given by (4.16) can be simplified to

$$\zeta = \zeta_i + \zeta_t \tag{4.19}$$

where ζ_t is defined as the total transition phase difference given by

$$\zeta_t = \angle(t_{20}^v t_{20}^{h*}) + \angle(t_{02}^v t_{02}^{h*}).$$

As expected the mean phase difference is the sum of the mean phase difference caused by the random media and the phase difference introduced by the interface.

4.4 Experimental Results

The mathematical framework for characterizing the MMW scattering response of road surfaces possibly covered with a layer of ice or water was established in the previous section. It was shown that the backscattering coefficients and the statistics of the phase difference can be obtained from the four independent elements of the medium. In this section polarimetric backscatter measurements at 94 GHz conducted on asphalt surfaces under a wide range of conditions are presented and compared with the theoretical results. In these experiments the University of Michigan fully polarimetric 94 GHz radar system was used to collect the backscattering response of the targets over the angular range $70° - 88°$. The gimbal assembly is used to scan the distributed targets (road surfaces) for spatially independent sampling as depicted in Figure 4.3. In this study at least eighty samples for each target at each incidence angle were collected to acquire the desired backscatter statistics. The measured data were calibrated using a metallic sphere according to the procedure outlined in [44]. The external calibration procedure removes the systematic errors, such as channel imbalances and antenna cross-talk, from the measured data.

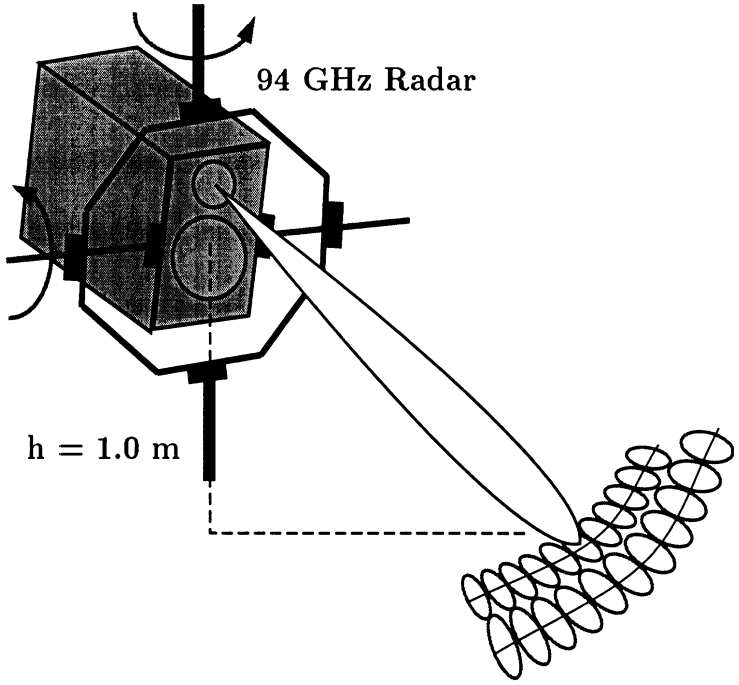

Figure 4.3: Configuration of the radar system for measuring the backscatter response of a distributed target.

4.4.1 Backscatter from Asphalt Surfaces

Two measurement sites were considered for the experiments on asphalt surfaces. In site 1, the asphalt surface was about a year old having a relatively smooth interface. Backscatter measurements were conducted for three different conditions at this site: (1) a dry asphalt surface, (2) a wet asphalt surface with a surface water content of 0.46 kg/m^2, and (3) an asphalt surface covered with a 1.4 mm-thick ice layer. Site 2 was chosen as the repeatability test site. The asphalt surface of this site, like site 1, was relatively new with a smooth surface. The roughness statistics of the asphalt surfaces were measured using a laser ranging system with a range resolution of 0.1 mm. At each site a minimum of 10 linear traces of 40 cm-long surface profiles were collected with a horizontal resolution of 0.2 mm. It was found that the surface roughness statistics of site 1 and site 2 were very similar with rms height and surface

$p_{1,a}/\kappa_{e,a}$	$p_{2,a}/\kappa_{e,a}$	$p_{3,a}/\kappa_{e,a}$	$p_{4,a}/\kappa_{e,a}$
2.36×10^{-2}	4.72×10^{-3}	1.16×10^{-2}	1.40×10^{-3}

Table 4.2: Normalized elements of phase matrix of asphalt mixtures at 94 GHz obtained from the polarimetric backscatter measurements of site 1.

correlation length of approximately 0.34 mm and 4.2 mm respectively.

The theoretical formulation provided in the previous section only accounts for the volume scattering and totally ignores the contribution from the rough surface scattering. The reflectivity and transmissivity of the coherent field (mean-field) at the rough interface between two homogeneous media are proportional to $e^{-k_0^2 \cos^2(\theta_0) s^2}$, where s is the rms height of the rough surface [62]. If this factor is close to unity, most of power remains in the coherent field and the contribution of the rough surface scattering is insignificant. This is the case for the asphalt surfaces of both site 1 and site 2. The measured backscatter data (backscattering coefficients and phase statistics) of the dry asphalt from site 1 was used in (4.14), (4.18), and (4.19) to find the phase matrix elements and are tabulated in Table 4.2.

Figure 4.4 shows the comparison between measurement and theoretical prediction for the co- and cross-polarized backscattering coefficients of the dry asphalt surfaces of site 1 and site 2. It is shown that the backscattering response of the asphalt surfaces is independent of site location and that the agreement between the measurements and the theory is excellent over all angles of incidence. The dashed lines in these figures indicate the system noise equivalent backscattering coefficients (noise floor). The system noise equivalent backscattering coefficients for site 2 were improved by using a coherent averaging technique during data collection.

As mentioned earlier, at site 1 polarimetric backscatter data were also collected

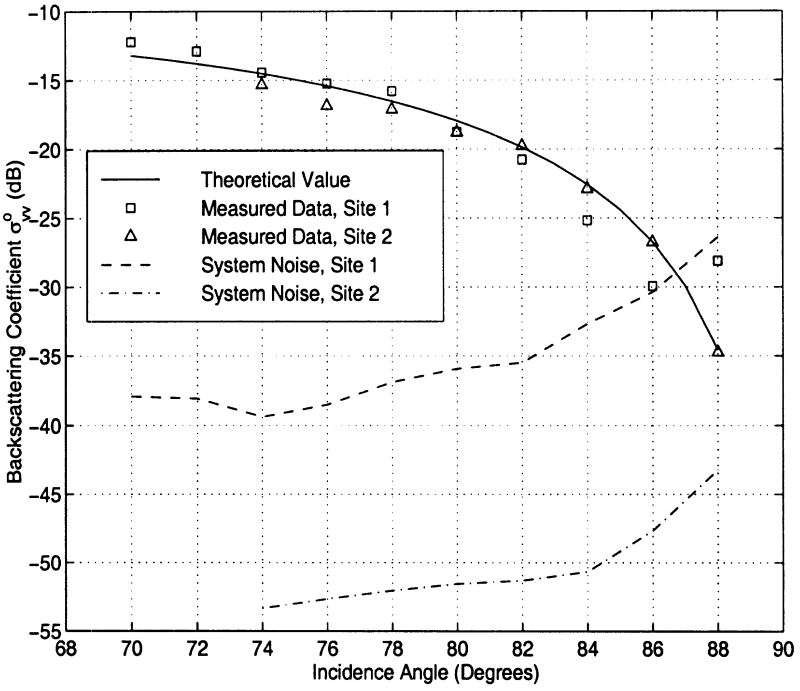

4.4(a) The vv response of dry asphalt surfaces.

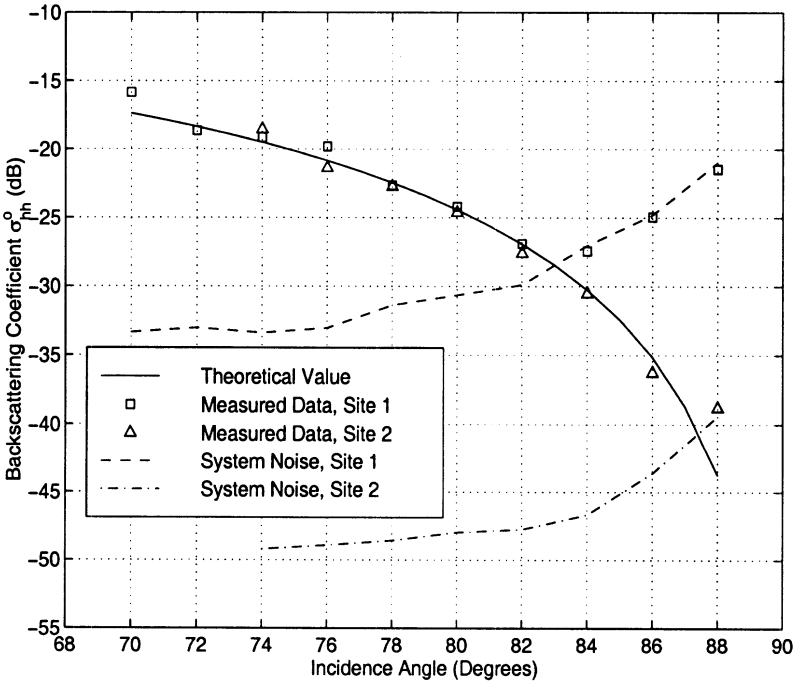

4.4(b) The hh response of dry asphalt surfaces.

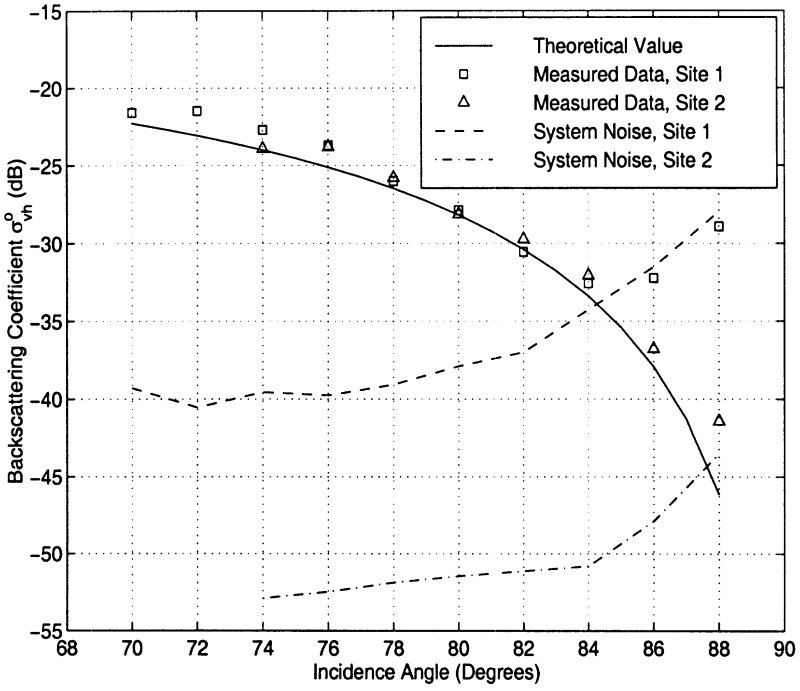

4.4(c) The vh response of dry asphalt surfaces.

Figure 4.4: The comparison between the measured data and the theoretical prediction for co- and cross-polarized backscattering coefficients of dry asphalt surfaces at site 1 and site 2.

from the asphalt surface covered with a thin layer of ice and water. Figure 4.5 shows the co- and cross-polarized measured and calculated backscattering coefficients of the ice-covered asphalt surface. In these calculations, the measured mean ice layer thickness of 1.4 mm and fresh-water ice dielectric constant of $\epsilon_i = 3.1 + j0.27$ were used [63]. As before the agreement is excellent over the angular range where the measurements were not corrupted by the system noise.

Figure 4.6 shows the theoretical and measured backscattering coefficients of the wet asphalt surface. It is shown that the radar backscatter response drops significantly when the surface becomes wet. The dielectric constant of water was first calculated using the Debye formulation given in [63]. It was found that the resulting

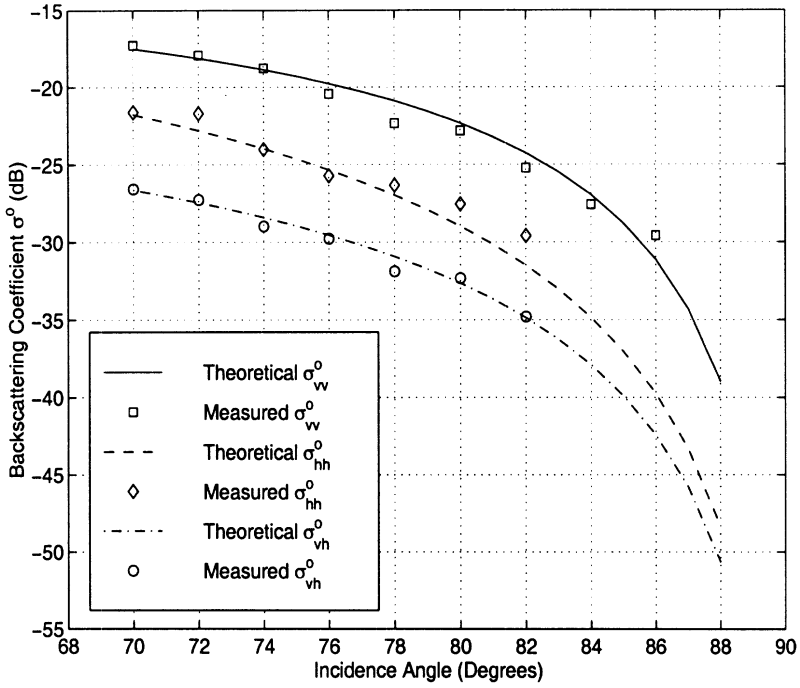

Figure 4.5: The comparison between the measured data and the theoretical prediction for co- and cross-polarized backscattering coefficients of the ice-covered asphalt surface of site 1.

dielectric constant ($\epsilon_w = 5.6 + j7.8$) provided an underestimation for the backscatter measurement. In this case a thin film of water covered the asphalt surface (average thickness = 0.46 mm); a significant fraction of the water molecules were bound to the surface. The dielectric constant of bound water is different from that of free water [63] and therefore the effective dielectric constant of a thin film of water is expected to be different as well. To characterize the effective dielectric constant of a thin film of water on an asphalt surface, the RCSs of the cylindrical asphalt samples were measured after a thin film of water was sprayed on their surfaces. The reflection coefficients of the wet asphalt surfaces were calculated from which the effective dielectric constant of thin water films was found to be $\epsilon_w = 5.6 + j1.7$. This value was used in the calculation of σ° and the results are shown in Figure 4.6. The curve of theoretical ϵ°_{vh} is observed to cross over the theoretical ϵ°_{hh} response at incidence

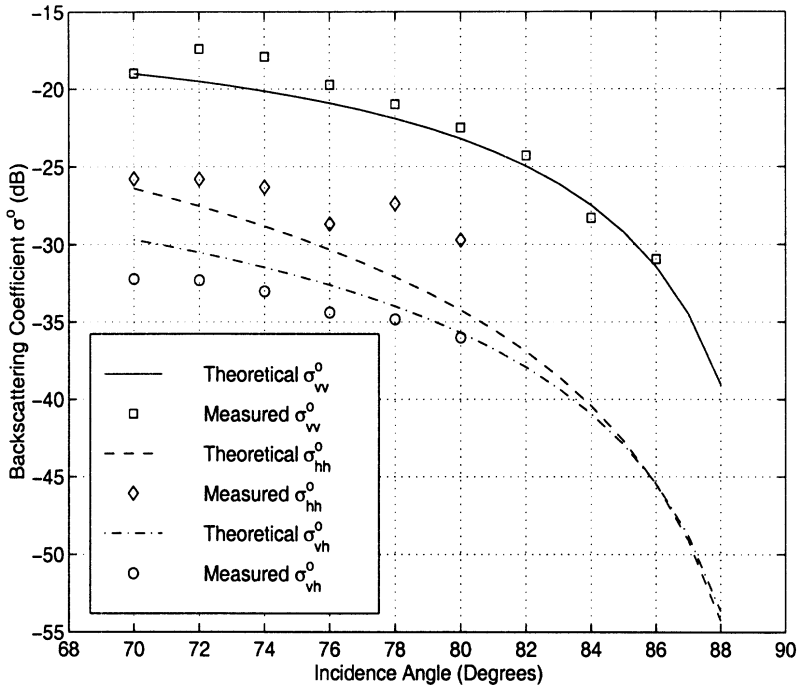

Figure 4.6: The comparison between the measured data and the theoretical prediction for co- and cross-polarized backscattering coefficients of the wet asphalt surface of site 1.

angles greater than 86°. This is caused by a faster increase of the transmissivity component $|t_{20}^v|^2$ compared to $|t_{20}^h|^2$ as incidence angle grows, as shown in Figure 4.7. The ratio of the two parameters at these angles surpasses 7 dB, which is given by the ratio of $p_{1,a}$ and $p_{2,a}$ in (4.14).

As is shown by (4.18) the degree of correlation of asphalt surfaces should be independent of incidence angle and surface cover. Figure 4.8 shows that the measured αs are indeed independent of incidence angle. However, there is some minor dependency on the surface cover type which may be the result of surface roughness, not accounted for in this model. Data measured at lower grazing angles are excluded because of noise corruption. Figure 4.9 shows the comparison between the calculated and measured mean phase difference (ζ). An average discrepancy of less than 10° is achieved.

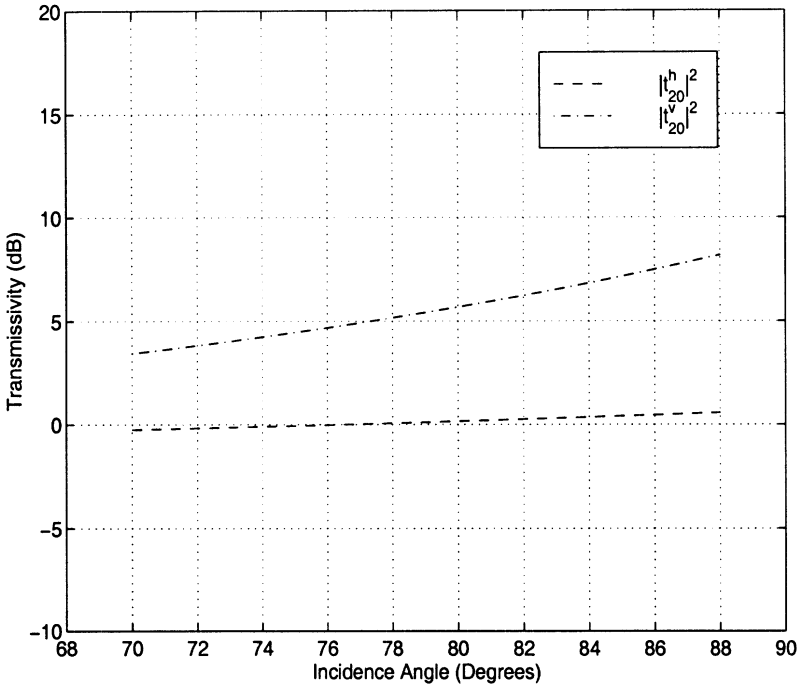

Figure 4.7: The comparison between $|t_{20}^h|^2$ and $|t_{20}^v|^2$ of the wet asphalt surface of site 1.

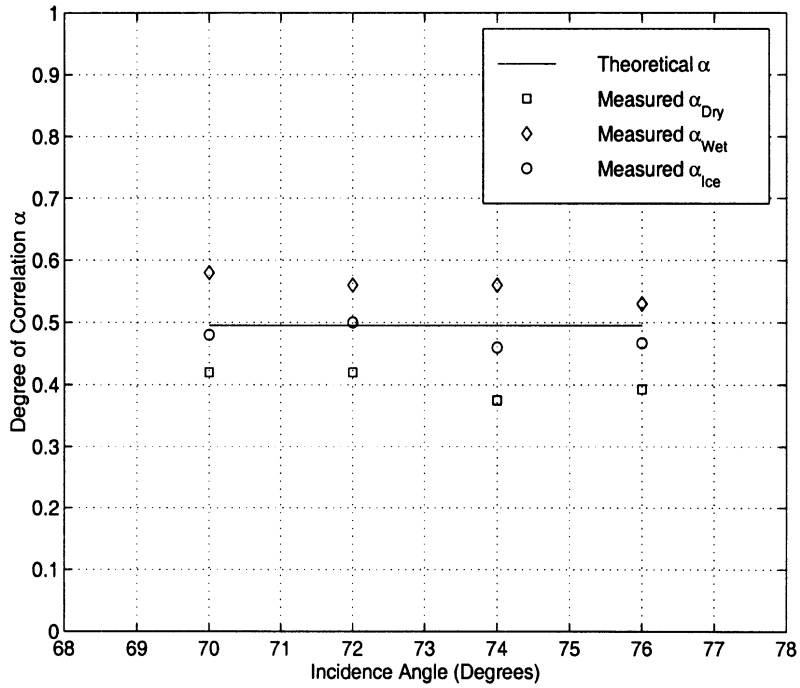

Figure 4.8: The measured and calculated degree of correlation (α) of dry, wet and ice-covered asphalt surfaces.

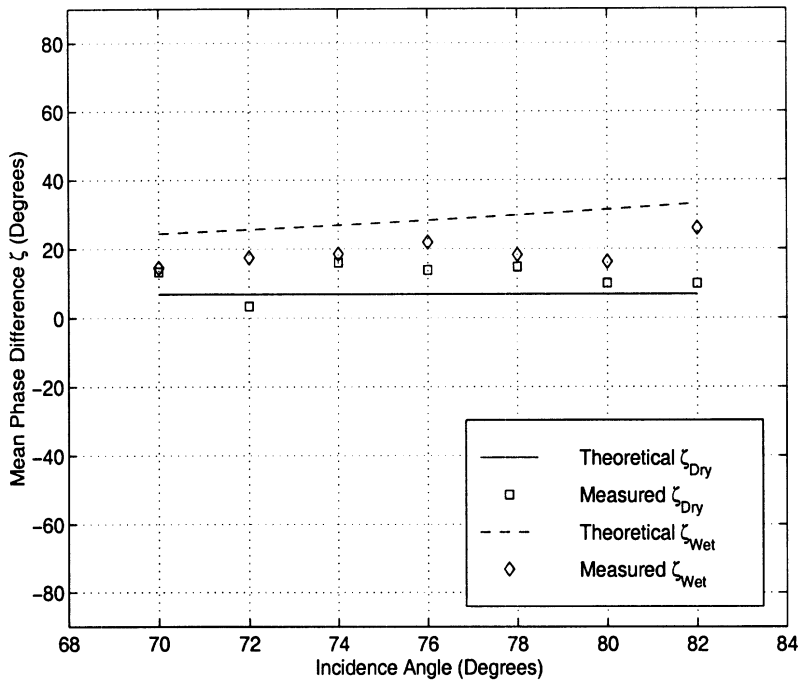

Figure 4.9: The measured and calculated mean phase difference (ζ) of dry and wet asphalt surfaces.

4.4.2 Backscatter from Concrete Surfaces

The polarimetric backscatter response of a concrete surface is considered here. The concrete surface used for this experiment has an rms height of 0.2 mm and a correlation length of 38.5 mm. Since the rms height of the surface is much smaller than the wavelength, the rough surface contribution can be ignored. Two physical conditions are considered : (1) a dry concrete surface, and (2) a concrete surface covered with an ice layer 1.7 mm thick. The measured backscatter data at an incidence angle of 74° under dry conditions were used to characterize the extinction and phase matrices of the concrete mixtures and are reported in Table 4.3. Figure 4.10 shows the comparison between the theoretical values predicted by the model and the measured data for the dry concrete surfaces. Excellent agreement is observed. The ice-covered concrete surface is considered next. The dielectric constant of ice at 0°C

$p_{1,c}/\kappa_{e,c}$	$p_{2,c}/\kappa_{e,c}$	$p_{3,c}/\kappa_{e,c}$	$p_{4,c}/\kappa_{e,c}$
6.4×10^{-3}	6.8×10^{-4}	3.4×10^{-3}	2.2×10^{-3}

Table 4.3: Normalized elements of phase matrix of concrete mixtures at 94 GHz obtained from the polarimetric backscatter measurements.

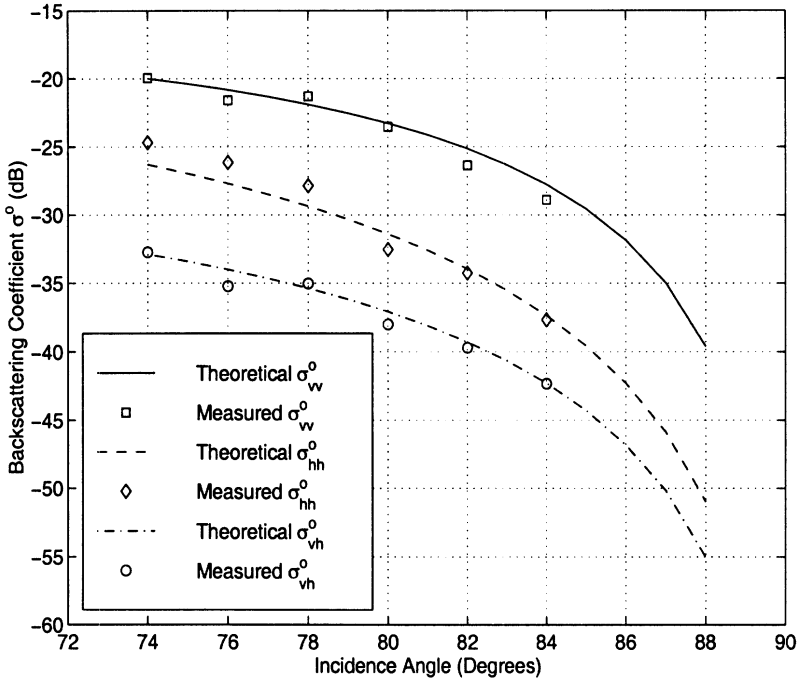

Figure 4.10: The comparison between the measured data and the theoretical predictions for the co- and cross-polarized backscattering coefficients of the dry concrete surface.

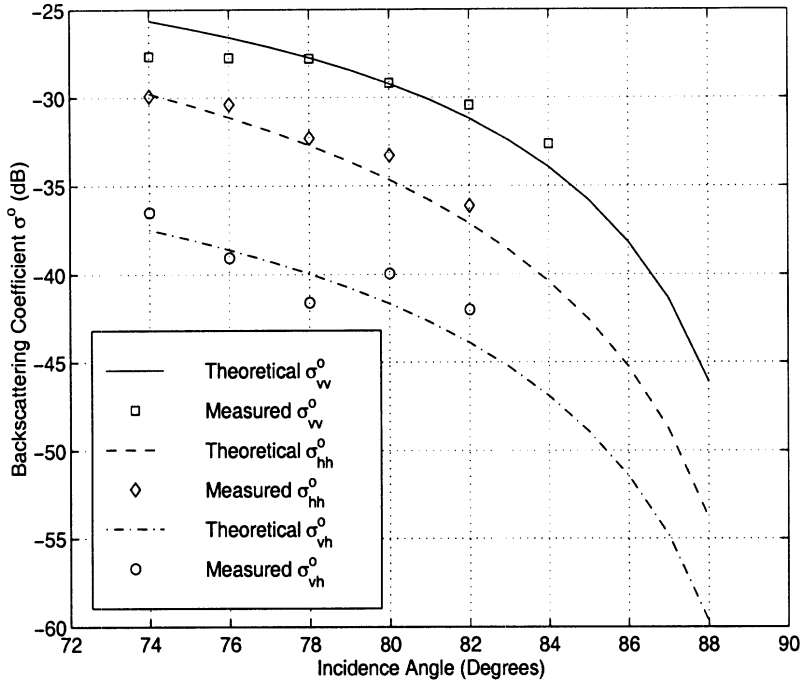

Figure 4.11: The comparison between the measured data and the theoretical predictions for the co- and cross-polarized backscattering coefficients of the ice-covered concrete surface.

(the temperature during the measurement) is taken as $\epsilon_i = 3.15 + j0.27$ [63]. Figure 4.11 displays an excellent agreement between the measured data and the values predicted by the model. The phase difference statistics are illustrated in Figure 4.12 and Figure 4.13. The discrepancy observed between the measured and theoretical values of α can be attributed to phase errors caused by the motion of the radar platform. For the mean phase difference ζ, an average difference of less than 15° is achieved.

4.5 Conclusions

The MMW polarimetric radar phenomenology of smooth road surfaces was investigated thoroughly. A scattering model based on the vector radiative transfer theory and experimental analysis was developed for predicting the radar backscattering re-

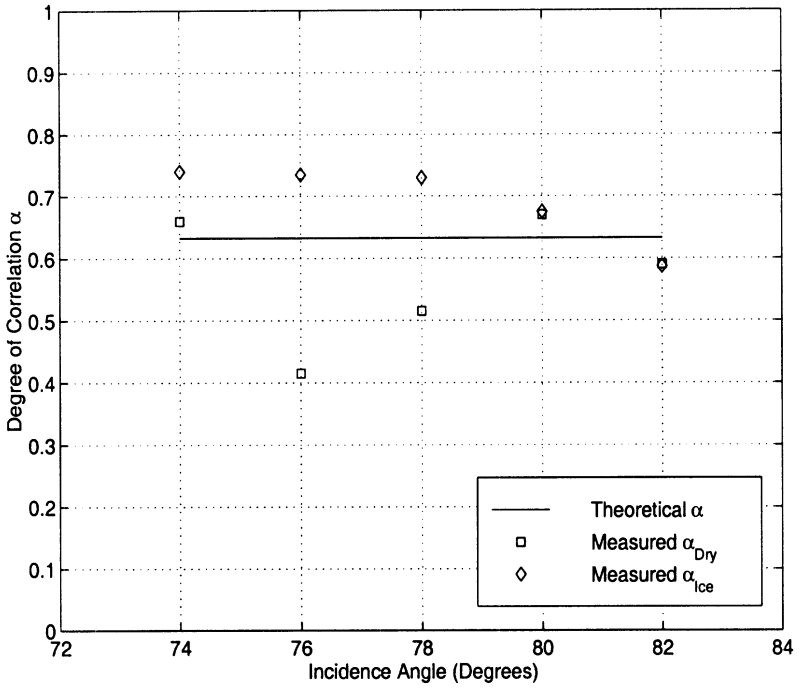

Figure 4.12: The measured and calculated degree of correlation (α) of dry and ice-covered concrete surfaces.

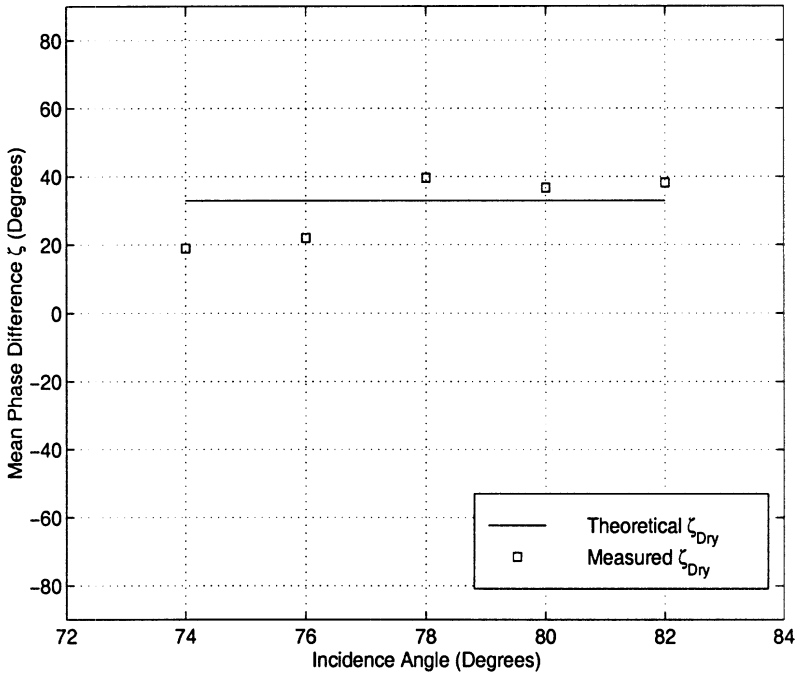

Figure 4.13: The measured and calculated mean phase difference (ζ) of the dry concrete surface.

sponse of smooth road surfaces at 94 GHz. First the effective dielectric constants of pavement mixtures were obtained using RCS measurements of cylindrical pavement mixture samples at normal incidence angles. The fundamental quantities of the RT model were obtained from a polarimetric backscatter measurement of dry road surfaces. These quantities were then used to predict the backscattering coefficients and phase difference statistics of the road surfaces covered with water and ice over a wide range of incidence angles. The University of Michigan W-band polarimetric scatterometer system was used to collect the polarimetric backscatter response of the road surfaces under many physical conditions. It was shown that the theoretical results and the measured quantities are in excellent agreement.

CHAPTER V

NEAR GRAZING INCIDENCE MILLIMETER-WAVE SCATTERING MODELS AND MEASUREMENTS FOR VARIOUS SURFACES

5.1 Introduction

Systematic characterization of the scattering behavior of traffic targets, clutter, and their associated interactions is required in order to design and assess the performance of millimeter-wave based sensors for Automated Highway System (AHS) applications. This can be pursued by investigating the polarimetric radar backscatter response of various road surfaces both theoretically and experimentally. In general, it is found that the overall scattering response of road surfaces is composed of volume and surface scattering components. A model for prediction of the backscatter response of smooth road surfaces under various weather conditions (covered with water or ice) was developed in Chapter 4. This hybrid scattering model is appropriate for dense random media and is based on vector radiative transfer (RT) theory, where the fundamental quantities of the RT model are characterized by measurement. There only the volume scattering was accounted for, however, experimental results show that the surface scattering cannot be ignored when the surface rough-

ness parameters become comparable to the radar wavelength. In this chapter, the previous study is extended to include the radar backscatter response of snow-covered smooth surfaces and rough asphalt or concrete surfaces. A complete investigation of the backscatter behavior of various road surfaces under different physical conditions is pursued.

Existence of a second layer of scatterers such as snow necessitates construction of a different volume scattering model. The phase and extinction matrices of a fresh snow layer can be computed using single scattering theory. Noting the azimuthal symmetry of snow particle distribution, ice particles in the snow medium are modeled as small spherical particles having the same volume as that of the snow flakes. The backscatter response of the snow-covered smooth asphalt or concrete surface is then computed from the superposition of the volume scattering from the snow layer and the underlying layer, since the incoherent scattering from these media are statistically uncorrelated.

For asphalt or concrete roads with a rough surface, the surface scattering component must be accounted for. Experimental results indicate that surface scattering becomes significant or even dominant when the surface roughness parameters are of the order of a wavelength. To develop a comprehensive scattering model for rough road surfaces, a surface scattering model known as the integral equation method (IEM) is incorporated into the volume scattering model developed for roads with a smooth surface. IEM is a surface scattering model that accounts for multiple scattering up to second-order and is expected to be valid for rough surfaces with low to moderate rms slope. Since the volumetric backscatter response is a gentle function of incidence angle, the surface roughness, which causes small variations in the transmitted ray direction, does not affect the volume scattering contribution. Therefore

the volume scattering and the surface scattering response can simply be added to predict the backscatter response of rough road surfaces.

This chapter is organized as follows. First the effective dielectric constant of snow is determined theoretically. Then the procedures for characterization of ground-truth data such as surface roughness parameters are given. In Section 5.3, the model for a multi-layer random medium with two volume scattering layers is formulated for the snow-covered smooth surfaces. The surface scattering model is briefly described in Section 5.3.2. The experimental procedure for the backscatter measurements and examination of the validity of the theoretical models are given in Section 5.4.

5.2 Characterization of Ground-truth Data

Determination of influential parameters of the scattering medium is an essential step towards the development of scattering models. For example, characterization of the scattering behavior of road surfaces requires knowledge of the effective dielectric constants of pavement mixtures and possible surface cover such as water, ice, or snow. The measurements of effective dielectric constants of pavement mixtures are described in Section 4.2. In this section, the effective dielectric constant of snow is examined. The Polder-Van Santen mixing formula is used. The measurement of the surface roughness statistics of rough interfaces between different media is also very important. The rms height and the correlation length are the most important surface parameters for modeling surface scattering. Both parameters are characterized experimentally.

5.2.1 Effective Dielectric Constant of Snow

The dielectric constant measurement of snow requires separate treatments for dry snow and wet snow. The case considered here is fresh dry snow. Modeling snow

flakes with equivalent spherical ice particles results in particle sizes that fall within the Rayleigh region. Hence the dielectric constant (ϵ_s) of dry snow can be calculated by the Polder-Van Santen mixing formula for spherical inclusions. With air as the host dielectric material and ice crystals as the inclusions, the real part and imaginary part of ϵ_s can be obtained from [63]

$$\epsilon_s' = (1 + 0.47v_i)^3, \qquad \epsilon_s'' = 3v\epsilon_i'' \frac{(\epsilon_s')^2(2\epsilon_s' + 1)}{(\epsilon_i' + 2\epsilon_s')(\epsilon_i' + 2(\epsilon_s')^2)} \tag{5.1}$$

where v is the volume fraction. The dielectric constant of ice is chosen to be $\epsilon_i = 3.15 + j0.025$ according to the temperature of $-20°$C during the measurement [63]. For a volume fraction of 0.0742 (obtained from the ground-truth measurement of the snow-covered smooth asphalt surface), the effective dielectric constant of the snow is found to be $\epsilon_s = 1.11 + j0.00074$.

5.2.2 Surface Roughness Statistics

Surface roughness statistics are described by two important factors: the rms height of surface roughness (s) and the surface autocorrelation function ($\rho(r)$). For one-dimensional surface profile measurements, s is obtained from discrete height samples $h_i(x_i)$ at an appropriate spacing Δx, normally chosen such that $\Delta x \leq 0.1\lambda$. The normalized autocorrelation function ($\langle\, h(x)h(x-x') \,\rangle$) at a spatial displacement of $x' = (j-1)\Delta x$ for the discrete case can be computed from

$$\rho(x') = \frac{\sum_{i=1}^{N+1-j} h_i h_{i+j-1}}{\sum_{i=1}^{N} h_i^2} \tag{5.2}$$

and the surface correlation length (ℓ) is defined as the displacement x' for which $\rho(x')$ is equal to $1/e$ [62].

Road Surfaces	s (mm)	ℓ (mm)
Smooth Asphalt	0.34	4.2
Smooth Concrete	0.2	38.6
Rough Asphalt	0.9	6.3

Table 5.1: The surface statistics of the road surfaces examined in this investigation.

The surface roughness statistics of the rough asphalt surface considered in this study were measured by a laser ranging system with a range resolution of 0.1 mm. Surface profiles from 10 different locations were collected with each linear trace being at least 40 cm long. The horizontal resolution was set to be 0.2 mm which satisfies the requirement $\Delta r \leq 0.1\lambda$. The measured s and ℓ for the rough asphalt surface are listed in Table 5.1.

For most road surfaces, the surface roughness exhibits a Gaussian height distribution with zero mean and standard deviation equal to s. This characteristic simplifies the analytical formulation of the surface scattering model. Figure 5.1 compares the measured surface roughness histogram of the rough asphalt surface with a Gaussian probability density function. The normalized autocorrelation function of the rough asphalt surface is illustrated in Figure 5.2 along with an approximate exponential function $\rho(r) = e^{-\frac{r}{\ell}}$.

5.3 Theoretical Analysis

The backscatter response of road surfaces comes from two major sources: the volume scattering from pavement mixtures and the surface scattering from the rough interface between the air and the pavement mixture. The volume scattering is already

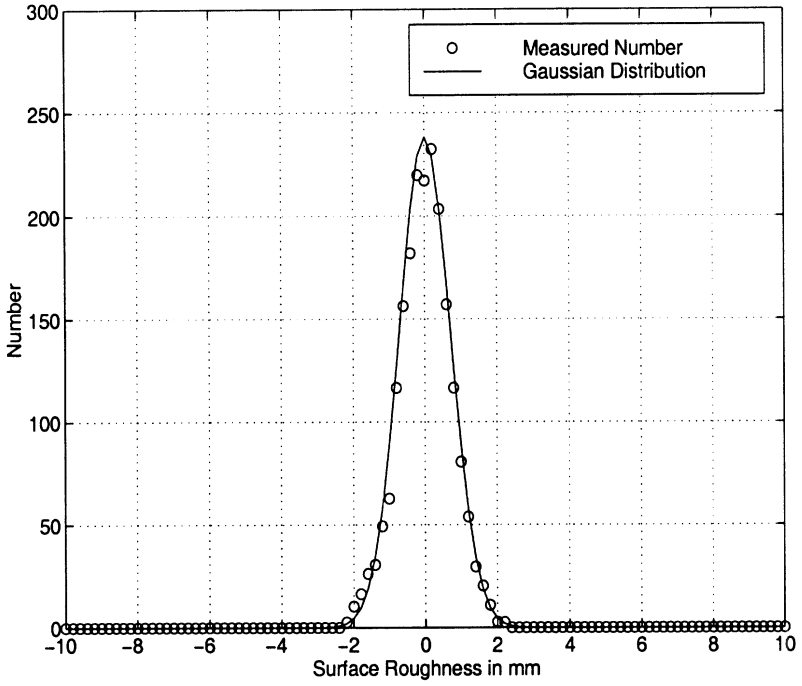

Figure 5.1: The surface roughness distribution of the rough asphalt surface.

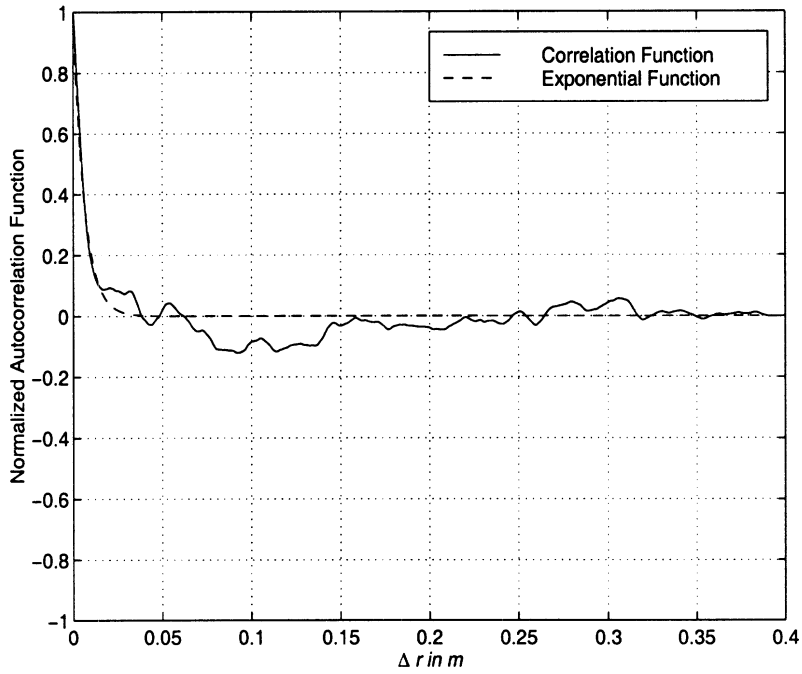

Figure 5.2: The normalized autocorrelation function of the rough asphalt surface and the exponential approximation.

described in Chapter 4 and will not be discussed here. Pertinent quantities such as the extinction and phase matrices are related to the physical parameters of the medium such as particle size, density, permittivity, and orientation distribution. For dense random media like pavement mixtures, these quantities are difficult to characterize analytically and are obtained experimentally. On the other hand, the extinction and phase matrices of snow can be described precisely by the Rayleigh scattering model.

To analyze the backscatter response from rough road surfaces, the effect of surface scattering cannot be ignored. Many approximate analytical solutions of the surface scattering problems have been introduced. The choice of the appropriate model depends on the normalized rms height (ks) and correlation length ($k\ell$). For surfaces with small rms roughness and slope, the small perturbation model (SPM) is often used [45,48]. The Kirchhoff approximation (KA) is usually used for surfaces with relatively small slopes and large radii of curvature [4]. Other techniques such as the phase perturbation method (PPM) [74] and the unified perturbation expansion (UPE) [49] are mainly used in the low frequency regime. To investigate the backscatter behavior of a rough asphalt surface at W-band, the IEM technique is selected. In the following, the scattering solutions for two different road surfaces are discussed.

5.3.1 Backscatter from Snow-covered Smooth Surfaces

Scattering from snow-covered road surfaces with a smooth interface can be treated as a scattering problem of a two-layer random medium. The geometry of this problem is shown in Figure 5.3. Consider the case of snow-covered smooth asphalt surfaces. As mentioned before, the underlying asphalt layer can be considered semi-infinite,

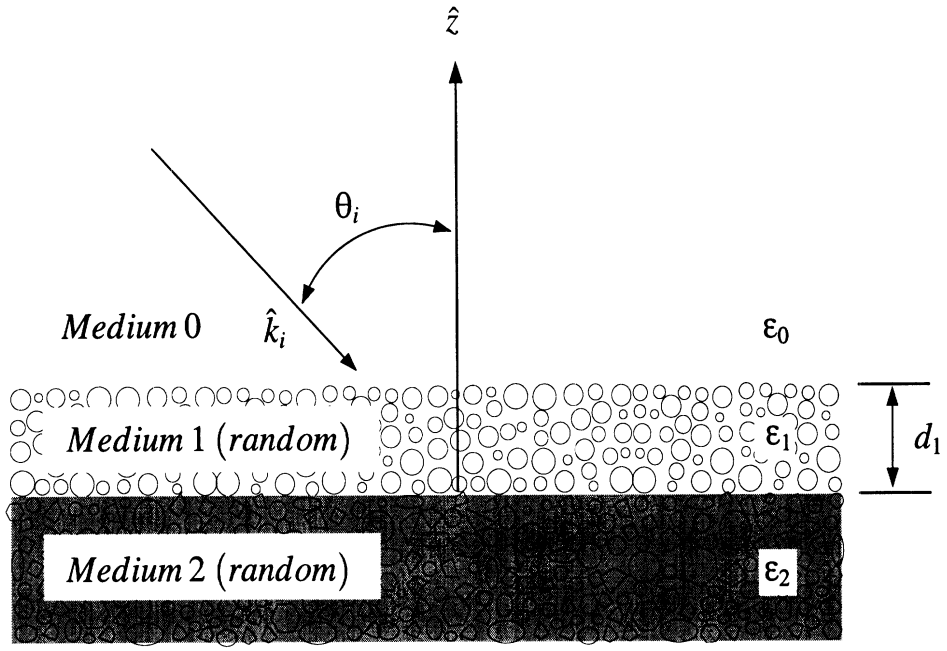

Figure 5.3: The geometry of the scattering from a multiple-layer medium with two volume scattering layers.

which reduces the boundary conditions to the following relatively simple forms

$$\begin{aligned}
\boldsymbol{I}^-(\pi-\theta_1,\phi_0,d_1^-) &= \boldsymbol{T}_{01}\boldsymbol{I}^i(\pi-\theta_0,\phi_0,d_1^+)\delta(\theta-\theta_0)\delta(\phi-\phi_0)+\boldsymbol{R}_{10}\boldsymbol{I}^+(\theta_1,\phi_0,d_1^-)\\
\boldsymbol{I}^+(\theta_1,\phi_0,0^+) &= \boldsymbol{R}_{12}\boldsymbol{I}^-(\pi-\theta_1,\phi_0,0^+)+\boldsymbol{T}_{21}\boldsymbol{I}^+(\theta_2,\phi_0,0^-) \qquad (5.3)\\
\boldsymbol{I}^-(\pi-\theta_2,\phi_0,0^-) &= \boldsymbol{T}_{12}\boldsymbol{I}^-(\pi-\theta_1,\phi_0,0^+)+\boldsymbol{R}_{21}\boldsymbol{I}^+(\theta_2,\phi_0,0^-).
\end{aligned}$$

Here $\boldsymbol{R}_{10}$ is the reflectivity matrix given by

$$\boldsymbol{R}_{10}=\begin{bmatrix}
|r_{10}^v|^2 & 0 & 0 & 0\\
0 & |r_{10}^h|^2 & 0 & 0\\
0 & 0 & \mathrm{Re}(r_{10}^v r_{10}^{h*}) & -\mathrm{Im}(r_{10}^v r_{10}^{h*})\\
0 & 0 & \mathrm{Im}(r_{10}^v r_{10}^{h*}) & \mathrm{Re}(r_{10}^v r_{10}^{h*})
\end{bmatrix} \qquad (5.4)$$

where r_{10}^v and r_{10}^h are the v-polarized and h-polarized Fresnel reflection coefficients at the interface of medium 1 and medium 0. The matrices $\boldsymbol{R}_{12}$ and $\boldsymbol{R}_{21}$ have a form similar to $\boldsymbol{R}_{10}$ using appropriate subscripts. $\boldsymbol{T}_{01}$, $\boldsymbol{T}_{12}$, and $\boldsymbol{T}_{21}$ have the same form as

$\boldsymbol{T}_{02}$ in (4.9) except for the change in the subscript; t_{01}^{v} and t_{01}^{h} are the v-polarized and h-polarized field transmission coefficients at the interface of medium 0 and medium 1. The field transmission coefficients at the interface of adjacent media m and n are given by

$$t_{mn}^{v} = (1 + r_{mn}^{v})\frac{\eta_n}{\eta_m}, \qquad t_{mn}^{h} = 1 + r_{mn}^{h}. \tag{5.5}$$

The scattering behavior of snow, unlike the pavement material, has been modeled successfully and reported in many references [60, 63]. The collected ground-truth shows that the average radius a of the ice crystals for the experiment conducted for the snow-covered asphalt surface is around 0.25 mm. Therefore the Rayleigh scattering model can be used ($ka = 0.5$) to predict the phase and extinction matrices of the snow layer. The phase matrix $\boldsymbol{P}_s$ of the Rayleigh scatterer has the following form

$$\boldsymbol{P}_s(\theta^s, \phi^s; \theta^i, \phi^i) = \begin{bmatrix} p_{11} & p_{12} & p_{13} & 0 \\ p_{21} & p_{22} & p_{23} & 0 \\ p_{31} & p_{32} & p_{33} & 0 \\ 0 & 0 & 0 & p_{44} \end{bmatrix} \tag{5.6}$$

where the subscript s denotes snow. The expressions for each element of $\boldsymbol{P}_s$ are presented in [60, 63] and are not repeated here. The extinction coefficient for snow $\kappa_{e,s}$ is the sum of the scattering coefficient $\kappa_{s,s}$ and the absorption coefficient $\kappa_{a,s}$. The scattering coefficient $\kappa_{s,s}$ is given by

$$\kappa_{s,s} = 2vk^4a^3 \left| \frac{\epsilon_s - \epsilon}{\epsilon_s + 2\epsilon} \right|^2 \tag{5.7}$$

where v is the volume fraction of the scatterers, ϵ_s is the dielectric constant of the ice particles, ϵ is the dielectric constant of the background material, and k is the

wavenumber in the background material. The absorption coefficient $\kappa_{a,s}$ is given by

$$\kappa_{a,s} = vk\frac{\epsilon_s''}{\epsilon}\left|\frac{3\epsilon}{\epsilon_s + 2\epsilon}\right|^2. \tag{5.8}$$

The co-polarized backscatter response of the snow-covered smooth asphalt surface follows from the first-order iterative solution of the RT equation subject to the boundary conditions in (5.3). The backscattered specific intensity can be related to the incident specific intensity by

$$\begin{aligned}
\boldsymbol{I}^s(\theta_0, \phi_0 + \pi, d_1^+) \;=\; & \frac{1}{\cos\theta_1}\boldsymbol{T}_{10}\boldsymbol{F}^+\left[\boldsymbol{P}_s(\theta_1, \phi_1 + \pi; \theta_1, \phi_1)\boldsymbol{F}^+\boldsymbol{R}_{12}\boldsymbol{T}_{01}\boldsymbol{I}_0^i e^{\frac{-2\kappa_{e,s}d_1}{\cos\theta_1}} d_1\right. \\
& \left. + \boldsymbol{P}_s(\theta_1, \phi_1 + \pi; \pi - \theta_1, \phi_1)\boldsymbol{F}^-\boldsymbol{T}_{01}\boldsymbol{I}_0^i\frac{\cos\theta_1}{2\kappa_{e,s}}\left(1 - e^{\frac{-2\kappa_{e,s}d_1}{\cos\theta_1}}\right)\right] \\
& + \frac{1}{\cos\theta_1}\boldsymbol{T}_{10}\boldsymbol{F}^+\boldsymbol{R}_{12}e^{\frac{-2\kappa_{e,s}d_1}{\cos\theta_1}}\left[\boldsymbol{P}_s(\pi - \theta_1, \phi_1 + \pi; \theta_1, \phi_1)\boldsymbol{F}^+\boldsymbol{R}_{12}\right. \\
& \boldsymbol{T}_{01}\boldsymbol{I}_0^i\frac{\cos\theta_1}{2\kappa_{e,s}}\left(1 - e^{\frac{-2\kappa_{e,s}d_1}{\cos\theta_1}}\right) + \boldsymbol{P}_s(\pi - \theta_1, \phi_1 + \pi; \pi - \theta_1, \phi_1) \\
& \left.\boldsymbol{F}^-\boldsymbol{T}_{01}\boldsymbol{I}_0^i d_1\right] + e^{\frac{-2\kappa_{e,s}d_1}{\cos\theta_1}}\boldsymbol{T}_{10}\boldsymbol{F}^+\boldsymbol{T}_{21}\boldsymbol{P}_a(\theta_2, \phi_2 + \pi; \pi - \theta_2, \phi_2) \\
& \boldsymbol{T}_{12}\boldsymbol{F}^-\boldsymbol{T}_{01}\boldsymbol{I}_0^i\frac{1}{2\kappa_{e,a}}
\end{aligned} \tag{5.9}$$

where the subscript a denotes the quantities of asphalt mixtures. The expressions for $\boldsymbol{F}^+$ and $\boldsymbol{F}^-$ are given by

$$\boldsymbol{F}^+ = \left(\bar{\mathbf{I}} - \boldsymbol{R}_{12}\boldsymbol{R}_{10}e^{\frac{-2\kappa_{e,s}d_1}{\cos\theta_1}}\right)^{-1}, \qquad \boldsymbol{F}^- = \left(\bar{\mathbf{I}} - \boldsymbol{R}_{10}\boldsymbol{R}_{12}e^{\frac{-2\kappa_{e,s}d_1}{\cos\theta_1}}\right)^{-1} \tag{5.10}$$

and $\bar{\mathbf{I}}$ is a 4×4 unitary matrix. Equation (5.9) indicates that the backscatter response of the snow-covered smooth asphalt surface consists of the volume scattering from the snow layer and the volume scattering from the underlying asphalt layer. The backscattering coefficients for the snow layer, based on the first-order iterative

solution of the RT equation, can be derived from (4.6) and (5.9) and expressed as

$$\begin{aligned}
\sigma_{vv,s}^{\circ(1)} &= \frac{3\kappa_{s,s}}{2}\cos\theta_0|t_{10}^v|^2|t_{01}^v|^2F_{11}^2\left[\frac{2d_1}{\cos\theta_1}\left(\sin^2\theta_1-\cos^2\theta_1\right)^2|r_{12}^v|^2e^{\frac{-2\kappa_{e,s}d_1}{\cos\theta_1}}\right.\\
&\left.+\frac{1}{2\kappa_{e,s}}\left(1-e^{\frac{-2\kappa_{e,s}d_1}{\cos\theta_1}}\right)\left(1+(|r_{12}^v|^2)^2e^{\frac{-2\kappa_{e,s}d_1}{\cos\theta_1}}\right)\right]\\
\sigma_{hh,s}^{\circ(1)} &= \frac{3\kappa_{s,s}}{2}\cos\theta_0|t_{10}^h|^2|t_{01}^h|^2F_{22}^2\left[\frac{2d_1}{\cos\theta_1}|r_{12}^h|^2e^{\frac{-2\kappa_{e,s}d_1}{\cos\theta_1}}\right.\\
&\left.+\frac{1}{2\kappa_{e,s}}\left(1-e^{\frac{-2\kappa_{e,s}d_1}{\cos\theta_1}}\right)\left(1+(|r_{12}^h|^2)^2e^{\frac{-2\kappa_{e,s}d_1}{\cos\theta_1}}\right)\right]\\
\sigma_{vh,s}^{\circ(1)} &= 0\\
\sigma_{hv,s}^{\circ(1)} &= 0
\end{aligned} \tag{5.11}$$

where the superscript (1) denotes the first-order iterative solution. F_{11} and F_{22} are given by

$$F_{11}=\left(1-|r_{10}^v|^2|r_{12}^v|^2e^{\frac{-2\kappa_{e,s}d_1}{\cos\theta_1}}\right)^{-1},\qquad F_{22}=\left(1-|r_{10}^h|^2|r_{12}^h|^2e^{\frac{-2\kappa_{e,s}d_1}{\cos\theta_1}}\right)^{-1}. \tag{5.12}$$

As given by (5.11), the first-order cross-polarized backscatter response predicted by the RT model is zero. Hence higher order solutions must be considered for determining the cross-polarized response. The cross-polarized backscattering coefficient derived from the second-order iterative solution is given by [60]

$$\begin{aligned}
\sigma_{hv,s}^{\circ(2)} &= 4\frac{\cos\theta_0}{\cos\theta_1}\left(\frac{3\kappa_{s,s}}{8}\right)^2|t_{10}^h|^2|t_{01}^v|^2F_{22}F_{11}\int_0^{\pi/2}d\theta'\frac{\sin\theta'}{\cos\theta'}\\
&\left[Q_1(\theta_1,\theta')+Q_2(\theta_1,\theta')+Q_3(\theta_1,\theta')\right]
\end{aligned} \tag{5.13}$$

where the superscript (2) denotes the second-order iterative solution. The expressions for $Q_1(\theta_1,\theta')$, $Q_2(\theta_1,\theta')$, and $Q_3(\theta_1,\theta')$ are given in the paper by Shin and Kong [56]. $\sigma_{vh,s}^{\circ(2)}$ can be obtained from $\sigma_{hv,s}^{\circ(2)}$ using the reciprocity theorem.

The expressions for the backscattering coefficients of the underlying asphalt layer can also be deduced from (4.6) and (5.9). Since the phase matrix of the asphalt

mixture $\boldsymbol{P}_a$ has the same form as $\boldsymbol{P}$ in (4.13), the backscattering coefficients can be expressed as

$$\begin{aligned}
\sigma^{\circ(1)}_{vv,a} &= 4\pi\cos\theta_0|t^v_{10}|^2|t^v_{21}|^2|t^v_{12}|^2|t^v_{01}|^2F^2_{11}e^{\frac{-2\kappa_{e,s}d_1}{\cos\theta_1}}\frac{p_{1,a}}{2\kappa_{e,a}} \\
\sigma^{\circ(1)}_{hh,a} &= 4\pi\cos\theta_0|t^h_{10}|^2|t^h_{21}|^2|t^h_{12}|^2|t^h_{01}|^2F^2_{22}e^{\frac{-2\kappa_{e,s}d_1}{\cos\theta_1}}\frac{p_{1,a}}{2\kappa_{e,a}} \\
\sigma^{\circ(1)}_{vh,a} &= 4\pi\cos\theta_0|t^v_{10}|^2|t^v_{21}|^2|t^h_{12}|^2|t^h_{01}|^2F_{11}F_{22}e^{\frac{-2\kappa_{e,s}d_1}{\cos\theta_1}}\frac{p_{2,a}}{2\kappa_{e,a}} \\
\sigma^{\circ(1)}_{hv,a} &= 4\pi\cos\theta_0|t^h_{10}|^2|t^h_{21}|^2|t^v_{12}|^2|t^v_{01}|^2F_{22}F_{11}e^{\frac{-2\kappa_{e,s}d_1}{\cos\theta_1}}\frac{p_{2,a}}{2\kappa_{e,a}}.
\end{aligned} \tag{5.14}$$

The quantities $\frac{p_{1,a}}{2\kappa_{e,a}}$ and $\frac{p_{2,a}}{2\kappa_{e,a}}$ are determined from the experimental data.

The overall backscatter response of the snow-covered smooth asphalt surface is the sum of the response from the snow layer and the response from the asphalt layer.

$$\begin{aligned}
\sigma^\circ_{vv} &= \sigma^{\circ(1)}_{vv,s} + \sigma^{\circ(1)}_{vv,a} \\
\sigma^\circ_{hh} &= \sigma^{\circ(1)}_{hh,s} + \sigma^{\circ(1)}_{hh,a} \\
\sigma^\circ_{vh} &= \sigma^{\circ(2)}_{vh,s} + \sigma^{\circ(1)}_{vh,a} \\
\sigma^\circ_{hv} &= \sigma^{\circ(2)}_{hv,s} + \sigma^{\circ(1)}_{hv,a}.
\end{aligned} \tag{5.15}$$

5.3.2 Backscatter from Rough Asphalt Surfaces

The measured backscattering coefficients of a rough asphalt surface with rms height 0.9 mm ($ks = 1.8$) were compared with the results predicted by the volume scattering model developed for smooth asphalt surfaces in Chapter 4. The comparison indicated that the volume scattering cannot accurately predict the overall backscatter response of such a surface. That is, a comprehensive scattering model should also account for the surface scattering component. The backscatter behavior of a rough surface can be described in terms of its surface roughness statistics, namely the rms height of the surface profile s and the surface autocorrelation function $\rho(r)$, and the permittivity contrast between two media.

The effective dielectric constant of asphalt at W-band was found to be $3.18+j0.1$ which presents a significant contrast to that of the upper medium (air). Hence a considerable rough surface scattering contribution is expected. Noting that the permittivity fluctuations within the asphalt medium are relatively small and somewhat independent of surface roughness statistics, the surface scattering contribution can be computed independently of the volume scattering. In other words, to compute the surface scattering component the asphalt medium is considered a homogeneous medium with a dielectric constant of $\epsilon_a = 3.18 + j0.1$.

Of the existing analytical models for rough surface scattering, the integral equation method (IEM) appears to be the most comprehensive. This method is adopted here for the calculation of the surface scattering contribution from rough asphalt surfaces. The formulation is obtained from a simplified second-order iterative physical optics (P. O.) approximation. Besides the term estimated by the standard Kirchhoff approximation, this formulation contains a complementary term to represent the second-order multiple scattering [17], that is

$$\begin{aligned} \hat{n} \times \mathbf{E} &= (\hat{n} \times \mathbf{E})_k + (\hat{n} \times \mathbf{E})_c \\ \hat{n} \times \mathbf{H} &= (\hat{n} \times \mathbf{H})_k + (\hat{n} \times \mathbf{H})_c \end{aligned} \tag{5.16}$$

where the subscripts k and c, respectively, denote the Kirchhoff and complementary components. Depending on the polarization, the Kirchhoff tangential fields can be approximated by the following expressions

$$\begin{aligned} (\hat{n} \times \mathbf{E})_{k,v} &= (1 - r^v)\, \hat{n} \times \hat{v} E^i \\ \eta\, (\hat{n} \times \mathbf{H})_{k,v} &= (1 + r^v)\, \hat{n} \times \left(\hat{k}_i \times \hat{v}\right) E^i \\ (\hat{n} \times \mathbf{E})_{k,h} &= (1 + r^h)\, \hat{n} \times \hat{h} E^i \\ \eta\, (\hat{n} \times \mathbf{H})_{k,h} &= (1 - r^h)\, \hat{n} \times \left(\hat{k}_i \times \hat{h}\right) E^i \end{aligned} \tag{5.17}$$

where r^v and r^h are the Fresnel reflection coefficients, E^i is the amplitude of the incident electric field and $\hat{k}_i$ is the unit vector in the incident direction. Similarly, the approximate expressions for the complementary tangential fields are given by

$$\begin{aligned}
(\hat{n}\times\mathbf{E})_{c,v} &\approx -\frac{1}{4\pi}\hat{n}\times\int\left[(1-r^v)\,\vec{\mathcal{E}}_v+(1+r^v)\,\vec{\mathcal{E}}_{vt}\right]ds' \\
(\hat{n}\times\mathbf{H})_{c,v} &\approx \frac{1}{4\pi}\hat{n}\times\int\left[(1+r^v)\,\vec{\mathcal{H}}_v+(1-r^v)\,\vec{\mathcal{H}}_{vt}\right]ds' \\
(\hat{n}\times\mathbf{E})_{c,h} &\approx -\frac{1}{4\pi}\hat{n}\times\int\left[(1+r^h)\,\vec{\mathcal{E}}_h+(1-r^h)\,\vec{\mathcal{E}}_{ht}\right]ds' \\
(\hat{n}\times\mathbf{H})_{c,h} &\approx \frac{1}{4\pi}\hat{n}\times\int\left[(1-r^h)\,\vec{\mathcal{H}}_h+(1+r^h)\,\vec{\mathcal{H}}_{ht}\right]ds'.
\end{aligned} \tag{5.18}$$

The expressions for $\vec{\mathcal{E}}_p$, $\vec{\mathcal{E}}_{pt}$, $\vec{\mathcal{H}}_p$, and $\vec{\mathcal{H}}_{pt}$ $(p=v,h)$ are given by Fung [17].

In accordance with the Stratton-Chu integral, the scattered far field in the medium above the rough surface can be written as

$$\mathbf{E}^s=\frac{jk}{4\pi R}e^{jkR}\int[\hat{k}_s\times(\hat{n}\times\mathbf{E})+\eta(\hat{n}\times\mathbf{H})]e^{-j(\mathbf{k}_s\cdot\mathbf{r})}ds \tag{5.19}$$

where $\mathbf{k}_s=k_{sx}\hat{x}+k_{sy}\hat{y}+k_{sz}\hat{z}$. Note that the $e^{-j\omega t}$ convention, used throughout this thesis, is adopted in (5.19). To calculate the backscattering coefficients, the incoherent scattered power must be determined. This is obtained by subtracting the coherent power from the total scattered power, that is,

$$P_{pq}=\langle E^s_{pq}E^{s\,*}_{pq}\rangle-\langle E^s_{pq}\rangle\langle E^s_{pq}\rangle^*. \tag{5.20}$$

Assuming a Gaussian surface roughness statistic, the averaging operation can be carried out analytically. The backscattering coefficient σ°_{pq} is related to the average power P_{pq} by

$$\sigma^\circ_{pq}=\left(4\pi R^2P_{pq}\right)/\left(|E^i|^2A_{illu}\right) \tag{5.21}$$

where A_{illu} is the illumination area. The co-polarized backscattering coefficients can

be estimated from [17] (in backscatter $k_{sz} = k_z$, $k_{sx} = -k_x$)

$$\sigma^{\circ}_{pp} = \frac{k^2}{2} e^{-2s^2 k_z^2} \sum_{n=1}^{\infty} s^{2n} |I^n_{pp}|^2 \frac{W^{(n)}(-2k_x, 0)}{n!} \tag{5.22}$$

where k_x and k_z are the components of the incident propagation vector $\mathbf{k}_i = k_x \hat{x} + k_y \hat{y} - k_z \hat{z}$ and $W^{(n)}$ is the roughness spectrum of the surface and is related to the nth power of the surface autocorrelation function, $\rho^n(r)$, by the Fourier transform as follows:

$$W^{(n)}(k_{sx} - k_x, k_{sy} - k_y) = \frac{1}{2\pi} \int \rho^n(x, y) e^{j(k_{sx} - k_x)x + j(k_{sy} - k_y)y} dx dy \tag{5.23}$$

and

$$I^n_{pp} = (2k_z)^n f_{pp} e^{-s^2 k_z^2} + \frac{k_z^n [F_{pp}(-k_x, 0) + F_{pp}(k_x, 0)]}{2} \tag{5.24}$$

where f_{pp} and $F_{pp}(\cdot, \cdot)$ are the Kirchhoff and complementary field coefficients and are approximated by the following forms

$$\begin{aligned}
f_{vv} &= \frac{2r^v}{\cos\theta_0} \\
f_{hh} &= -\frac{2r^h}{\cos\theta_0} \\
F_{vv}(-k_x, 0) + F_{vv}(k_x, 0) &= \frac{2\sin^2\theta_0 (1 + r^v)^2}{\cos\theta_0} \left[\left(1 - \frac{1}{\epsilon_r}\right) \right. \\
&\quad \left. + \frac{\mu_r \epsilon_r - \sin^2\theta_0 - \epsilon_r \cos^2\theta_0}{\epsilon_r^2 \cos^2\theta_0} \right] \\
F_{hh}(-k_x, 0) + F_{hh}(k_x, 0) &= -\frac{2\sin^2\theta_0 (1 + r^h)^2}{\cos\theta_0} \left[\left(1 - \frac{1}{\mu_r}\right) \right. \\
&\quad \left. + \frac{\mu_r \epsilon_r - \sin^2\theta_0 - \mu_r \cos^2\theta_0}{\mu_r^2 \cos^2\theta_0} \right].
\end{aligned} \tag{5.25}$$

In the equations above, the local incidence angle in the Fresnel reflection coefficients, r^v and r^h, is approximated by the global incidence angle.

$\kappa_{s,s}$	$\kappa_{a,s}$	$\kappa_{e,s}$
5.7818	1.2574	7.0392

Table 5.2: The scattering coefficient $\kappa_{s,s}$, absorption coefficient $\kappa_{a,s}$, and extinction coefficient $\kappa_{e,s}$ of a snow medium with volume fraction of 0.0742 and average particle radius of 0.25 mm at 94 GHz.

5.4 Experimental Results

In this section, the validity of the models developed in the previous sections is verified experimentally. The results of the polarimetric backscatter measurements at 94 GHz on the aforementioned surfaces are presented and compared with the theoretical values predicted by the models. The University of Michigan 94 GHz fully polarimetric radar was used to perform the backscatter measurements at near grazing incidence angles (from 70° to 88°). The frequency decorrelation behavior of the backscatter response of the distributed targets is expected to increase the number of independent samples [53]. At least 80 independent samples were used in the backscatter measurements. An external calibration technique was used to remove the systematic errors such as channel imbalances, antenna cross-talk, and the imperfection of polarization switches [44].

First, the backscatter response of the snow-covered smooth asphalt surface is investigated. The snow examined here is fresh dry snow with a thickness of 6.4 mm and a density of 0.068 g/cm^3. The average size of the ice crystals was measured to be 0.25 mm and a dielectric constant of the ice crystals of $\epsilon_r = 3.15 + j0.025$ is used according to the ambient temperature of -20°C during the measurement [63]. The scattering, absorption, and extinction coefficients of the snow medium are calculated from (5.7) and (5.8) and are listed in Table 5.2. On the other hand, the extinction

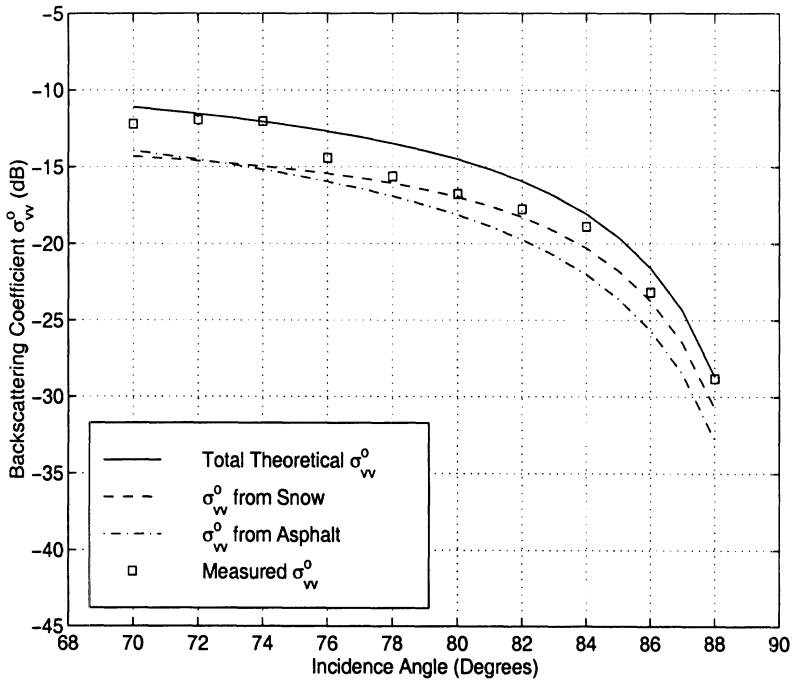

5.4(a) The vv response of the snow-covered smooth asphalt surface.

and phase matrices of the underlying asphalt layer were determined experimentally as described in Chapter 4. The normalized elements of the phase matrix of the asphalt mixture at 94 GHz are listed in Table 4.2. Figure 5.4(a)–(c) compares the measured backscattering coefficients with the simulation results. The individual backscatter contributions from the snow layer and the asphalt layer are also included. It is quite obvious that σ^o_{hh} is dominated by the backscatter from the snow layer. For vertical polarization, the volume scattering from snow and asphalt are comparable, whereas for cross-polarized term, backscatter from asphalt is the dominant component.

The next case investigated is the backscatter response of rough asphalt surfaces. The site selected for the measurement has an rms height of 0.9 mm and a correlation length of 6.3 mm. The correlation function is approximated by an exponential function. The overall backscatter response is computed from the superposition the volume scattering from the asphalt mixtures and the surface scattering from the

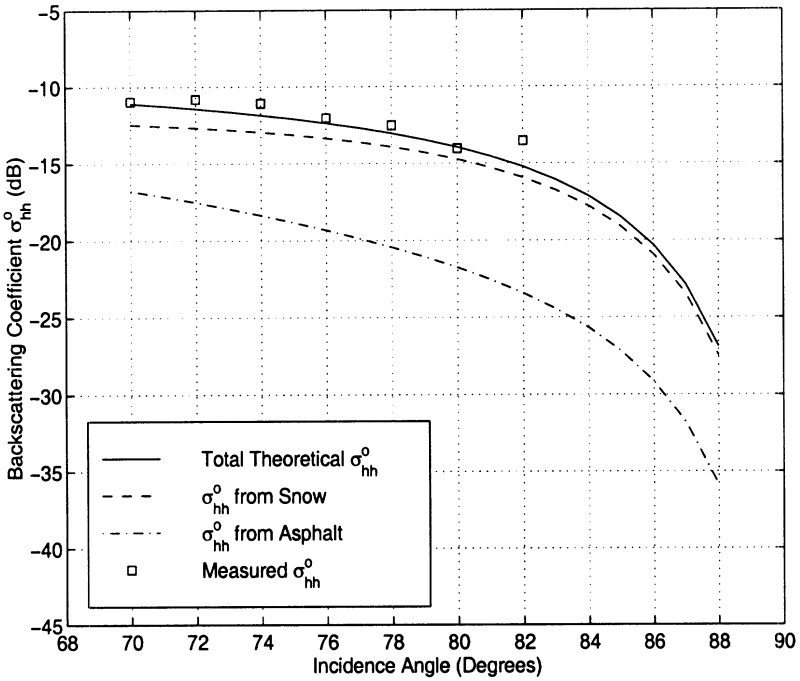

5.4(b) The hh response of the snow-covered smooth asphalt surface.

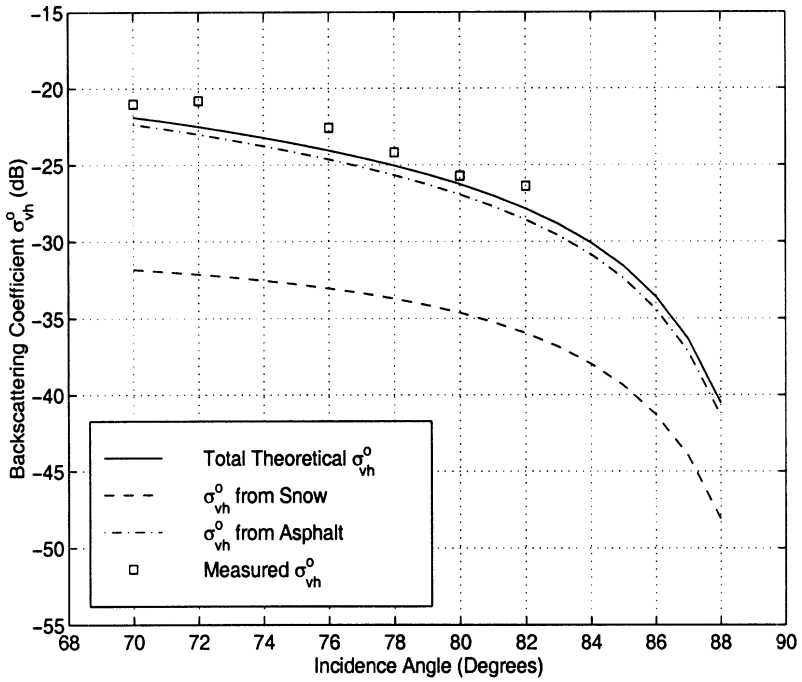

5.4(c) The vh response of the snow-covered smooth asphalt surface.

Figure 5.4: The comparison between the measured data and the theoretical predictions for the co- and cross-polarized backscattering coefficients of the snow-covered smooth asphalt surface.

rough interface. Since the rms slope of the surface is relatively small and the angular dependence of the volume scattering is very gentle, the volume scattering component is calculated using the hybrid scattering model assuming a smooth interface. The IEM is employed to calculate the surface scattering response using the surface roughness statistics. Figure 5.5(a)–(b) compares the measured data to the theoretical predictions for the co-polarized backscattering coefficients of the rough asphalt surface. The individual contributions from the volume and surface scattering components are also shown. The comparison demonstrates good agreement between the experimental data and the theoretical results. Figure 5.6 shows the measured data and the volume scattering component of the cross-polarized backscatter response. The IEM formulation for cross-polarized backscatter does not converge and hence is not compared. It is shown that a significant portion of the cross-polarized backscatter is generated from the rough interface for which we do not have a reliable theoretical model. It is worth mentioning that an ice-covered rough asphalt surface would behave as an ice-covered smooth asphalt surface since the dielectric constant of ice and that of the asphalt mixture are almost the same.

5.5 Conclusions

The polarimetric backscatter behavior of asphalt road surfaces under a variety of conditions are investigated thoroughly at W-band frequencies and accurate theoretical models capable of predicting the backscatter response near grazing incidence are developed. The surfaces considered are: (1) a snow-covered smooth asphalt surface, and (2) a rough asphalt surface. The volume scattering from asphalt mixtures is predicted by the hybrid scattering model developed earlier for smooth asphalt surfaces. For the snow-covered smooth asphalt surface, the first-order iterative solution of the

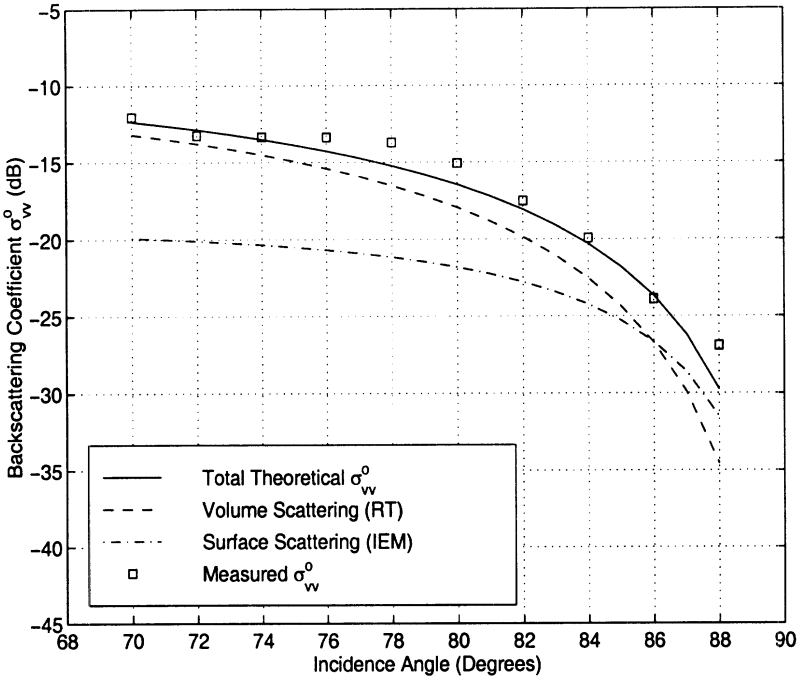

5.5(a) The vv response of the rough asphalt surface.

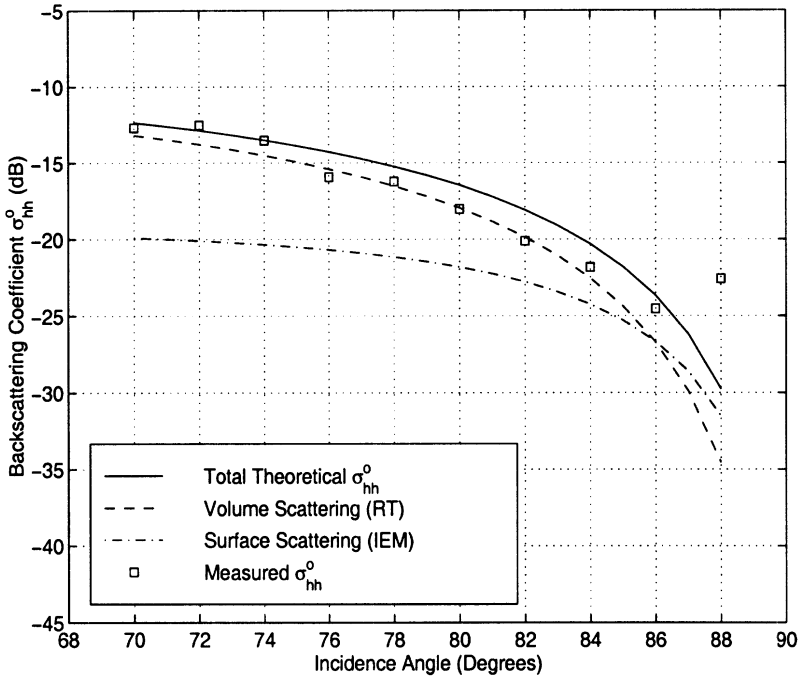

5.5(b) The hh response of the rough asphalt surface.

Figure 5.5: The comparison between the measured data and the theoretical predictions for the co-polarized backscattering coefficients of the rough asphalt surface.

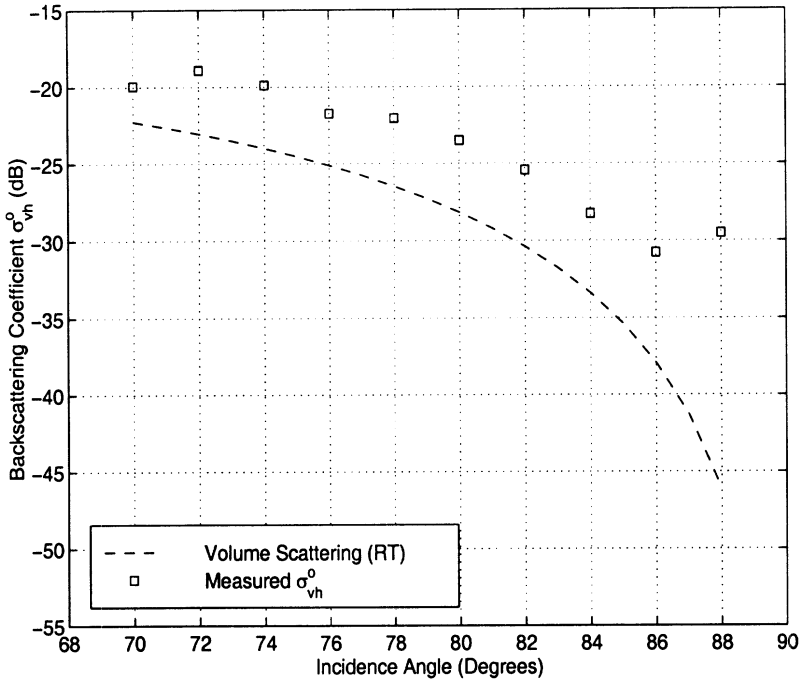

Figure 5.6: The measured data and the volume scattering component of the cross-polarized backscattering coefficient of the rough asphalt surface (IEM formulation does not converge for the cross-polarized backscattering coefficient).

radiative transfer equation is used to calculate the volume scattering from the snow layer for the co-polarized components of the backscatter. To find the cross-polarized response, the second-order iterative solution is employed. The result is combined with the volume scattering from the underlying asphalt layer to predict the overall backscatter response. The scattering behavior from the rough asphalt surface includes both surface scattering from the rough interface and volume scattering from the asphalt mixtures. The surface scattering can be predicted by the IEM formulation only for the co-polarized components. For these cases excellent agreement between the theory and measurement is observed.

CHAPTER VI

POLARIMETRIC CHARACTERIZATION OF DEBRIS AND FAULTS IN THE HIGHWAY ENVIRONMENT AT MILLIMETER-WAVE FREQUENCIES

6.1 Introduction

Each year numerous automotive accidents are reported. Many of these are attributed to road surface conditions and objects or obstacles on road surfaces. Design of a reliable automotive radar sensor requires thorough knowledge of backscatter responses of road surfaces and typical debris and faults on road surfaces. The problem of polarimetric radar scattering from road surfaces are considered in Chapter 4 and Chapter 5 where accurate theoretical models are developed for the determination of backscatter response of asphalt and concrete surfaces under a wide varieties of physical conditions. These models are successfully compared with careful backscatter measurements of bare and water-, ice-, and snow-covered smooth and rough asphalt and concrete surfaces over a wide range of incidence angles at W-band frequencies. A potential application of these models and measurements will be demonstrated in Chapter 7 where the design of an affordable millimeter-wave (MMW) radar is proposed for determination of road surface conditions. A desirable feature of automotive

radar sensors is the detection of debris and faults in the highway environment and the provision of an advance warning to drivers. The debris commonly encountered on the highway with potential threat to vehicle safety are bricks, scrap metal, and bolts *etc.* Potholes and cracks are typical faults seen on road surfaces. Debris and faults may be detected by comparing the radar cross section (RCS) values of the targets on asphalt surfaces with the backscatter from the asphalt surfaces alone. The backscatter from road surfaces is statistical in nature and as a result has a wide fluctuation range. Therefore in order to detect an obstacle with a very low false alarm rate the RCS of the target should be larger than the maximum RCS of the surfaces for a prescribed confidence range. The backscatter response of some non-hazardous targets such as cracks on road surfaces which generate strong backscatter should also be determined and compared with the RCSs of desired targets for the evaluation of false alarm rate.

Since the RCS of a point target is influenced by many physical parameters such as material, size, shape, and target orientation, a complete polarimetric characterization of debris and faults on road surfaces would be very difficult. This problem can be solved by resorting to analytical solutions. Two theoretical models are developed to predict the backscatter response of cracks perpendicular to the antenna boresight. The first model simulates a crack by two impedance wedges next to each other. The method developed by Maliuzhinets [39,40] is used to calculate the total field in the presence of an impedance wedge at normal incidence condition. A non-uniform expression for impedance wedge diffraction is chosen to represent the diffraction coefficient. The diffracted fields from two adjacent wedges are then added coherently. At high MMW frequencies the radius of curvature of asphalt or concrete crack edges become comparable with the wavelength and the wedge model may become invalid.

For these situation a second model for curved edges based on the scattering from impedance cylinders is developed. The simulation results of the second model exhibit better agreement with the measured data at 94 GHz than do those of the first model. Also a physical optics model is developed for predicting scattering solid objects with perpendicular facets such as bricks and right-angled iron and simulation results are compared with the backscatter measurements of a brick and a piece of right-angled iron on an asphalt surface at 94 GHz.

This chapter begins with a description of the experimental setup for the backscatter measurements of debris and faults on asphalt surfaces. Then the RCS threshold value is defined in terms of the antenna gain function, the antenna height, and the backscattering coefficient of the road surfaces. This value is used to determine the detectability of various debris and faults on asphalt surfaces. Next the backscatter response of debris on asphalt surfaces is examined. The polarimetric backscatter measurements of lane-guide reflectors are also included. The detectability of the debris and reflectors is then evaluated. The backscatter behavior of faults on asphalt surfaces is described in Section 6.4 along with investigation of their detectability. The backscatter characterization of typical roadside boundaries such as pebbles, curbs, and guard-rails is also performed experimentally. Detection of these targets is important because of the fact that drowsiness and fatigue are among the leading causes of sideward crashes. Besides alerting the drowsy driver, the backscatter response could also provide valuable information for cruise control applications. Section 6.5 includes the backscatter responses of the roadside boundaries.

6.2 Measurement Setup and Detectability

The University of Michigan 94 GHz fully polarimetric radar system was employed to conduct the backscatter measurements. The system bandwidth is set to 1 GHz to improve the range resolution of the point target responses for time-domain gating during post-processing. Finite asphalt surfaces of dimension 91.5 cm by 91.5 cm by 6.4 cm were constructed for the indoor measurements. These sample surfaces could easily be mounted on a turnable for RCS pattern measurements of point targets on asphalt surfaces. The backscatter response of point targets on an asphalt sample surface were measured at incidence angles from 76° to 86°. The quantities of interest are the backscatter from the point targets and their interaction with the asphalt surface. The leading edge of asphalt samples were covered by radar absorbing material to reduce edge diffraction at near grazing incidence. Background subtraction and range gating were used to remove the unwanted signal, followed by a calibration procedure to remove systematic errors such as channel imbalance and antenna cross-talk from the measured data [44].

As mentioned earlier road surfaces at MMW frequencies can be modeled as random media whose backscatter is statistical in nature and is usually composed of surface and volume scattering components. Since in most practical situations the radar footprint covers a large number of scatterers over the asphalt surface and within the asphalt medium, according to the central limit theorem, the backscattered field obey a Gaussian statistics. It is well known that statistics of the backscatter field intensity (power) has exponential distribution given by

$$f_\sigma(\sigma_a) = \frac{1}{\overline{\sigma}} e^{-\frac{\sigma_a}{\overline{\sigma}}} \tag{6.1}$$

where $\overline{\sigma}$ is the mean backscatter from the illuminated portion of the distributed

target (the asphalt surface). This mean value is a function of the target backscatter coefficient σ°, the antenna pattern, incidence angle and antenna height

$$\overline{\sigma} = \sigma^\circ \int_{Lit} \int_{Area} \frac{G^2(x,y)}{r^4(x,y)}\, dx\, dy = \sigma^\circ A_{illu} \tag{6.2}$$

where $G(x,y)$ and $r(x,y)$ are the antenna gain and the distance from the antenna to a point within the lit area respectively and A_{illu} is known as effective illuminated area. To examine the detectability of a point target over an asphalt surface with a reasonable false alarm rate (FAR), the RCS of the illuminated area of asphalt (σ_a) must be compared with the RCSs of the point targets (σ_p). Choose a threshold level σ_a^{th} based on a given maximum false alarm rate, a criteria for target detectability is obtained. For a maximum false alarm rate (MFAR) of FAR, σ_a^{th} is set so that

$$\int_0^{\sigma_a^{th}} f_\sigma(\sigma_a)\, d\sigma_a = 1 - \text{MFAR}. \tag{6.3}$$

Using (6.1) in (6.3) we find

$$\sigma_a^{th} = -\overline{\sigma} \ln(\text{MFAR}). \tag{6.4}$$

Note that the RCS quantities in (6.4) are all in linear scale. Hence for a maximum false alarm rate of 10^{-5}, the RCS of the point targets must be 10.6 dB above $\overline{\sigma} = \sigma^\circ A_{illu}$. It is obvious that smaller targets can be detected reliably for antenna with small footprint. This threshold value (σ_a^{th}) used in this investigation is obtained from the backscattering coefficients ($\sigma^\circ(\theta_i)$) of a smooth asphalt surface measured by a single-antenna radar mounted at vehicle bumper height (43 cm) and the gain function of the antenna is approximated by a Gaussian function:

$$G(\theta,\phi) = e^{\frac{-a_0\theta^2}{\beta^2}}$$

where a_0 is 2.7726 and β is the half-power beamwidth, equal to 1.4°. The detectability of point targets on asphalt surfaces is examined at an incidence angle of 80°.

6.3 Debris and Lane-guide Reflectors on Road Surfaces

In this section the backscatter measurements and models for some points targets on asphalt surfaces are presented and their detectability is examined. Three common types of highway debris are considered: bricks, scrap metal, and bolts. Also the measured backscatter behavior of lane-guide reflectors as a function of aspect angle is presented here.

6.3.1 Targets with Planar Facets

In this section a simple scattering model based on physical optics (P. O.) approximation for targets with planar surfaces, such as bricks and right-angled iron, is developed and the results are compared with backscatter measurements. At W-band frequencies the sizes of most targets of interest (those that create hazardous conditions for automobiles) are large compared to the wavelength and their permittivity has a sufficiently large imaginary part, thus P. O. model provides accurate results.

The backscatter response of a brick on an asphalt surface can be obtained from that of a planar dielectric surface above an infinite ground plane (asphalt surface). The bistatic scattering from a planar dielectric surface whose dimensions are large compared to the wavelength can be modeled using the physical optics approximation. The expression for the bistatic far-field amplitude of a dielectric plate with arbitrary orientation is given by [51]

$$\begin{aligned} \boldsymbol{S} &= \frac{jk_o}{4\pi}\int_{Lit}\Big[(1-r^h)(\mathbf{E}_o\cdot\hat{t})(\hat{n}'\cdot\hat{k}_i)\hat{k}_s\times(\hat{k}_s\times\hat{t})+(1+r^h)(\mathbf{E}_o\cdot\hat{t})\hat{k}_s\times(\hat{n}'\times\hat{t}) \\ &\quad +Z_o(1-r^v)(\mathbf{H}_o\cdot\hat{t})(\hat{n}'\cdot\hat{k}_i)\hat{k}_s\times\hat{t}-Z_o(1+r^v)(\mathbf{H}_o\cdot\hat{t})\hat{k}_s\times\hat{k}_s\times(\hat{n}'\times\hat{t})\Big] \\ &\quad e^{jk_o(\hat{k}_i-\hat{k}_s)\cdot\mathbf{r}'}ds' \end{aligned} \tag{6.5}$$

where $\mathbf{E}_o$ and $\mathbf{H}_o$ are the amplitudes of the incident electric and magnetic fields,

r^v and r^h are the local Fresnel reflection coefficients of the dielectric plate, $\hat{k}_i = k_x^i\hat{x} + k_y^i\hat{y} + k_z^i\hat{z}$ and $\hat{k}_s = k_x^s\hat{x} + k_y^s\hat{y} + k_z^s\hat{z}$ are the unit vectors along the incident and scattered directions respectively, $\hat{t}$ is the unit vector perpendicular to the local plane of incidence and is defined as

$$\hat{t} = \frac{\hat{n}' \times \hat{k}_i}{|\hat{n}' \times \hat{k}_i|}.$$

An analytical expression for $\boldsymbol{S}$ can be obtained based on the stationary phase approximation in which the non-exponential portion of the integrand is evaluated at the SP point. The elements of the scattering matrix $\boldsymbol{S}$ are found to be

$$\begin{aligned}
S_{vv} &= -\left[r^v(\hat{n}'\cdot\hat{v}_i)(\hat{n}'\cdot\hat{v}_s) + r^h(\hat{n}'\cdot\hat{h}_i)(\hat{n}'\cdot\hat{h}_s)\right]\frac{\hat{n}'\cdot\hat{k}_i}{|\hat{n}'\times\hat{k}_i|^2}Q \\
S_{vh} &= -\left[r^v(\hat{n}'\cdot\hat{h}_i)(\hat{n}'\cdot\hat{v}_s) - r^h(\hat{n}'\cdot\hat{v}_i)(\hat{n}'\cdot\hat{h}_s)\right]\frac{\hat{n}'\cdot\hat{k}_i}{|\hat{n}'\times\hat{k}_i|^2}Q \\
S_{hv} &= -\left[r^v(\hat{n}'\cdot\hat{v}_i)(\hat{n}'\cdot\hat{h}_s) - r^h(\hat{n}'\cdot\hat{h}_i)(\hat{n}'\cdot\hat{v}_s)\right]\frac{\hat{n}'\cdot\hat{k}_i}{|\hat{n}'\times\hat{k}_i|^2}Q \\
S_{vv} &= -\left[r^v(\hat{n}'\cdot\hat{h}_i)(\hat{n}'\cdot\hat{h}_s) + r^h(\hat{n}'\cdot\hat{v}_i)(\hat{n}'\cdot\hat{v}_s)\right]\frac{\hat{n}'\cdot\hat{k}_i}{|\hat{n}'\times\hat{k}_i|^2}Q
\end{aligned} \tag{6.6}$$

with

$$Q = -\frac{jk_o}{4\pi}\int_{Lit} e^{jk_o(\hat{k}_i-\hat{k}_s)\cdot\mathbf{r}'}ds'. \tag{6.7}$$

To compute the backscatter from this plate when it is placed above a dielectric ground plane, the bistatic direction ($\hat{k}_s$) must be chosen so that the reflected $\hat{k}_s$ from the asphalt surface is along $-\hat{k}_i$ direction. The unit vector in the backscatter direction $\hat{k}_r$ is related to $\hat{k}_s$ by

$$\hat{k}_r = \hat{k}_s - (2\hat{z}'\cdot\hat{k}_s)\hat{z}' = -\hat{k}_i. \tag{6.8}$$

Hence $k_x^s = -k_x^i$, $k_y^s = -k_y^i$, and $k_z^s = k_z^i$. For a brick with vertical facets the evaluation of the integral given by (6.7) is rather simple. Referring to Figure 6.1 and

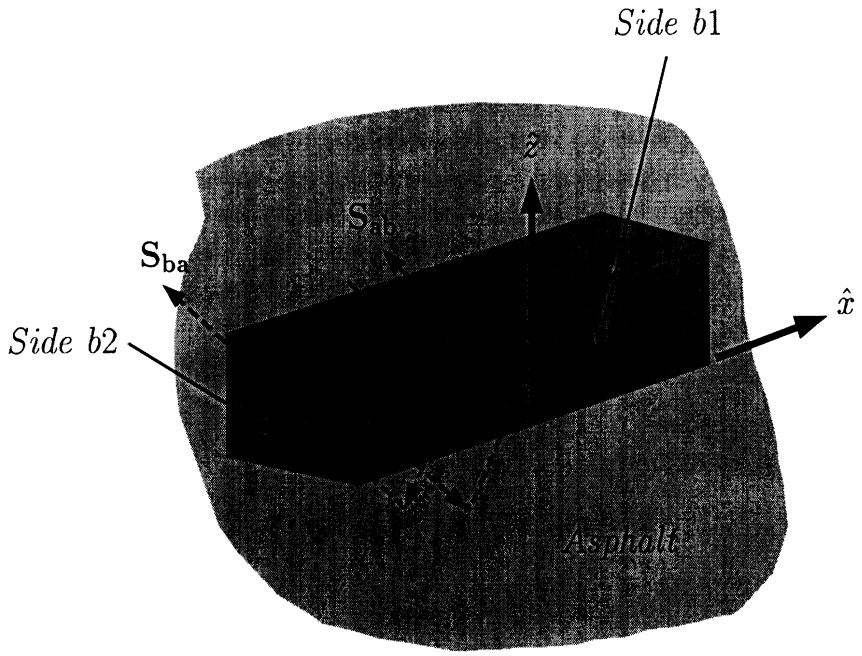

Figure 6.1: The scattering mechanisms of the backscatter response of the brick on an asphalt surface.

recognizing significant backscatter originates only from two brick surfaces, namely side $b1$ and side $b2$, the expressions of Q for both sides have the following form:

$$\begin{aligned} Q_{b1} &= -\frac{jk_o A_{b1}}{2\pi}\frac{\sin U}{U} \\ Q_{b2} &= -\frac{jk_o A_{b2}}{2\pi}e^{-jU}e^{jV}\frac{\sin V}{V} \end{aligned} \tag{6.9}$$

where A_{b1} and A_{b2} are the areas of $b1$ and $b2$ sides respectively. U and V are given by

$$U = k_o k_x^i a \qquad V = k_o k_y^i b,$$

and a and b are the dimensions of the brick. The total backscatter from a plate above a ground plane is composed of two components: (1) the bistatic scattering from the plate reflected off of the ground plane, and (2) bistatic scattering from the plate when illuminated by the reflected incident wave (illumination by the image wave). The scattering matrix associated with the first term is denoted by $\boldsymbol{S}_{ba}$ and is given

by

$$\boldsymbol{S}_{ba} = \begin{bmatrix} r_a^v & 0 \\ 0 & r_a^h \end{bmatrix} \begin{bmatrix} S_{vv,b} & S_{vh,b} \\ S_{hv,b} & S_{hh,b} \end{bmatrix} \tag{6.10}$$

where r_a^v and r_a^h are the local Fresnel reflection coefficients for the asphalt surface. The scattering matrix associated with the second term denoted by $\boldsymbol{S}_{ab}$ can be obtained by taking the transpose of $\boldsymbol{S}_{ba}$ according to the reciprocity theorem. The total scattering matrix $\boldsymbol{S}$ is the coherent sum of $\boldsymbol{S}_{ab}$ and $\boldsymbol{S}_{ba}$:

$$\boldsymbol{S} = \boldsymbol{S}_{ab} + \boldsymbol{S}_{ba} = (\boldsymbol{S}_{ba})^T + \boldsymbol{S}_{ba}. \tag{6.11}$$

To examine the validity of this formulation, a brick of size 20 cm by 10 cm by 5.7 cm is placed on top of the finite asphalt surface for backscatter measurement. The orientation of the brick with the 20 cm by 5.7 cm side facing the radar system is defined as the 0° azimuthal angle as shown in Figure 6.2(a). At incidence angles from 76° to 86°, the backscatter response of the brick was measured as a function of azimuthal angle. Five independent samples were collected for each angle. Figure 6.2(b) shows the backscatter response of the brick on the asphalt surface as a function of azimuthal angle at an incidence angle of 80°. The threshold values defined for MFAR of 10^{-5} are included to determine the detection of the brick on asphalt surfaces (3 dB footprint area $\simeq$ 0.021 m^2). Excellent detectability is observed at 0° and 90° azimuthal angles. It is also noticed that the hh polarization offers the best separation between the brick and the asphalt response. Therefore it is the preferred polarization to detect bricks on asphalt surfaces. To compare the analytical solution with the measured backscatter response of the brick on the asphalt surface, the effective dielectric constant of the brick is needed. The L-band microstrip ring resonator described in Appendix B may be used to estimate the effective dielectric constant of

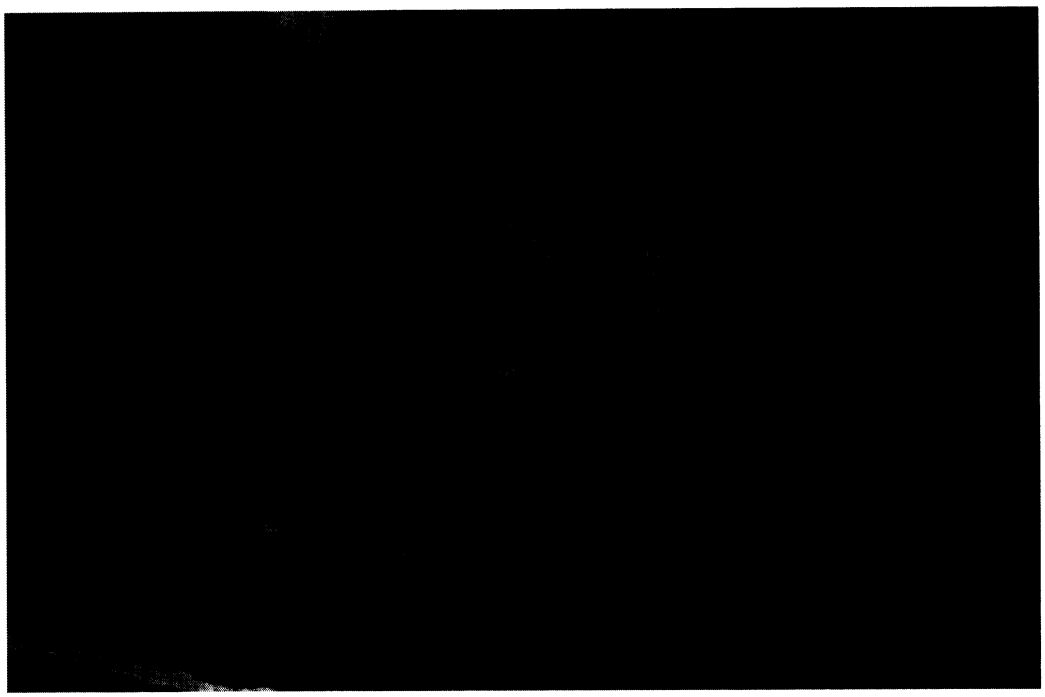

6.2(a) The brick at 0° azimuthal angle. (The radar is positioned off the front of the image.)

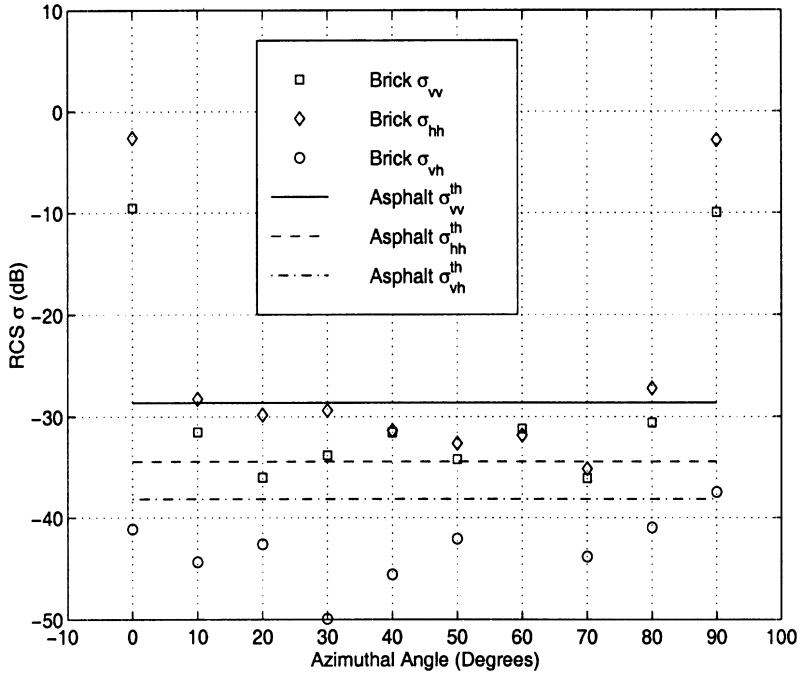

6.2(b) The RCS at an incidence angle of 80°.

Figure 6.2: The picture and the backscatter response of the brick on the asphalt surface at an incidence angle of 80°.

bricks at 94 GHz since the real part of the effective dielectric constant is almost independent of frequency. The effective dielectric constant was found to be $3.67 + j0.063$. The simulation results based on the P. O. model for the backscatter RCSs of the brick on asphalt surfaces are displayed in Figure 6.3(a) as a function of azimuthal angle. A comparison between the theoretical values and the measured data at azimuthal angles near 0° and 90° is shown in Figure 6.3(b). In this comparison ±0.5° uncertainty is allowed in the azimuthal misalignment of the brick with respect to the radar boresight. These errors can be attributed to the mechanical tolerance of the turntable used for these measurements. Figure 6.4 shows the comparison between the theoretical values and the measured data of the backscatter RCS ratio σ_{vv}/σ_{hh} at near 0° azimuthal angle, which shows a relatively good agreement considering the fact that the surface of the brick is not exactly flat.

The same P. O. model can be applied to right-angled iron with some minor modifications. In this case as shown in Figure 6.5 depending on the incidence angle, part of the scattered signal from the vertical plate is reflected off of the perfectly conducting surface and part of it is reflected off of the asphalt surface. Accounting for the appropriate reflection coefficients and considering the phase difference of the backscatter due to the thickness of the metal, the scattering from each part can be added coherently. A dihedral is chosen to simulate the backscatter response of scrap metal on the asphalt surface. This dihedral has a metal thickness of 0.6 cm and inner dimension of 4.5 cm by 4.5 cm by 5 cm. The 0° azimuthal angle is defined as the orientation with the open angle of the dihedral facing the radar system. The backscatter measurement of the dihedral on the asphalt surface was conducted at the same incidence angles as for the brick. The results at an incidence angle of 80° are shown in Figure 6.6. A backscatter pattern similar to that of the brick is

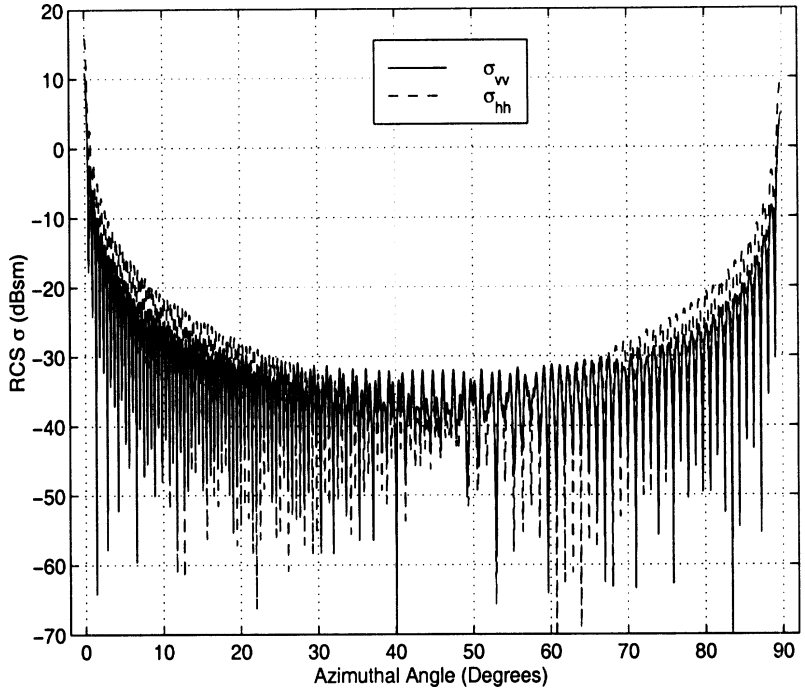

6.3(a) The simulation results of the backscatter RCSs.

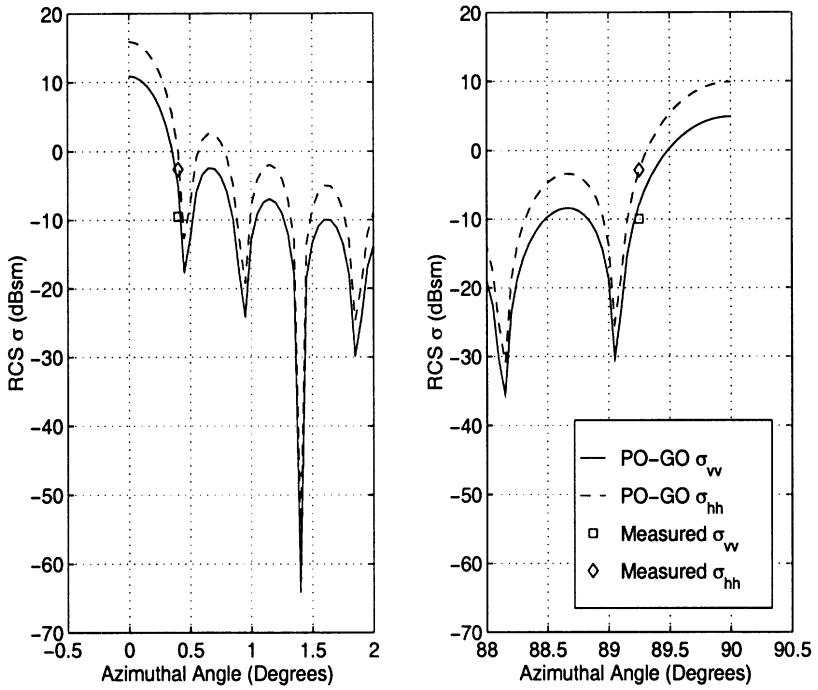

6.3(b) The comparison between the measured data and the simulation results.

Figure 6.3: The simulation results of the backscatter RCSs of the brick on asphalt surfaces at an incidence angle of 80° and the comparison with the measured data at azimuthal angles of 0° and 90°.

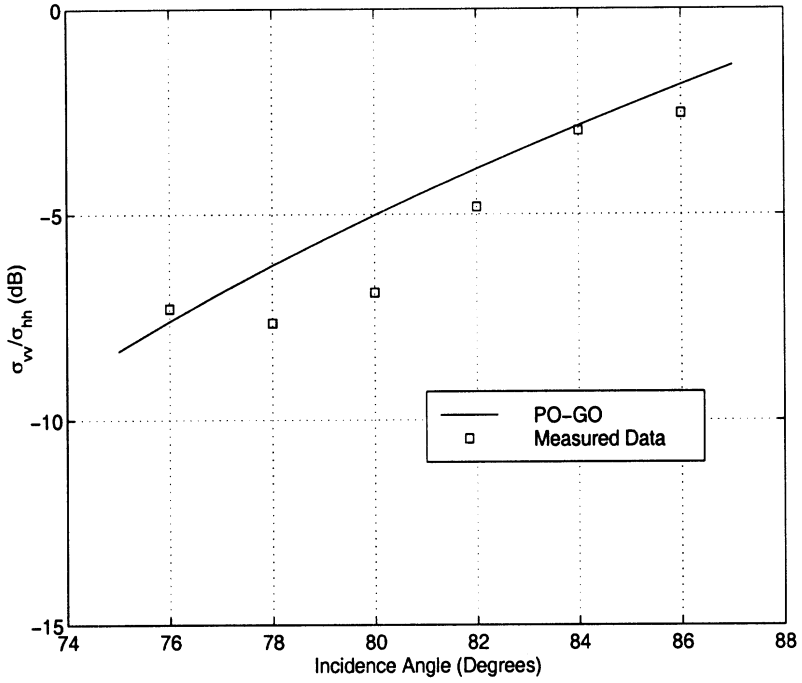

Figure 6.4: The comparison between the simulation results and the measured data for the backscatter RCS ratio σ_{vv}/σ_{hh} of the brick on the asphalt surface at near 0° azimuthal angle.

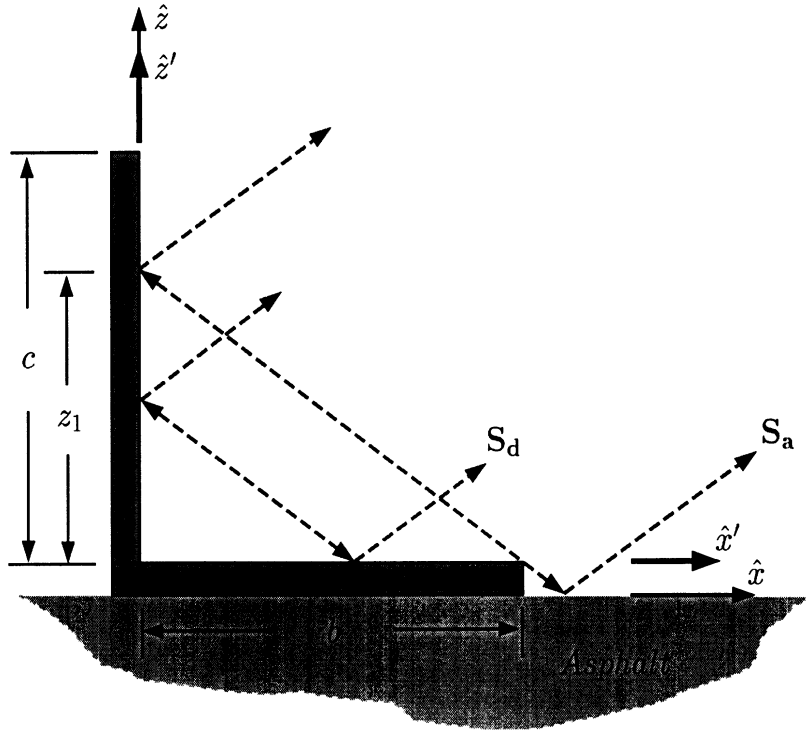

Figure 6.5: The scattering mechanisms of the backscatter response of the right-angled iron on asphalt surfaces at an azimuthal angle of 0°.

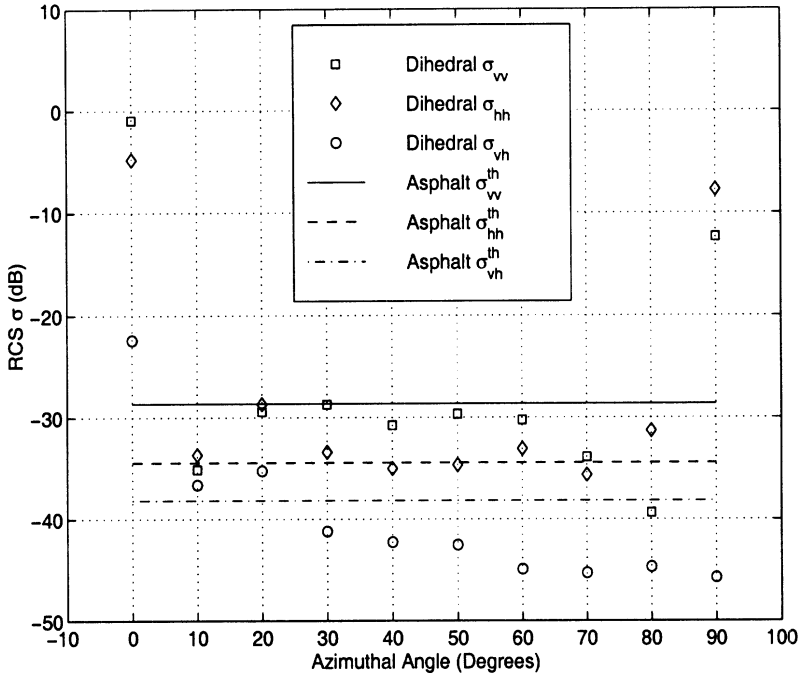

Figure 6.6: The backscatter response of the dihedral on the asphalt surface at an incidence angle of 80°.

observed. Good detection can be obtained at azimuthal angles of 0° and 90°. The hh polarization is the preferred polarization for dihedral detection on asphalt surfaces. The simulation results based on the P. O. model for the backscatter RCS ratio σ_{vv}/σ_{hh} at near 0° azimuthal angle are compared with the experimental results. Figure 6.7 shows excellent consistency between the theoretical values and the measured data.

6.3.2 Other Point Targets

The backscatter of a bolt and an embedded lane-guide reflector are presented as other typical objects on asphalt surfaces. The bolt investigated has a length of 7.5 cm and a 3 cm head. The 0° azimuthal angle is defined as that orientation with the bolt head pointing towards the radar system. Figure 6.8 shows the backscatter response of the bolt at an incidence angle of 80°. The threshold values are also included for comparison. Similar conclusions are drawn as for the brick and the dihedral.

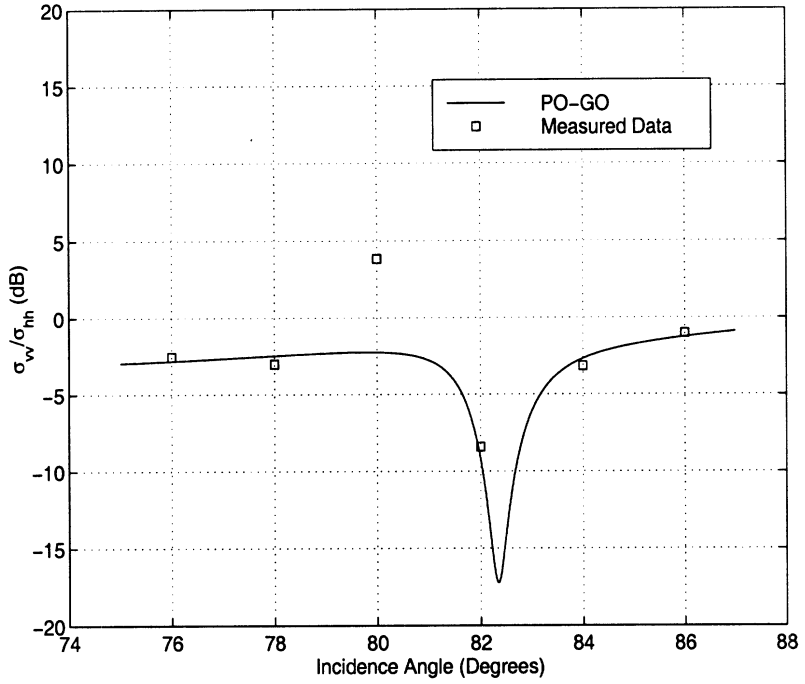

Figure 6.7: The comparison between the simulation results and the measured data for the backscatter RCS ratio σ_{vv}/σ_{hh} of the dihedral on the asphalt surface at near 0° azimuthal angle.

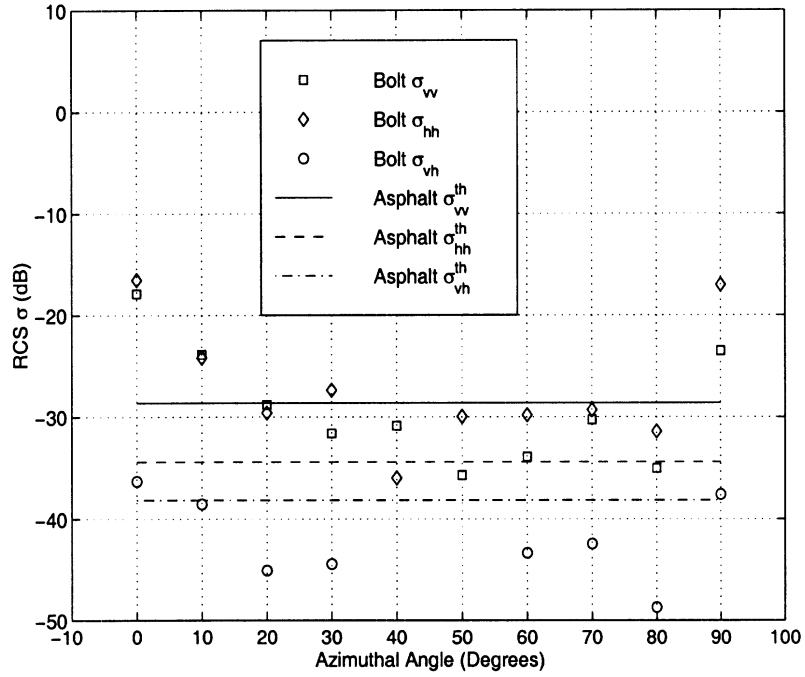

Figure 6.8: The backscatter response of the bolt on the asphalt surface at an incidence angle of 80°.

Another type of target frequently encountered in the highway environment are structures for lane-guiding purpose. Examples are cylindrical poles, yellow paint, and reflectors. The reflectors are chosen for this study because of their strong backscatter responses and widespread usage. Most reflectors are made of iron with a plastic lens in the central area. The iron is half-buried in the asphalt and the lens is tilted for light reflection, as shown in Figure 6.9(a). The 0° azimuthal angle is defined by the orientation for which the normal direction of the lens points at the radar system. The backscatter response of a reflector at an incidence angle of 80° is shown in Figure 6.9(b). It is observed that the maximum backscatter response occurs at a 0° azimuthal angle. The hh polarization is again the preferred choice for reflector detection.

6.4 Road Surface Faults

In this section, the polarimetric backscatter behavior of typical road surface faults is considered. Two types of faults are examined: (1) road surface cracks, and (2) potholes. Although cracks do not pose any safety threat, the study of their backscatter response is important as far as the false alarm rate caused by cracks is concerned. On the other hand detection of potholes is important as they degrade the driving conditions and can lead to vehicle damage or even cause fatal accidents.

The cracks seen on road surfaces are oriented in various directions. Only those cracks oriented perpendicular to antenna boresight have significant backscatter response and will be characterized here. Two finite asphalt surfaces were placed together with a gap left in between to simulate a crack for indoor measurement. At incidence angles of 76°, 80°, and 84°, the backscatter measurements were conducted for cracks of widths 2.54 cm and 5.08 cm. For the footprint size used in this exper-

6.9(a) The lane-guide reflector.

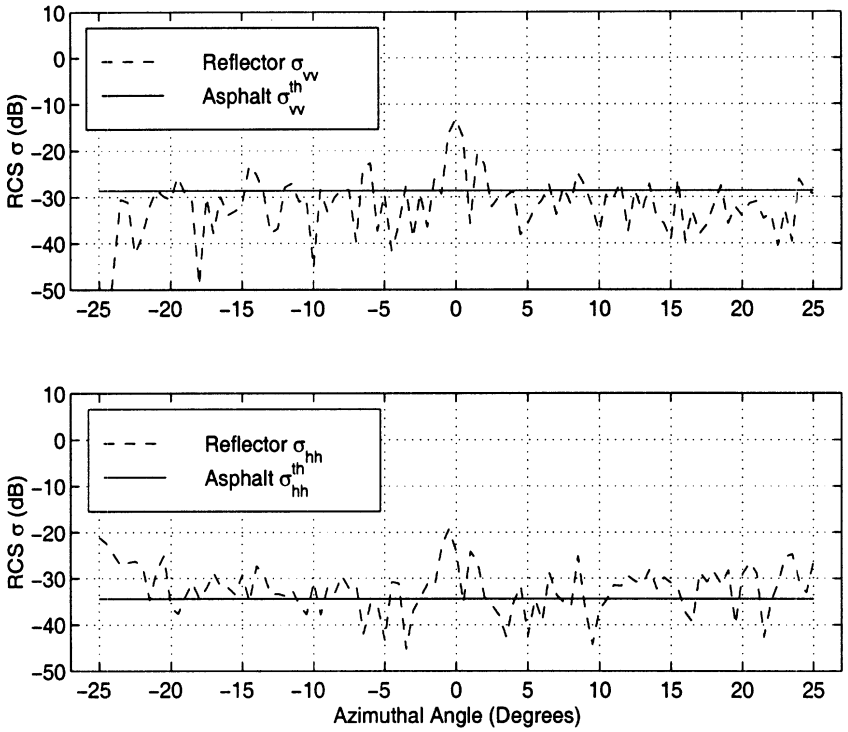

6.9(b) The RCS at incidence angle of 80°.

Figure 6.9: The picture and the backscatter response of the reflector half-buried in asphalt at an incidence angle of 80°

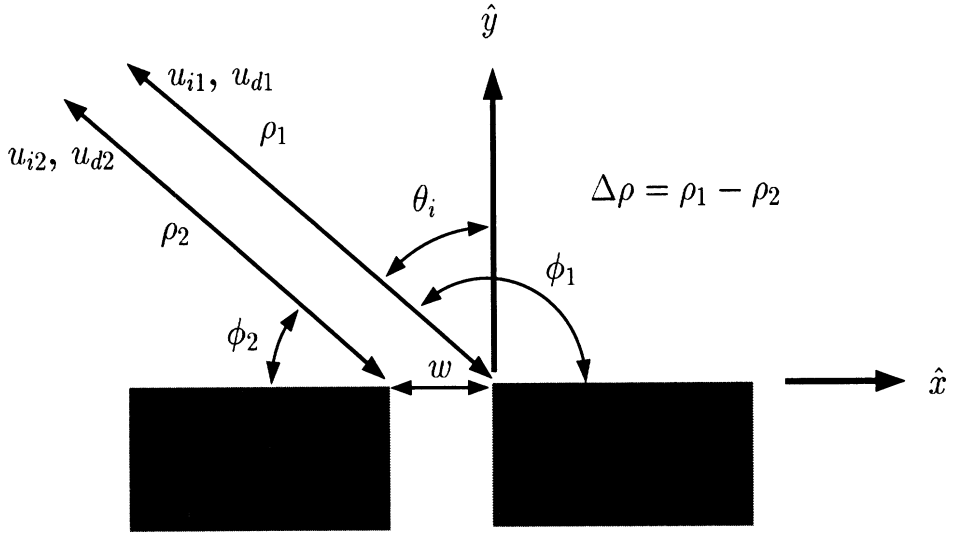

Figure 6.10: The crack modeled by two right-angled impedance wedges next to each other.

iment the volume scattering contribution from the asphalt mixtures in comparison to the backscatter from the cracks is insignificant and can be ignored. At least 10 independent samples were used in the crack measurements. The measured backscatter response of cracks is reported in terms of the average backscatter power per unit length (dBsm/m), dividing the measured average RCS by the effective illuminated length.

To predict the backscatter response of cracks a first-order diffraction solution of two adjacent impedance wedges are considered (see Figure 6.10). Figure 6.11 shows the wedge geometry and the coordinate system. For an impedance wedge illuminated by a plane wave

$$\mathbf{u}^i \ (\mathbf{E}^i \text{ or } \mathbf{H}^i) = e^{-jk_0\rho\cos(\phi-\phi_0)}\hat{z} \tag{6.12}$$

at normal incidence, the diffracted field can be expressed in terms of the non-uniform diffraction coefficient D^{nu} as [25,55]

$$u_z^d = \frac{e^{jk_0\rho}}{\sqrt{\rho}} D^{nu}(\phi, \phi_0, \theta_+, \theta_-) \tag{6.13}$$

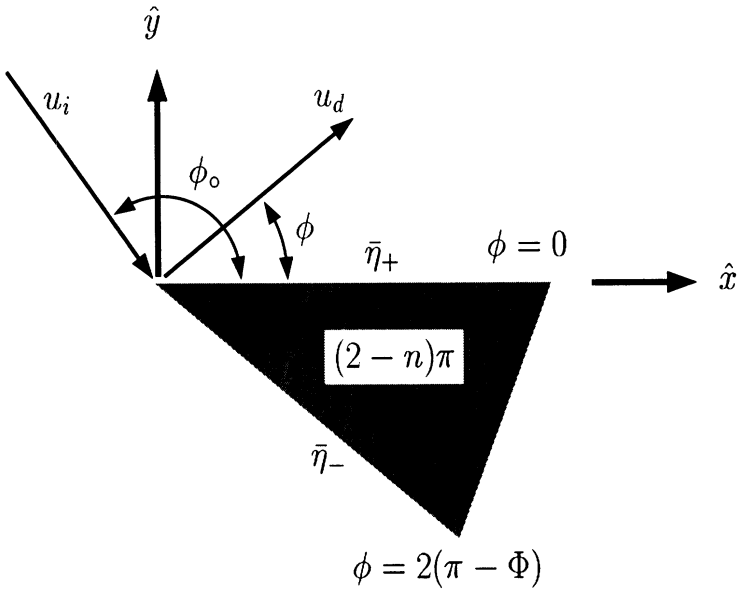

Figure 6.11: The wedge geometry and the coordinate system.

where ϕ and ϕ_o are the observation and incidence angles, θ_+ and θ_- are the angles which satisfy the following relationship

$$\sin(\theta_\pm) = \begin{cases} \bar{\eta}_\pm & \text{(v polarization)} \\ 1/\bar{\eta}_\pm & \text{(h polarization)} \end{cases},$$

$\bar{\eta}_\pm$ are the normalized impedances of the two faces of the wedge. The non-uniform diffraction coefficient D^{nu} has the following expression

$$\begin{aligned} D^{nu}(\phi, \phi_o, \theta_+, \theta_-) &= \frac{-je^{-j\frac{\pi}{4}}}{n\sqrt{2\pi k_0}} \frac{\sin(\frac{\phi_o}{n})}{\Psi(\frac{n\pi}{2} - \phi_o)} \left[\frac{\Psi(\pi + \frac{n\pi}{2} - \phi)}{\cos(\frac{\pi-\phi}{n}) - \cos(\frac{\phi_o}{n})} \right. \\ &\quad \left. - \frac{\Psi(-\pi + \frac{n\pi}{2} - \phi)}{\cos(\frac{\pi+\phi}{n}) - \cos(\frac{\phi_o}{n})} \right] \end{aligned} \tag{6.14}$$

where $\Psi(\alpha)$ is the Maliuzhinets meromorphic function defined as

$$\begin{aligned} \Psi(\alpha) &= \Psi_\Phi(\alpha + \Phi + \frac{\pi}{2} - \theta_+)\Psi_\Phi(\alpha - \Phi - \frac{\pi}{2} + \theta_-) \\ &\quad \Psi_\Phi(\alpha + \Phi - \frac{\pi}{2} + \theta_+)\Psi_\Phi(\alpha - \Phi + \frac{\pi}{2} - \theta_-). \end{aligned}$$

The approximate formulation for the function $\Psi_\Phi(z)$ depends on the amplitude of the argument. The expressions are available in the literature by Senior and Herman

[25, 55]. A crack can be considered to be two right-angled impedance wedges next to each other, as shown in Figure 6.10. For right-angled impedance wedges, the parameters n and Φ have values of 1.5 and 0.75π respectively. The two-dimensional RCS, σ_{2D}, is defined as

$$\sigma_{2D} = \lim_{\rho \to \infty} 2\pi\rho \frac{|u^d|^2}{|u^i|^2} = 2\pi |D^{nu}(\phi, \phi_o, \theta_+, \theta_-)|^2. \tag{6.15}$$

The RCS of the crack, σ_{2D}^c, can be obtained by adding the diffracted fields from two wedges coherently, then applying equation (6.15) to give the expression

$$\sigma_{2D}^c = 2\pi |D_1^{nu}(\phi_1, \phi_{o1}, \theta_+, \theta_-) + e^{-2jk_0 \sin\theta_i w} D_2^{nu}(\phi_2, \phi_{o2}, \theta_+, \theta_-)|^2. \tag{6.16}$$

The measured quantity is the three-dimensional RCS, σ_{3D}^c. Conversion from σ_{2D} to σ_{3D} can be accomplished by the expression given in [51]

$$\sigma_{3D} = \frac{2L^2}{\lambda} \sigma_{2D}. \tag{6.17}$$

By setting L=1 m, the RCS per unit length of cracks is obtained.

Figure 6.12 shows the comparison between the measured data and the simulation results based on diffraction from two impedance wedges. Good agreement is observed. In particular, both results indicate that the hh response is greater than the vv response. The slight discrepancy at lower grazing angles can be attributed to the non-ideal modeling of the crack edge by a right-angle wedge at millimeter-wave frequency because of random distribution of rocks and sand along the crack edge. The results also indicate that the diffracted fields from a crack at incidence angles from 74° to 86° are insensitive to the crack width. This is due to the fact that the diffracted field from the impedance wedge near the source is negligible ($D_1^{nu} \gg D_2^{nu}$).

The aforementioned disagreement at lower grazing angles can be improved by modeling the crack edge as an impedance cylinder. The radius of the cylinder is selected based on the rock size distribution of asphalt mixtures as shown in Table 4.1.

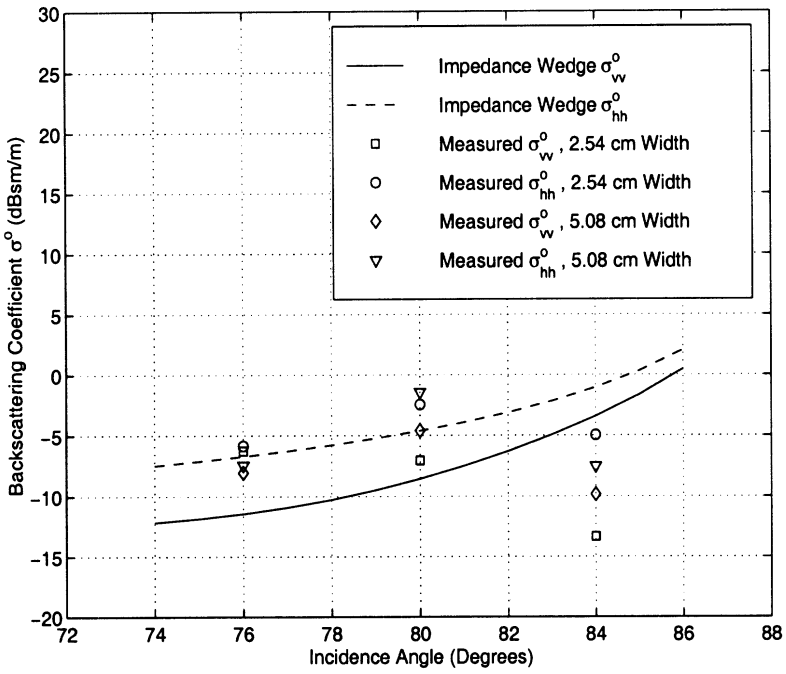

Figure 6.12: The comparison between the measured results of the cracks of two widths and the simulation results based on diffraction from two right-angled impedance wedges.

The cylinder models the curve describing the crack edge, improving the backscatter prediction. In the wedge model, it is found that the backscatter response of the crack is dominated by the diffraction from the wedge further away from the source. The same conclusion can be reached when the corners are modeled by curved surfaces. In this case a specular point on the surface of the cylinder further away from the source predominantly contributes to the backscatters. Therefore only the backscatter response of a single impedance cylinder, representing the further crack edge, is considered here. Figure 6.13 shows the geometry and the coordinate system of the impedance cylinder. For a plane wave as in (6.12) at normal incidence, the total field exterior to an impedance cylinder of radius ρ_o can be expressed in an eigen-expansion

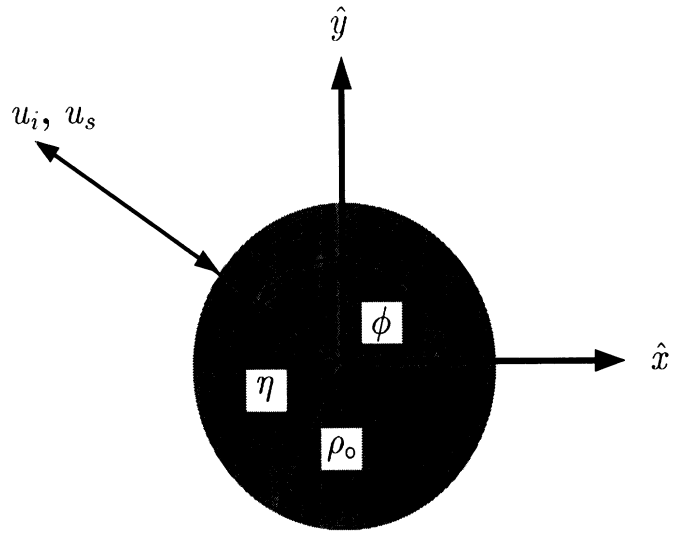

Figure 6.13: The geometry and the coordinate system for the model based on scattering from an impedance cylinder.

form [3,20,55]

$$u_z^t = \sum_{n=-\infty}^{\infty} j^{-n} \left[J_n(k_0\rho) + a_n H_n^{(2)}(k_0\rho) \right] e^{jn\phi} \tag{6.18}$$

where J_n is the Bessel function of the first kind, $H_n^{(2)}$ is the Hankel function of the second kind, and a_n are the amplitude coefficients of the scattered field. a_n can be determined by applying the impedance boundary condition

$$\hat{n} \times \hat{n} \times \mathbf{E} = -\eta\, \hat{n} \times \mathbf{H} \tag{6.19}$$

to the total field in (6.18). The coefficients a_n have the following forms for v and h polarizations

$$a_n = \begin{cases} \dfrac{j\eta J_n(k_0\rho_o) - \eta_0 J_n'(k_0\rho_o)}{\eta_0 H_n^{(2)\prime}(k_0\rho_o) - j\eta H_n^{(2)}(k_0\rho_o)} & \text{(v polarization)} \\ \\ \dfrac{j\eta_0 J_n(k_0\rho_o) - \eta J_n'(k_0\rho_o)}{\eta H_n^{(2)\prime}(k_0\rho_o) - j\eta_0 H_n^{(2)}(k_0\rho_o)} & \text{(h polarization)} \end{cases} \tag{6.20}$$

where J_n' and $H_n^{(2)\prime}$ are the derivatives of J_n and $H_n^{(2)}$ with respect to $k_0\rho$ and can be

expressed in terms of J_n and $H_n^{(2)}$ as

$$\begin{aligned}\frac{d}{d(k_0\rho)}J_n(k_0\rho) &= J_{n-1}(k_0\rho) - \frac{n}{k_0\rho}J_n(k_0\rho)\\ \frac{d}{d(k_0\rho)}H_n^{(2n)}(k_0\rho) &= H_{n-1}^{(2n)}(k_0\rho) - \frac{n}{k_0\rho}H_n^{(2n)}(k_0\rho).\end{aligned}$$

In the far field, the $H_n^{(2)}(k_0\rho)$ can be approximated by the expression given in [3]

$$H_n^{(2)}(k_0\rho) \overset{k_0\rho\to large}{\simeq} \sqrt{\frac{2j}{\pi k_0\rho}}j^n e^{-jk_0\rho}. \tag{6.21}$$

The backscattered field from an impedance cylinder of radius ρ_o can be written as

$$u_z^s = \sqrt{\frac{2}{\pi k_0\rho}}e^{j(\frac{\pi}{4}-k_0\rho)}\sum_{n=-\infty}^{\infty} a_n e^{jn\phi_o}. \tag{6.22}$$

From the definition of σ_{2D} in (6.15) and the conversion factor needed to change σ_{2D} to σ_{3D} in (6.17), the backscattering coefficient of the impedance cylinder can be obtained. The ensemble average of the backscatter power is calculated using the backscatter of impedance cylinders of various radii and unit length which are chosen based on the particle size distribution. The simulation results based on the scattering from an impedance cylinder are compared with the measured data as shown in Figure 6.14.

6.4.1 Potholes

The potholes seen on the road surfaces vary in shape and size. General descriptions of the backscatter response of potholes are difficult. An asphalt slab with a cylindrical hole of 10 cm diameter is used to simulate the pothole as shown in Figure 6.15(a). The backscatter response of the pothole was measured at incidence angles from 74° to 86°. A pothole of depth 3.81 cm was considered. Five independent samples were collected for the measurement. The results are shown in Figure 6.15(b) along with the comparison with the threshold values. It is observed that the hh polarization is the preferred polarization for pothole detection.

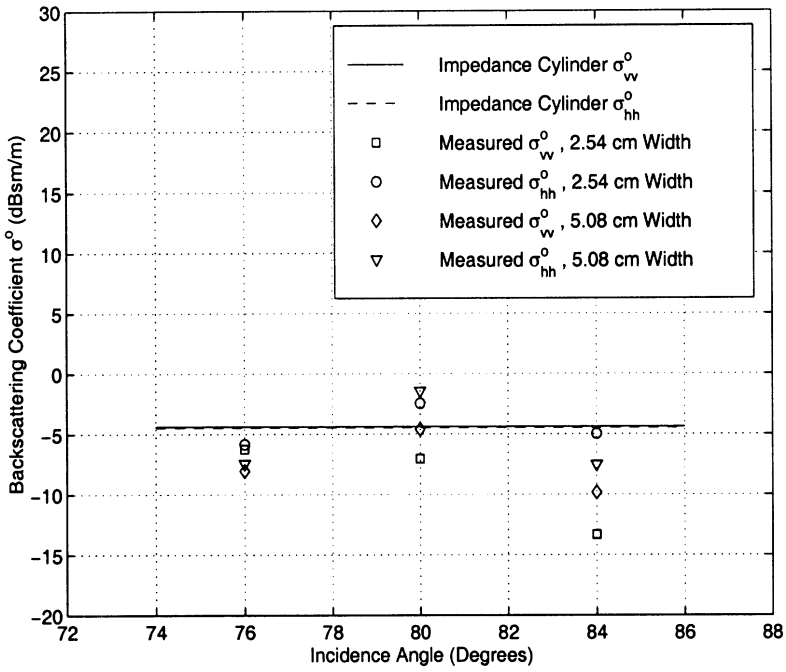

Figure 6.14: The comparison between the measured results of the cracks of two widths and the simulation results based on scattering from an impedance cylinder.

6.5 Roadside Boundaries

The backscatter behavior of roadside boundaries are of interest because of their application in autonomous vehicle control. The backscatter response of roadside boundaries are studied in this section. Typical roadside boundaries are curbs, guardrails, and gravel road shoulder. Their backscatter measurements of roadside boundaries were conducted outdoors. Most of the roadside boundaries examined here are considered as one-dimensional distributed targets. Therefore the ensemble backscatter power per unit length (rather than the RCS) are reported. Their backscatter responses were measured at one specific incidence angle and expressed as a function of azimuthal angle.

Most commonly, gravels and pebbles are used as road shoulders. The selection

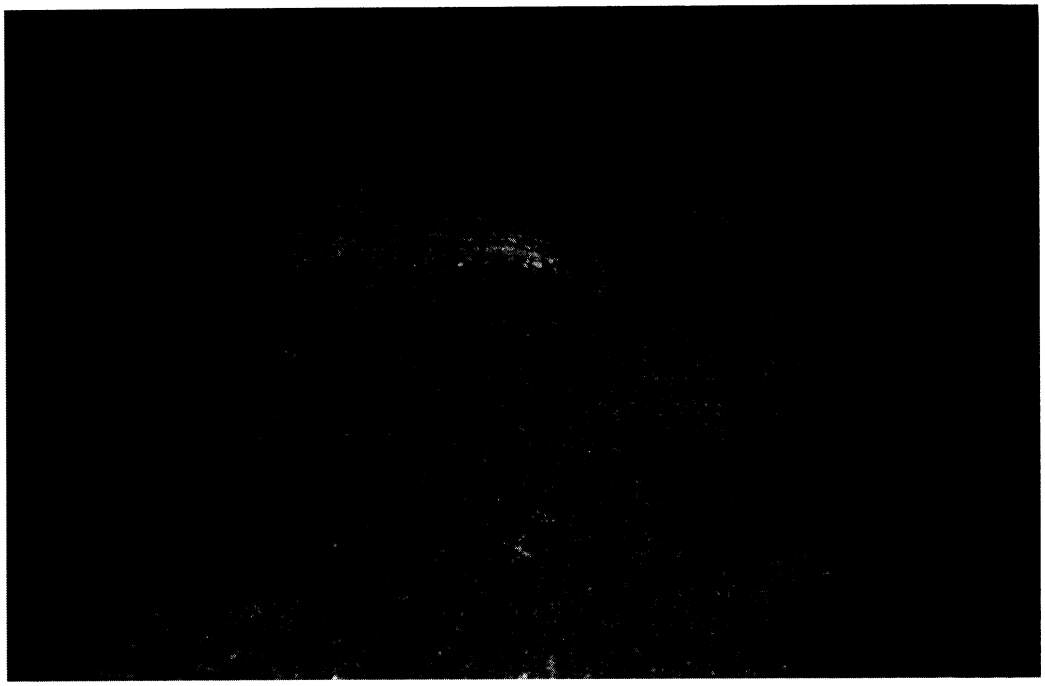

6.15(a) The pothole in this investigation.

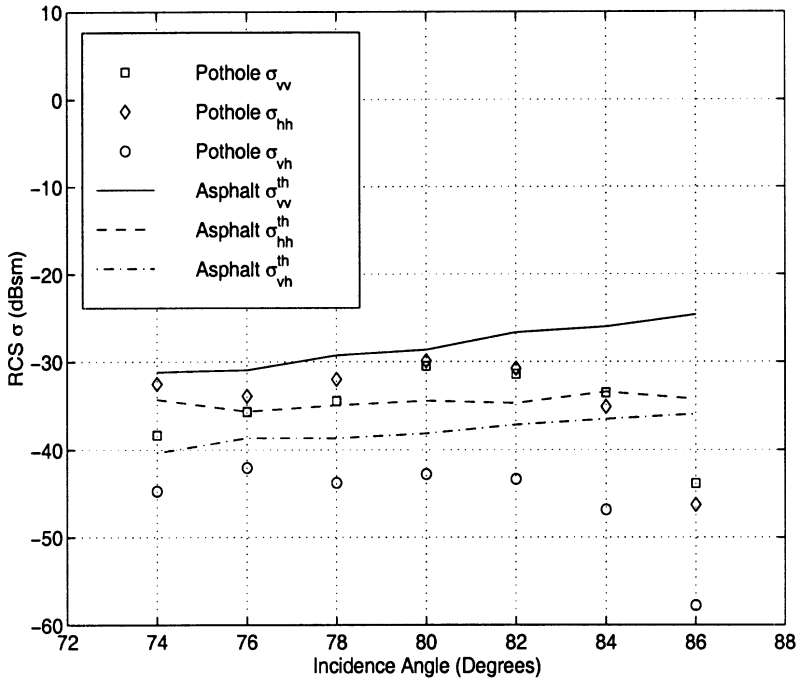

6.15(b) The RCS of the pothole of depth 3.81 cm.

Figure 6.15: The picture and the backscatter response of the pothole of depth 3.81 cm.

Sieve Size in cm	% Passing
3.18	100
2.54	97.8
2.22	95.9
1.91	93.2
1.59	87.7
1.27	77.9
0.95	61.9
0.64	33.3

Table 6.1: The rock size distribution of the pebbles in this investigation.

of rocks for roadside depends on availability. The backscatter response of a surface covered by pebbles is determined by the dielectric properties of the rocks, size distribution, and surface roughness statistics. The size distribution of the pebbles in this investigation is listed in Table 6.1. The backscatter measurements were conducted at incidence angles in the range of 74° – 88°. Eighty independent samples were collected for each incidence angle. The backscatter response of the pebbles is shown in Figure 6.16.

6.5.1 Curbs

The curb, as shown in Figure 6.17(a), is considered to be a one-dimensional distributed target. The transverse dimension of the curb examined here has a vertical height of 14 cm, upper horizontal length of 15.3 cm (next to the grass), and lower horizontal length of 38 cm (next to the asphalt). The backscatter measurements were conducted at an incidence angle of 82°; thirty independent samples were taken.

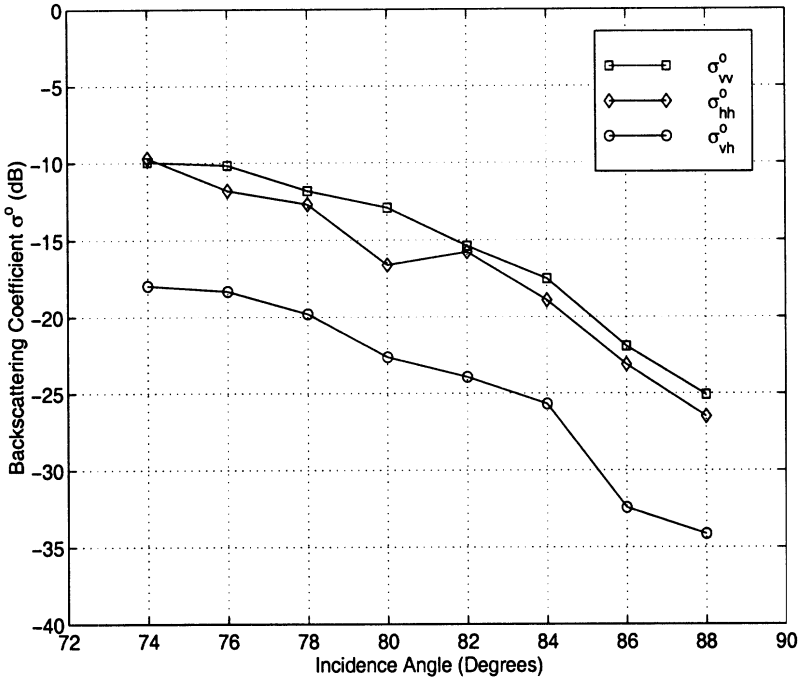

Figure 6.16: The backscatter response of the pebbles.

Figure 6.17(b) shows the backscatter responses as a function of azimuthal angle ϕ, where ϕ is defined as the angle between the antenna boresight and the curb.

6.5.2 Guardrails

Guardrails vary in height, size, and the distance between poles. The guardrail in this investigation has a height of 50 cm (from the center to the ground), width of 33 cm, and a distance between poles of 2.2 m as shown in Figure 6.18(a). The backscatter measurements were conducted at an incidence angle of 84°. Thirty independent samples were taken and the ensemble backscatter power per unit length is shown in Figure 6.18(b).

6.6 Conclusions

In this chapter the near grazing backscatter behavior of debris on road surface and surface faults is investigated at W-band frequencies. For targets with planar

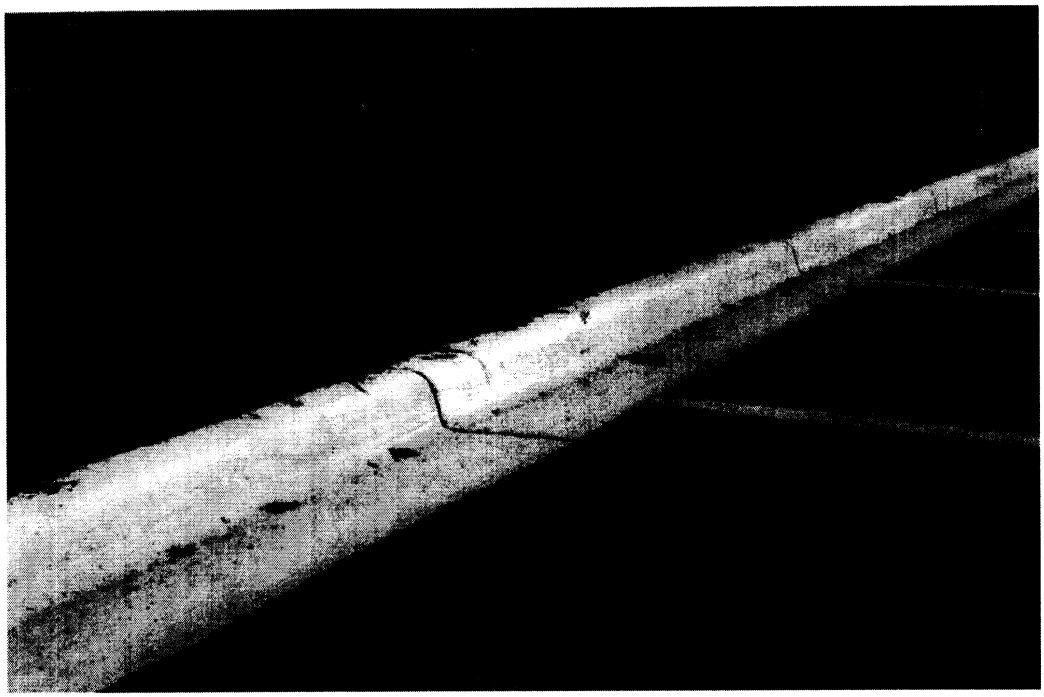

6.17(a) The curb.

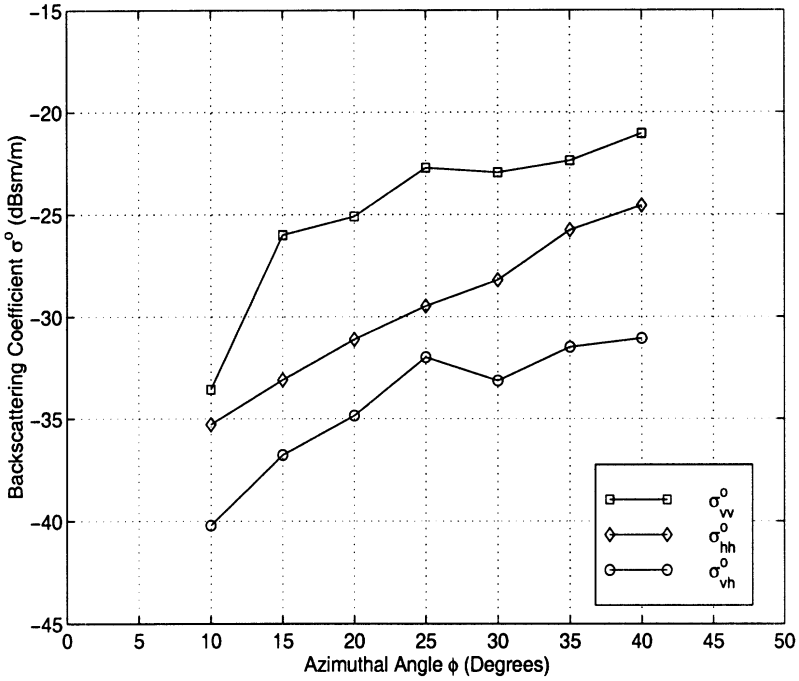

6.17(b) The backscatter response of the curb.

Figure 6.17: The picture and the backscatter response of the curb.

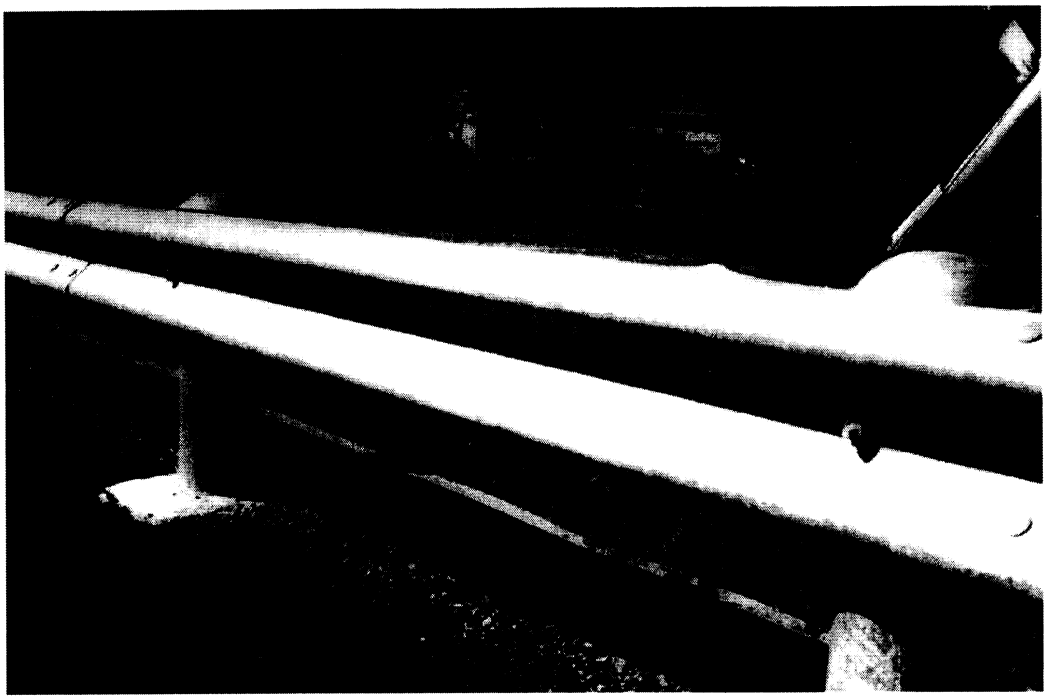

6.18(a) The guardrail.

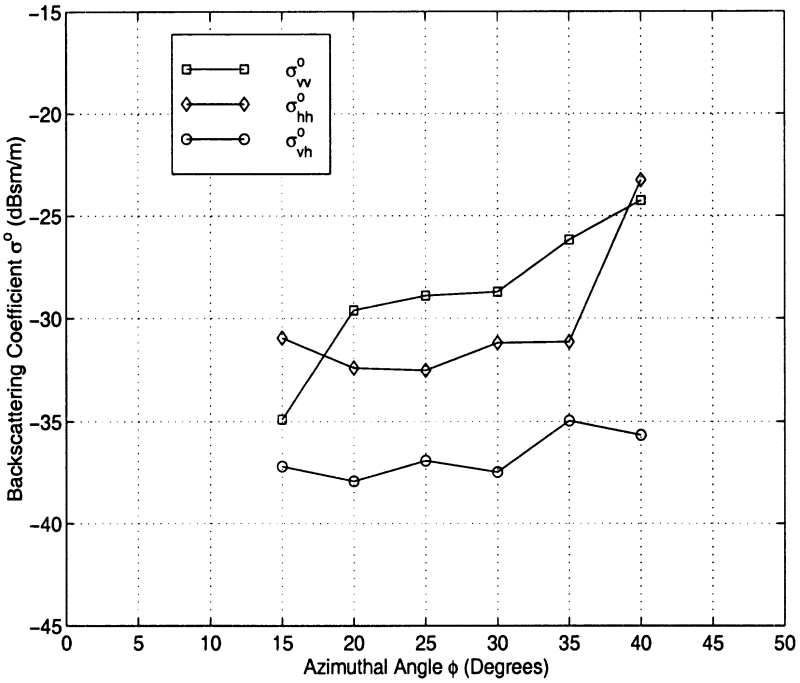

6.18(b) The backscatter response of the guardrail.

Figure 6.18: The picture and the backscatter response of the guardrail.

facets a physical optics scattering model is developed. This model is tested against the backscatter measurements of a brick and right-angled iron on an asphalt surface. The backscattering coefficient of asphalt surfaces is used to determine a threshold value for the detectability of the point targets based on a specified false alarm rate. Also two theoretical models, one based on diffraction from impedance wedges and the other one based on scattering from impedance cylinders, are used to predict the backscatter response of a crack. It is shown that both these models are capable of predicting the backscatter response from a crack reasonably. The polarimetric measurements of various roadside boundaries is also included. The experimental results indicate that the detectability of targets on the road and surface faults is a function of the azimuthal orientation of the targets as well as the system parameters such as incidence angle and polarization. Since the backscatter from asphalt surfaces assumes its lowest value at hh polarization whereas most targets show a maximum RCS at hh polarization, hh polarization was found to be the most suitable polarization for target detection.

CHAPTER VII

CHARACTERIZATION OF OPTIMUM POLARIZATION FOR MULTIPLE TARGET DISCRIMINATION USING A GENETIC ALGORITHM

7.1 Introduction

In this chapter we confine our interest to the problem of characterizing the optimum polarization combination of the receive and transmit antennas for target classification. As stated earlier, in radar scattering problems in which target discrimination cannot be accomplished on the basis of a difference in range, the polarization spectrum (signature) may be the appropriate tool to differentiate between different targets or between targets and clutter. This idea stems from the fact that the polarization for which the radar receives the maximum or minimum scattered power (optimum polarization) from a target may be different from the optimum polarizations of the other targets or its surrounding clutter. Reported polarimetric techniques for target discrimination have been limited to the special case of two targets because of the complex nature of the optimization problem. For example, in the method proposed by Ioannidis and Hammers [29] the optimum polarizations are obtained from a constrained maximization of two bilinear forms, representing the signal-to-

clutter backscatter ratio. A method suggested by Van Zyl *et al.* [71] is based on the normalized root-mean-square (rms) of the difference in the received powers of two targets. In this method, the received powers are calculated for N polarization configurations (N points on the Poincaré sphere) to obtain the rms of the power difference. In many cases of practical importance, more than two targets are of interest. The complex optimization problem of finding the receive and transmit polarizations of a non-polarimetric radar will be addressed using a stochastic optimization method.

Stochastic algorithms such as simulated annealing [34] and genetic algorithms [11,27] offer an alternative to traditional gradient-based optimization methods when the dimension of the parameter space is large or when the objective function is non-differentiable. In recent years, application of genetic algorithms to a variety of optimization problems in electromagnetics has been successfully demonstrated [6,22,42]. Genetic algorithms (GAs) mimic the processes of natural selection and evolution, by modeling genetic recombination and mutation. The entire parameter space is discretized and, using a Monte Carlo simulation of the evolution process on a randomly selected subset of the discretized parameter space, the objective function is optimized. Genetic algorithms offer certain advantages over the traditional gradient-based (TGB) optimization algorithms. The most important feature of GAs is that the optimization is accomplished globally, that is, the probability of converging to a weak local minimum is very low, unlike for the TGB algorithms. This is particularly the case when the objective function is highly non-linear and the dimension of the parameter space is large. GAs are insensitive to the smoothness condition objective function and after convergence provide a list of high quality solutions which can further be assessed according to criteria not included in the objective function. On the other hand there are certain disadvantages associated with GAs. A major drawback

of GAs is their computational inefficiency. Basically, many more evaluations of the objective function are required to achieve convergence with GAs than with TGBs. Another shortcoming of GAs is that they do not provide any insight into the character of the objective function during the course of the optimization process. It should also be noted that the converged solution may not necessarily be the true extremum of the objective function.

In this chapter application of GAs for characterization of optimum antenna polarizations of a non-polarimetric radar is considered. The goal is to achieve multiple target classification with the lowest possible error probability. The objective function is defined so that the solution will directly specify the threshold levels for target classification. In this procedure it is assumed that the polarimetric responses of the targets are known. The chapter is organized as follows: first the objective function of the optimization problem is described, then in Section 7.3 the procedure for implementing a genetic algorithm for the problem at hand is provided. In Section 7.4, the performance of GAs in characterizing the optimum polarizations is presented. In this section both point targets and distributed targets are considered.

7.2 Problem Formulation

As mentioned earlier, the goal of the optimization problem is characterization of the optimum polarizations of a non-polarimetric radar for target classification. Apart from the classical problem of target detection in different clutter backgrounds, other practical applications can be mentioned. Due to recent advances in technology, development of light-weight small-size millimeter-wave (MMW) radar based sensors for a myriad of civilian and defense applications has become economically viable [58]. For example, a simple MMW continuous wave radar system can be designed to be

mounted on a vehicle to assess the road conditions such as the surface roughness, surface wetness, and the existence of an ice or snow layer on the road surface. This information can then be linked to the anti-lock brake or traction control systems of the vehicle. In Section 7.4 this specific example accompanied by experimental results is described in detail.

Let us consider a non-polarimetric radar system. This radar must measure the radar cross section (RCS) or backscattering coefficient of a point or distributed target chosen from N_t different types of targets and then identify the target. Since the target identification must be accomplished with a single measured data point, it is desired that the backscatter power from different targets be as distinct as possible. The polarization configuration resulting in the most distinct radar cross sections or backscattering coefficients for different targets is thus selected. The success of a target discriminator based on the optimum polarization relies on the *a priori* knowledge of the polarimetric responses of the desired targets. Knowing the scattering matrices of the point targets or the covariance matrices of the distributed targets, the RCSs or backscattering coefficients for a given pair of transmit and receive polarizations can be determined analytically using

$$\sigma_n(\psi_r, \chi_r, \psi_t, \chi_t) = 4\pi \tilde{B}(\hat{P}_r, \hat{P}_t) C_n B^*(\hat{P}_r, \hat{P}_t), \quad n \in \{1, \cdots, N_t\} \tag{7.1}$$

where ψ_i and χ_i are the tilt and ellipticity angles of the polarization ellipse for transmit $(i = t)$ and receive $(i = r)$ antennas. In (7.1) C_n is the covariance matrix

of the nth target given by

$$C_n = \begin{pmatrix} \langle S_{vv}S_{vv}^* \rangle & \langle S_{vv}S_{vh}^* \rangle & \langle S_{vv}S_{hv}^* \rangle & \langle S_{vv}S_{hh}^* \rangle \\ \langle S_{vh}S_{vv}^* \rangle & \langle S_{vh}S_{vh}^* \rangle & \langle S_{vh}S_{hv}^* \rangle & \langle S_{vh}S_{hh}^* \rangle \\ \langle S_{hv}S_{vv}^* \rangle & \langle S_{hv}S_{vh}^* \rangle & \langle S_{hv}S_{hv}^* \rangle & \langle S_{hv}S_{hh}^* \rangle \\ \langle S_{hh}S_{vv}^* \rangle & \langle S_{hh}S_{vh}^* \rangle & \langle S_{hh}S_{hv}^* \rangle & \langle S_{hh}S_{hh}^* \rangle \end{pmatrix} \tag{7.2}$$

and $B(\hat{P}_r, \hat{P}_t)$ is the polarization cross-product vector given by

$$B(\hat{P}_r, \hat{P}_t) = \begin{pmatrix} \hat{P}_v^r \hat{P}_v^t \\ \hat{P}_v^r \hat{P}_h^t \\ \hat{P}_h^r \hat{P}_v^t \\ \hat{P}_h^r \hat{P}_h^t \end{pmatrix}. \tag{7.3}$$

In (7.3) the polarization unit vector $\hat{P}_i$ is calculated from

$$\hat{P}_i = \frac{\hat{v} + a_i e^{-j\delta_i} \hat{h}}{\sqrt{1 + a_i^2}}$$

where, in terms of the ellipticity and tilt angles, a_i and δ_i are [36]

$$\begin{aligned} \tan \delta_i &= \frac{\tan 2\chi_i}{\sin 2\psi_i} \\ a_i &= \tan \left[\frac{1}{2} \cos^{-1}(\cos 2\chi_i \cos 2\psi_i) \right]. \end{aligned} \tag{7.4}$$

It should be noted that determination of δ_i from (7.4) is not unique and often leads to confusion. The following constraints remove the ambiguity

$$\begin{aligned} &\text{if} \quad \chi_i \leq 0 \quad \Rightarrow \quad \delta_i \leq 0 \\ &\text{if} \quad \chi_i \geq 0 \quad \Rightarrow \quad \delta_i \geq 0 \\ &\text{if} \quad \psi_i > 0 \quad \Rightarrow \quad |\delta_i| < \pi/2 \\ &\text{if} \quad \psi_i < 0 \quad \Rightarrow \quad |\delta_i| > \pi/2. \end{aligned}$$

The search in the optimization problem has to be performed for pairs of (ψ_t, χ_t) and (ψ_r, χ_r) in a four-dimensional vector space bounded by

$$-90° \leq \psi_i \leq +90° \quad -45° \leq \chi_i \leq +45° \quad (i \in \{r, t\})$$

so that the σ_ns for $n = 1, \cdots, N_t$ are most distinct. Before the optimization problem can be formulated, this objective function must be expressed in a mathematical form. In the problem of two-target classification ($N_t = 2$) the objective function is the maximization of the ratio

$$r(\psi_r, \chi_r, \psi_t, \chi_t) = \frac{\sigma_2}{\sigma_1} \tag{7.5}$$

or the difference

$$d_{12}(\psi_r, \chi_r, \psi_t, \chi_t) = |f(\sigma_2) - f(\sigma_1)| \tag{7.6}$$

where $f(\cdot)$ is a user defined function. The problem is well-defined in this case and an analytical solution to the constrained maximization problem can be obtained [29]. However, for more than two targets a definition for the objective function is not straightforward and the optimization problem becomes very complex. Noting that the objective function defined by (7.5) is a subset of (7.6), we adopt functional (7.6) as a measure of the distance between two functions. The difficulty arises from the fact that a set of input parameters that maximizes the distance between the mth and nth targets (d_{mn}) may minimize the distance between two other targets. In this case even expressing the objective function mathematically seems rather difficult. Using an analogy between the backscatter functions and points confined within a planar geometrical boundary, the following definition for the objective function is derived. Basically the optimum point in the four-dimensional vector space is a point such that the minimum distance among all possible pairs of functions is maximized.

Mathematically the objective function can be expressed as

$$\text{Maximize}\{\text{Min}\{d_{mn}(\psi_r, \chi_r; \psi_t, \chi_t)\}, \quad \forall\, m, n \in \{1, \cdots, N_t; m \neq n\}\} \tag{7.7}$$

subject to: $\psi_r, \psi_t \in [-90°, 90°]$ and $\chi_r, \chi_t \in [-45°, 45°]$. Noting that for N_t targets there are $\frac{N_t(N_t-1)}{2}$ distance functions to be computed, analytical determination of the optimum point in the four-dimensional vector space is very difficult, if not impossible. In this case the objective function is piecewise continuous with unknown discontinuity points. The optimization problem is similar to the *minimax* problem [18] for which the standard approach is to transfer the original problem into a smooth but non-linearly constrained problem. For example, by introducing a new variable D which is a lower bound on the distance function, d_{mn}, we need to

$$\text{Maximize } \{D\} \quad D \in (0, \infty) \tag{7.8}$$

subject to: $d_{mn}(\psi_r, \chi_r; \psi_t, \chi_t) \geq D$, $\forall\, m, n \in 1, \cdots, N_t$. Systematic solutions to this problem exist when the distance functions are linear. Other than the special case of linear functions, hybrid optimization methods based on *a priori* knowledge of the function's discontinuity points and assumptions on the smoothness of the objective function must be tried. In this chapter instead of approaching the optimization problem from a classical point of view, a discrete numerical approach based on genetic algorithms will be used.

Another important issue in the optimization problem is the selection of an appropriate function f used in the distance function given by (7.6). The function can be chosen to be linear, compressor, or expander. A linear function preserves the significance of distance between two RCSs independent of the absolute values of the RCSs whereas a compressor or an expander function puts more emphasis on the difference when the absolute values of the RCSs are relatively small or large respectively. In

dealing with distributed targets, the quantity of interest is the backscattering coefficient (σ°) which is proportional to the mean of the backscattered power. The probability density function describing the statistics of backscatter power for most practical cases is exponential. A feature of the exponential distribution is that its mean to standard deviation ratio is unity. Therefore the uncertainty in estimation of the σ° of a target increases for targets with large σ°. This property requires that the differences between backscattering coefficients of targets with large σ° be larger than those of targets with small σ°. In other words a compressor function must be used. A logarithmic function is an excellent choice for this application [68]. This can be demonstrated by considering estimation of σ° using N independent samples. In this case the standard deviation of the estimate of the mean is $\sigma^\circ/\sqrt{N}$. A confidence region for the estimate defined by peak-to-peak variation around the mean for a linear function is $2\sigma^\circ/\sqrt{N}$ which increases with increasing σ°. However, for logarithmic functions the same confidence region will be mapped to

$$CR = 10\log(\sigma^\circ + \sigma^\circ/\sqrt{N}) - 10\log(\sigma^\circ - \sigma^\circ/\sqrt{N}) = 10\log(\frac{\sqrt{N}+1}{\sqrt{N}-1})$$

which is a constant independent of σ°. Therefore by maximizing the minimum distance between the backscattering coefficients in the dB scale, the separation between the confidence boundaries of the targets is maximized as well.

7.3 Optimization Procedure Using a Genetic Algorithm

In this section a brief overview of genetic algorithms is provided. An excellent tutorial article by Haupt [23] provides more details. Genetic algorithms are probabilistic optimization methods that use an iterative search technique based on ideas from evolutionary principles. The algorithm follows a number of *ad hoc* steps including: (1) discretization of the parameter space, (2) development of an arbitrary

encoding algorithm to establish a one-to-one relationship between each code and the discrete points of the parameter space, (3) random generation of a trial set known as the initial population, (4) selection of high performance parameters according to the objective function known as natural selection, (5) mating and mutation, and (6) recursion of steps 4 and 5 until a convergence is reached. Consider an N-dimensional optimization problem where N parameters are to be chosen so that the objective function F is extremized. In implementation of GAs each parameter is represented by a gene which is simply the binary representation of the parameter. A trial solution comprised of N genes is referred to as a chromosome. The goal is to find the chromosome which best satisfies the objective function.

The first step in implementing a GA is to discretize the parameter space so that the quantization error in calculation of the objective function is below a tolerable threshold. Over-sampling of the parameter space would result in an inefficient optimization procedure. The binary transformation of the discretized parameters can be arbitrary; however, it must be one-to-one and onto. This ensures that for every binary string of say n_p digits, there is a parameter p in the discrete space.

The optimization procedure starts with initialization of the population. A population of a size specified by the user is generated randomly. A simplified flow chart of a GA is shown in Figure 7.1. Once the initial population is created, their performance (fitness) is calculated according to the objective function. Chromosomes then go through a selection operation where only the most fit chromosomes are preserved. The selection operator can either be stochastic or deterministic. In the stochastic approach known as the Roulette Wheel selection method [19], a portion of the original chromosomes survive with a probability density function directly proportional to the objective function values associated with the chromosomes. In the deterministic ap-

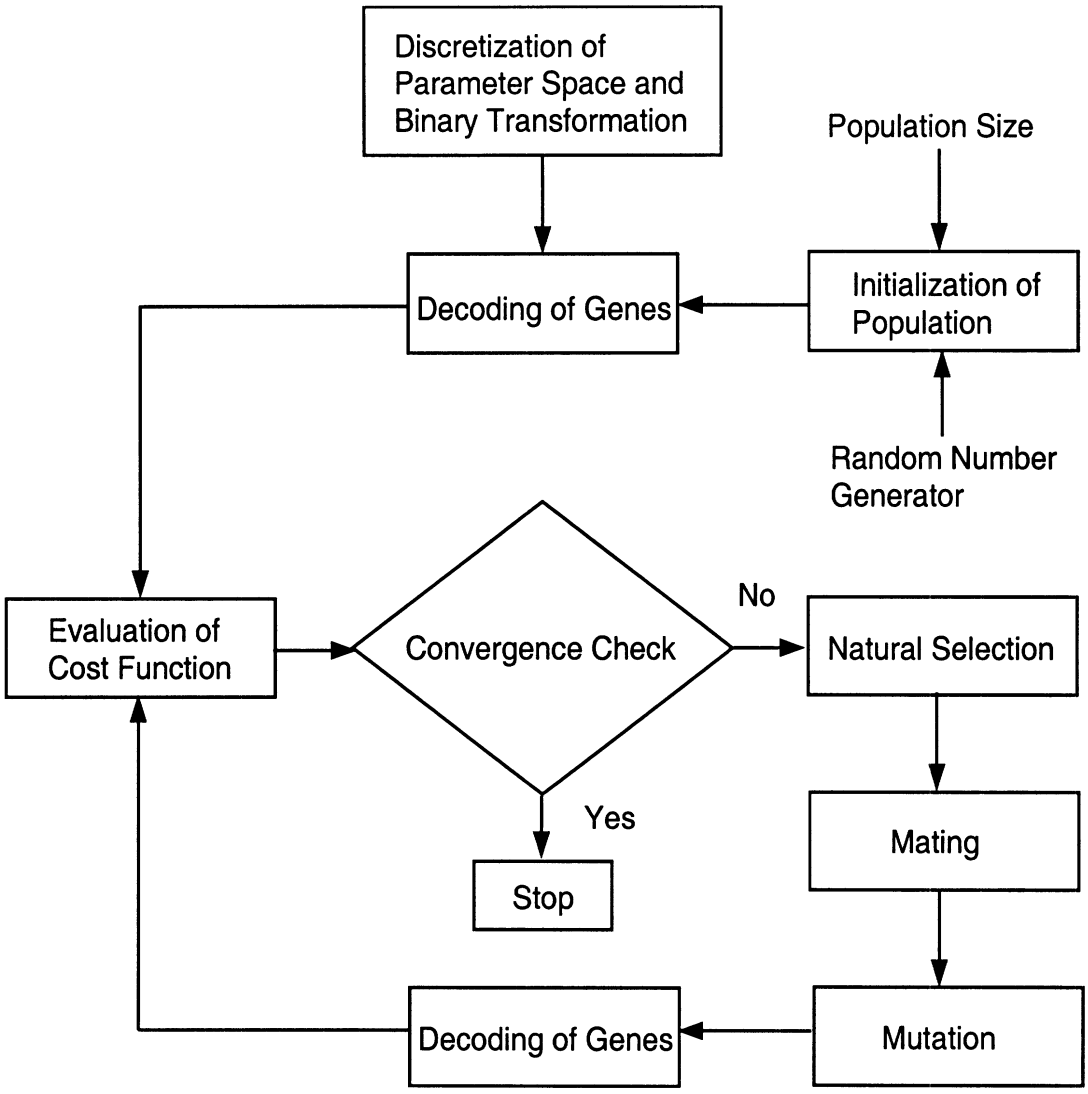

Figure 7.1: Flow chart of the genetic algorithm.

proach, the chromosomes are ranked according to their objective function values and those above a certain threshold are kept [23]. The deterministic selection approach was adopted here.

The next step in the optimization procedure is the mating of the surviving chromosomes, referred to as parents. This step is accomplished using an operator known as the crossover operator. The crossover operator acts on parent chromosomes and generates offspring by swapping portions of the genetic codes of the parents. In this algorithm a single crossover point is selected randomly and two offspring are gener-

ated. The binary codes of the children to the left of the crossover point are the same as those of their parents and their remaining codes are obtained by swapping the binary codes of the parents. The purpose of mating is to construct new chromosomes with higher fitness values. The last step before the fitness evaluation of the new chromosomes is mutation. The mutation process is carried out on a chromosome by changing a bit from 0 to 1 or *vice versa*. The purpose of mutation is to maintain population diversity among the new generations which in effect provides new search regions for the optimization algorithm. Probability of bit mutation per iteration should be kept low enough so that the highly fit chromosomes are not destroyed. A bit mutation probability of less than 1% is recommended. After mutation the performance of the new chromosomes is evaluated and the process is repeated until convergence.

An encoding procedure must be established to provide a one-to-one mapping between the discretized parameter space and a binary code. First consider the discretization of the parameter space. One important issue in a discretization process is the resolution. A fine resolution increases the accuracy at the expense of increasing the search domain. It is noted that the radar backscatter cross sections for point targets and backscattering coefficients for distributed targets are very smooth functions of the transmitter and receiver polarization angles (ψ, χ). Thus an angular resolution on the order of 1° is sufficient for most practical applications. Another issue is the discretization scheme. For near circular polarizations, the sensitivity of the RCS or the backscattering coefficient to variations in the tilt angle is very low. A uniform discretization of the parameter space then seems illogical. There is a one-to-one correspondence between the polarization state of the receiver or transmitter and a point on the surface of Poincaré sphere, which suggests a uniform discretization of

the sphere surface. The area of a pixel on the surface of a Poincaré sphere is given by

$$\Delta A = 4r^2 \cos 2\chi \Delta\chi \Delta\psi.$$

Requiring equal pixel area independent of ψ and χ, the total number of pixels are obtained from

$$N_p = \frac{\pi}{\cos 2\chi \Delta\chi \Delta\psi}.$$

To establish a one-to-one correspondence between the discrete points on the surface of a Poincaré sphere and a complete set of binary codes, N_p must be equal to 2^n for some integer n. Choosing a fixed resolution for $\Delta\chi = 1°$, the resolution for tilt angle as a function of χ can be obtained from

$$\Delta\psi = \frac{10314 \times 2^{-n}}{\cos 2\chi} \quad \text{(degrees)}. \tag{7.9}$$

In order to achieve almost equally-spaced points on the sphere surface, $n = 13$ can be chosen. Guided by (7.9) and after some inspection, the number of discrete points $k(\chi)$ on circles of constant χ is obtained and reported in Table 7.1. Note that according to this discretization scheme

$$\sum_{m=-45}^{45} k(m) = 8192,$$

as expected. Each polarization is indexed by numbering the points from 0 (south pole) to 8191 (north pole). The relationship between the polarization state (ψ, χ) and its decimal representation p is given by

$$\begin{aligned} &\text{For } m = \ -45 \ \text{ to } \ 45 \\ &\chi = \ m° \\ &\psi = \ \frac{180\ell}{k(m)} \qquad \ell = 0, \cdots, k(m) - 1 \\ &p = \ \sum_{m'=-45}^{m-1} k(m') + \ell \end{aligned}$$

χ	± 45	$\pm$ 44	± 43	± 42	± 41	± 40	± 39	± 38	± 37	± 36	± 35	± 34
$k(\chi)$	1	3	6	10	20	26	30	36	40	44	48	54

χ	± 33	± 32	± 31	± 30	± 29	± 28	± 27	± 26	± 25	± 24	± 23	± 22
$k(\chi)$	58	64	68	72	76	82	86	90	92	96	100	104

χ	± 21	± 20	± 19	± 18	± 17	± 16	± 15	± 14	± 13	± 12	± 11	± 10
$k(\chi)$	106	106	112	112	118	118	120	124	126	128	128	130

χ	± 9	± 8	± 7	± 6	± 5	± 4	± 3	± 2	± 1	0
$k(\chi)$	132	134	137	140	142	144	148	152	154	158

Table 7.1: Uniform discretization scheme of Poincaré sphere, where $k(\chi)$ is the number of points on circles of constant χ.

Now expressing p in terms of a 13-bit binary code, we have established a one-to-one correspondence between a polarization state and a binary code. Combining the binary codes for the transmit and receive polarization states, a 26-bit binary code is obtained which represents a discrete point within the domain of the input parameter space. According to our discretization scheme there are a total of 67,108,864 possible chromosomes in the discretized parameter space.

7.4 Results and Discussions

In this section performance of the genetic algorithm in characterization of optimum radar polarizations is studied by considering two examples. In the first example the optimization problem for four point targets based on synthetic data is examined. The second example is concerned with a practical application of MMW radar sensors

for characterization of road surface conditions. The GA is used to determine the polarization states of the transmitter and receiver of a non-polarimetric MMW radar for the purpose of classifying the road surfaces into four categories: (1) dry asphalt surface, (2) wet asphalt surface, (3) ice-covered asphalt surface, and (4) snow-covered asphalt surface. For the point target classification example, we chose four targets with similar RCSs. These include a metallic sphere, a composite target made up of two thin cylinders $\lambda/8$ apart oriented 45° with respect to the reference vertical direction, a dihedral corner reflector, and a thin vertical cylinder whose scattering matrices are given by:

$$\boldsymbol{S}_s = \begin{pmatrix} 1 & 0 \\ 0 & 1 \end{pmatrix}, \qquad \boldsymbol{S}_c = \frac{\sqrt{2}}{2}\begin{pmatrix} 1 & -j \\ -j & 1 \end{pmatrix},$$

$$\boldsymbol{S}_d = \begin{pmatrix} 1 & 0 \\ 0 & -1 \end{pmatrix}, \qquad \boldsymbol{S}_v = \begin{pmatrix} 1 & 0 \\ 0 & 0 \end{pmatrix}.$$

The GA developed in this chapter allows the user to choose the size of population and to initiate the algorithm with different sets of initial population. The population size must be chosen according to the size of discretized parameter space (in this case 2^{26}). If the population size too small, the algorithm may converge to a weak local maximum. On the other hand the algorithm becomes numerically very inefficient if the population size is large. For this problem it was found that a population size on the order of $70 - 100$ provides satisfactory results.

Figure 7.2(a) shows the convergence rate of the GA for the four point target problem with three statistically independent initial population sets. In this figure the performance measure, which is simply the minimum RCS difference (in dB) between any two targets among the aforementioned four targets, is displayed. The

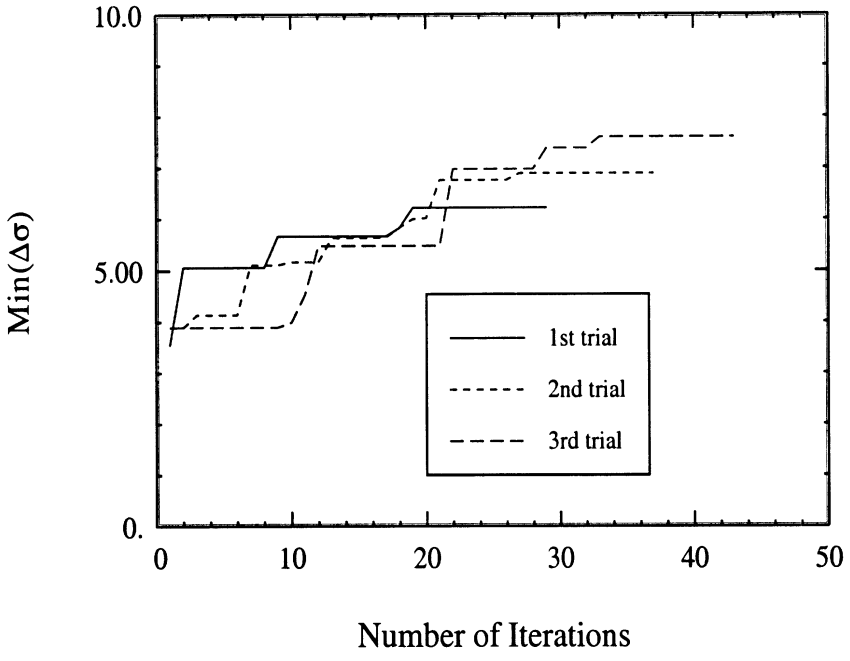

7.2(a)

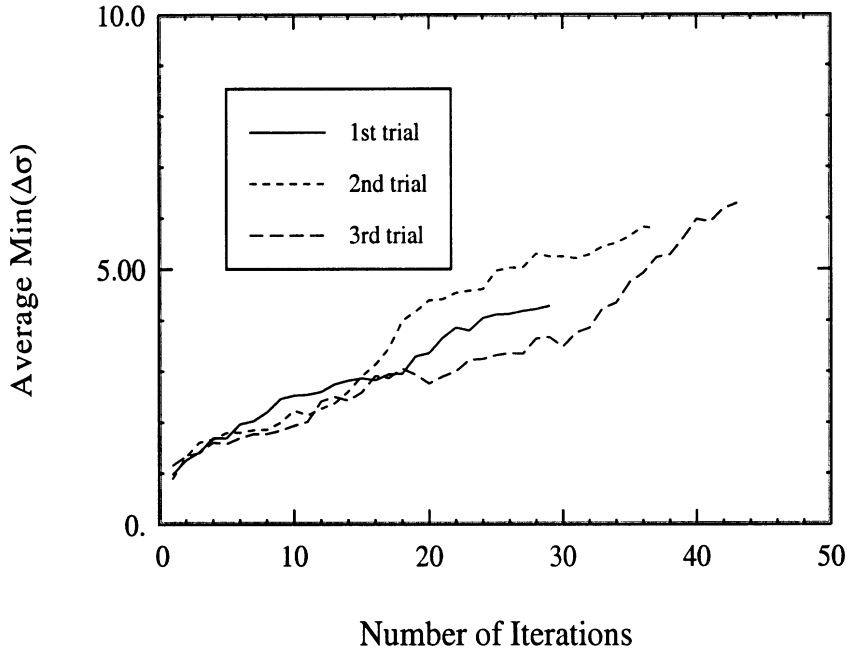

7.2(b)

Figure 7.2: The convergence performance of the GA in characterizing the optimum polarization for classification of the four point targets.

	ψ_r	χ_r	ψ_t	χ_t	σ_s	σ_c	σ_d	σ_v	Min($\Delta\sigma$)
1st	47.1	-10.0	-44.33	-8.0	-16.55	-1.59	10.9	4.76	6.2
2nd	-46.3	9.0	54.0	6.0	-3.84	-10.73	10.90	3.21	6.9
3rd	-47.5	4.0	52.1	2.0	-4.43	-14.30	10.96	3.36	7.6

Table 7.2: The optimum polarization states derived by the GA using three independent initial population sets for discriminating four point targets and their RCSs at the optimum polarizations.

solutions (ψ_r, χ_r, ψ_t, χ_t) for the three different initial population sets together with the RCSs of the targets and the maximized minimum RCS difference Min($\Delta\sigma$) at the optimum polarizations are reported in Table 7.2. Although at the third trial a better solution is obtained it can be seen that in all three cases the algorithm finds comparable and reasonable results. The results clearly indicate that there exist polarizations for optimal multiple target classification even for targets with comparable RCSs. To examine whether the algorithm is converging to a maximum or it is randomly searching the parameter space, the average of the performance measure of all chromosomes for each generation as the process evolves can be studied. Figure 7.2(b) shows an increasing trend for the average of the performance measure as the algorithm converges.

Next four distributed targets are considered. In this example a practical application would be the optimal design of an affordable MMW radar sensor for automotive applications that can assess traction of road surfaces. For this purpose a relatively smooth asphalt surface with rms height of 0.34 mm was chosen. The same asphalt surface was considered under four different conditions. These were: (1) a dry asphalt surface, (2) a wet asphalt surface with a water content of 0.8 kg/m^2, (3) an asphalt

surface covered by an ice layer of thickness 1.4 mm, and (4) an asphalt surface covered by a snow layer of thickness 6.4 mm and density 68 kg/m^3. The University of Michigan fully polarimetric 94 GHz scatterometer was used to characterize the polarimetric responses of the asphalt surfaces. This system operates at 93.5 GHz with a bandwidth of 0.5 GHz. The backscatter measurements were conducted over the incidence angular range of $70° - 88°$. To characterize the statistics of the backscatter responses, more than eighty independent spatial samples were collected for each target. Systematic measurement errors such as channel imbalances, antenna cross-talk, polarization switch distortions, and erroneous radiometric calibration constant are accounted for by using an external calibration procedure [44]. The backscattering coefficients of the four asphalt surfaces as a function of incidence angle are shown in Figure 7.3(a - c). After the calibration procedure, the covariance matrices of the asphalt surfaces at 74° were fed to the GA and the results are reported in Table 7.3 for three different initial population sets. For each case the approximate computer time to arrive at an optimal solution using this algorithm (GA) is less than 1 minute on a SPARC 20 workstation. In this table the subscripts d, w, i, and s denote dry, wet, ice, and snow respectively. The performance is similar, although the solutions are different. A minimum $\sigma°$ difference of 6 dB among different surface road conditions is obtained which allows for a reliable target classification. Figure 7.4(a) and (b) show the convergence behavior of the algorithm in this case. As expected the average of performance measure for each generation improves as the algorithm approaches the convergence point.

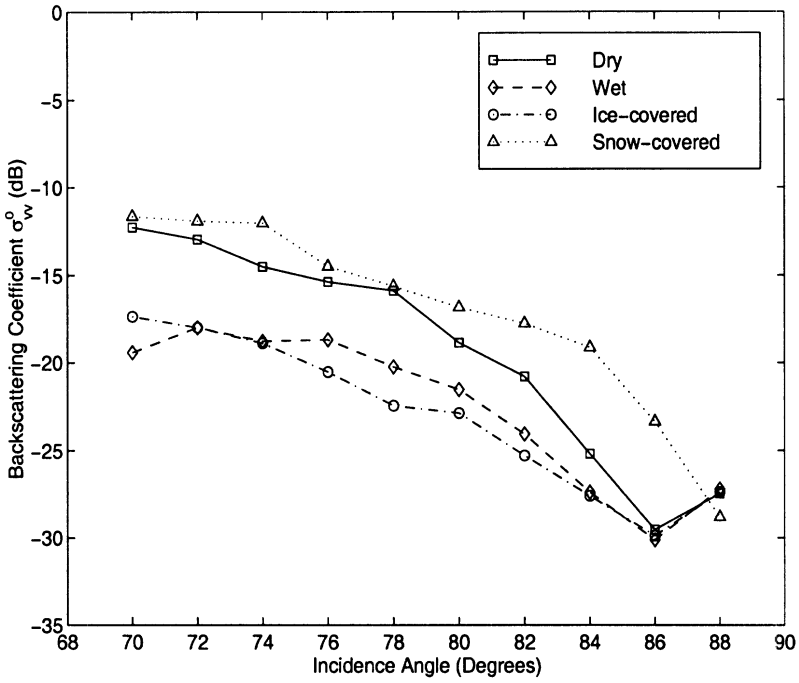

7.3(a) σ°_{vv} of the asphalt surface under four different weather conditions.

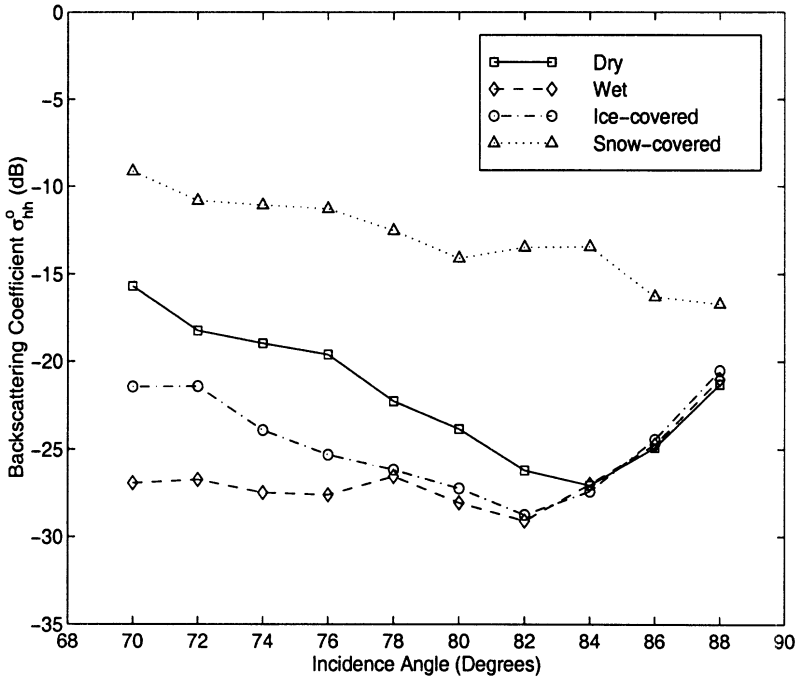

7.3(b) σ°_{hh} of the asphalt surface under four different weather conditions.

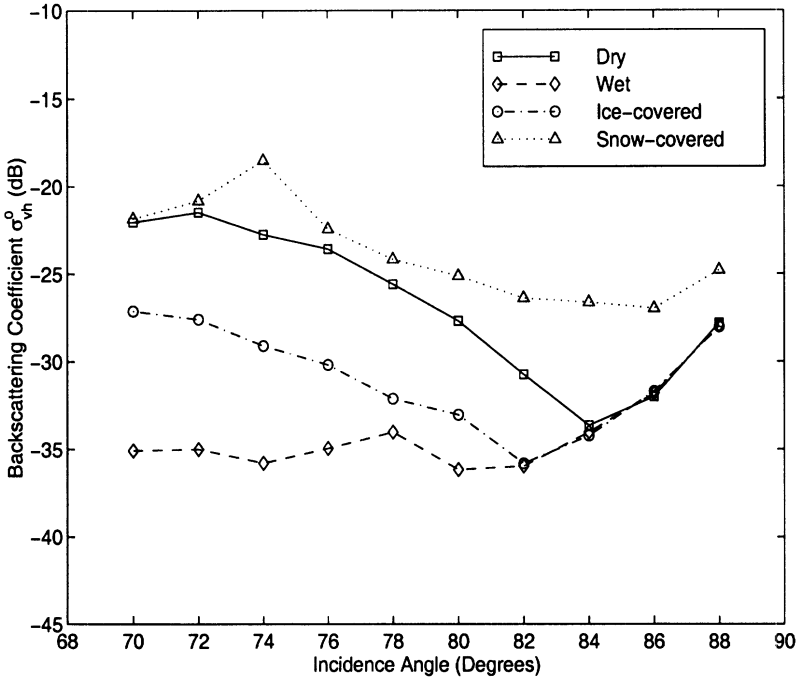

7.3(c) σ°_{vh} of the asphalt surface under four different weather conditions.

Figure 7.3: The measured backscattering coefficients (a) σ°_{vv}, (b) σ°_{hh}, and (c) σ°_{vh} of the dry asphalt, wet asphalt, ice-covered asphalt, and snow-covered asphalt at 94 GHz as a function of incidence angle.

	ψ_r	χ_r	ψ_t	χ_t	σ°_d	σ°_w	σ°_i	σ°_s	Min($\Delta\sigma^{\circ}$)
1st	-87.3	9.0	-5.6	32.0	-21.2	-33.45	-27.25	-15.25	5.98
2nd	16.8	17.0	-86.2	4.0	-22.10	-34.43	-28.20	-15.92	6.10
3rd	-86.2	5.0	15.6	22.0	-21.88	-34.25	-27.94	-15.64	6.06

Table 7.3: The optimum polarization states derived by the GA using three independent initial population sets for discriminating four distributed targets and their RCSs at the optimum polarizations.

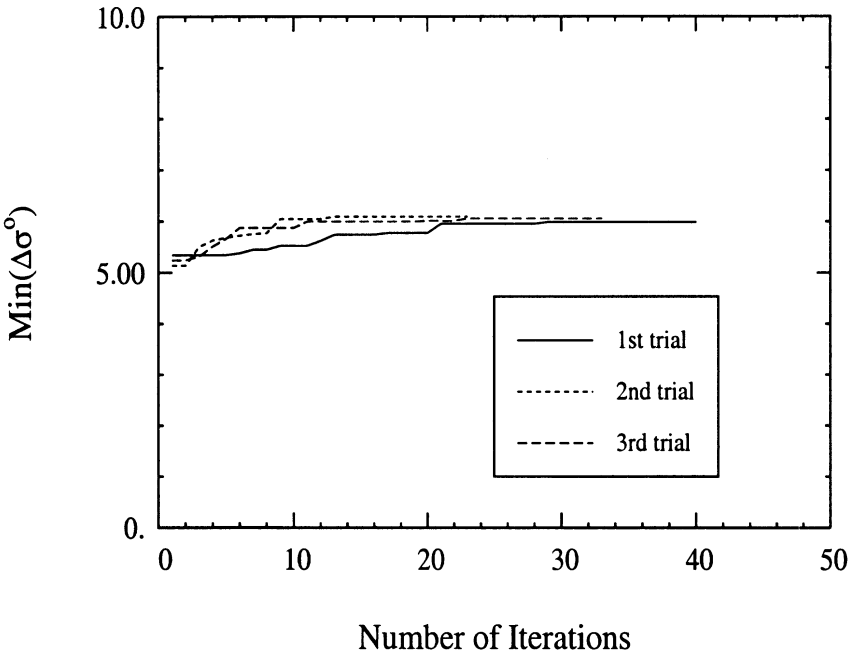

7.4(a)

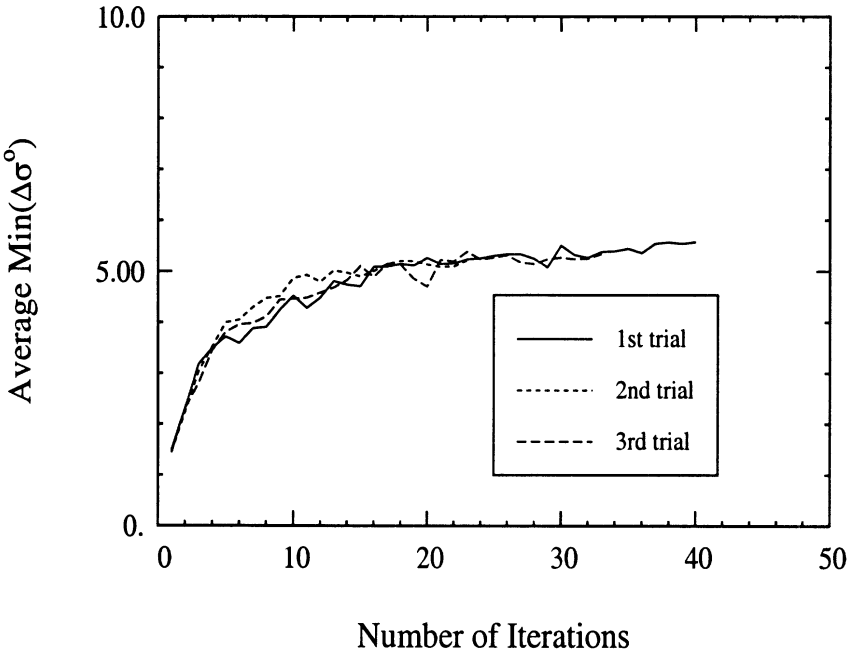

7.4(b)

Figure 7.4: The convergence performance of the GA in characterizing the optimum polarization for classification of the four distributed targets.

7.5 Conclusions

Determination of polarization states of the transmitter and receiver antennas of a non-polarimetric radar for optimal target classification was considered in this chapter. Assuming that the polarimetric responses of the targets under consideration are known *a priori*, the optimization problem was formulated to search for a pair of polarization configurations so that at these polarizations the minimum separation of the backscatter power between any two targets among all possible targets is maximized. To achieve this goal, a global search routine based on a genetic algorithm was used. The success of the GA was demonstrated by applying the algorithm to examples of point and distributed targets. The issues regarding the user defined parameters of the algorithm such as the population size and probability of mutation as well as the convergence property of the algorithm were discussed. Optimal polarization synthesis for a non-polarimetric MMW radar system considered for assessing traction of road surfaces was carried out based on a set of polarimetric backscatter measurements of asphalt surfaces under different physical conditions at 94 GHz.

CHAPTER VIII

CONCLUSIONS AND RECOMMENDATIONS

8.1 Summary

This thesis provides complete polarimetric characterization of common traffic targets and clutter to satisfy the requirements of radar polarimetry techniques in AHS applications. The main contributions of this thesis are:

1. Low grazing incidence polarimetric measurements of targets frequently encountered in the highway environment at millimeter-wave frequencies.

2. Development of analytical models to predict the backscatter response of various road surfaces under different weather conditions, of targets with planar facets on road surfaces, and of road surface faults.

3. Design of an innovative approach based on the genetic algorithm to search for the optimum polarizations of transmit and receive antennas, to allow multiple target classification using a simple non-polarimetric radar.

In the following, the emphases of each chapter are reiterated.

Chapter 2 describes the radar system used to conduct the backscatter measurements. The system was designed to operate in coherent mode as well as coherent-on-receive mode. Given the instability of phase measurement in the outdoor environ-

ment, the coherent-on-receive mode was chosen for the polarimetric measurements of distributed targets. A calibration technique, developed earlier for the 35 GHz radar system, is used to characterize the distortion parameters associated with the imperfections of the radar system components. These systematic errors are removed later in post-processing. The measurement accuracy of this radar system is evaluated by measuring the scattering matrices of a sphere and a cylinder. Excellent agreement between the theoretical and measured scattering matrices of the test targets was obtained.

Chapter 3 illustrates a practical example of the radar polarimetry technique, with application to collision avoidance radar sensors. Wave polarization is exploited to solve typical problems encountered in wave propagation. Interference can be minimized by choosing orthogonal polarizations for transmit and receive antennas. Selecting optimum polarizations for both antennas can maximize the signal to clutter ratio. A typical traffic scene was measured to examine the effect of wave polarization on the multi-path problem. The chirp z transform is used to convert the measured frequency-domain data to time-domain response to provide the range information. Images of this scene were generated for different combinations of transmit and receive polarizations. It is observed that the signal level of the imaginary targets caused by multi-path can be reduced significantly by choosing the appropriate polarizations.

The investigation of the backscatter response of smooth road surfaces at 94 GHz is conducted in Chapter 4. First the effective dielectric constants of pavement mixtures were determined by the inverse scattering algorithm. Then a theoretical approach based on the vector radiative transfer (RT) theory was pursued to predict the backscatter response of smooth road surfaces. However, fundamental parameters of the RT model were characterized experimentally. The first-order iterative solu-

tion is used to derive the backscatter model for the present problem by solving the vector integro-differential equation subject to the appropriate boundary conditions. The model is capable of predicting the backscattering coefficients as well as the co-polarized phase difference statistics of smooth asphalt and concrete surfaces. Dry, wet (for asphalt surfaces only), and ice-covered conditions are considered. A set of backscatter measurements was performed on smooth road surfaces at near grazing incidence angles to confirm the validity of the analytical model. Good agreement is observed between the measured data nd the theoretical results.

Chapter 5 extends the study to include the backscatter behavior of two other road surfaces: the snow-covered smooth asphalt surface and the rough asphalt surface. For the former, the first-order iterative solution of the vector RT equation is used to calculate the volume scattering from the snow layer for the co-polarized backscatter response. The Rayleigh scattering model was adopted to characterize the phase and extinction matrices of the snow layer. An analytical expression for the cross-polarized backscatter response of the snow layer is obtained from the second-order iterative solution. The backscattering from the snow layer is combined with the volume scattering from the underlying asphalt layer to provide the overall backscatter response. The backscatter behavior of the rough asphalt surface consists of surface scattering from the rough interface and volume scattering from the asphalt mixture. The integral equation method (IEM) formulation is employed to model the surface scattering response. The simulation results were compared to the experimental data for these two cases. The validity of both models were justified.

The polarimetric characterization of debris and faults on road surfaces is reported in Chapter 6. The detectability of each target is determined in terms of a threshold value defined by the measured RCS of asphalt surfaces and the maximum false

alarm rate. Theoretical models were developed to predict the backscatter response of road surface faults and targets with planar facets on road surfaces. Models based on diffraction from impedance wedges and on scattering from impedance cylinders are used to predict the backscatter from a crack. Model based on physical optics approximation is used to predict the backscatter from a brick or a right-angled iron on road surfaces. The theoretical predictions show good agreement with the experimental data. This chapter also includes the backscatter behavior of various roadside boundaries. Their backscatter information could be used to provide safety features for automotive radar sensors to prevent sideward crashes.

For multiple target classification, Chapter 7 proposes a stochastic technique (the genetic algorithm) to search for the optimum polarizations of transmit and receive antennas. The required backscatter information of the targets under consideration can be provided by the analytical models developed previously. The genetic algorithm offers many advantages over the traditional gradient-based optimization algorithms. Global optimization is one of the important features. However, it also suffers the drawback of computational inefficiency. The performance of the genetic algorithm was evaluated by considering their application to examples of point and distributed targets. A set of optimum polarizations was obtained for each case, providing satisfactory multiple target classification.

8.2 Recommendations for Future Work

Most of the analytical models developed in this thesis are used to predict the backscatter behavior of road surfaces under various physical conditions. In Chapter 4 the hybrid scattering model is developed for the backscatter response of smooth road surfaces. However, the range of validity does not cover the case of wet smooth

concrete surfaces because the effective dielectric constant of wet concrete mixture is undetermined. Unlike the non-absorptive asphalt mixture, the concrete mixture has an effective dielectric constant which changes with the addition of water. The relationship between the effective dielectric constant and the water content of the concrete mixture must be characterized before seeking the backscatter response of wet concrete surfaces.

In Chapter 5 the co-polarized backscatter response of the rough asphalt surface was modeled successfully by a combination of the IEM formulation and volume scattering. Since the IEM equation does not converge for the cross-polarized backscattering coefficient, other theoretical models are needed to predict the cross-polarized component of the surface scattering. The study could be extended to include the backscatter response of rough asphalt surfaces under other weather conditions. New models are required to predict the backscatter in these cases.

The backscatter behavior of pebbles was experimentally characterized in Chapter 6. An analytical model could be established with the knowledge of the dielectric properties of rocks, statistics of rock size distribution, and pebble surface roughness statistics. These could be input to a packing algorithm [57] to predict the backscatter response of pebbles. On the other hand the theoretical models developed to predict the backscatter response of cracks should also apply for potholes. However, the concave geometry of the pothole edges is expected to complicate the problem.

This investigation includes scientific study as well as engineering applications. The high frequency backscatter behavior of traffic targets and clutter was fully examined and analyzed. An instrumentation millimeter-wave polarimetric radar system was constructed. This system demonstrates the capability of providing a safer transportation environment by applying the knowledge gained from the research. The

combination of the results from this investigation with modern microwave monolithic integrated circuit (MMIC) technology is expected to deliver safer and more reliable automotive radar sensors of great commercial value.

APPENDICES

APPENDIX A

MECHANICAL ASSEMBLY OF THE GIMBAL

The gimbal shown in Figure 3.3 is constructed for the purpose of generating radar images of traffic scenes as well as collecting the backscatter responses of different road surfaces. The height, width, and depth of the overall structure are 1 m, 0.7 m, and 0.6 m respectively. The dimensions were chosen so that the gimbal fits into a middle-size van for outdoor measurements. Considering the light-weight requirement, most of the materials used for construction are aluminum tubing. All joints are welded together to prevent system vibration during scanning. The gimbal consists of two frames, one stationary and the other one rotatable about an axis connected to the stationary frame, and facilitates elevation-over-azimuth scanning. In this configuration, any elevation angle can be chosen for a specific azimuth angle. The RF unit is attached to the inner frame via two axial rods passing through a pair of pillow blocks. This mechanism allows the RF unit to rotate about axis #1 (see Figure 3.4) which is equivalent to scanning in the elevation direction. The same method is used to attach the inner frame to the outer frame using a pair of flange bearings. The inner frame can spin around axis #2 and that allows the RF unit to scan in azimuth. In order to scan in both azimuth and elevation, two linear actuators are used. Each linear actuator is powered by its own DC motor. The

motion control card inside the 486 processor based control unit commands the DC motors of both linear actuators in order to create a torque causing the inner frame or the RF unit to rotate about their axes. The length of the stroke determines the maximum angular range of scanning. A set of light (0.68 kg) linear actuators with stroke length of 0.25 m is chosen as a compromise between the requirements of compact size and wide angular scanning capability. This linear actuator allows an azimuthal angular range of $\pm 20°$ and elevation angular range of $\pm 15°$. Due to the inherent inertia of this structure, some of the tuning parameters like the proportional gain, the derivative gain, and the integral gain of the motion control card need to be adjusted to prevent possible overshooting oscillation or under-damping. Typical values range between 500 and 2000 for the proportional gain, between 1000 and 8000 for the derivative gain, and between 16 and 64 for the integral gain. Two incremental encoders are used to monitor the movements of the linear actuators by examining the rotation of the axial rods. Both axes of rotation are connected to two individual encoders through universal/lateral displacement couplers. These couplers allow 10° angular and 1 mm radial misalignment between the encoder shaft and axis of rotation. Hence, minor errors in aligning the axial rod and the shaft can be tolerated. With a resolution of 1800 counts/turn the encoder allows the gimbal to move with an accuracy of two tenths of a degree. The outputs of the encoder are connected back to the motion control card. This controller performs all servo loop calculations and the command position trajectory calculation. Immediately after receiving timer interrupt, the motion control card reads all encoder inputs and stores them into memory. Then it calculates the analog control voltage (or pulse rate) based on a proportional integral derivative (PID) servo control algorithm. The input of the PID algorithm is the current position error. The current position error equals

the difference between the command position and the actual position. The actual position is measured by the feedback encoder circuit, and the command position is determined by the trajectory calculator. This error is the basis for changes in the analog control voltage. The analog control voltage is connected to a voltage-to-frequency converter. The converter generates a pulse train, amplified by a pulse width modulation (PWM) servo amplifier, to drive the DC step motor. The relationship between the analog control voltage and the pulse output rate is constant and linear over the entire frequency range. This feedback algorithm provides the automatic error correction capability to move the RF unit to the desired position. An important issue in the feedback system is the slack in the joints at each end of the linear actuators. Too much space in the joints would result in the free movement of the frame or of the RF unit, which could lead to the malfunction of the automatic error correction.

APPENDIX B

A MICROSTRIP RING RESONATOR FOR SOIL MOISTURE MEASUREMENTS

B.1 Introduction

Successful modeling and understanding of global change are dependent upon an improved understanding of climatic and hydrologic processes. Soil moisture and its spatial and temporal variations play an important role in such models. Radar remote sensing of soil moisture has been an active area of research over the past two decades. Characterization of the dependence of the dielectric constant of soil to its moisture content is an important step in this endeavor. In this appendix the theoretical and experimental aspects of a field-portable device for accurate measurement of both the real and imaginary parts of soil dielectric constant are discussed.

Two commonly used methods for the field measurement of the dielectric constant of soil are time-domain reflectometry (TDR) and a reflection coefficient measurement using an open-ended coaxial probe. In the TDR method the dielectric constant of the soil medium is determined from the delay time of the reflected wave from the open ends of a buried two-wire transmission line [59]. The time delay can only provide the information about the real part of dielectric constant (ϵ_r'). The accuracy of the TDR method is limited by the temporal resolution of the system. In the coaxial probe

method [67], the complex dielectric constant is estimated from the measured complex reflection coefficient of the open-ended coaxial line pressed against the unknown material. The accuracy of this technique is limited by the small dynamic range of the reflection coefficient as a function of ϵ_r'. Another problem with this technique when applied to soil is the small contact area of the coaxial tip which may be comparable in size to the soil particles. It should also be noted that soil dielectric measurement using a coaxial probe is very sensitive to the applied pressure which degrades the accuracy of this measurement technique.

In this appendix a microstrip ring resonator for the dielectric constant measurement of soil is proposed to overcome the aforementioned problems with the existing devices. Application of ring resonators in characterizing the dielectric properties of materials is not a new idea [5, 26, 69]. However, these techniques are specialized for dielectric measurements of thin materials in a stripline configuration and/or only consider characterization of the real part of low dielectric materials. Since both the real and imaginary parts of the dielectric constant of soil have a wide dynamic range with respect to the soil moisture content and the measurement configuration is different from those reported in the literature, a careful theoretical and experimental study of the proposed problem is required. The dielectric measurement technique is very similar to the standard cavity measurement technique [10] with a subtle difference. Basically, the real and imaginary parts of the dielectric constant are to be inferred from the shift in the resonant frequency and the change in the quality factor of the resonator after placing the resonator in contact with the soil medium. The subtlety stems from the fact that the microstrip resonator can be regarded as a partially-filled resonant cavity and therefore the simple relationship between the dielectric constant and the measured changes in the resonant frequency and the quality factor can no

longer be applied. Although the partially-filled nature of the microstrip resonators complicates the retrieval of dielectric constant from the measured quantities, it is a desirable feature in the soil dielectric constant measurements. In the standard cavity measurement, if the loss tangent of the dielectric material exceeds 0.05, it becomes practically impossible to measure the resonant frequency (f_o) and the quality factor (Q) of the loaded cavity accurately. However, for the partially-filled resonators the changes in f_o and Q are substantially less affected by the loading dielectric material. It is shown that with appropriate microstrip resonator design, the dielectric constant of soil with a moisture content as high as 40% can easily be measured.

In Section B.2 the theoretical analysis of the problem is given. In this analysis, which will be referred to as the forward problem, a numerical solution for calculating the resonant frequency and the quality factor of the resonator in terms of ϵ_r' and ϵ_r'' is provided. The numerical solution is based on a quasi-static formulation. Since microstrip resonators are constructed on a finite substrate, the effect of finite substrate width is also investigated. In Section B.3 the inverse problem is considered. There, a simple algorithm for retrieval of ϵ_r' and ϵ_r'' from the measured changes in f_o and Q based on regressional analysis is developed. Finally in Section B.4 experimental results are presented. It is shown that the accuracy of the quasi-static solution degrades as the dielectric constant of the unknown material increases. This phenomenon has also been observed in stripline resonators [5]. In this section the theoretical results based on the quasi-static analysis are slightly modified to agree with experimental data obtained from reference dielectric samples. To verify the accuracy of this hybrid model, the dielectric constant of sandy soil with different moisture contents was measured using a prototype microstrip ring resonator and the results are compared with those measured by three other independent methods.

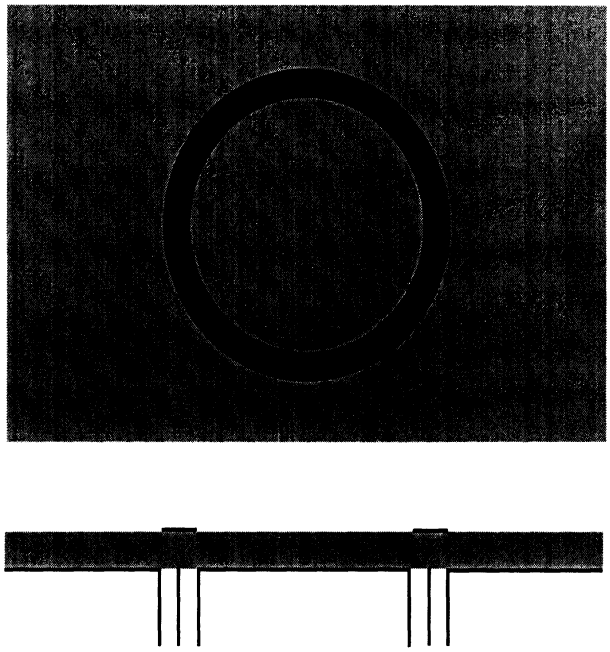

Figure B.1: Top view and side view of a ring resonator used in this investigation.

B.2 Theory

A microstrip ring resonator is a simple transmission line resonator whose geometry is shown in Figure B.1. The resonator is excited by a transmission line through a capacitive coupling at two feed points. At certain frequencies, depending on the electrical length (perimeter) of the resonator, a standing wave pattern forms around the circular path of the resonator. The maximum voltage of the standing wave occurs at the exciting point. The resonant frequencies correspond to a condition where the perimeter of the ring is an integral multiple of the guided wavelength, that is,

$$\lambda_g = \frac{\pi d}{n} \qquad n = 1, 2, 3, \cdots$$

where d is the diameter of the ring and λ_g is a function of the microstrip parameters w_s, h, ϵ_s, and ϵ_2 as shown in Figure B.2.

At resonant frequencies there exists a voltage maximum $\frac{\pi d}{2}$ away from the excitation point. By placing a capacitively coupled transmission line at this voltage

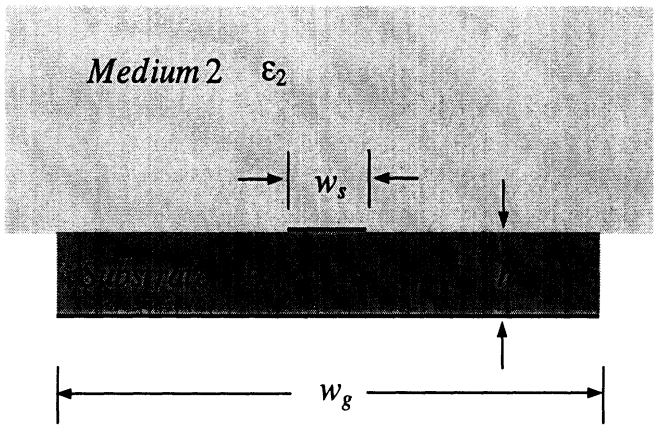

Figure B.2: Geometry of a microstrip line in contact with a half-space homogeneous dielectric medium.

maximum point, the field in the resonator can be probed to detect the resonant frequencies. Basically the transmission coefficient S_{21} of the two-port resonator is measured as a function of frequency and the resonant frequencies are identified as frequencies for which $|S_{21}|$ is maximized. It should be noted that the coupling capacitors tend to lower the resonant frequency and these must be as small as possible for accurate measurement of the resonant frequency. Spectral measurement of $|S_{21}|$ can also reveal the quality factor of the resonator which is a measure of power loss in the resonator. The dissipated power in the resonator includes the dielectric loss, the conductor loss, and the radiation loss. For a given microstrip resonator with known substrate dielectric constant ϵ_s, strip width w_s, and substrate height h an algorithm is sought for computation of the complex dielectric constant of the half-space medium in contact with the ring resonator from the spectral measurement of $|S_{21}|$. To establish the relationship between the complex dielectric constant of the unknown medium and the measured guided wavelength and the Q of the resonator, the quasi-static approximation for microstrip transmission lines is used. Strictly speaking, microstrip structures cannot support TEM waves. However, at low frequency

where the substrate height and strip width are small compared to the wavelength, it is expected that the quasi-static approximation would provide accurate results [14]. The quasi-static approximations found in the literature are usually concerned with lossless dielectrics. In what follows a brief derivation of Poisson's equation for lossy dielectrics is given from which an integral equation for the charge distribution on the microstrip will be obtained. Starting from Maxwell's equations for time-harmonic fields

$$\nabla \times \mathbf{H} = -j\omega\epsilon'\mathbf{E} + \sigma\mathbf{E}, \tag{B.1}$$

$$\nabla \cdot \mathbf{D} = \rho_c + \rho_{imp}; \qquad \mathbf{D} = \epsilon'\mathbf{E} \tag{B.2}$$

where ρ_c is the conduction charge density, ρ_{imp} is the impressed charge density and ϵ' and σ are the permittivity and conductivity of the medium respectively. The conduction current $\mathbf{J} = \sigma\mathbf{E}$ can be related to the conduction charge density ρ_c through the continuity relationship $\nabla \cdot \mathbf{J} = j\omega\rho_c$ and therefore

$$-\frac{j\sigma}{\omega}\nabla \cdot \mathbf{E} = \rho_c. \tag{B.3}$$

Combining (B.2) and (B.3) and defining the complex permittivity as $\epsilon = \epsilon' + \frac{j\sigma}{\omega}$, it can easily be shown that

$$\epsilon\nabla \cdot \mathbf{E} = \rho_{imp}. \tag{B.4}$$

For TEM waves the electric and magnetic fields are irrotational and therefore the electric field can be obtained from a complex potential function ϕ through

$$\mathbf{E} = -\nabla\phi$$

which together with (B.4) results in

$$\nabla^2\phi = -\frac{\rho_{imp}}{\epsilon}. \tag{B.5}$$

Assuming that the ground plane and the metallic strip of the microstrip are at potentials zero and V_o, (B.5) can be solved subject to the boundary conditions. In this case $\rho_{imp} = \rho(x)$ is the induced charge distribution on the strip. If $G(x, y, x', y')$ represents the Green's function of the problem, then the complex potential function can be obtained from

$$\phi(x, y) = \int_{\frac{-w}{2}}^{\frac{w}{2}} \rho(x') G(x, y, x', y') dx'.$$

Using the Fourier transform technique, the Green's function for the microstrip problem is found to be

$$G(x - x', y, h) = \frac{1}{\pi} \int_0^\infty \frac{e^{-\alpha(y-h)} \cos(\alpha(x - x'))}{(\epsilon_s \coth(\alpha h) + \epsilon_2)\alpha} d\alpha \tag{B.6}$$

where ϵ_s is the dielectric constant of the substrate and ϵ_2 is the dielectric constant of the upper half-space. Since the potential function is known over the metallic strip, the integral equation for the induced charge density can be derived by evaluating the potential over the strip and is given by

$$V_o = \int_{\frac{-w}{2}}^{\frac{w}{2}} \rho(x') G(x - x', h, h) dx'. \tag{B.7}$$

The integral equation can be solved numerically using the method of moments and the point matching technique. Subdividing the strip into N sufficiently small cells, (B.7) can be cast into a matrix equation

$$\bar{\bar{Z}} \bar{R} = \bar{V}$$

where $\bar{R}$ is the vector of unknown charge density and $\bar{V}$ is the excitation vector whose entries are constant V_o potentials. To evaluate entries of $\bar{\bar{Z}}$, the Green's function given by (B.6) must be computed for different values of observation (x_m) and source (x_n) points. The decay rate of the integrand of (B.6) (when $y = h$) as a function of α is

rather poor: the asymptotic behavior of the integrand for large values of α is $\frac{1}{\alpha(\epsilon_s+\epsilon_2)}$. To improve the convergence rate the order of integrations in (B.7) can be changed and the entries of the matrix are found to be

$$Z_{mn} = \frac{2}{\pi}\int_0^\infty \frac{\sin(\alpha\frac{\Delta x}{2})\cos(\alpha(x_m - x_n))}{\alpha^2[\epsilon_s \coth(\alpha h) + \epsilon_2]}d\alpha \tag{B.8}$$

where $\Delta x = \frac{w}{N}$. It is noted that the impedance matrix is Toeplitz and symmetric, that is, $Z_{mn} = Z_{pq}$ when $m - n = p - q$ and $Z_{mn} = Z_{nm}$. Thus the integral in (B.8) need be evaluated only N times to fully characterize the impedance matrix. Once the impedance matrix is characterized the charge density can be obtained from

$$\bar{R} = \bar{\bar{Z}}^{-1}\bar{V}.$$

The quantities of interest in the microstrip resonator are the electrical length and the quality factor of the resonator which are directly related to the line capacitance and conductance. The line capacitance is proportional to the total charge in phase with the voltage and the line conductance is proportional to the conduction current. The total complex charge on the strip represented by $Q = Q_r + jQ_i$ can be obtained from

$$Q = \int_{\frac{-w}{2}}^{\frac{w}{2}} \rho(x)dx \simeq V_o \sum_i \sum_j Z_{ij}^{-1},$$

from which the line admittance can be calculated and is given by

$$Y = \frac{I}{V_o} = j\omega\frac{Q}{V_o} = j\omega\sum_i\sum_j Z_{ij}^{-1}.$$

It can be shown that over a narrow range of frequency the microstrip line behaves like a capacitor in parallel with a resistor. The line capacitance and conductance are

thus given by

$$C = \sum_i \sum_j Re[Z_{ij}^{-1}] \quad F/m \tag{B.9}$$

$$G = -\omega \sum_i \sum_j Im[Z_{ij}^{-1}] \quad S/m. \tag{B.10}$$

For wide-band applications a more complicated equivalent circuit must be considered. Assuming that the substrate material and the upper half-space medium are non-magnetic, the line inductance becomes a function of only the geometrical features of the line and can be obtained from magneto-static analysis. An alternative approach is to find the line capacitance of the air-filled microstrip line (C_o) and find the line inductance from

$$L = \frac{1}{C_o V_p^2}$$

where $V_p = 3 \times 10^8$ m/s is the phase velocity of the air-filled line [14]. To check the validity and accuracy of the numerical method, the line capacitance computed by the method of moments with $\epsilon_2 = 1.0$ and $\epsilon_s = 6.15$ is compared with the line capacitance computed using the conformal mapping technique, as shown in Figure B.3.

The quality factor of the resonator is defined as the ratio of the total average energy stored in the resonator to the power dissipated in a cycle. At resonance $W_e = W_m = \frac{1}{4}CV^2$, thus the quality factor due to the dielectric loss can be obtained from [10]

$$Q_d = \omega \frac{W_e + W_m}{P} = \omega \frac{\frac{1}{2}CV^2}{\frac{1}{2}GV^2} = \frac{\omega C}{G}. \tag{B.11}$$

Another issue of practical importance is the finite extent of the substrate. The theoretical analysis given above is valid when the microstrip ground plane is infinitely large. In practice the resonator substrate is finite and its effect on the line capacitance and conductance per unit length derived for microstrip with an infinite ground plane

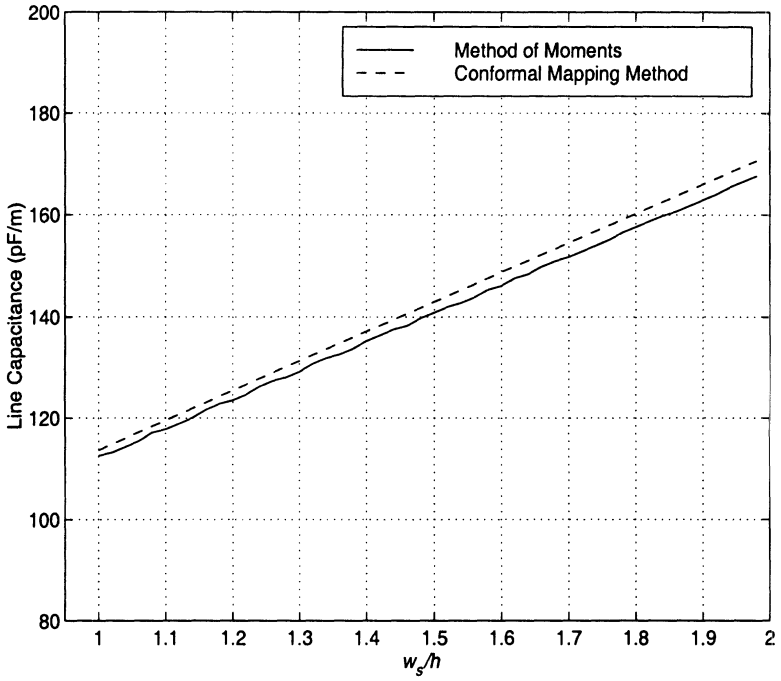

Figure B.3: Comparison between method of moments (solid line) and conformal mapping method (dashed line) in calculation of the line capacitance of a microstrip line with $\epsilon_s = 6.15$.

must be investigated. Figure B.2 shows a microstrip with a finite substrate and ground plane in contact with a half-space homogeneous medium. Our objective is to find the smallest substrate width w_g for which the difference between the line capacitance per unit length in this case and that of the infinite substrate is negligible. A simple integral equation for the surface charge density on the strip and ground plane is obtained. The substrate dielectric is replaced by the induced polarization charge

$$\rho_p = \epsilon_o(\epsilon_s - 1)\left[\delta(\mathbf{r} - \mathbf{r}_c)\hat{n} \cdot \mathbf{E} - \nabla \cdot \mathbf{E}\right] \tag{B.12}$$

where $\mathbf{r}_c$ is a position vector that specifies the contour of the substrate ($\mathcal{C}$) and $\hat{n}$ is an outward unit vector normal to the substrate boundary. After applying Green's theorem, the integral equation for the surface charge density and the complex potential

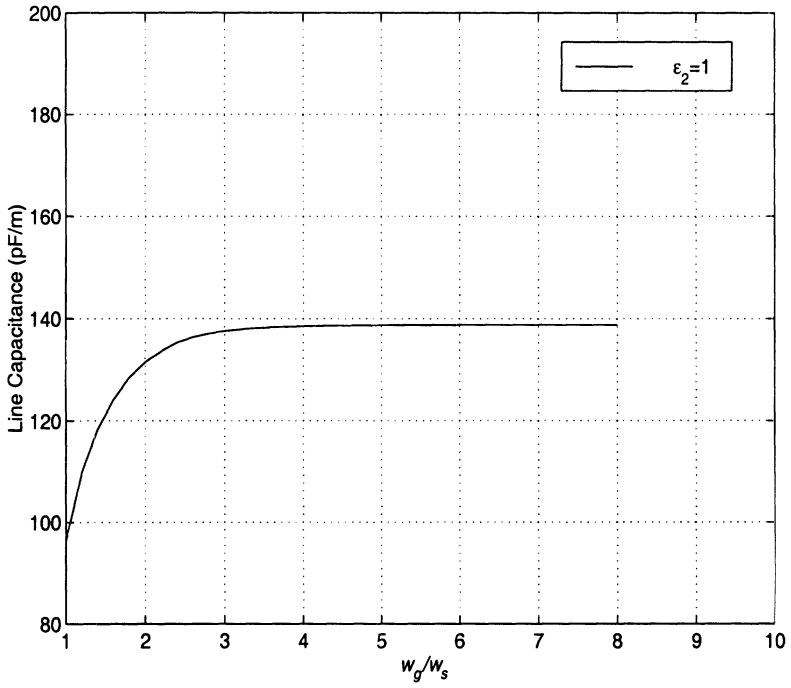

Figure B.4: Line capacitance of a finite substrate microstrip line with $\epsilon_s = 6.15$ and $w_s/h = 1.46$ as a function of w_g/w_s.

function is found to be

$$\begin{aligned}(\frac{\epsilon_s+1}{2})\phi(x,y) &= -\epsilon_o(\epsilon_s-1)\int_C \phi(x',y')\frac{\delta G(x,y;x',y')}{\delta n'}dc \\ &+ \int_{-w_s/2}^{w_s/2} \rho_s(x')G(x,y;x',0)dx' \\ &+ \int_{-w_g/2}^{w_g/2} \rho_g(x')G(x,y;x',-h)dx' \end{aligned} \tag{B.13}$$

where $G(x,y;x',y')$ is the Green's function of the half-space dielectric problem and is given by

$$G(x,y;x',y') = \frac{-1}{2\pi\epsilon_o}\left[\ln\sqrt{(x-x')^2+(y-y')^2} - \frac{\epsilon_2-1}{\epsilon_2+1}\ln\sqrt{(x-x')^2+(y+y')^2}\right]. \tag{B.14}$$

Once the integral equation is solved numerically the line capacitance and conductance per unit length can be obtained as shown before. Figure B.4 shows the line capacitance of a finite substrate microstrip line with $\epsilon_s = 6.15$, $h = 0.245$ cm, and

$w_s = 0.37$ cm as a function of w_g/w_s for $\epsilon_2 = 1$. It is shown that when $w_g/w_s > 5$ the infinite substrate formulation is sufficiently accurate for computation of the line capacitance.

B.3 Inversion Algorithm

In this section a retrieval algorithm for the complex dielectric constant of a half-space dielectric medium in contact with a microstrip ring resonator is sought. Following the standard cavity dielectric measurement approach the real and imaginary parts of the effective dielectric constant of the loaded resonator can be obtained, from which the complex dielectric constant of the half-space medium is inferred. Basically, first the resonant frequencies of the loaded (resonator in contact with the dielectric medium) and unloaded (resonator in free space) resonators are found from the measured frequency spectrum of $|S_{21}|$. Then noting that at resonance the electrical length of the resonator is equal to the guided wavelength, it can easily be shown that

$$\frac{f_u}{f_\ell} = \frac{Re[\sqrt{\epsilon_{e,\ell}}]}{\sqrt{\epsilon_{e,u}}} \tag{B.15}$$

where f_ℓ and f_u are, respectively, the resonant frequencies of the loaded and unloaded resonators. Since the ring resonator is a transmission line resonator, the relationship between the effective dielectric constant and the line parameters can be obtained from:

$$k_o\sqrt{\epsilon_e} = \omega\sqrt{LC(1 - j\frac{G}{\omega C})}.$$

Assuming that the substrate is lossless ($G_u = 0$) and noting that the line inductance is not a function of dielectric loading, it can be shown that

$$C_\ell = C_u\frac{\epsilon'_{e,\ell}}{\epsilon_{e,u}} \tag{B.16}$$

and

$$\frac{G_\ell}{\omega_\ell C_u} = \frac{\epsilon''_{e,\ell}}{\epsilon_{e,u}}. \tag{B.17}$$

Comparing (B.17) to (B.11) and using (B.16), the imaginary part of the effective dielectric constant of the loaded resonator can be obtained from

$$\epsilon''_{e,\ell} = \frac{\epsilon'_{e,\ell}}{Q_d}. \tag{B.18}$$

Using (B.15) and (B.18) the real part of the effective dielectric constant of the loaded resonator $\epsilon'_{e,\ell}$ in terms of measured $\frac{f_u}{f_\ell}$ and Q_d and $\epsilon_{e,u}$ can be obtained. Once $\epsilon'_{e,\ell}$ and $\epsilon''_{e,\ell}$ are known the line capacitance and conductance can be derived from (B.16) and (B.17).

Besides the dielectric loss, other factors such as radiation and conduction losses determine the quality factor of the resonator. If Q_u represents the quality factor of the unloaded resonator and Q_d is the quality factor due to the dielectric loss, the measured quality factor of the resonator (Q_m) can be obtained from [10]

$$\frac{1}{Q_m} = \frac{1}{Q_u} + \frac{1}{Q_d}. \tag{B.19}$$

Equation (B.19) can be used to measure Q_d when the radiation losses of the loaded resonator and unloaded resonator are the same or the radiation loss is negligible compared to the conductor and substrate losses. This can be verified by measuring the quality factor of the resonator when loaded with different lossless dielectrics. However, if the radiation loss is significant and varies with dielectric loading, (B.19) can be modified to

$$\frac{1}{Q_m} = \frac{1}{Q_u} + \frac{1}{Q_r} + \frac{1}{Q_d} \tag{B.20}$$

where Q_r is the quality factor due to radiation loss and its dependence on ϵ_2' must be determined empirically. As will be shown later, for most soil conditions $Q_d << Q_u$ and therefore characterization of Q_r with respect to ϵ_2' is not necessary.

The last step in the inversion algorithm is the computation of ϵ_2' and σ_2 from the measured C_l and G_l. In the previous section a numerical forward model for computation of the line capacitance and conductance in terms of ϵ_2' and σ_2 was developed. The forward model reveals that C_l and G_l are smooth functions of ϵ_2' and σ_2. Over the region of interest for ϵ_2' and σ_2 these functions are one-to-one, which implies that the inverse functions exist. Since $C(\epsilon_2', \sigma_2)$ and $G(\epsilon_2', \sigma_2)$ are gentle functions of ϵ_2' and σ_2, the inverse functions are also gentle functions of C and G. To demonstrate this fact, ϵ_2' and σ_2 versus the line capacitance and conductance of a microstrip with $\epsilon_s = 6.15$, $h = 0.245$ cm, and $w_s = 0.37$ cm are calculated numerically and are shown in Figures B.5 and B.6. It is shown that the line capacitance is strongly dependent on ϵ_2' and less influenced by σ_2 as expected. Also the line conductance is most sensitive to σ_2 and to a lesser extent to ϵ_2' . Therefore the inverse functions can simply be approximated by their Taylor series expansions, that is

$$\begin{aligned}\epsilon_2 \approx\ & a_0 + a_1 C + a_2 G + a_3 CG + a_4 C^2 + a_5 G^2 + a_6 CG^2 + a_7 C^2 G + a_8 C^3 + a_9 G^3 \\ & + a_{10} C^2 G^2 + a_{11} CG^3 + a_{12} C^3 G + a_{13} C^4 + a_{14} G^4 \qquad \text{(B.21)}\end{aligned}$$

$$\begin{aligned}\sigma_2 \approx\ & b_0 + b_1 C + b_2 G + b_3 CG + b_4 C^2 + b_5 G^2 + b_6 CG^2 + b_7 C^2 G + b_8 C^3 + b_9 G^3 \\ & + b_{10} C^2 G^2 + b_{11} CG^3 + b_{12} C^3 G + b_{13} C^4 + b_{14} G^4. \qquad \text{(B.22)}\end{aligned}$$

The coefficients of the polynomials can be obtained from the forward model using at least fifteen pairs of (C, G). However, in order to find a better estimate of the coefficients many more data points over the region of interest should be used in a least-mean-square estimator. Once the coefficients are determined, the measured C

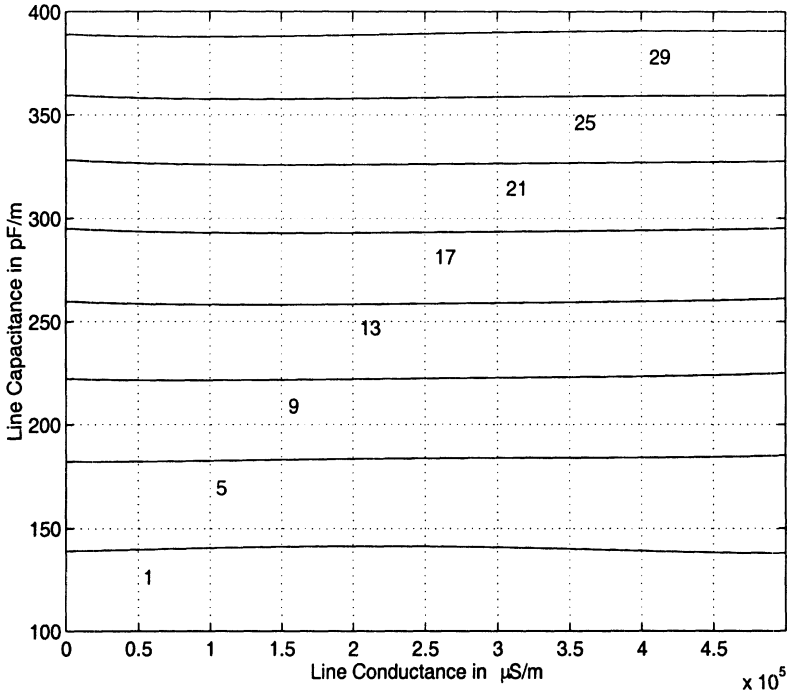

Figure B.5: Contour map of the real part of dielectric constant as a function of line conductance and capacitance for a microstrip line with $\epsilon_s = 6.15$ and $w_s/h = 1.46$.

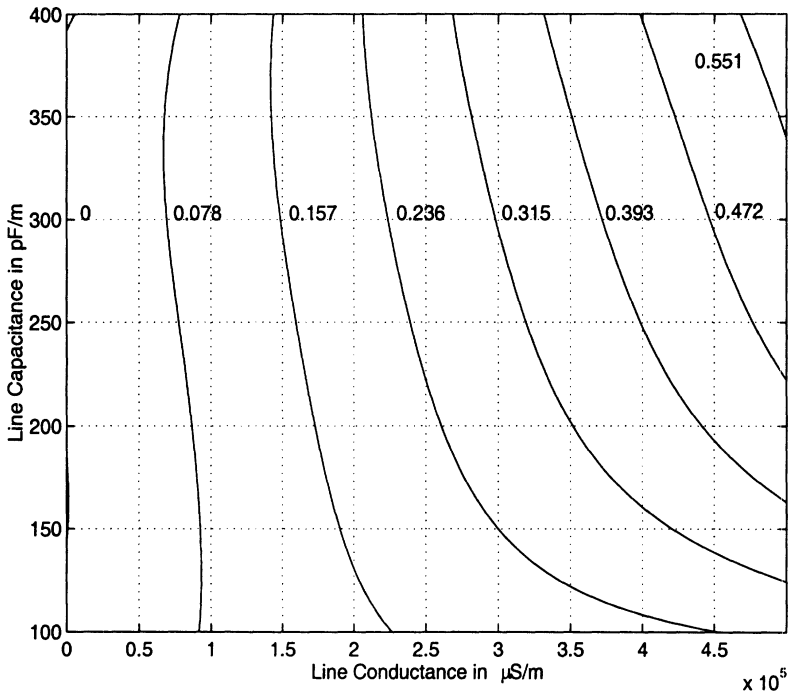

Figure B.6: Contour map of conductivity as a function of line conductance and capacitance for a microstrip line with $\epsilon_s = 6.15$ and $w_s/h = 1.46$.

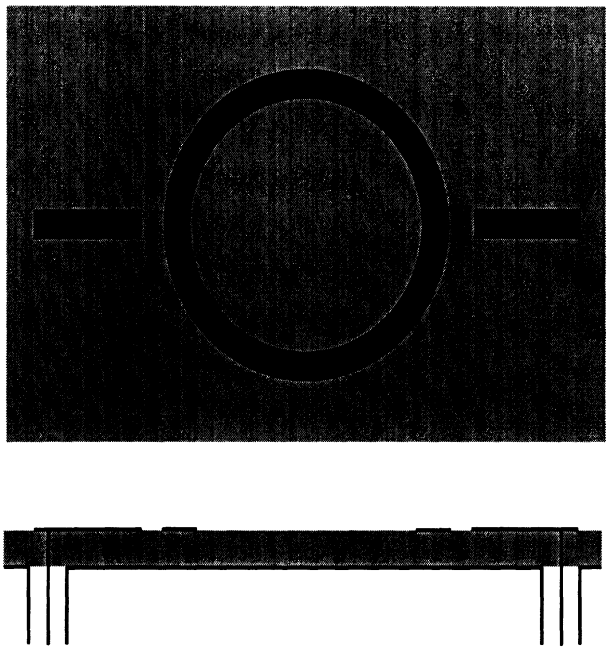

Figure B.7: Top view and side view of a conventional ring resonator.

and G can be used directly in (B.21) and (B.22) to find the unknowns ϵ_2' and σ_2.

B.4 Experimental Results

In this section the design considerations for the development of a prototype microstrip ring resonator and some experimental results are given. Prompted by the need for a high quality factor transmission line resonator, the ring resonator was preferred to other types of transmission line resonators, such as the half-wavelength straight line resonator. Another attractive feature of this resonator in measuring the dielectric constant of soil is its relatively large contact area with the soil medium. The coupling of energy to the resonator is accomplished using an unconventional method. Ring resonators are usually excited by a microstrip line through a capacitive air gap as shown in Figure B.7. However, for dielectric measurement applications it is better to excite the resonator with an open-ended coaxial line placed right underneath of the conducting strip as shown in Figure B.1. In this method the coupling capacitance of

the resonator is not affected by the dielectric constant of the unknown material and therefore the quality factor due to the resonator coupling (Q_u) remains unchanged. Another important design parameter is the resonator filling factor. This parameter signifies the percentage of the stored electric energy in the substrate to the overall stored energy. For example to measure very lossy dielectrics a large filling factor is required to keep most of the field lines inside the substrate. The filling factor is directly proportional to the line capacitance of the unloaded microstrip (inversely proportional to the unloaded characteristic impedance).

A microstrip ring resonator with a moderate filling factor that would allow accurate dielectric measurement of soil with volumetric moisture contents varying from 0% to 30% was designed using trial and error. It was found that a line with a characteristic impedance of 50 Ω would satisfy the filling factor requirements. For the prototype design, a Duroid 6006 substrate with $\epsilon_s = 6.15$ and $h = 0.254$ cm was used. The strip width and the ring perimeter for the required unloaded characteristic impedance of 50 Ω and a resonant frequency of 1.25 GHz were calculated to be $w_s = 0.37$ cm and $\ell = 11.35$ cm respectively. The dimension of the finite substrate was chosen so that the constraint $w_g/w_s > 5$ is satisfied for every point on the circular ring of the resonator. To examine the accuracy of the measurement technique and the aforementioned inversion algorithm, lossless reference dielectric samples were measured. An HP 8720 Network Analyzer with synthesized source was used to measure the quality factors and resonant frequencies reported. Five thick reference dielectric slabs (Stycast) with nominal dielectric constants of 3, 6, 10, 13, and 16 were measured using the prototype resonator. It was found that the measurement accuracy degrades as the dielectric constant of the medium increases.

The experiments indicate that the quasi-static approximation overestimates the

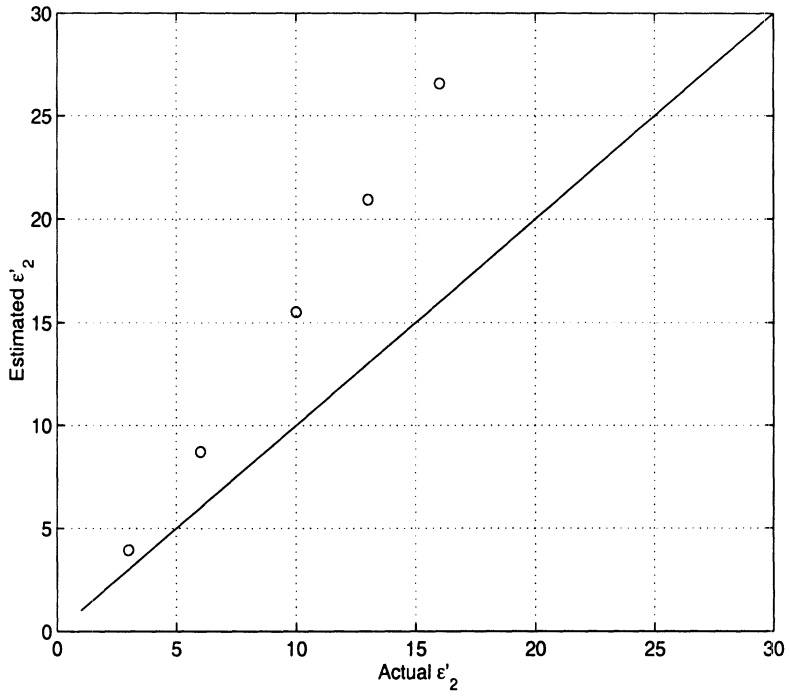

Figure B.8: Actual ϵ_2' vs estimated ϵ_2'.

line capacitance when the dielectric constant of the half-space medium is increased. Figure B.8 shows the actual dielectric constant versus the dielectric constant estimated by the quasi-static approximation. To investigate this phenomenon, two methods were pursued: (1) experimental, and (2) numerical. In the experimental investigation the effect of surface waves and the quasi-TEM nature of the approximate solution were examined. It is known that when the substrate height h is large the structure becomes capable of supporting surface waves in the substrate. Three thinner substrates were used to construct ring resonators (all with a characteristic impedance of 50 Ω) and the measurements with reference samples were repeated. The discrepancies were the same, independent of substrate thickness. Next we examined the effect of the quasi-TEM approximation in our formulation. For this purpose, a resonator was made from Duroid 6010 substrate with $\epsilon_s = 10$ and used to measure the permittivity of the Stycast sample with dielectric constant 10. In this

case the medium surrounding the microstrip is homogeneous and the fundamental mode of propagation is TEM. However, a discrepancy in the measured dielectric on the same order as before was observed. Having obtained inconclusive results from our experimental investigation, we resorted to numerical techniques. First a full-wave analysis for calculation of the effective propagation constant in microstrip lines based on the method of moments was used [30]. It was found that for the frequencies and microstrip dimensions used in this investigation the quasi-static solution provided very accurate results. Next the problem was analyzed completely using a three-dimensional FDTD numerical code [12]. After 20,000 iterations, corresponding to 7 hours CPU time on a Cray super-computer, it was found that the resonant frequency obtained by the FDTD method had a larger discrepancy with the measurement than did that obtained from the quasi-static method. One possible reason for the larger error is that the time-domain methods may not be very suitable for resonant structures.

As a last resort it was decided to rectify the problem by including an empirical correction factor in the quasi-static solution. Denote the line capacitances derived from the quasi-static solution and those measured from the inversion algorithm by C_q and C_m respectively. Figure B.9 shows the discrepancy in the line capacitance ($\Delta C = C_q - C_m$) as a function of the five measured dielectric constants. Since the measured discrepancy is a smooth function of ϵ_2 and no discrepancy exists when $\epsilon_2 = 1$ the following expression for the corrected line capacitance is obtained:

$$C_c = C_q - k(\epsilon_2' - 1), \tag{B.23}$$

where $k = 3.3572 \times 10^{-12}$ is calculated using a least-mean-square linear estimator. This corrected line capacitance is then used in (B.21) and (B.22) to derive the coef-

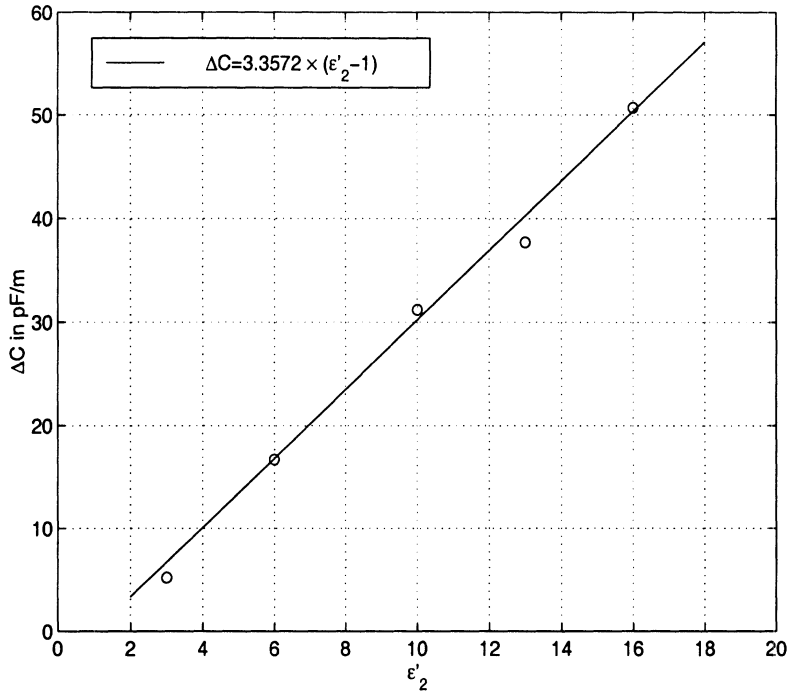

Figure B.9: ΔC as a function of ϵ_2'.

ficients $a_1 \cdots a_{14}$ and $b_1 \cdots b_{14}$.

To verify the accuracy of the ring resonator technique, a low loss liquid (heptane) of known dielectric constant was measured. The result was compared to the measurement performed by the cavity resonator technique and listed in Table B.1 where an excellent agreement is shown. Next, the behavior of the dielectric constant of sandy soil as a function of moisture content is studied. The prototype ring resonator is used to measure soil samples with volumetric moisture contents ranging from 0% to 30%. Figure B.10 shows typical responses of the ring resonator in contact with soil samples having moisture contents ranging from 0% to 30%. Three other independent techniques were also used to measure the soil samples, namely the open-ended coaxial probe, the cavity resonator, and the air-filled coaxial line. The dielectric measurement using the air-filled coaxial line is based on the reflection coef-

	ϵ_r'	ϵ_r''
Ring Resonator	1.85	0.0031
Cavity Resonator	1.81	0.0029

Table B.1: The dielectric constant of heptane measured by the ring resonator technique and the cavity resonator technique.

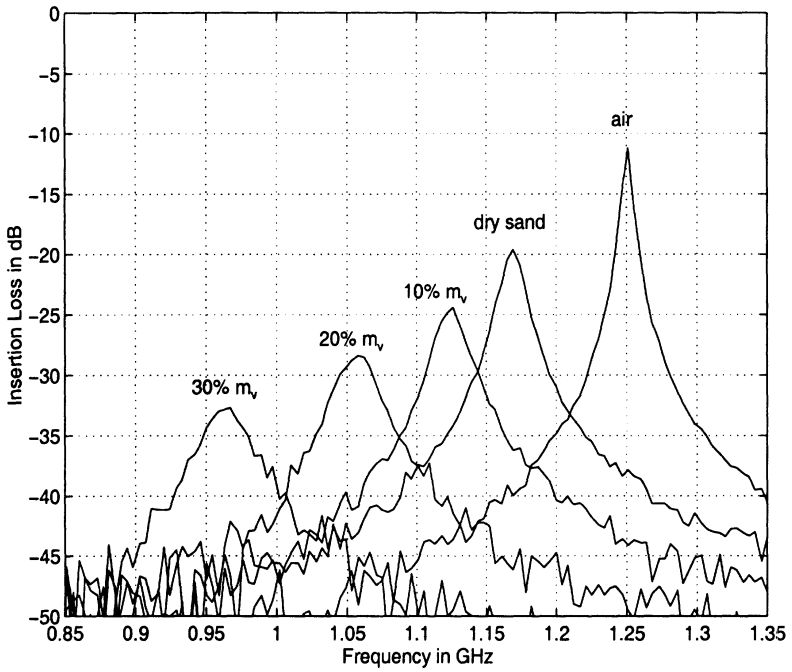

Figure B.10: Sand moisture spectral response.

ficient measurement of a short-circuited coaxial line filled with soil samples. In this method the middle section of a long hollow coaxial line is used as the sample holder as shown in Figure B.11. Measuring the reflection coefficient over a wide bandwidth (B) and using the time-domain capability of the network analyzer, the reflected signal is measured after traveling twice through the sample. The hollow section of the coaxial line must be longer than the spatial resolution ($3 \times 10^8/2B$) of the system. Figure B.12 shows the steps involved in measuring the reflection coefficient of the

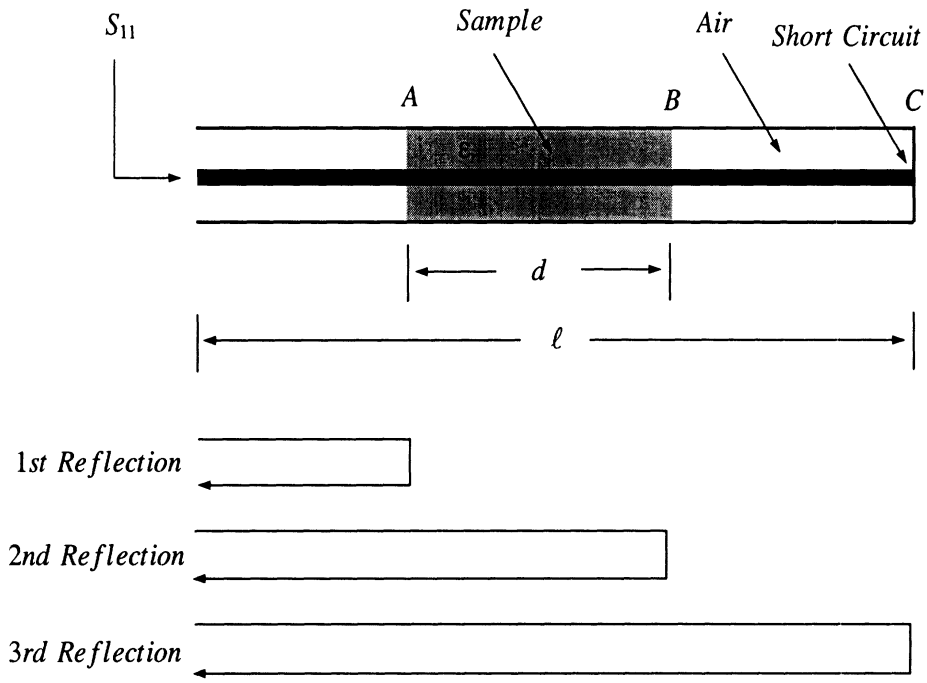

Figure B.11: The air-filled coaxial line sample holder.

short circuit for a 50 Ω air-line of length $l = 50$ cm filled with $d = 20$ cm of dry sand. The measured complex reflection coefficient is related to the dielectric constant of the sample through

$$S_{11} = -(1 - R^2)^2 e^{-j2k_o l} e^{-j2k_o(\sqrt{\epsilon_r}-1)d}, \tag{B.24}$$

where $R = \frac{1-\sqrt{\epsilon_r}}{1+\sqrt{\epsilon_r}}$ is the reflection coefficient at the interface of air and soil. By inverting (B.24) the real and imaginary parts of the soil dielectric are obtained. The accuracy of this method decreases as the imaginary part of the dielectric constant increases unless the sample length is decreased.

Figures B.13 and B.14 show the measured real and imaginary parts of the dielectric constants of the sandy soil with seven different moisture contents using the four independent measurement techniques. The cavity method could only be used for the 0% and 5% moisture conditions and shows an excellent agreement with the ring resonator measurement. For the real part of the dielectric constant the agreement

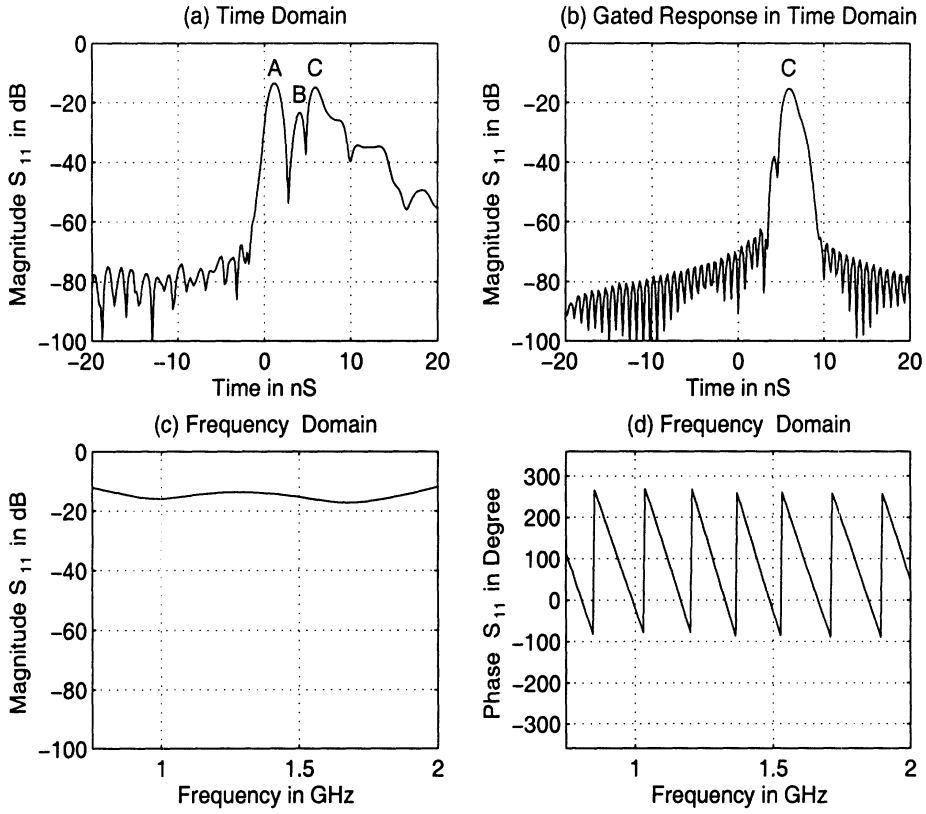

Figure B.12: Steps in the measurement of the short circuit reflection coefficient: (a) time-domain response of the total reflection coefficient, (b) gated time-domain response of the short circuit, (c) magnitude and (d) phase of the short circuit reflection coefficient.

among all four techniques is very good. However, it is seen that the coaxial probe overestimates the imaginary part of the dielectric constant as the moisture content increases.

B.5 Conclusions

Theoretical, numerical, and experimental aspects of a microstrip ring resonator based dielectric measurement device are discussed in this appendix. The real and imaginary parts of the dielectric constant of a homogeneous medium in contact with the ring resonator are calculated from the shift in the resonant frequency and the change in the quality factor of the resonator. The forward problem is solved by a nu-

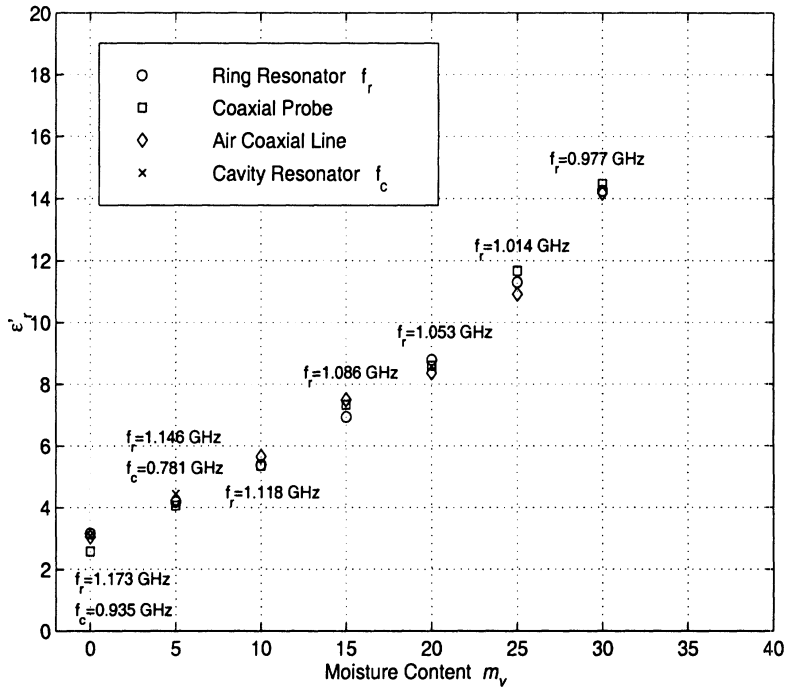

Figure B.13: Different methods for measuring ϵ'_r of sandy soil with various moisture contents.

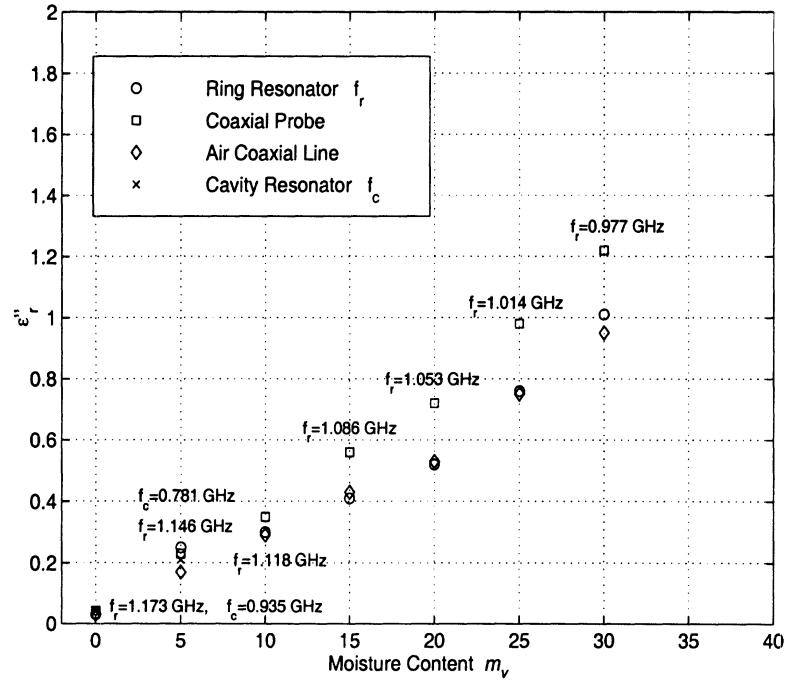

Figure B.14: Different methods for measuring ϵ''_r of sandy soil with various moisture contents.

merical analysis of the quasi-static solution. For the inverse problem simple algebraic expressions based on regression analysis of the forward problem are obtained. Measurements of reference dielectric samples showed that the accuracy of the quasi-static solution decreases as the dielectric constant of the half-space medium increases. To identify the source of error, full-wave numerical analysis and extensive experiments were conducted. Efforts in identifying the source of errors were inconclusive. The errors in the quasi-static solution are corrected empirically and inversion expressions obtained. The validity of the ring resonator measurement technique is demonstrated by comparing the measured dielectric constants of sandy soil with different moisture contents with those obtained from three other measurement methods. It is shown that the measurement technique is both accurate and versatile. The ring resonator, because of its large contact area, is very suitable for dielectric measurement of soil and can easily be implemented into a field portable device.

BIBLIOGRAPHY

BIBLIOGRAPHY

[1] 1990 Standard Specifications For Construction, pp. 466–483, Michigan Department of Transportation, 1990.

[2] 1996 Annual Book of ASTM Standards, Section 4 "Construction," pp. 137–142, 1996.

[3] C. A. Balanis, *Advanced Engineering Electromagnetics*, Chapter 11, John Wiley & Sons, New York, 1989.

[4] P. Beckmann and A. Spizzichino, *The Scattering of Electromagnetic Waves from Rough Surfaces*, Pergamon, New York, 1963.

[5] P. A. Bernard and J. M. Gautray, "Measurement of Dielectric Constant Using a Microstrip Ring Resonator," *IEEE Trans. on Microwave Theory and Techniques,* vol. 39, no. 3, pp. 592–595, March 1991.

[6] Alona Boag, Amir Boag, E. Michielssen, and R. Mittra, "Design of Electrically Loaded Wire Antennas Using Genetic Algorithms," *IEEE Trans. Antennas Propagat.,* vol. 44, no. 5, pp. 687–695, May 1996.

[7] W. M. Boerner, M. B. El-Arini, C. Y. Chan, and P. M. Mastoris, "Polarization Dependence in Electromagnetic Inverse Problems," *IEEE Trans. Antennas Propagat.,* vol. AP-29, no. 2, pp. 262–271, March 1981.

[8] M. C. Burl, W. W. Irving, and L. M. Novak, "Optimal Polarimetric Processing for Enhanced Target Detection," *IEEE Trans. Aerospace Electron. Sys.*, vol. 29, pp. 234–244, Jan. 1993.

[9] M. J. Campbell and J. Ulrichs, "Electrical Properties of Rocks and Their Significance for Lunar Radar Observations," *J. Geophys. Res.,* vol. 74, pp. 5867–5881, 1969.

[10] R. E. Collin, *Foundations for Microwave Engineering*, Chapter 7, McGraw-Hill, New York, 1966.

[11] K. A. DeJong, "An Analysis of the Behavior of a Class of Genetic Adaptive Systems," Ph.D. Dissertation, The University of Michigan, Ann Arbor, 1975.

[12] N. Dib, Personal Communication.

[13] D. Eliyahu, "Vector Statistics of Correlated Gaussian Fields," *Physical Review*, vol. 74, no. 4, pp. 2881–2892, April 1993.

[14] R. S. Elliott, *An Introduction to Guided Waves and Microwave Circuits*, pp. 61–67, Prentice Hall, Englewood Cliffs, New Jersey, 1993.

[15] K. Enke, 7th International Technological Conference on Experimental Safety Vehicles, 1979.

[16] L. Eriksson and S. Broden, "High Performance Automotive Radar," *Microwave Journal*, pp. 24–38, Oct. 1996.

[17] A. K. Fung, *Microwave Scattering and Emission Models and Their Applications*, Chapter 5, Artech House, Norwood, Massachusetts, 1994.

[18] P. E. Gill, W. Murray, and M. H. Wright, *Practical Optimization*, pp. 96–98, Academic Press, London, 1981.

[19] D. E. Goldberg, *Genetic Algorithms in Search, Optimization, and Machine Learning*, Addison-Wesley, Reading, Massachusetts, 1989.

[20] R. F. Harrington, *Time-harmonic Electromagnetic Fields*, Chapter 5, McGraw-Hill, New York, 1961.

[21] R. Hartikka, A. Nashashibi, K. Sarabandi, P. Siqueira, F.T. Ulaby, P. Lang, S. Lohmeier, R. McIntosh, and J. Mead, "Handbook of Millimeter-wave Polarimetric Radar Response of Terrain," Technical Report, The Radiation Lab., The University of Michigan, Ann Arbor, Michigan, Jan. 1995.

[22] R. L. Haupt, "Thinned Arrays Using Genetic Algorithms," *IEEE Trans. Antennas Propagat.*, vol. 42, no. 7, pp. 993–999, 1994.

[23] R. L. Haupt, "An Introduction to Genetic Algorithms for Electromagnetics," *IEEE Antennas Propagat. Magazine,* vol. 37, no. 2, pp. 7–15, April 1995.

[24] A. Hendry and G. C. McCormick, "Deterioration of Circular Polarization for Clutter Cancellation in Anisotropic Precipitation Media," *Electron. Lett.,* vol. 10, pp. 165–166, 1974.

[25] M. Herman, "High Frequency Scattering from Canonical Impedance Structures," Ph.D. Dissertation, The University of Michigan, 1987.

[26] R. K. Hoffman, *Handbook of Microwave Integrated Circuits*, Artech House, Norwood, Massachusetts, 1987.

[27] J. H. Holland, "Genetic Algorithms," *Scientific American,* pp. 66–72, July 1992.

[28] J. R. Huynen,"Phenomenological Theory of Radar Targets," Ph.D. Dissertation, Drukkerij Bonder-Offset, N.V., Rotterdam, 1970.

[29] G. A. Ioannidis and D. E. Hammers, "Optimum Antenna Polarization for Target Discrimination in Clutter," *IEEE Trans. Antennas Propagat.*, vol. 27, pp. 357–363, May 1979.

[30] R. W. Jackson and D. M. Pozar, "Full-wave Analysis of Microstrip Open-end and Gap Discontinuities", *IEEE Trans. on Microwave Theory and Techniques,* vol. MTT-33, no. 10, pp. 1036–1042, Oct. 1985.

[31] I. R. Joughin, D. P. Winebrenner, and D. B. Percival, "Probability Density Functions for Multi-look Polarimetric Signatures," *IEEE Trans. Geosci. Remote Sensing,* vol. 32, no. 3, pp. 562–574, May 1994.

[32] J. R. Kendra, "Microwave Remote Sensing of Snow: An Empirical/Theoretical Scattering Model for Dense Random Media," Ph.D. Dissertation, The University of Michigan, 1995.

[33] E. M. Kennaugh, "Effect of the Type of Polarization on Echo Characteristics," Report 389-9, Antenna Laboratory, The Ohio State University, Columbus, Ohio, Sept. 1951.

[34] S. Kirkpatrick, J. C. D. Gelatt, and M. P. Vecchi, "Optimization by Simulated Annealing," *Sci.,* vol. 220, pp. 671–680, 1983.

[35] J. A. Kong, *Electromagnetic Wave Theory*, Chapter 3, John Wiley & Sons, New York, 1990.

[36] J. D. Kraus, *Electromagnetics*, 4th Edition, pp. 605, McGraw-Hill, New York, 1992.

[37] C. M. Lam and A. Ishimaru, "Calculation of Mueller Matrices and Polarization Signatures for a Slab of Random Medium Using Vector Radiative Transfer," *IEEE Trans. Antennas Propagat.,* vol. 41, no. 7, pp. 851–862, July 1993.

[38] M. Lax, "Multiple Scattering of Waves, II. The Effective Field in Dense Systems," *Physical Review,* vol. 85, no. 4, pp. 621–629, Feb. , 1952.

[39] G. D. Maliuzhinets, "Some Generations of the Method of Reflections in the Theory of Sinusoidal Wave Diffraction," Doctoral dissertation, Fiz. Inst. Lebedev, Acad. Nauk. SSR (in Russian).

[40] G. D. Maliuzhinets, "Excitation, Reflection and Emission of Surface Waves from a Wedge with Given Face Impedances," *Sov. Phys. Doklady*, 3, pp. 752–755.

[41] G. C. McCormick and A. Hendry, "Polarization Related Parameters for Rain: Measurements Obtained by Radar," *Radio Science,* vol. 11, pp. 731–740, Aug./Sept. 1976.

[42] E. Michielssen, J. Sajer, S. Ranjithan, and R. Mittra, "Design of Lightweight, Broad-band Microwave Absorbers Using Genetic Algorithms," *IEEE Trans. Microwave Theory Techniques,* vol. 41, no. 6/7, pp. 1024–1031, 1993.

[43] A. Nashashibi and K. Sarabandi, "Experimental Characterization of the Effective Propagation Constant of Dense Random Media," *IEEE Trans. Antennas Propagat.,* submitted for publication (August 1995).

[44] A. Nashashibi, K. Sarabandi, and F. T. Ulaby, "A Calibration Technique for Polarimetric Coherent-on-receive Radar System," *IEEE Trans. Antennas Propagat.,* vol. 43, no. 4, pp. 396–404, April 1995.

[45] M. Nieto-Vesperinas, "De-polarization of Electromagnetic Waves Scattered from Slightly Rough Random Surfaces: A Study by Means of the Extinction Theorem," *J. Opt. Soc.* 72(5), pp. 539–547, 1982.

[46] D. Polder and J. H. Van Santen, "The Effective Permeability of Mixtures of Solids," *Physics*, vol. 12, no. 5, pp. 1257–1271, Aug. 1946.

[47] A. V. Oppenheim and R. W. Schafer, *Digital Signal Processing*, Prentice-Hall, Englewood Cliffs, New Jersey, 1975.

[48] S. O. Rice, "Reflection of Electromagnetic Wave by Slightly Rough Surfaces," *Communications in Pure and Applied Mathematics*, vol. 4, pp. 351–378, 1951.

[49] E. Rodriguez and Y. Kim, "A Unified Perturbation Expansion for Surface Scattering," *Radio Science*, vol. 27, no. 1, pp. 79–93, Jan./Feb. 1992.

[50] T. Rose, "Intelligent Vehicle Highway Systems: Going Places Fast," *Microwave Journal*, pp. 172–178, May 1993.

[51] K. Sarabandi, "Electromagnetic Scattering from Vegetation Canopies," Ph.D. Dissertation, The University of Michigan, 1989.

[52] K. Sarabandi, "Derivation of Phase Statistics of Distributed Targets from the Mueller Matrix," *Radio Science,* vol. 27, no. 5, pp. 553–560, Sept./Oct. 1992.

[53] K. Sarabandi, "Δk-Radar Equivalent of Interferometric SAR's: A Theoretical Study for Determination of Vegetation Height," *IEEE Trans. Geosci. Remote Sensing,* vol. 35, no. 5, Sept. 1997.

[54] K. Sarabandi and P. Siqueira, "Numerical Scattering Analysis for Two-dimensional Dense Random Media: Characterization of Effective Permittivity," *IEEE Trans. Antennas Propagat.,* vol. 45, no. 5, pp. 858–867, May 1997.

[55] T. B. A. Senior and J. L. Volakis, *Approximate Boundary Conditions in Electromagnetics*, Chapter 4, IEE Press, London, 1995.

[56] R. Shin and J. A. Kong, "Radiative Transfer Theory for Active Remote Sensing of a Homogeneous Layer Containing Spherical Scatterers," *J. Appl. Phys.,* vol. 52, no. 6, pp. 4221–4230, June 1981.

[57] P. Siqueira, "Wave Propagation and Scattering in Dense Random Media," Ph.D. Dissertation, The University of Michigan, 1996.

[58] Y. Takimoto and M. Kotaki, "Recent Development of Millimeter-wave Applications in Japan," *Microwave Journal*, pp. 214–226, May 1996.

[59] G. C. Topp and J. L. Davis, "Measurement of Soil Water Content Using Time-domain Reflectometry (TDR): A Field Evaluation," *Soil Sci. Soc. Am. J.,* vol. 49, pp. 19–24, 1985.

[60] L. Tsang, J. A. Kong, and R. Shin, *Theory of Microwave Remote Sensing,* John Wiley & Sons, New York, 1985.

[61] L. Tsang and A. Ishimaru, "Radiative Wave Equations for Vector Electromagnetic Propagation in Dense Non-tenuous Media," *J. Electromagn. Waves Appl.*, vol. 1, no. 1, pp. 52–72, 1987.

[62] F. T. Ulaby, R. K. Moore, and A. K. Fung, *Microwave Remote Sensing*, vol. II, Chapters 11 and 12, Artech House, Norwood, Massachusetts, 1982.

[63] F. T. Ulaby, R. K. Moore, and A. K. Fung, *Microwave Remote Sensing*, vol. III, Chapter 13 and Appendix E, Artech House, Norwood, Massachusetts, 1986.

[64] F. T. Ulaby and C. Elachi, *Radar Polarimetry for Geoscience Applications,* Chapters 2 and 3, Artech House, Norwood, Massachusetts, 1990.

[65] F. T. Ulaby, K. Sarabandi, K. McDonald, M. Whitt, and M. C. Dobson, "Michigan Microwave Canopy Scattering Model," *Int. J. Remote Sensing*, vol. 11, no. 7, pp. 1223–1253, July 1990.

[66] F. T. Ulaby, M. W. Whitt, and K. Sarabandi, "AVNA-based Polarimetric Scatterometers," *IEEE Antennas Propagat. Magazine*, vol. 32, 1990.

[67] F. T. Ulaby, T. H. Bengal, M. C. Dobson, J. R. East, J. B. Garvin, and D. L. Evans, "Microwave Dielectric Properties of Dry Rocks," *IEEE Trans. on Geoscience and Remote Sensing,* vol. 28, no. 3, pp. 325–336, May 1990.

[68] F. T. Ulaby, personal communication.

[69] P. V. Vainikainen, E. G. Nyfors, and M. T. Fischer, "Radiowave Sensor for Measuring the Properties of Dielectric Sheets: Application to Veneer Moisture Content and Mass per Unit Area Measurement," *IEEE Trans. Inst. Measurement,* vol. 36, no. 4, Dec. 1987.

[70] J. J. van Zyl, "On the Importance of Polarization in Radar Scattering Problems," Ph.D. Dissertation, California Institute of Technology, 1986.

[71] J. J. van Zyl, N. Engheta, C. H. Papas, C. Elachi, and H. A. Zebker, "Modeling of Backscatter from Vegetation Layers," *IEEE Geoscience and Remote Sensing Symposium Digest,* vol. 1, pp. 389–394, 1985.

[72] H. A. Wallace and J. R. Martin, *Asphalt Pavement Engineering,* Chapter 3, McGraw-Hill, New York, 1967.

[73] R. West, L. Tsang, and D. P. Winebrenner, "Dense Medium Radiative Transfer Theory for Two Scattering Layers with a Rayleigh Distribution of Particle Sizes," *IEEE Trans. Geosci. Remote Sensing,* vol. 31, no. 2, pp. 426–437, March 1993.

[74] D. Winebrenner and A. Ishimaru, "Investigation of a Surface Field Phase Perturbation Technique for Scattering from Rough Surfaces," *Radio Science*, vol. 20, no. 2, pp. 161–170, March/April 1985.

[75] J. D. Woll, "Radar Based Vehicle Collision Warning System,"